DYNAMIC FUNCTIONAL CONNECTIVITY BETWEEN CORTEX AND MUSCLES

by

Sagi Perel

B.Sc., Electrical Engineering and Computer Science, Tel-Aviv University, 2005

Submitted to the Graduate Faculty of

the Swanson School of Engineering in partial fulfillment

of the requirements for the degree of

Doctor of Philosophy

University of Pittsburgh

2012

UNIVERSITY OF PITTSBURGH

SWANSON SCHOOL OF ENGINEERING

This dissertation was presented

by

Sagi Perel

It was defended on

April 30th 2012

and approved by

Andrew B. Schwartz, Ph.D., Professor, Department of Neurobiology

Robert E. Kass, Ph.D., Professor, Department of Statistics

Douglas J. Weber, Ph.D., Assistant Professor, Department of PM&R

Xudong Zhang, Ph.D., Associate Professor, Department of Orthopedic Surgery

Dissertation Director: Andrew B. Schwartz, Ph.D., Professor, Department of Neurobiology

DYNAMIC FUNCTIONAL CONNECTIVITY BETWEEN CORTEX AND MUSCLES

Sagi Perel, PhD

University of Pittsburgh, 2012

The motor-cortex is recognized as the origin of the major direct path from cortex to muscles. Although it has been studied for over a century, relatively little is known about how the motor cortex facilitates reach-to-grasp movements. We collected a rich dataset from monkeys trained to reach and grasp objects of different shapes, presented at various orientations and spatial locations. We simultaneously recorded single-unit activity from motor cortical areas (mainly the caudal bank of the pre-central gyrus), EMG activity from selected muscles (in the arm, wrist and hand) and high-resolution kinematic data from the wrist and hand.

We show that motor-cortical neurons modulate their activity in an object specific manner, resulting in object specific co-activation of muscles and joint movements. We studied the multivariate relationships between the firing rates of individual neurons, EMG, joint angles and joint angle velocities and found that both EMG and kinematic features were encoded in the neural firing rates. Kinematic features were much better predictors of neural firing rates than EMG. We found that the best predictors of neural firing rates were neither individual muscles or joints, nor kinematic or EMG synergies extracted using PCA/ICA, but neuron-specific combinations of EMG and kinematic features. We show better predictions of both muscle activations and JA values by combining the activity of a few tens of sequentially recorded neurons; suggesting that neural activity contains synergistic information related to EMG, not independently present in individual neurons.

By using functional connectivity, defined as the probability of observing changes in EMG following spikes from a trigger neuron, we further elucidated motor cortical activity to muscle activation. By studying both the short-time scale functional connectivity, on the order of milliseconds; and long-time scale functional connectivity, on the order of hundreds of milliseconds, we found

that flexible long-time scale functional connections between individual neurons and muscles were modulated by kinematic features that could account for the relatively weaker neural firing rate relation to EMG. To support our findings, we show examples of simultaneous short-time scale functional connectivity and conclude that neuronal-muscular functional connectivity is flexible and task-dependent.

TABLE OF CONTENTS

LIST OF TABLES

LIST OF FIGURES

PREFACE

First and foremost, I thank my advisor, Andrew Schwartz, whose infectious scientific enthusiasm made this endeavor an enjoyable one. Our frequent discussions and his guidance have helped me steer my way through the obstacles which are often part of experimental research. I have learned a lot from him about critical thinking and "looking at the big picture".

I would like to acknowledge the many other people who have been part of my professional life in the past 7 years. I thank the members of our lab who provided support and assistance in various ways: Meel Velliste, with whom I spent countless hours making the neural prosthetics project a reality; Chance Spalding, for his help in surgeries and the initial experimental setup; Laurel Sinko, for animal training, electrode crafting and professional help; George Fraser, for his help with surgeries, and his amazing ability to manufacture hardware, saving me long hours of work; Steve Chase, for his constructive advice with data analysis; and Scott Kennedy, for his help with animation rendering. I want to thank other members of the lab with whom I had fun and useful discussions: Angus McMorland, Andrew Whitford, Michael Palazzolo, Samuel Clanton and Morgan Jeffries. I would also like to thank our rotation students: Hrishikesh Rao and Sharlene Flesher, for help with data analysis. I owe a tremendous debt of gratitude to Valérie Ventura, who broadened my knowledge of statistics, helped shape my ideas into working models, and helped me make this project a success. I also thank Rob Kass for insightful suggestions about data analysis.

On a personal level, I thank my parents, who encouraged me to follow my dreams and provided daily support from the other side of the ocean. Last and most important, my wife, Tal and my sons, Tom and Yuval, who stood by me, gave me freedom to pursue my passion, provided emotional support and the much appreciated everyday fun. Thank you.

1.0 INTRODUCTION AND BACKGROUND

1.1 VIEWS OF THE MOTOR CORTEX

The classic work of Fritsch and Hitzig [20] has demonstrated three important points. First, the cortex has a meaningful function. Second, the cortex is excitable. Third, the cortex has a gross topographical representation of the body. Subsequent studies revolved around the idea that the primary motor cortex is a somatotopic array of upper motor neurons, each projecting to spinal motoneuron pools of a few muscles. Attempts were made to localize motor functions in the cortex more and more precisely using minimum current, resulting in detailed motor cortex maps (Leyton and Sherrington [38], Penfield and Rasmussen [49]). The focus was set on the representation of muscles in the motor cortex rather than the representation of movement. The motor cortex was thought to be a mosaic of points, each activating one or two muscles, thus causing a flick or a twitch. Its role was presumed to combine these flicks into coordinated movements.

Evarts [11] launched the era of single neuron recording in behaving monkeys in the late 60s, and although he supported the locality theory, evidence from micro-electrode recording eventually led researchers to abandon it. This evidence suggested that the motor cortical map of the body is fractured and intermingled, and that the motor cortex does not control individual muscles. Rather, the connectivity from motor cortex to muscles seemed more complex.

Single neuron recording allowed investigation of neural tuning during voluntary movement. At first, mostly single joint movements were studied, but during the 1980*s*, experiments investigating multi-joint movements were conducted. Motor neuronal activity has been correlated with a variety of parameters such as force [11], end point velocity [22], joint rotation [18] and more. However, the question of whether the motor cortex codes low level parameters such as muscle tension as well as high level kinematic parameters remains unanswered to date. In a classic paper, Phillips [50]

addresses the issue of ”muscles VS movements”: does the motor cortex control individual muscles or coordinated movements? He argues against the belief that there are two alternative hypotheses: muscles or movements, such that one or the other could be refuted by an experiment; reasoning that while it is possible that the motor cortex ”thinks“ in terms of movements or muscles, one does not negate the other. Only by carefully studying cortico-spinal connectivity during a wide repertoire of behaviors, Phillips believed, can we hope to gain more insight to how motor-cortical activity is related to both muscle contraction and movement.

Anatomical studies have shown that motor cortex projects to motoneuronal pools in the primate spinal cord both directly (monosynaptically) and indirectly (polysynaptically). This suggests that the motor cortex has the capability to affect muscle contraction. Other studies have shown that projections from subcortical and spinal structures also converge in the motoneuronal pools; indicating that the combination of cortical, subcortical and spinal projections determines the excitability of the motor units responsible for muscle contraction. The relative contributions of these different sources and how they combine to generate movement are still poorly understood and are the focus of ongoing work.

1.2 ANATOMICAL CONNECTIVITY BETWEEN CORTEX AND MUSCLES

Skeletal muscles are contractile elements driven by spinal motoneurons. Each muscle is composed of several compartments containing muscle fibers. Each muscle fiber is innervated by a single motoneuron, but a single motoneuron innervates more than one muscle fiber. Therefore, in order to facilitate efficient contraction of the whole muscle, motoneurons have to fire in a coordinated fashion. Motoneurons are somatotopically organized in the spinal cord so the ones innervating a particular muscle are arranged in a column and are segregated from the ones innervating other muscles. Motoneuronal columns of synergists are interleaved, which makes their mutual activation easier, whereas columns of antagonists are spatially segregated.

Spinal motoneurons receive inputs from cortical neurons via several pathways, including the corticospinal, corticobulbar and rubrospinal tracts. They also receive extensive sensory input from Golgi tendon organs, muscle spindles, mechanoreceptors and other sensory neurons; most of which

mediates spinal reflexes. Most of the input to alpha-motoneurons originates in spinal interneurons, such as Renshaw cells.

Motor cortical neurons make either monosynaptic or polysynaptic connections to spinal motoneurons, but the majority of the cortical input to motoneurons is polysynaptic. In a recent study, rabies virus was used to identify neuronal inputs to spinal motoneurons [56]. When injected into a muscle, this virus transports transneuronally in the retrograde direction over a period of days, labeling first order neurons and then second order, third order neurons etc. The results demonstrated that motoneurons receive direct inputs from dorsal root ganglion cells (muscle spindle afferents), spinal interneurons, and corticomotoneuronal (CM) cells in layer V of the motor cortex. Third order neurons in motor cortex, synapsing on spinal interneurons and CM cells were found both in layers III and V. Most of the cells innervating digit muscles were found predominantly in the bank of the central sulcus, rather than the precentral gyrus. The study also compared a map generated by electrically stimulating parts of the motor cortex to the anatomical map derived from the rabies virus labeling. Some overlap between the two maps was present, but it was clear that stimulating an area where CM cells innervating digit muscle are present, could elicit shoulder movements and not necessarily digit movements. On the other hand, stimulating an area where almost no CM cells were present, elicited digit movements. This strengthens the view that CM cells innervating different motoneuronal pools are intermingled and not arranged in cortical columns. It also demonstrates that anatomical connectivity does not guarantee functional connectivity: that a CM cell and a motoneuron are anatomically connected, does not imply that CM cell activity would facilitate motoneuronal firing. A single CM cell is only one out of thousands of inputs to the motorneuronal pool and in order to facilitate the motoneuron to fire, other inputs have to be simultaneously active.

A follow up study [57] confirmed the results above and also suggested an anatomical division of M1 into a rostral region, lacking CM cells, and a caudal region, buried within the bank of central sulcus, which exists only in higher primates and contains most CM cells. The rostral region was termed ”old M1“. It contains neurons projecting down through the corticospinal tract (CST) synapsing directly to interneurons in the intermediate zone of the spinal cord. Therefore, these neurons affect motoneurons through a polysynaptic (at least disynaptic) pathway. The caudal region was termed ”new M1“. It contains a population of CM cells which also project down through the CST and makes a direct monosynaptic connection to motoneurons in the ventral horn of the

spinal cord. The conclusion of the study was that the ”new” M1 bypasses the spinal interneuronal network, therefore enabling novel patterns of motor output to emerge, especially ones essential for highly skilled movements. These conclusions were based on anatomical evidence, and functional studies confirming such segregation are yet to be conducted.

1.3 FUNCTIONAL CONNECTIVITY BETWEEN CORTEX AND MUSCLES

1.3.1 DYNAMIC CONNECTIVITY BETWEEN CORTEX AND MUSCLES

A high degree of correlation between the spiking activity of a single motor cortical neuron and the presence of contraction in a single muscle does not necessarily indicate a causal relationship and does not preclude significant correlation to other co-activated muscles. Fetz and Finocchio [13, 14] studied the stability of the relationship between motor cortical neurons and contraction of muscles included in their muscle field. A monkey was trained to perform isometric contractions in one of four forelimb muscles, while the arm was immobilized to prevent movement. The monkey was able to activate one muscle at a time, while suppressing EMG activity in the other recorded muscles. Fetz and Finocchio then recorded the activity of motor cortical neurons, identified as pyramidal tract neurons (PTNs), which were selectively active for only one of the four muscles. They reinforced the monkey, using food reward, to produce bursts of activity in the recorded neuron, while suppressing EMG activity in all four recorded muscles. After many repetitions, the monkey was able to successfully activate the cortical neuron, while no measurable EMG was present in the recorded muscles. They also attempted the reverse dissociation, in which the monkey was reinforced for producing EMG activity in the relevant muscle, without activating the cortical neuron. This was never fully achieved, as the monkey was only able to reduce the firing of the cortical neuron. These results demonstrated a flexible relationship between the neurons and muscles under study. Fetz and Finocchio hypothesized that output from the cortical neuron was dependent on other spinal connections which modified their activity to prevent the motor cortical output from eliciting muscle contraction. A possible explanation of the failure of the reverse dissociation was that at least some activity in the recorded neurons was necessary to elicit contraction in the muscle

tested, and the resistance of the relationship to the reverse dissociation was suggested to indicate a causal connection. Fetz and Finocchio noted that the flexibility of the association did not preclude a causal relationship since it is possible that the influence of the neuron was canceled by other spinal or cortical circuitry.

Correlations, as measured by covariation over relatively long timescales (few hundred milliseconds), are neither necessary nor sufficient to demonstrate anatomical connectivity between a motor cortical neuron and a muscle. A number of studies have examined the cross-correlation of motor cortical neuronal activity and limb muscles and have demonstrated that the probability of muscle activity increased or decreased following neuronal spikes. Those changes often began late, were slow and lasted for too long to provide evidence of a direct effect of the cortical neuron on muscle activity. However, a demonstration of a fast change in the probability of motor unit activity following spikes from a cortical neuron, occurring at the appropriate monosynaptic latency, could provide evidence in favor of a causal relationship. The motor cortical neuron would then have to be a corticomotoneuronal cell, with a direct projection to the motoneuronal pool.

Fetz et al. [16], have examined 200 motor cortical neurons, which covaried their activity during movement. Of those, 54 neurons showed transient increases in EMG activity following the cortical spikes, with onset latencies between 4.3 and 11.5ms. 35 neurons were identified as PTNs, and out of those only 4 showed the transient increases in EMG, termed post-spike facilitation (PSpF). Post-spike facilitation was observed in either a single muscle, or a group of synergistic muscles; but post-spike suppression was not detected, even in antagonist muscles. Fetz et al. concluded that corticomotoneuronal cells have a very limited muscle field, and could only engage a small number of related muscles. The observed post-spike effects (PSE) were very small, indicating that a single corticomotoneuronal cell has a very small excitatory influence on the motoneurons through its synapses. The fact that the monosynaptic effect was detected only for a small fraction of the studied neuron-muscle pairs suggests that most PTNs do not make a direct connection to spinal motoneurons. The commonly observed correlation between cortical activity and EMG, often seen for many muscles simultaneously, might reflect net changes in spinal interneurons excitability, affected by the cortical spikes.

1.3.2 SHORT AND LONG TIME-SCALE CORRELATIONS BETWEEN CORTEX AND MUSCLES

Fetz et al. introduced the method of spike-triggered averaging (SpTA) for the detection of post-spike effects [15, 16]. A spike-triggered average (SpTA) shows changes in a muscle's EMG activity following spikes from a cortical neuron. Pre-analysis, EMG is usually rectified to minimize the cancelations caused by averaging overlapping positive and negative components of motor unit action potentials. Given K cortical spikes and simultaneously recorded EMG activity, rectified spike-triggered EMG snippets are collected around every spike, and the SpTA is computed by averaging these snippets across time according to

$$SpTA(t) = \frac{1}{K}\sum_{k=1}^{K} EMG_k(t), \tag{1.1}$$

where typically, $t = -20:40ms$ relative to the spike trigger at $t = 0$.

If a characteristic bump or trough appear in the average at an appropriate latency, this is taken as evidence in favor of underlying synaptic connectivity between the cortical neuron and the pool of motoneurons projecting to the recorded muscle.

Long time-scale correlations are measured using Pearson's correlation. Let X and Y be two random variables, with expected values μ_X,μ_Y, and standard deviations σ_X,σ_Y. The correlation coefficient between X and Y is defined as:

$$\rho_{XY} = \frac{COV(X,Y)}{\sigma_X \sigma_Y} = \frac{E[(X-\mu_X)(Y-\mu_Y)]}{\sigma_X \sigma_Y} \tag{1.2}$$

The *sample correlation coefficient* is used to estimate the correlation coefficient. Given samples x_i and y_i, where $i = 1,\ldots,n$, taken from X and Y, their sample correlation coefficient is

$$r_{xy} = \frac{\sum_{i=1}^{n}(x_i-\bar{x})(y_i-\bar{y})}{(n-1)s_x s_y} = \frac{\sum_{i=1}^{n}(x_i-\bar{x})(y_i-\bar{y})}{\sqrt{\sum_{i=1}^{n}(x_i-\bar{x})^2 \sum_{i=1}^{n}(y_i-\bar{y})^2}} \tag{1.3}$$

Fetz and Finocchio [15] were the first to compare short to long time-scale correlation between neuronal firing rate and a muscle's EMG activity. They examined four wrist and elbow muscles and a sequentially recorded population of motor cortical neurons during isolated isometric muscle contractions. They found significant peaks in the cross-correlogram of some neurons and muscles,

but none was a significant post-spike effect. They concluded that "correlations in the sense of covariation are neither necessary nor sufficient evidence to establish anatomical connections".

Miller et al. [42] recorded activity from red nucleus neurons and EMG from 12 muscles during a food retrieval task. They found long-timescale correlations with a mean value of 0.25 between most neurons and a subset of the recorded muscles. In a related paper, they also computed SpTAs for the neuron-muscle pairs and concluded that pairs with significant post-spike facilitation (PSpF) tended to have relatively strong long time-scale correlations as well.

Bennett and Lemon [2] investigated the relationship between the level of EMG activity and the size of PSpFs during a precision grip task. They concluded that while some CM neurons' firing rate showed strong correlation to the target muscle EMG; for most of them, the correlation was weak or nonexistent. Two mechanisms were suggested as an explanation. First, CM neurons facilitate different muscles and may exhibit different activity levels for different periods of the task. Second, a spinal cord mechanism exists, which adjusts the excitability of the motoneuronal pool and by that changes the efficacy of the CM neuron excitatory post-synaptic potential (EPSP) on the motoneuronal pool.

McKiernan et al. [41] tested the correspondence of PSpF and PSpS to the magnitude and sign of the cross-correlograms of single units and 24 hand and arm muscles. They showed that the magnitude of PSpF was weakly correlated with the magnitude of the long-timescale cross correlation peak. They suggested a model where a motoneuronal pool sums inputs from many sources including: CM cells, afferents, intrinsic spinal cord neurons and polysynaptic cortical neurons. Any one CM neuron then makes only a small contribution to the overall activity of the motoneuronal pool.

The discrepancy between short- and long-time scale correlations might seem odd at first, especially for CM neurons. However, it is reasonable, taking into account that PSEs represent an increased motoneuronal discharge probability, time-locked to spikes from a CM neuron. The synaptic contribution of a single CM neuron to motoneuron discharge is very small, and therefore the probability of spikes from a single CM neuron causing motoneuronal discharge is also very small. Only a few percentage of the CM neuron spikes are exactly time-locked to motoneuronal spikes [1, 55]. All other spikes still contribute to motoneuronal excitation, which is reflected

both in the SpTA baseline and long-term correlation. The long-term correlation is important as well, since it represents coactivation.

The SpTA baseline is often indicative of long-term correlations: a rising baseline indicates that a neuron positively covaries with EMG; and a falling baseline indicates that a neuron negatively covaries with EMG. When a neuron fires during phasic EMG bursts, an upwards curved convex baseline appears; and the baseline is downwards concave if the neuron fires between the EMG bursts. An inflected baseline indicates that the neuron was active during a period of sudden change in EMG [9].

1.3.3 DYNAMIC SHORT TIME-SCALE FUNCTIONAL CONNECTIVITY

Relatively few studies examined changes in SpTAs between different behavioral tasks ([37, 5, 9, 10]), mainly due to the large volume of data required to detect PSEs for one task alone. Current recording technology allows us to record from the bank of M1 using only acute electrodes, which prevents recording from CM neurons over periods longer than a few hours.

Davidson et al. [10] examined the throughput from single motor cortex neurons to muscles during a task where the animal was rewarded for enhancing functional connectivity. The paradigm included an epoch in which the animal performed a hand squeeze task, followed by an epoch where it was rewarded for increasing the firing rate of the recorded cortical neuron and the activity of one selected muscle. In every epoch, a different target muscle was selected. SpTAs computed for the different epochs showed that PSpF PSEs changed from one epoch to another. In most cases, the changes in PSpF/PSpS could be attributed to either a change in the cortical neuron's firing rate (increased intracortical excitability), the level of ongoing EMG (change in excitation of motoneurons), or synchrony effects in the SpTA. However, in 10% of the cases, none of these factors could account for the change. Two subcortical mechanisms were suggested to contribute to functional connectivity changes. First, some PSEs could be mediated through disynaptic linkages, which could have been inactive during certain epochs. Second, EPSPs produced by single CM neurons are known to be relatively small. During some epochs, they might have been amplified up to five fold by persistent inward currents (which are facilitated by monoaminergic drives, such as sero-

tonin & noradrenalin, from axons [30]). Therefore, the efficacy of CM synapses on motoneurons was speculated to change between behavioral epochs.

1.3.4 EVIDENCE IN FAVOR OF POLYSYNAPTIC FUNCTIONAL CONNECTIVITY BETWEEN CORTEX AND MUSCLES

The roles of the polysynaptic and monosynaptic pathways in the corticospinal tract, both originating in the motor cortex and terminating in the spinal cord, are still unknown. While it has been shown that the vast majority of cortical input to spinal motoneurons is polysynaptic in origin [36], the functional roles of both pathways are still under debate. Anatomical and functional evidence in favor of the possibility that polysynaptic neurons have effect on the control of movement in primates is described in this section.

Pierrot-Deseilligny [51] has argued for the existence of a pre-motoneuronal system in humans, similar to the C3-C4 system known from the cat model, based on stimulation studies. In these studies, the homonymous median nerve was stimulated with various intensities and the electrical activity of flexor carpi radialis (FCR) motor units was recorded. For high intensities, an increased firing probability consistent with monosynaptic delay across spinal inter-segments was detected. To reduced the MU firing probability due to monosynaptic EPSPs evoked by the stimulation, the investigators used low intensity stimulation, delivered at a fixed delay after the previous MU spike. The delay was adjusted so that the afterhyperpolarization following the previous MU spike would reduce the firing probability due to monosynaptic EPSP, but would have little effect on non-monosynaptic EPSPs, occurring after the afterhyperpolarization had decayed. For those conditions, the investigators found a statistically significant non-monosynaptic excitation in $33/50$ FCR motor units. Similar results were obtained for other arm, wrist and finger muscles, all but the intrinsic finger muscles. Fetz et al. [17] have shown that spinal interneurons have response characteristics which are sometime similar to those of cortical neurons, thus may be involved in more than low level control of motoneurons. They studied a variety of tasks and concluded that spinal interneurons are also involved in early stages of movement preparation. They pointed a few key differences in the response characteristics of CM neurons and spinal interneurons. CM neurons seem to represent muscle synergies better, since they show more PSpF/PSpS in larger muscle

groups, they show inhibition of antagonists and fire more specifically for particular movements. Spinal interneurons usually affect only one or a few muscles and they have broad tuning over a wide variety of movements.

Olivier et al. [45] have stimulated the pyramidal tract in awake and lightly sedated monkeys and simultaneously recorded from single motor units. They have found no response at latencies suitable to polysynaptic connections. Thus, they concluded that under the conditions they tested, there was no positive evidence for the transmission of cortical excitation to motoneurons by polysynaptic pathways. Contrarily, Isa et al. [31] have proposed that an indirect CM pathway exists in primates. Using a combination of stimulation, lesion and blocking inhibition, they have shown that a group of propriospinal neurons in the C3-C4 segments could mediate disynaptic excitation to MNs. They also made lesions in the corticospinal tract between the C4 and C5 segments in order to interrupt the monosynaptic pathways while preserving most of the C3-C4 descending axons. The monkeys regained the ability to perform dexterous finger movements and also independent control of different fingers to some extent. A monkey with a lesion in the C1-C2 segments did not regain any independent finger movement. Based on those results, they contrasted the conclusions of Olivier et al. [45] and hypothesized that propriospinal neurons could deliver disynaptic excitation to motoneurons.

1.3.5 LONG TIME-SCALE FUNCTIONAL CONNECTIVITY

Holdefer and Miller [29] recorded from an unidentified population of M1 neurons and EMG from 8 or 11 muscles during a reach-to-press task. The neural population could have included both CM neurons and neurons with polysynaptic linkages to motoneurons. They computed the cross correlation of every cortical neuron with all the recorded muscles and constructed a vector containing the maximal cross correlation value per pair in the range of lags $[0-150ms]$. The results showed that neurons were typically correlated with a group of functionally related muscles, or a muscle synergy (e.g.: finger extensors). The cross correlation vectors were clustered and some well-separated groups were identified. Based on these results, it was hypothesized that neurons in M1 encode the activity of muscle synergies. However, this analysis was limited by the absence of more variable movements; and did not compare the muscle correlation vectors to kinematic correlation vectors.

Jackson et al. [34] have recorded the activity of various M1 neurons using a chronic implant during a trained task, free behavior and natural sleep. EMG activity from various muscles was also recorded. They computed the cross correlations between the cortical neurons and the EMG activity for each one of the behaviors above. It was shown that the firing rate of some neurons correlated consistently to muscles during all behaviors but natural sleep, even over long periods of time (several days). Although the patterns of correlations could differ across different behaviors, the general trend supported the idea that data collected during trained tasks can be informative as to how the CNS behaves during free behavior. They suggested that a consistent relationship exists between the cortex and muscles even during free behavior, supporting the Holdefer and Miller [29] hypothesis that motor cortical neurons encode muscle activity.

1.4 MOTOR CORTICAL TUNING DURING GRASPING

Many studies have related motor-cortical neural activity to various extrinsic movement parameters, such as position, direction, velocity and acceleration of the arm end-point during reaching movements [23, 21, 43, 48, 47, 62]. Other studies have related motor cortical activity to static and dynamic forces [12, 28, 55].

Fewer studies have examined the relationship of neural activity to hand kinematics and EMG activity during reach to grasp, or grasp only tasks. Poliakov and Schieber [54] used clustering analysis to show that sequentially recorded motor-cortical neurons do not tend to show similar patterns of activity during individual finger movements. They found two consistent groups across monkeys: one group with increased activity for most movements, and another which decreased its activity for most movements. Smaller non-consistent groups were found for each monkey, each selective to one of two movements. They concluded that the hand area of motor cortex contains limited functional grouping, and that the combined activity of diverse M1 neurons facilitates finger movements.

Morrow and Miller [44] have used a population of sequentially recorded M1 neurons to reconstruct the envelope of EMG signals during a precision grip task. Using a linear model, they showed that 30 neurons were sufficient to provide satisfactory fits. However, the model trained

on precision grip data, failed to generalize to predict EMG recorded during a power grasp task. A follow up study from the same group, by Pohlmeyer et al. [52], used simultaneously recorded M1 neurons to predict trial-to-trial EMG from upper arm muscles, during a reaching task, showing fits in the range of $R^2 = 0.6 - 0.7$.

Townsend et al. [64] applied a spike-triggered regression approach, using a linear-nonlinear generalized linear model (GLM) to study how motor cortical neurons encode muscle activity. They predicted neural firing rate from EMG activity during a precision grip task with a compliant load. They compared a linear model with a linear-nonlinear model and concluded that the relationship of the neurons to their 9-dimensional muscle space was linear in nature. In other words, there was no advantage to using a nonlinear model. They also compared the predictions of firing rates using kinematic data (finger position and velocity) to those using EMG, and found no significant difference; although nonlinear models using the kinematic data were usually better than linear models. They suggested that the motor-cortex consists of neurons encoding both EMG and kinematics.

Hamed et al. [24] used populations of neurons to decode single and two-finger movements, and wrist, with 2 movement types each (flexion/extension). They report nearly perfect finger movement decoding using $20 - 30$ neurons, and accuracies around 90% when decoding two-finger movements using 100 neurons. Interestingly, they report that when the decoder was trained on single finger movements, it then failed to generalize for decoding multi-finger movements. They hypothesized that the neural and muscle activations required to move two fingers are not a simple linear combination of the activations required to move each finger individually; since during individual finger movement, muscles affecting multiple fingers contract and cause adjacent fingers to move together.

Hendrix et al. [27] studied neurons recorded in M1 and PMd during a reach-to-grasp task, in which the monkeys could not see their hands nor the object, and were trained to identify the object by touch. A computer display indicated the required force level to generate on the object, and a force feedback as well. The monkeys were free to place their hands on the objects as they wished, as long as they generated the required force. They report that most neurons showed object specific and grasp dimension specific tuning; indicating grip aperture tuning.

Vargas-Irwin et al. [67] used neuronal data from multi-electrode recording in M1 to show that individual neurons are typically modulated by multiple joints kinematics. The tuning of individual neurons spanned a continuum of arm, wrist and hand kinematics combinations; and most neurons

were not preferential to subsets of kinematics. Around $50-70\%$ of the neurons showed hand, or hand and arm related tuning; with very few showing wrist only, or wrist and hand tuning.

Saleh et al. [58] investigated hand preshaping during a grasp only task, where monkeys grasped objects moved towards their hands by a robot, while their arms were restrained. They used a GLM to predict neural firing rate from 6 joint angle positions and 6 joint angle velocities, shifted at 8 time lags compared to the firing rate. They found the neurons encoded combinations of joint angles and joint angle velocities at different lags. A large percentage of the neurons encoded wrist and index finger PIP flexion/extension.

A follow up paper [59] examined a reach and grasp task, in which neural firing rates were predicted using a similar GLM model, including 20 joint angular positions and 20 joint angular velocities, shifted at 8 time lags compared to the neural data (a total of 320 kinematic parameters). The authors used PCA to reduce the dimensionality of the kinematic parameters, and found that using 5 principal components (PCs) caused their model's prediction power to saturate. They concluded that neurons in the M1 gyrus encode general aspects of reach to grasp, such as coordinated movements of joints, rather than fine finger movement, thought to be represented by the higher order PCs. They concluded that neurons encode multiple reach and grasp features, represented as extensive temporal combinations of joint angles and joint angular velocities, up to $360ms$ around the spikes ($-44ms$ before, $320ms$ after).

1.5 EMG AND JOINT ANGLE SYNERGIES

The primate hand is a complex structure, containing 18 joints and 39 muscles, which can be described in terms of degrees of freedom (DOF): joints correspond to DOF in kinematic space, whereas muscles correspond to DOF in muscle space. The large number of DOF in the hand, allows for a variety of hand shapes and postures. However, the number of DOF spanning either space is bigger than the number of DOF required to define a reach and grasp movement, hence the CNS has to somehow deal with the redundant DOF. For example, to define a target for reaching, only 3 DOF are needed- the 3 spatial coordinates of the target, whereas the arm contains 7 DOF for reaching (three at the shoulder, two at each the elbow and the wrist). Bernstein formalized

this as the DOF problem [3]. He hypothesized that the CNS might be using motor primitives as building blocks to construct complex movements. These motor primitives reduce the problem of redundancy by constraining the biomechanical system (for example: coupling of different joints or simultaneous activation of muscles). They also make control easier by reducing the number of DOF to be controlled independently.

Recent studies have used principal components analysis (PCA) to extract lower dimensionality representations of the primate hand (postural synergies) during static grasping [70] or reach-to-grasp movements [60, 39]. Others have used various factor analysis-related methods to describe lower dimensionality representation of muscle activation (muscle synergies) in frogs (behaviors ranging from kicking to swimming)[8], non-human primates performing reach to grasp [4, 46] and humans [70, 7]. It should be noted that only one of these studies [70], has recorded simultaneous hand kinematics and EMG during a reach-to-grasp task; to examine both postural and muscle synergies.

Tresch [65] reviewed and compared common methods to extract synergies, focusing on their ability to recover synergies in simulated EMG data sets. The following methods were compared: PCA, factor analysis using varimax rotation (FA), independent component analysis (ICA), nonnegative matrix factorization (NMF), and a version of ICA where PCA was first used to reduce the dimensionality of the data set. All methods share the same model: given N samples recorded from M muscles, represented as a matrix, the following model decomposes the EMG to simultaneous activation of synergies:

$$EMG = WC \Rightarrow EMG_n = \sum_{i=1}^{N} C_i \vec{W}_i + \varepsilon \tag{1.4}$$

where EMG is an $N \times M$ matrix; C_i is the activation coefficient for the $i-th$ basis vector at sample n; W_i is the $i-th$ basis vector (also M-dimensional); and ε is an M-dimensional noise vector. The difference between the methods lies in their assumptions and how they compute the basis vectors [26, 32]. PCA uses a linear transformation, calculated from the data covariance matrix to find an orthogonal basis, where synergy activations (the principal components, or projections) have descending variance: the first synergy activation (principal component) accounts for the most variance in the data and the last principal component, the lowest. FA with varimax rotation finds an orthogonal transformation which maximizes the sum, over all synergies (factors), of the variance of the activation coefficients (squared loadings). The motivation is to make it as easy as possible

to identify each muscle with a few synergies. ICA represents a multidimensional random vector as a linear combination of non-Gaussian random variables that are as statistically independent as possible. NMF assumes that both the data and the synergies are assumed to be non-negative, an assumption that fits rectified EMG data well. It computes the matrices W and C by maximizing a log-likelihood from a model where x_{ij} has a Poisson distribution.

Tresch [65] found that PCA performed the worst, while factor analysis with varimax rotation performed as well as ICA and NMF. They report that empirically, ICA applied to a subspace defined by PCA was the best method, although they could not find a theoretical justification. Overall, they conclude that all the methods provide similar results when applied to both simulated and experimental data.

However, that kinematic or EMG data can be mathematically described using a smaller number of DOF, does not indicate that the CNS necessarily utilizes this control scheme. In addition, if the CNS uses any postural or muscle synergies, they do not have to necessarily correspond to the mathematically derived synergies. Only by relating neural data to putative synergies, can the validity of the motor primitives hypothesis be tested.

1.6 MAIN RESEARCH QUESTIONS

The work presented so far provides the necessary background to evaluate the unique contribution of this dissertation, motivated by two novel hypotheses. First, it is hypothesized that the motor-cortex operates through a flexible network, capable of dynamically changing its effects on muscles. Second, although motor cortical activity is known to correlate with movement parameters, we argue that its muscle facilitation is modulated by the task at hand: the context in which the movement is performed, affects how motor cortical activity affects muscle activity. This hypotheses are translated to concrete research questions below.

Research Questions

1. *How are motor-cortical neurons tuned to both muscle activity and kinematics during reach to grasp movements?*

   Some studies have related motor-cortical activity to either muscle activity or kinematic features, during reach or grasp movements; but since different behavioral tasks were used, it not clear how to combine the results. We will characterize motor cortical tuning to *both* muscle activity and kinematic features during reach to grasp movements, and compare our results to previously published work.

2. *Is functional connectivity between the motor cortex and muscles dynamic?*

   In our context, functional connectivity is defined as $P(\Delta EMG \text{ at time } t+\Delta t | \text{spike at time t}, X)$; where X represents all other inputs contributing to EMG facilitation besides the spikes from the recorded neuron. Some studies have used reaching or grasping tasks to suggest that long-time scale functional connectivity between neurons and muscles may be static [29, 34]; while others suggest dynamic short-time scale functional connectivity [10, 9]. We will test whether changes in functional connectivity occur in the context of a rich reach-to-grasp task, using both long- and short-time scale correlations, when possible. To achieve that, new methods for the estimation of functional connectivity will be developed. Two classic methods are typically used to measure functional connectivity: sample correlation is used to estimate long-time scale functional connectivity, and SpTA is used to measure short-latency functional connec-

tivity. Since pair-wise sample correlation does not measure *conditional* correlation, we will develop a model capable of estimating cortico-muscle long-time scale correlation conditioned on kinematic covariates. Since SpTA's detection power is limited by the large number of spikes required to detect PSEs, we will develop more efficient detection methods to detect short-time scale functional connectivity.

3. *Are changes in functional connectivity related to kinematic features?*

   We show that functional connectivity is dynamic and related to changes in the kinematic covariates. Our model suggests that motor-cortical neurons are driven by task requirements; required movement or force patterns generated by muscle activation. The effect of cortical neurons on muscle activation is dynamic and dependent on task requirements.

This dissertation is divided to the following chapters:

- Chapter 2 describes the behavioral task, the surgical and experimental procedures and data collection methods.
- Chapter 3 explores interesting aspects of the EMG and kinematic data, motivating some of the results in later chapters. The relationships between and within EMG and kinematics, and their task specificity are assessed.
- Chapter 4 explores the activity patterns of the recorded neural population and their task specificity. The multivariate relationship between neural activity, EMG and kinematic features is described.
- Chapter 5 presents novel methods for the detection of short-term functional connectivity. This chapter has been submitted as a paper.
- Chapter 6 details models for estimating long-term functional connectivity between a neuron and a muscle (or a group of muscles), conditioned on one, or more, kinematic features. Both short- and long-term functional connectivity in our data are assessed.
- Chapter 7 summarizes our findings and relates this work to previous published results.

2.0 METHODS

2.1 EXPERIMENTAL PROCEDURES

2.1.1 BEHAVIORAL SETUP

The experimental setup was designed to study reach-to-grasp movements. A monkey was comfortably seated in a chair in front of a six degrees-of-freedom industrial robot (Denso Robotics, CA). Its head and one arm were restrained while the other hand was free to reach and grasp objects presented by the robot. Custom made software interacted with the robot and other devices, controlled the behavioral task and collected data which included single-unit activity (up to 5 simultaneous electrodes), electromyography (EMG) activity from 16 muscles and high resolution kinematic data from the wrist and hand.

A recording session consisted of 4 presentation blocks. In every block, the robot would pick up objects and present them, one at a time, at randomly selected predetermined targets. A target included a spatial location and an orientation, unique for every object. The combination of an object and target was termed an *attitude*. Each attitude was repeated 5 times in every presentation block, resulting in 20 repetitions in one recording session. Figure 2.1 shows the 7 objects used in this task. A different number of targets was chosen for every object (see Table 1), totaling in 40 possible unique attitudes, or 800 trials in one recording session.

Trials consisted of epochs, defined in Figure 2.2. The task was self-driven, as the monkey had to initiate every trial by placing its hand on a pad situated at waist level (see Figure 2.3 Top). It then had to keep its hand on the pad for a period selected at random from a uniform distribution in the range $[400-700ms]$ (*Hold-A*). During Hold-A, the room was dark and the robot moved an object to the next target. If the monkey lifted its hand from the pad before Hold-A was over, the

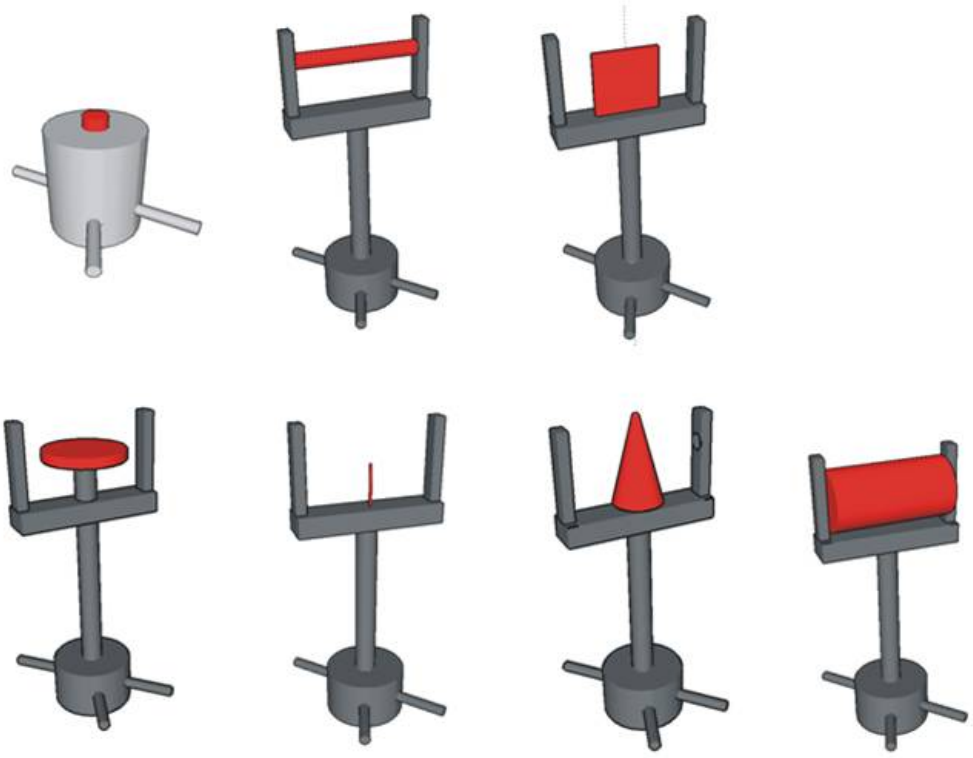

Figure 2.1: **Objects used in the grasp task:** Top row: (left to right) Button, small handle, small rectangle. Bottom row: (left to right) Disk, small precision, small cone, small bar.

trial would fail. Otherwise, a dim light would turn on, serving as a ”go” cue for the monkey. The monkey had to respond by identifying the target and lifting its hand within $[400-600ms]$ (*Reaction time*), or the trial would fail. A successful reach to the object had to be completed within $1000ms$ (*MoveA*, Figure 2.3 Bottom), and the object had to be statically grasped for $[250-350ms]$ (*HoldB*). A water reward was given for successful trials and the lights would turn off, instructing the monkey to move its hand back to the pad to initiate the next trial (*MoveB*).

The pad and all objects were equipped with pressure sensitive sensors, connected to the computer using a digital-input-output (DIO) card. In order for the computer to detect a successful grasp, the monkey had to keep continuous contact with all the force sensors of an object, ensuring similarity of hand conformations between repeated reaches to the same attitude.

Table 1: Attitudes used in the grasp task

	Object	**Number of Targets**	
1	Button	5	
2	Small handle	7	
3	Small rectangle	7	
4	Disk	7	Monkey B only
5	Small precision	7	
6	Small cone	7	
7	Small Bar	2	Monkey E only
	Total	**40**	

The set of objects in Figure 2.1 was selected to facilitate a variety of hand shapes. For every object, targets were selected to sample different wrist orientations with similar hand shapes. Every object had either $7, 5$ or 2 targets associated with it. The 5 targets group included: horizontal, abduction, adduction, flexion and extension of the wrist. The 7 targets group included two other wrist orientations: 45 degrees to the left and right (which were combinations of abduction/adduction and flexion/extension). The 2-target group sampled hand pronation and supination.

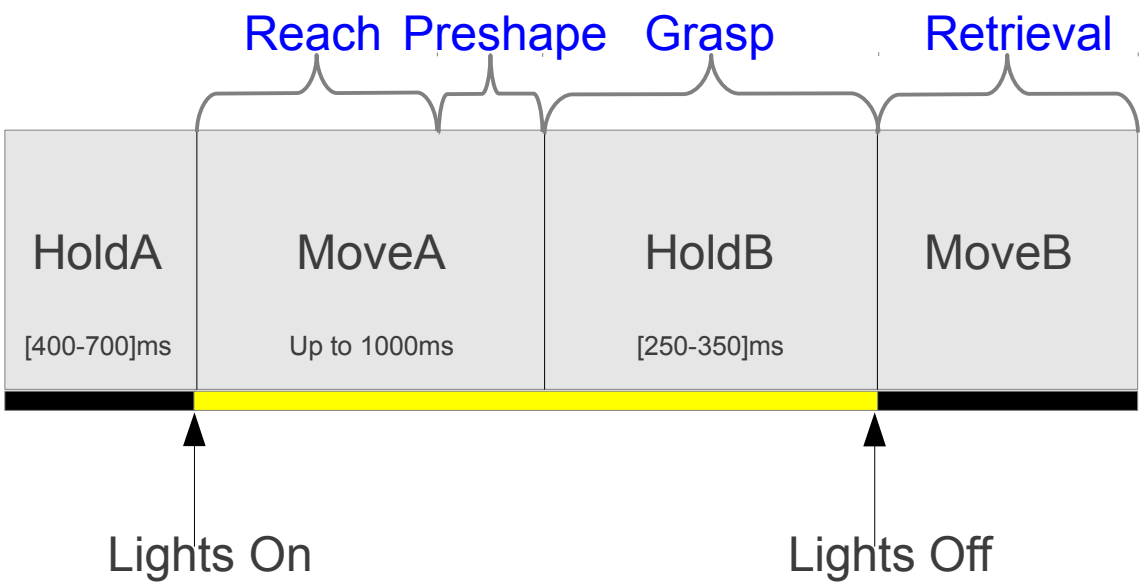

Figure 2.2: **Grasp task epochs**

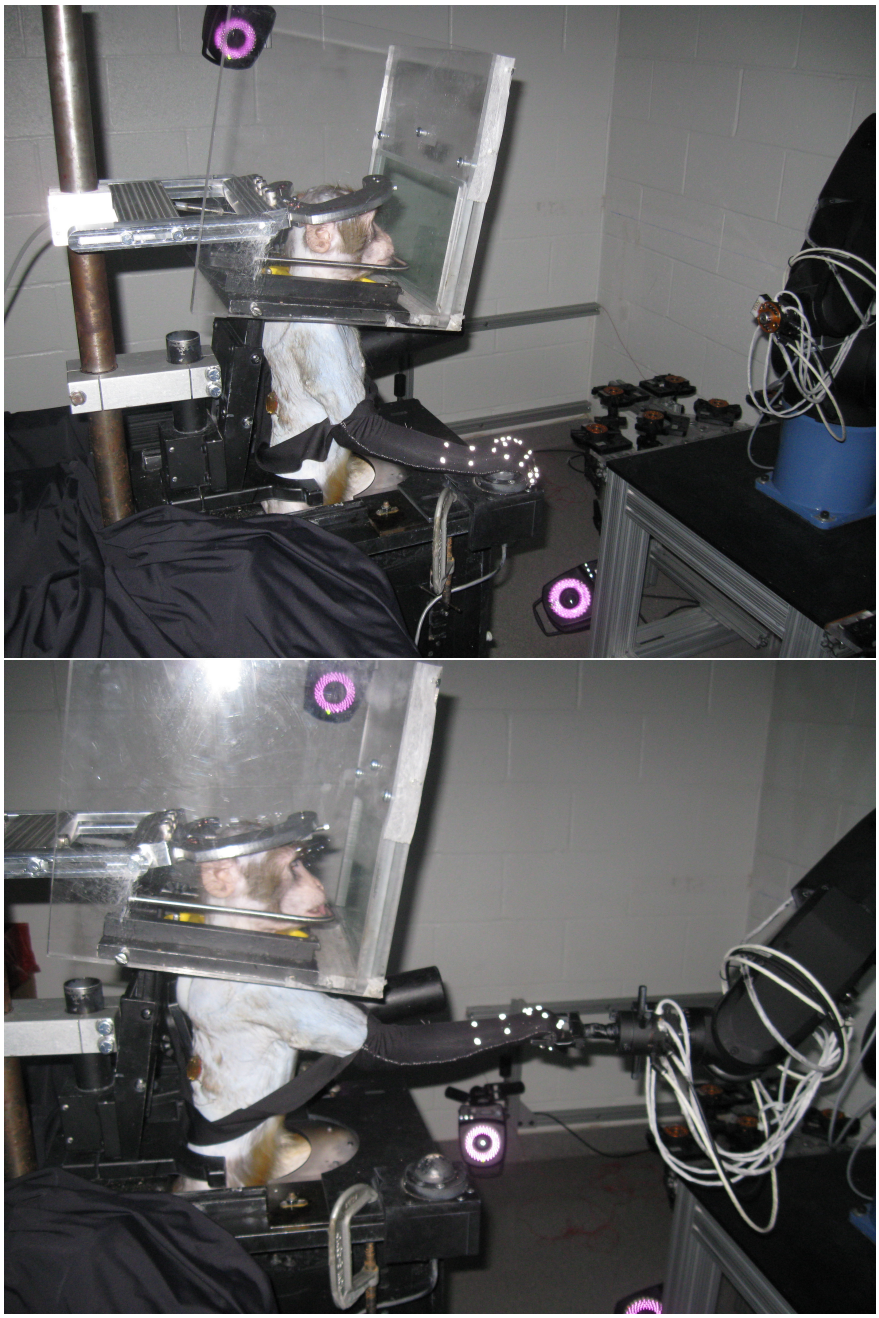

Figure 2.3: **Example Epochs in a trial. Top**: HoldA. **Bottom**: Hold-B

2.1.2 SURGICAL & RECORDING PROCEDURES

2.1.2.1 EMG IMPLANT FABRICATION An EMG implant, consisting of 16 custom made patch electrodes and a connector, was fabricated before surgery (adapted from Miller et al. [42]). A series of measurements from the approximate location of the connector on the animal's back to all target muscles were taken prior to fabricating the implant, to ensure that electrode wires would be long enough. An extra 10% was added to every measurement as a precaution. The EMG electrodes were manufactured from patches of medical grade Silastic sheeting (Bioplexus Corp) cut to the appropriate size for the target muscle, and threaded with partially exposed stainless steel wires (AS632, Cooner Wire). Every electrode included 3 parallel recording wires (see Figure 2.4): the middle one served as a reference channel and the two others served as signal channels. This allowed for redundancy, in case of noise or artifacts on a recording channel. Only one differential pair for every electrode was used during data recording. For small monkeys ($4-5kg$), patches of the following sizes were used: $5mm, 3mm, 2mm$. For bigger monkeys ($>5kg$), patches of the following sizes were used: $7mm, 5mm, 3mm$. Large patches were used for arm and shoulder muscles (biceps, triceps, deltoid). Medium patches were used for extrinsic wrist muscles and small patches were used for extrinsic digit muscles. The size of the Silastic sheet was based on the length of the exposed recording wires. For example, a $3mm$ patch electrode included 3 parallel recording wires, each with a $3mm$ exposed lead, and $3mm$ spacing between them. The Silastic patch sizes used are listed in table 2. The wires were threaded through the patch, with all exposed leads on one side of the patch. The other side of the patch was covered in a thin flat layer of Silastic medical adhesive (A-100, Factor II) to provide insulation and hold the recording wires in place. The free wire leads were weaved into a braid, for convenience.

A custom made plastic shell (Delrin or Ultem) was machined to house a 51 pin connector (Bi-Lobe, A29000-051, Omnetics Connector Corporation). The recording wires from all EMG electrodes were hand-soldered, with the use of a magnifying microscope, to the matching wires in an Omnetics connector. This proved to be easier than hand soldering directly to the Omnetics connector. The solder joints were first covered with a bead of instant adhesive (LOCTITE 4014 Prism Medical Device Adhesive) and then with a bead of medical adhesive.

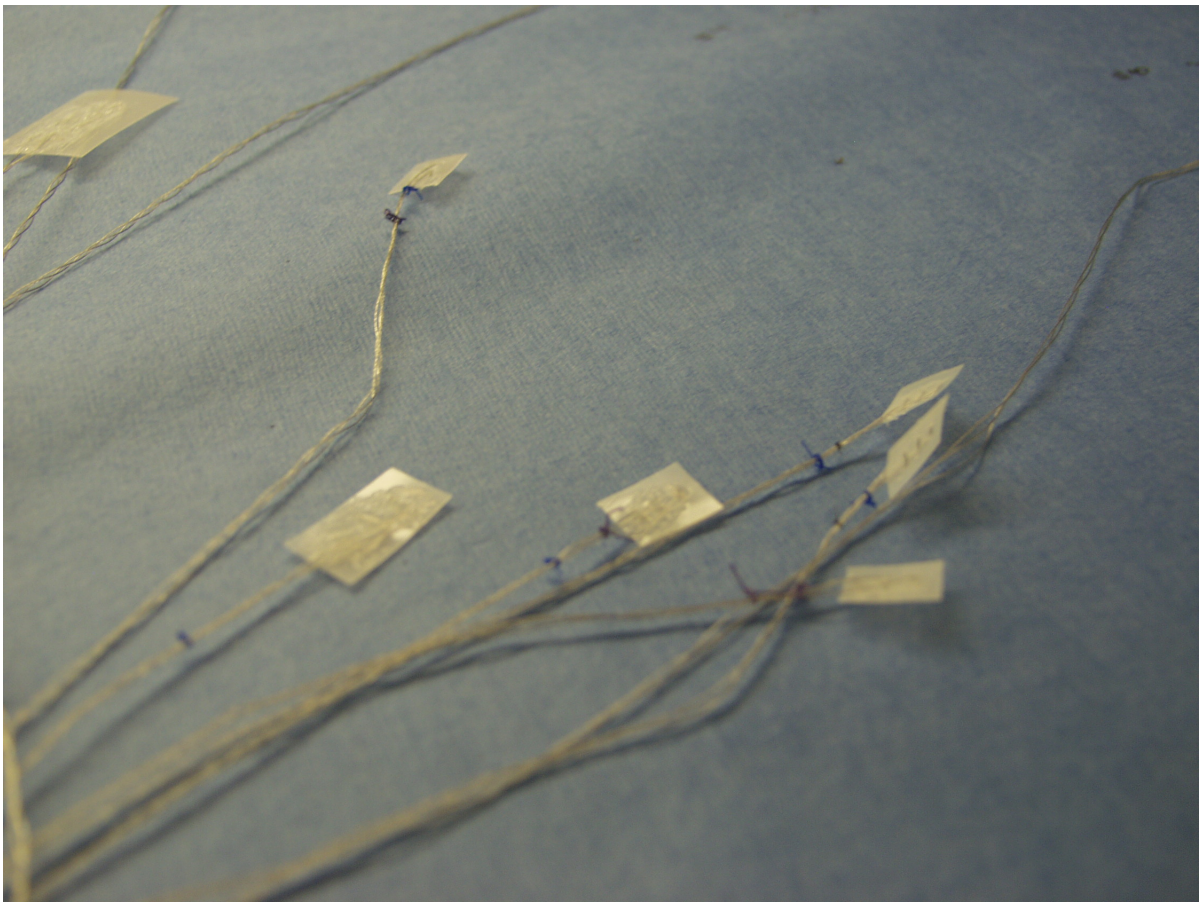

Figure 2.4: **EMG electrodes**

EMG electrode impedance was tested by placing one electrode at a time in a saline bath, and connecting the two leads of an impedance meter (BAK Electronics) to two pins on the Omnetics connector, matching a pair of recording wires on the electrode. Typical impedance values were in the range of $5 - 20k\Omega$. The patch electrodes and the wires were carefully cleaned with an alcohol swab prior to sterilization, to remove dust and oil residues from the fingers.

Table 2: EMG electrodes size specifications

	Exposed recording wire length	Silastic Sheet Size
1	$3mm$	$1.3cm$ x $1cm$
2	$5mm$	$2cm$ x $1cm$
3	$7mm$	$3cm$ x $2cm$

2.1.2.2 SURGICAL PROCEDURES Animals were induced with $10mg/kg$ ketamine intramuscularly followed by $2-3\%$ isoflurane inhalant. The EMG patch electrodes were tunneled subcutaneously to the target muscle and sutured to the epimysium. This allowed for reliable chronic EMG recordings from muscles over a period of months. The Omnetics connector was implanted on the animal's back, below the scapula. After the animal had recovered from the EMG surgery, a second surgery was carried out to mount a titanium chamber to the skull, centered on the approximate location of the primary motor cortex hand area for acute neural recordings.

Table 3 lists the implanted muscles for monkey E, with their anatomical roles and abbreviations as used throughout this study. The same muscles were implanted in monkey B, with the exception of Abductor Pollicis Longus (APL): Pectorialis Major (PEC) was implanted instead.

Table 3: List of implanted muscles

	Name	**Code**	**Anatomical Role**
1	Anterior Deltoid	ADLT	Abducts arm, flex and medial rotate
2	Biceps	BIC	Supinates forearm, flexes elbow, weakly flexes shoulder
3	Triceps Long Head	TRILO	Extends elbow, stabilize shoulder
4	Triceps Lateral Head	TRILA	Extends elbow, retracts capsule of elbow joint on extension
5	Brachioradialis	BRC	Flexes arm at elbow, brings forearm into mid-prone position
6	Extensor Carpi Ulnaris	ECU	Wrist extension and adduction
7	Flexor Carpi Ulnaris	FCU	Wrist flexion and adduction
8	Extensor Digitorium Communis	EDC	Extends all joints of fingers
9	Extensor Digiti Minimi	EDM	Extends all joints of little finger
10	Extensor Carpi Radialis Longus	ECR	Wrist extension and abduction
11	Flexor Carpi Radialis	FCR	Wrist flexion and abduction
12	Flexor Digitorum Superficialis C1	FDS	Flexion of PIP1 – 4, then MCP and wrist
13	Flexor Digitorum Profundus	FDP	Flexion of DIP1 – 4, then PIP, MCP and wrist
14	Flexor Digitorum Superficialis C2	FDS2	Flexion of IP 1 – 4, then PP and wrist
15	Pronator teres	PRT	Pronates forearm and flexes elbow
16	Abductor Pollicis Longus	APL	Flex and abduct arm

2.1.2.3 NEURAL AND EMG RECORDING PROCEDURES A five-channel Mini-Matrix system (Thomas Recording) was used to record electrical activity from the animal's brain (Figure 2.5). Recording electrodes were fabricated using materials purchased from Thomas Recording. Each electrode consisted of glass insulated tungsten wire, beveled at one end to a sharp recording tip to assist dural penetration. This resulted in typical impedance values in the range of $0.5 - 1.5M\Omega$. The tungsten wires were threaded through a $15mm$ piece of silicon tubing. With the recording tip extended through the tube, the other end of the wire was crushed to remove the glass insulation, and was then immobilized in a solder joint. A gold pin was connected to the solder joint via a wire, allowing to connect the recording electrode to one of the appropriate ports on the Mini-Matrix.

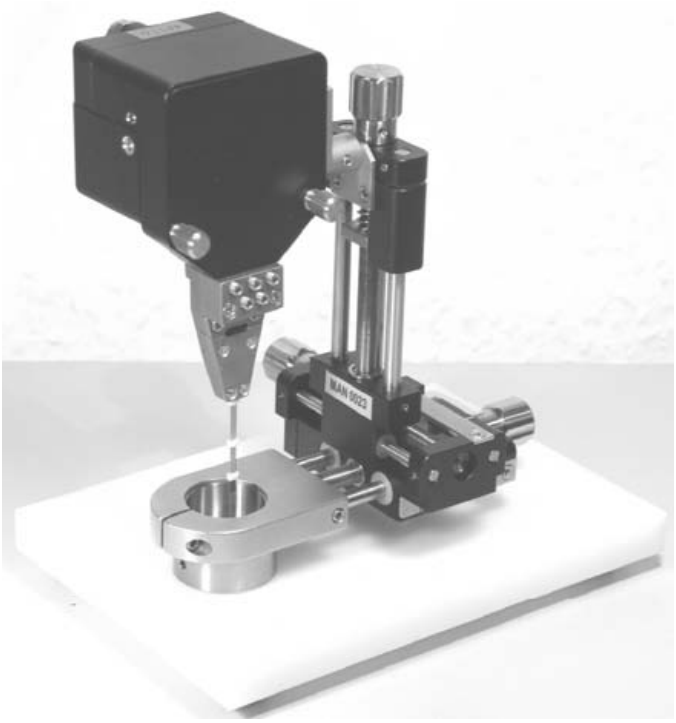

Figure 2.5: **The five-channel Mini-Matrix Thomas Recording drive**

On every recording day, the animal's recording chamber was opened and washed with saline. A potential recording site was selected and a small patch of dura was carefully dissected under a magnifying microscope using sterile surgical micro instruments. The Mini-Matrix drive was mounted on the recording chamber and its guide tubes lowered to make contact with the dura at the

selected recording site. 5 recording electrodes, pre-loaded in the drive, were then slowly advanced out of the guide tubes at a speed of $3\mu m/sec$. Following dural penetration, the electrodes were further driven to a depth of $3000\mu m$ from the surface of the dura and left to stabilize for at least an hour.

The electrodes were subsequently moved at a speed of $5\mu m/sec$ until at least one neuron was isolated on each electrode. A 16-channel Pentusa recording system (Tucker Davis Technologies, TDT) was used to display and record the waveforms from the neural and EMG electrodes. Spike waveforms were sorted on-line using two discriminator bars, and both spike time stamps and waveform snippet data were stored for off-line analysis. EMG data was stored at a sampling rate of $4882.8125Hz$.

At the end of every recording session, intra-cortical micro-stimulation (ICMS) was delivered through every electrode which had neurons isolated on it, to locate potential pyramidal tract neurons. Brief bipolar monophasic pulses (total duration 300ms, pulse width 2ms, 20hz frequency, 10-50μA) were delivered using a stimulator (ISOFLEX brand); and responses were recorded when the monkey's arm was in a resting state. A passive exam was also conducted, including passive movements of the arm, wrist and digits.

2.1.2.4 EMG DATA PROCESSING Raw EMG activity was bandpass filtered at $10-2000Hz$ in real time by the TDT system, and stored at a sampling rate of $4882.8125Hz$. The data was filtered offline to remove noise and movement artifacts using a bandpass FIR filter (Kaiser Window, $70-2400Hz$). Some EMG channels included heartbeat artifacts, which were filtered out using an adjusted bandpass filter ($130-2400Hz$). These artifacts occurred only in monkeys B and E, probably due to imperfect insulation of the Omnetics connector.

2.1.2.5 NEURAL DATA PROCESSING Spikes were discriminated as data was being collected using traditional "box sorting" (a pair of bars positioned over superimposed snippet waveforms). The electrode was moved continuously, since movement relative to the neuronal cell bodies would often change the waveform amplitude and cause difficulty in sorting neurons offline. In some cases, it was hard to isolate two or more neurons recorded on the same electrode, and off-line

sorting was performed using the stored snippet waveforms. Table 4 lists the number of neurons recorded in the different experiments.

Table 4: Experimental Data sets

	Subject	Number of recording days	Number of neurons
1	V Left hemisphere	30	Preliminary data not used in the analysis
2	B Left hemisphere	54	160
3	E Left hemisphere	12	51
4	E Right hemisphere	40	171

2.2 OFF-LINE NEURAL DATA PROCESSING

For some analyses, spike times were converted to a smooth continuous firing rate, calculated using adjusted 50*ms* bins (see below) using a method we call *fractional firing rate*. This method uses the inter-spike intervals (ISI) to calculate a firing rate different than zero for bins where no spikes occur. Figures 2.6 and 2.7 show a comparison between firing rates computed by:

1. Binning the spikes to obtain spike counts and dividing by the bin width to obtain firing rates
2. Binning the spikes to obtain spike counts, dividing by the bin width to obtain firing rates, and spline-smoothing the firing rates
3. Computing fractional firing rates per the algorithm detailed below

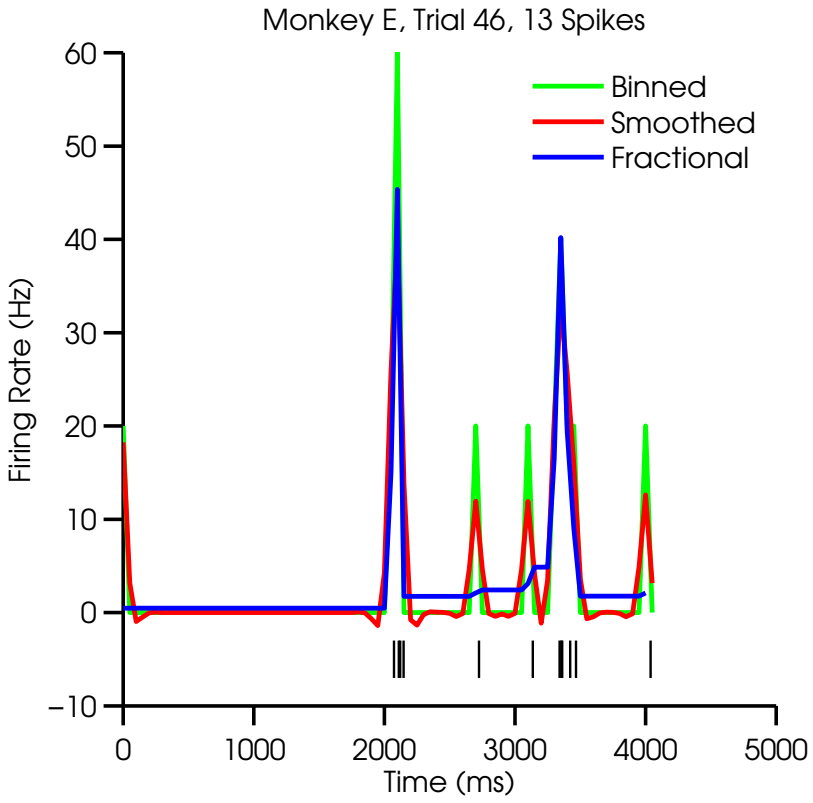

Figure 2.6: **Firing rate computation 1:** Firing rates computed using 50*ms* bins (green), 50*ms* bins with spline-smoothing (red) and fractional firing-rates method (blue). This trial contained only 13 spikes. Although the smooth and fractional firing rates are similar, some differences exist. Spline-smoothing produces undesirable negative firing rates, and is affected more by isolated individual spikes (for example, the spikes around 3000*ms*).

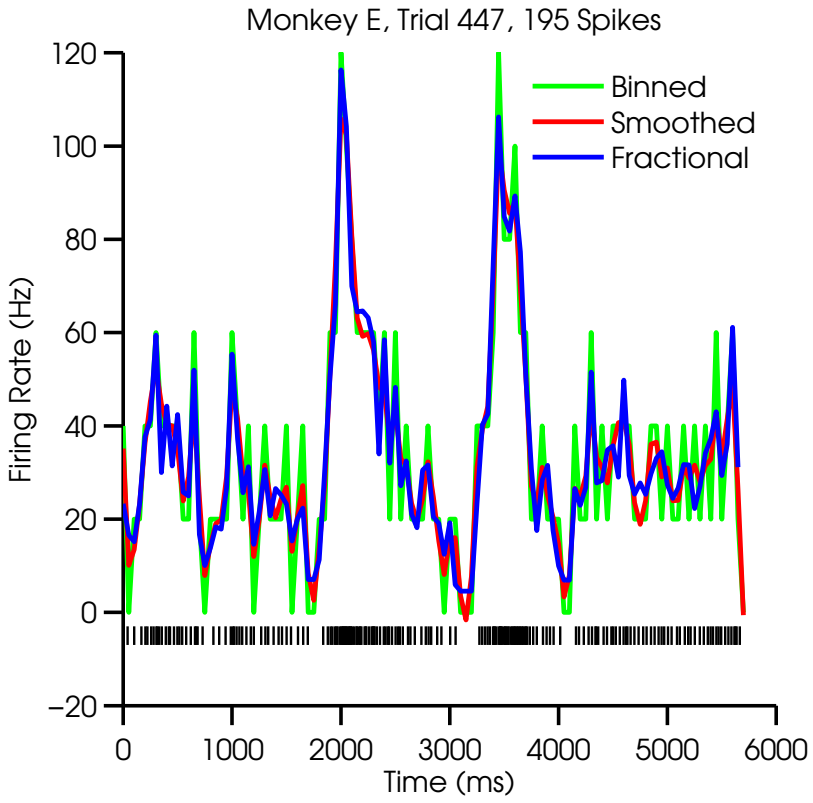

Figure 2.7: **Firing rate computation 2:** Firing rates computed using 50*ms* bins (green), 50*ms* bins with spline-smoothing (red) and fractional firing-rates method (blue). This trial contained 195 spikes. The smooth and fractional firing rates are very similar.

Given K spikes times $s_1,\ldots,s_K$; a time internal $[t_{start},t_{end}]$ in which we would like to calculate the firing rate and a desired bin size T_{bin}, fractional firing rates are computed as follows:

1. Denote $t_1,\ldots,t_N$, the starting times of the N bins resulting from dividing $[t_{start},t_{end}]$ to bins sized T_{bin}
2. Calculate $meanISI = (t_N - t_1)/K$
3. Add artificial first and last spikes (to eliminate edge effects)
   - If $s_1 > t_1$ (first spike occurred after the start time of the first bin), then set $s_0 = min(t_1, s_1 - meanISI)$; else $s_0 =$ the last spike time before t_1.
   - If $s_K < t_N$ (last spike occurred before the start time of the last bin), then set $s_{K+1} = max(t_N, s_K + meanISI)$; else $s_{K+1} =$ the first spike time after t_N.
4. Calculate the firing rate in every bin as a vector λ:
   For i=1,...,N
   - Find the first spike before bin i (s_{before}) and after bin i (s_{after})
   - Count $NumSpikes_i$, the number of spikes in bin i
   - If $NumSpikes_i == 0$, set $binCount_i = T_{bin}/(s_{after} - s_{before})$
   - If $NumSpikes_i > 0$:
     - Calculate the fractional count of s_{first}, the first spike in the bin: $fracCount_{first} = (s_{first} - t_i)/(s_{first} - s_{before})$
     - Calculate the fractional count of s_{last}, the last spike in the bin: $fracCount_{last} = (t_{i+1} - s_{last})/(s_{first} - s_{before})$
     - Set $binCount_i = fracCount_{first} + NumSpikes_i + fracCount_{last}$
   - Set $\lambda[i] = binCount_i/T_{bin}$

We often used what we termed *adjusted* 50*ms bins*. Trials tended to have different durations, even repetitions to the same attitude, due to changing reaction times, different reaching speeds, different hand preshaping times and randomized HoldB times (the required duration to press the object during the static grasp). Using fixed 50*ms* bins would result in a different number of bins for every trial; which was problematic when combining data across trials. We therefore computed, for every session, the average trial duration (from the beginning of MoveA to the end of the static

grasp), denoted T; and assigned it a bin width of $50ms$. For every trial, we computed its duration t_i, and assigned it an adjusted bin width of $(50ms \times \frac{T}{t_i})$. Trials longer than T were assigned bin widths bigger than $50ms$, and trial shorter than $50ms$ were assigned bin widths smaller than $50ms$. We essentially distributed the difference in trial durations uniformly across the trial; which is a reasonable assumption, since we could not always determine the cause of the duration differences in a reliable manner.

2.3 KINEMATIC DATA PROCESSING

2.3.1 KINEMATIC DATA RECORDING PROCEDURES

High resolution kinematic data was recorded using a state-of-the-art motion tracking system (Vicon Inc). The system consisted of 12 motion tracking cameras, hardware control boxes interfaced to the cameras using standard network cables, and specialized software (Nexus, versions $1.2 - 1.6$). The cameras emitted infra red light which was reflected from passive markers back to the cameras, and digitized as a stream of images at a rate of $200Hz$. The Nexus software analyzed the images from all cameras in real time to reconstruct the $3D$ marker positions (see Spalding [63] for details).

The passive markers were custom made at our laboratory, by coating $3mm$-diameter semi-spherical plastic toy eyes with special reflective tape (Vicon Inc). Markers were sewn to a custom fit glove which was placed on the monkey's hand at the beginning of every recording session (Figure 2.8). The glove contained 23 markers: 4 on the forearm, 3 on the palm of the hand, 4 on the thumb segments and 3 markers on every phalange of the remaining 4 fingers. The finger markers were placed on the approximate center of each phalange. The first marker was placed between the metacarpal phalangeal joint (MCP) and the proximal interphalangeal joint (PIP); the second marker was placed between the PIP joint and the distal IP joint (DIP) and the third marker was placed on the fingernail.

The Vicon tracking software reconstructed and labeled the markers in real time by using a kinematic model of the hand and stored $3D$ positions for every labeled marker. While tracking quality was satisfactory for monkey V, whose hand was approximately the size of a 7 y.o. human,

tracking quality was worse for monkeys B and E. Their smaller hands, approximately the size of a human baby, forced the markers to be positioned closer together on the glove, often causing the tracking system to ignore or confuse adjacent markers. To discard outliers, marker positions were manually reviewed using custom software, which visualized a reconstruction of the 23 markers on an animated hand. Trials with simple tracking errors, such as mislabeled markers, were corrected; while trials with missing data or bad marker positions were discarded. Between $10-15\%$ of the marker data for monkeys B and E was discarded following manually inspection, compared with 5% for monkey V.

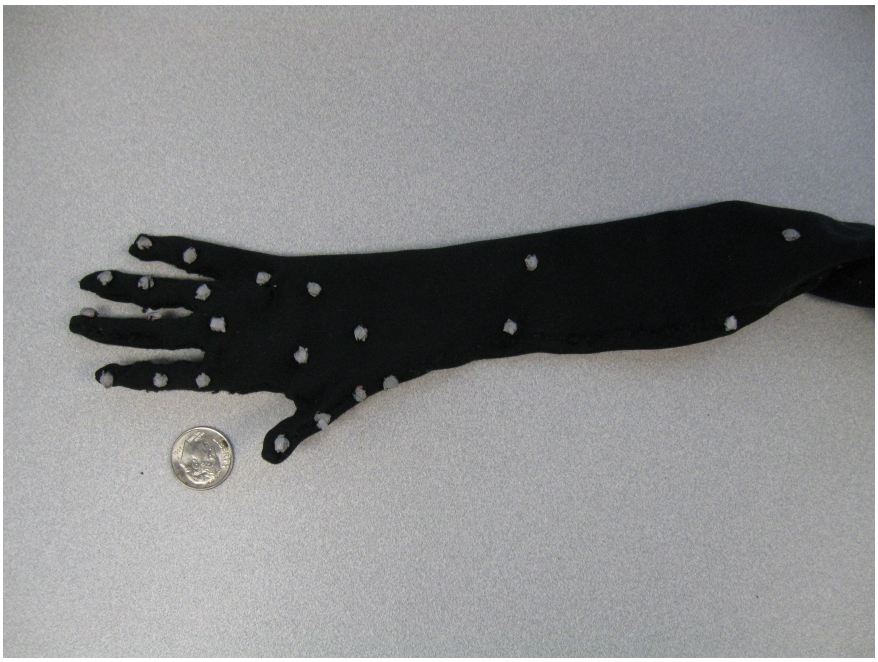

Figure 2.8: **Picture of a Vicon Glove**

The first three data sets collected (monkeys V and B, see Table 4) contained only the real-time marker $3D$ position data computed by the Nexus software during the experiment. For the last two data sets (monkey E), a combined software and hardware upgrade allowed for image data from all 12 cameras to be stored in real time, in addition to the $3D$ real time marker positions. The image data were used for off-line marker reconstruction and manual labeling, resulting in much better data quality. However, manual labeling proved to be too time consuming (around 5 months to manually label one dataset), and an automated algorithm was developed and implemented to auto-

label marker data and fill in gaps. Less than 1% of the kinematic data labeled by the automated algorithm was discarded following manual inspection.

The corrected marker $3D$ positions were low-pass filtered using an FIR filter (Kaiser window, corner frequency of $10Hz$) to eliminate noise. A custom algorithm, developed at our laboratory, was used to estimate joint centers and joint angles (JAs) from the marker data (see Spalding [63] for details).

3.0 DESCRIPTIVE ANALYSIS

3.1 SUMMARY STATISTICS

3.1.1 SINGLE TRIAL DATA

Figures 3.1 and 3.2 show data from a single trial, where monkey E reached to grasp the small handle at the adduction presentation position. The data includes spike trains from 7 simultaneously recorded neurons, EMG from 16 muscles, and 23 joint angles (JAs). Vertical lines in the two figures indicate the beginning of Move-A, and the beginning and end of the static grasp epoch.

While a few muscles were somewhat active during the inter-trial epoch, EMG activity during the movement and grasp epochs was much larger. The temporal order of muscle activation, shown in Figure 3.1, was common across all attitudes. Arm muscles were activated first to move the hand toward the object, followed by the wrist and finger extensors, to extend the wrist and fingers. As the hand moved closer to the object, wrist and finger flexors were activated to preshape the hand. During the static grasp epoch, arm muscles were active to stabilize the arm, while wrist and finger flexors and extensors were active to apply the required force on the object. Figure 3.3 contains spline-smoothed EMG activity for a different trial, with EMG activity for arm, wrist and finger muscles grouped on a separate axis. In this trial, monkey E performed a precision grip at the extension presentation position. The muscle activation order is similar to the one in Figure 3.1.

The joint angles in Figure 3.2 also demonstrate a characteristic temporal activation. First, the wrist was extended, followed by extension of the fingers. As the hand was transported closer to the object, the wrist was flexed to orient the hand at the desired angle to appropriately grasp the object, and the fingers begin to flex in preparation for grasping.

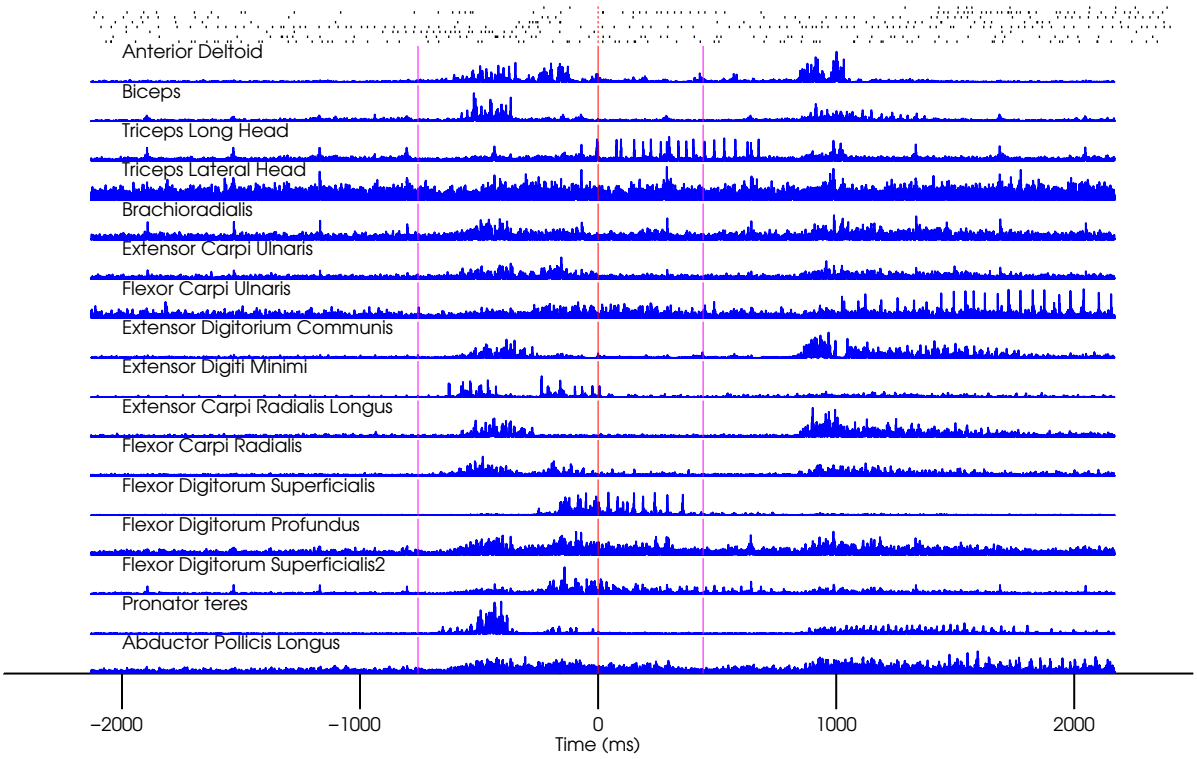

Figure 3.1: **Single trial data:** Data taken from session 647, trial 140. The top panel includes spikes trains from 8 simultaneously recorded neurons. The bottom panels include rectified EMG activity from 16 muscles. Time 0 corresponds to the beginning of the static grasp epoch, also indicated by red vertical lines. The beginning of the MoveA epoch and the end of the static grasp epoch are indicated by magenta vertical lines to the left and right of time zero. Data following the end of the static grasp epoch includes the retrieval of the arm back to the start pad.

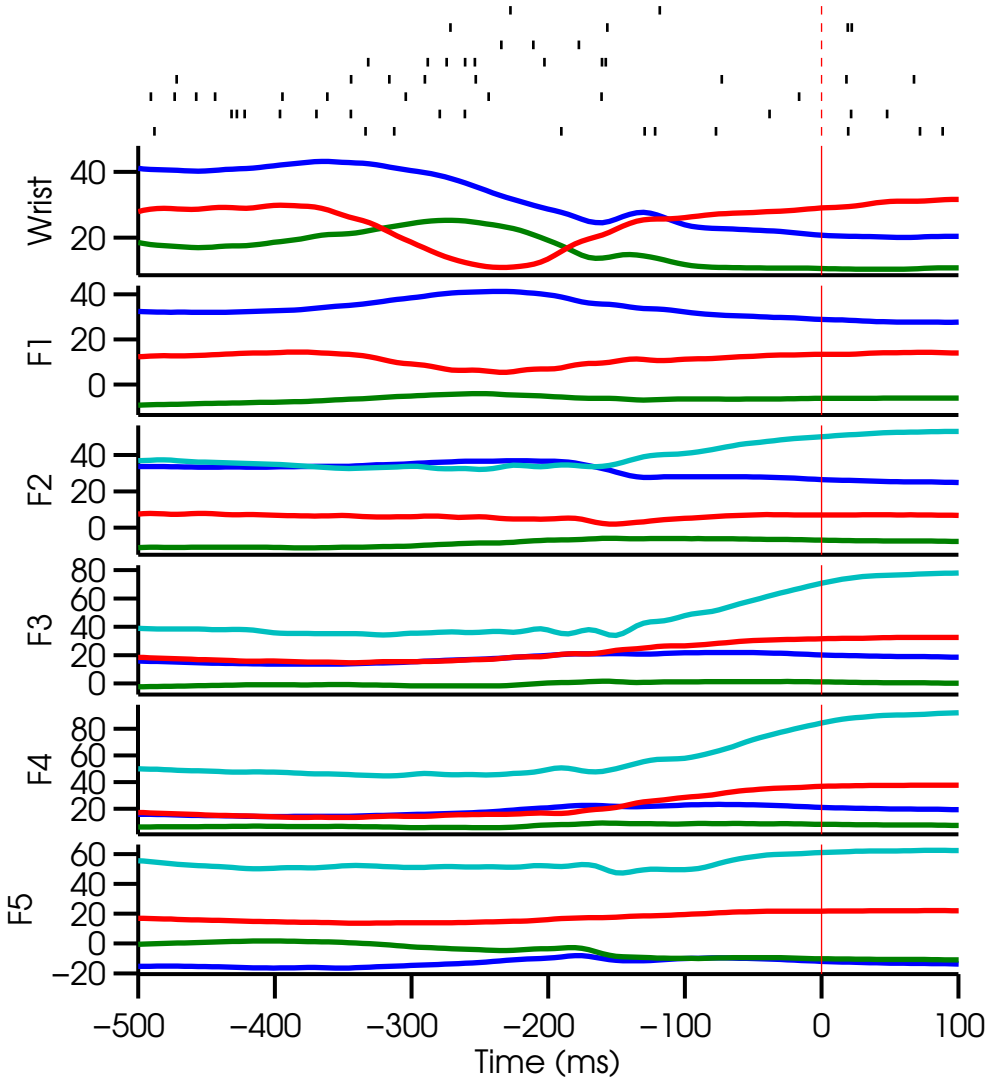

Figure 3.2: **Single trial data:** Data taken from session 647, trial 140. The top panel includes spikes trains from 8 simultaneously recorded neurons. The other panels include joint angles in degrees. The wrist panel includes: flexion (blue), abduction (green), rotation (red). The finger panels include: MCP flexion (blue), MCP abduction (green), PIP flexion (red), DIP flexion (cyan). Time 0 corresponds to the beginning of the static grasp epoch, also indicated by red vertical lines. Note that most of the change in joint angles takes place in the 400*ms* preceding the static grasp.

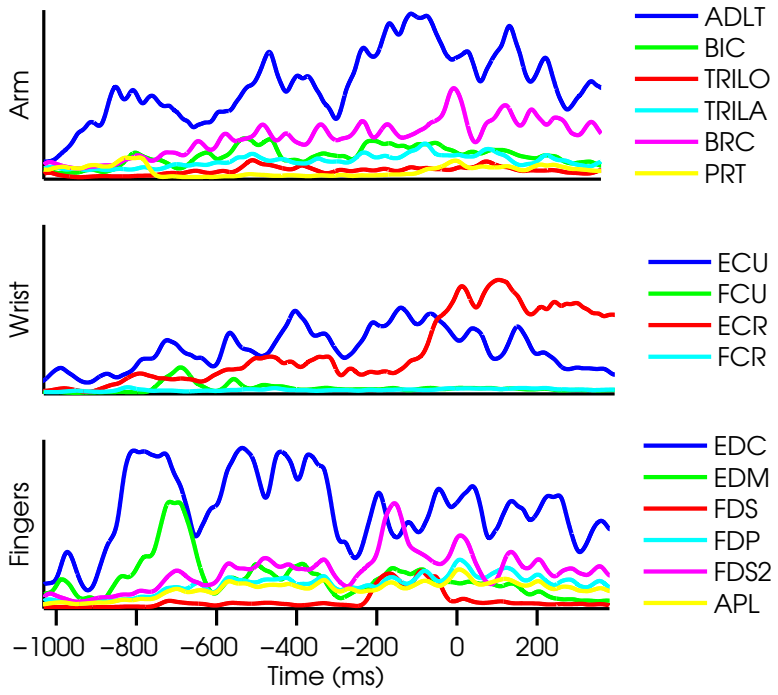

Figure 3.3: **Single trial smoothed EMG data:** Data taken from session 647, trial 30. Note the similarity in muscle activation order to Figure 3.1. Time zero indicates the beginning of the static grasp epoch.

3.1.2 EMG AND JA VARIABILITY ACROSS TRIALS

Figure 3.4 demonstrates the temporal variability in EMG data, for monkey E, across repeated trials to the same attitude. It contains superimposed smoothed EMG activity from 3 representative muscles, over 45 repeat trials to one of the attitudes (small bar, horizontal target). Figure 3.5 shows the corresponding joint angles. In order for a trial to be considered successful, the monkey had to make contact with force sensors on the object. This requirement forced it to shape its hand in an object-specific manner. Comparison of the two figures suggests that while the monkey's movement was indeed very similar across repeat trials, evidenced by similar JA values at different times throughout the trials, EMG activity shows a higher degree of variability. Different EMG activity patterns can elicit similar joint movements for several reasons. First, any single joint movement is determined by the combination of forces produced by multiple co-active muscles. For example, during wrist flexion, wrist flexors and extensors are both often active. Therefore, EMG recorded from a muscle should not be expected to linearly relate to the movement of the joint upon which it acts, since it also depends on other muscles. Second, EMG activity is the summation of action potentials from multiple motor-units. The translation of action potentials to muscle contraction and pulling force depends on various factors, among them muscle fatigue, velocity and length. Therefore, similar EMG activity levels may not elicit the same amount of force, and could be followed by different joint angular movements. A similar conclusion can be reached by examining Figures 3.6 and 3.7, containing data from 20 repeated trials, during which monkey B reached and grasped the small rectangle object at the flexion presentation position.

A more quantitative analysis of EMG variability, for monkey E, is shown in Table 5 and Figure 3.8. Table 5 lists summary statistics computed from unrectified EMG samples, spanning an entire session. Most muscles demonstrate similar variance and range values, indicating that EMG electrodes tended to record similar voltage ranges across muscles. Examining the 10^{th} and 90^{th} percentiles, we can conclude that negative and positive parts of the motor unit action potentials tended to be symmetrical. Figure 3.8 contains a box plot with summary statistics of the rectified EMG samples used in Table 5. Five muscles display higher mean activity than the others: anterior deltoid, flexor carpi ulnaris, extensor digitorium communis, flexor digitorium superficialis and abductor pollicis longus. This is most likely due to the placement of EMG electrodes relative to the

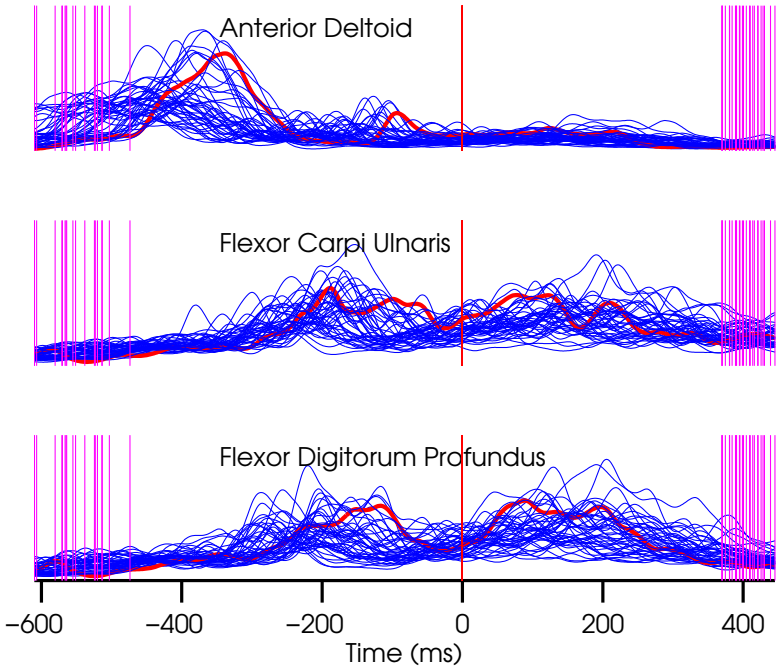

Figure 3.4: **Temporal EMG variability across trials: monkey E:** spline smoothed EMG activity for 3 representative muscles from 45 repeat trials of the same attitude are superimposed (blue traces). EMG activity from a random trial is highlighted in red, demonstrating the temporal variability across trials. Time zero represents the beginning of the static grasp epochs, also indicated by a red vertical line. The beginning of MoveA and the end of the static grasp epoch, for every trial, are indicated by magenta vertical lines.

neuromuscular junction on every muscle; combined with the constraints of the reach to grasp task, where some wrist and finger muscles are bound to be more active than others. We explore that further in Sections 3.2 and 3.3. Figure 3.9 contains the same analysis for monkey B. Only extensor digitorium communis and flexor digitorium profundus show higher mean values compared with the other muscles. The mean EMG levels are similar to those found in monkey E (Figure 3.8).

Quantitative analysis of JA variability, for monkey E, is shown in Table 6 and Figure 3.10. Table 6 lists summary statistics computed from JAs, spanning an entire session. All JA values are within a reasonable physiological range. Unlike humans, Rhesus macaque monkeys do not tend to move their thumb independently of the other fingers. Yet, according to Table 6, the thumb

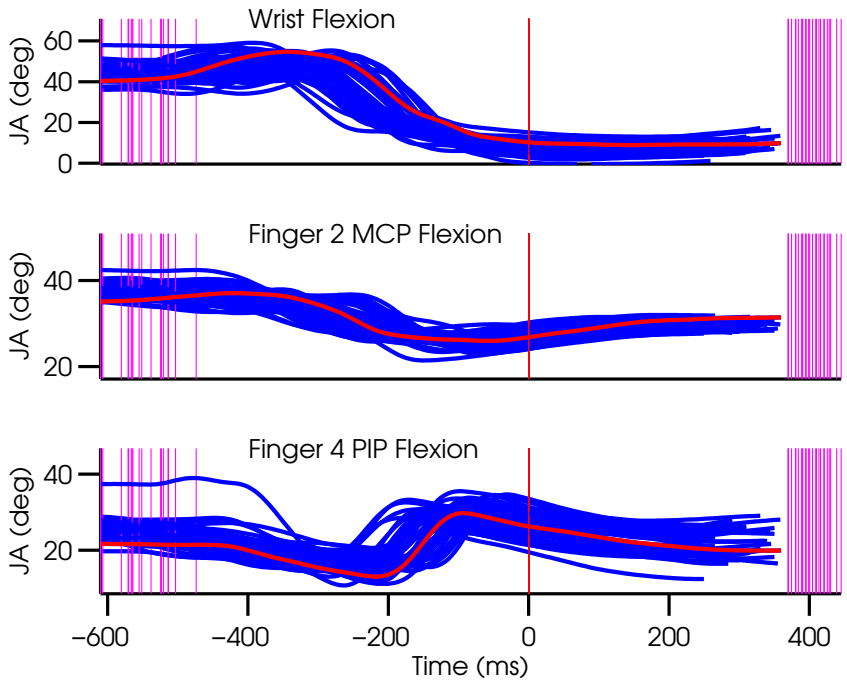

Figure 3.5: **Temporal JA variability across trials: monkey E:** 3 representative joint angles from 45 repeat trials of the same attitude are superimposed (blue traces). JA from a random trial is highlighted in red, demonstrating the temporal variability across trials. Time zero represents the beginning of the static grasp epochs, also indicated by a red vertical line. The beginning of MoveA and the end of the static grasp epoch, for every trial, are indicated by magenta vertical lines.

DIP exhibits a bigger range of motion than the other DIP joints. We determined the cause was inaccurate JA estimates for some trials, rather than independent thumb movement. In monkeys B and E, the thumb DIP segment was very small and the Vicon marker used to track it covered the entire segment. Hence, for some trials, it was hard to obtain accurate JA estimates from the marker $3D$ positions for that joint. Therefore, thumb DIP JA values were eliminated from any analysis when they were not reasonable, or vastly dissimilar from other DIP JAs.

Figure 3.10 contains a box plot with summary statistics of the JAs used in Table 6. The means of the DIP JAs are higher than the MCP or PIP joints, indicating that the DIP joint tended to naturally be more flexed. The minimal and mean wrist flexion angles are positive, indicating that

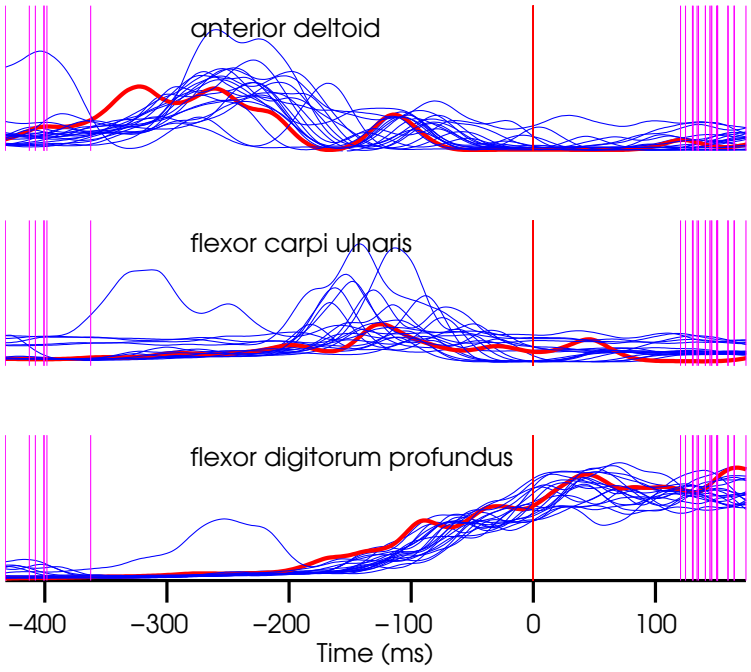

Figure 3.6: **Temporal EMG variability across trials: monkey B:** spline smoothed EMG activity for 3 representative muscles from 20 repeat trials of the same attitude are superimposed (blue traces). EMG activity from from a random trial is highlighted in red, demonstrating the temporal variability across trials. Time zero represents the beginning of the static grasp epochs, also indicated by a red vertical line. The beginning of MoveA and the end of the static grasp epoch, for every trial, are indicated by magenta vertical lines.

monkey E tended to extend his wrist when placing its hand on the start pad. Figure 3.11 shows the results of this analysis for monkey B. The overall pattern is similar to Figure 3.10, except for two differences. First, the thumb DIP JA is not as variable as in monkey E, due to the larger hand size which led to a more reliable calculation of JAs. Second, the mean wrist JAs are negative, as opposed to positive for monkey E. This is due to a sign convention used by our JA calculation software for the wrist: the data for monkey B was collected from the right arm, and the data for monkey E was collected from the left arm. Some signs representing anatomical directions (flexion/extension, abduction/adduction, rotation) were reversed, so that positive adduction, for example, would represent movement in the same external coordinate system, for both hands.

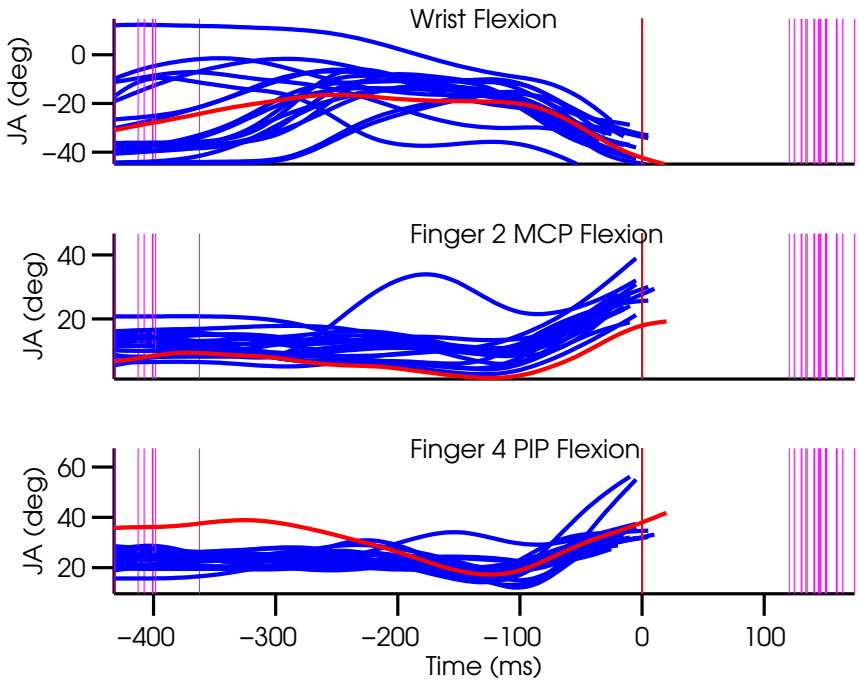

Figure 3.7: **Temporal JA variability across trials: monkey B:** 3 representative joint angles from 20 repeat trials of the same attitude are superimposed (blue traces). JA from a random trial is highlighted in red, demonstrating the temporal variability across trials. Time zero represents the beginning of the static grasp epochs, also indicated by a red vertical line. The beginning of MoveA and the end of the static grasp epoch, for every trial, are indicated by magenta vertical lines.

Figures 3.12 and 3.13 show another interesting characteristic of the monkey E's movement. Both contain superimposed JA values from 60 randomly selected trials, aligned by the time of maximal speed for each trial. As the hand reached its maximal speed during the reach epoch, the wrist and fingers were shaped similarly across trials, even though the monkey was reaching to grasp different objects at different targets. This indicates that monkey E did not tend to preshape its hand at the beginning of the reach. The small variability in JAs prior to the maximal speed indicates the monkey tended to maintain similar hand and wrist shape between trials. Figures 3.14 and 3.15 show that monkey B also did not tend to preshape its hand at the beginning of the trial; and did not maintain similar hand and wrist shapes between trials.

Table 5: EMG summary statistics computed from unrectified EMG samples for a full session, for monkey E. Values are in millivolts.

		10^{th} **prctile**	**Median**	**Mean**	90^{th} **prctile**	**SD**	**Range**
1	ADLT	-0.24701	0.0020187	$8.4168e-09$	0.25238	0.44704	13.6177
2	BIC	-0.12633	0.00037773	$-2.1575e-07$	0.13025	0.23596	13.3476
3	TRILO	-0.12577	-0.0010168	$-3.1361e-06$	0.12545	0.27227	14.5539
4	TRILA	-0.12485	0.0013678	$2.0238e-06$	0.13131	0.2879	15.6267
5	BRC	-0.09592	-0.00060033	$-1.0177e-07$	0.095717	0.19402	11.7412
6	ECU	-0.11862	0.00043633	$1.1987e-06$	0.11604	0.24565	11.7155
7	FCU	-0.50879	0.002052	$5.6012e-06$	0.52235	0.54978	13.298
8	EDC	-0.82958	0.022644	$6.9352e-06$	0.86865	0.94822	17.577
9	EDM	-0.19618	0.00084468	$-6.3726e-06$	0.19599	0.32435	10.7709
10	ECR	-0.20031	-0.0019501	$4.5238e-07$	0.19839	0.49516	13.1281
11	FCR	-0.10542	0.0010161	$-1.5451e-06$	0.10857	0.12605	9.0685
12	FDS	-0.21831	-0.00027789	$-8.0725e-07$	0.22073	0.2569	10.3939
13	FDP	-0.23183	0.00015728	$1.0587e-06$	0.23321	0.26105	9.6046
14	FDS2	-0.47546	0.0039998	$-9.8775e-06$	0.50735	0.55369	13.5313
15	PRT	-0.13539	0.0015787	$-1.4517e-06$	0.16062	0.38896	13.5913
16	APL	-0.43666	0.0030011	$1.8764e-06$	0.43058	0.45085	15.5086

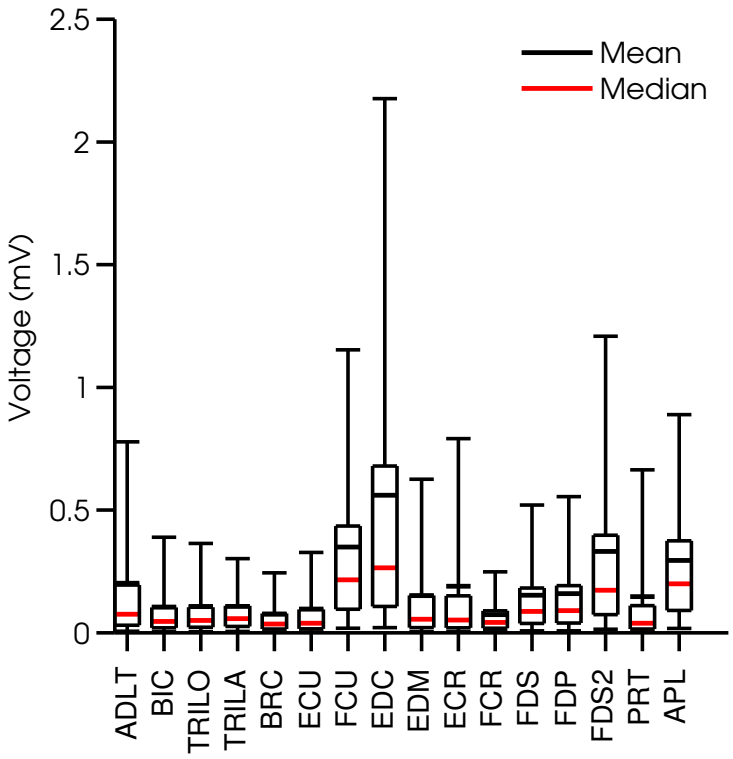

Figure 3.8: **Summary statistics boxplot: monkey E:** for rectified EMG samples from a full session. The boundaries of the boxes are the 1^{st} and 3^{rd} quartiles. The mean and median are indicated by horizontal lines. The whiskers extend to the minimal and maximal values, after removing outliers.

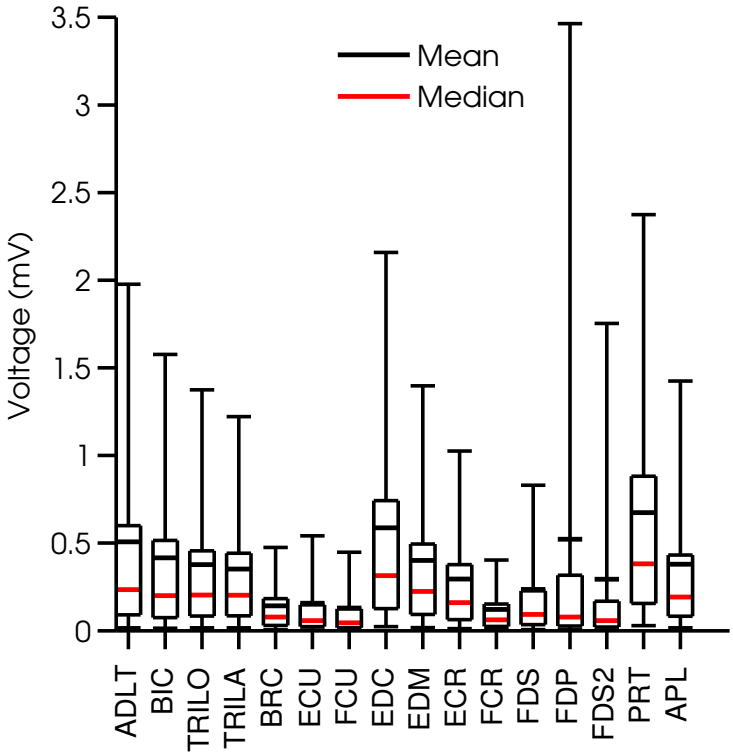

Figure 3.9: **Summary statistics boxplot: monkey B:** for rectified EMG samples from a full session. The boundaries of the boxes are the 1^{st} and 3^{rd} quartiles. The mean and median are indicated by horizontal lines. The whiskers extend to the minimal and maximal values, after removing outliers.

Table 6: JA summary statistics computed from a full session for monkey E. Values are in degrees.

		1^{st} **quartile**	**Median**	**Mean**	3^{rd} **quartile**	**SD**	**Range**
1	WRFL	23.5932	37.2817	32.8737	43.4361	13.8671	29.8422
2	WRAB	10.5607	17.5564	15.6859	23.6587	10.9976	20.029
3	WRRO	13.6021	23.5386	19.7078	31.1806	15.7459	34.7775
4	F1MFL	33.1978	36.4153	37.153	40.2331	6.3284	11.3241
5	F1MAB	−12.6991	−10.0372	−9.0787	−5.6239	5.2651	10.495
6	F1PFL	−10.5668	7.6996	−0.1239	11.4502	16.756	36.4351
7	F1DFL	47.1588	75.8613	60.3078	90	44.8206	56.6745
8	F2MFL	22.1861	29.8086	28.6963	35.2075	8.2264	17.7207
9	F2MAB	−12.4873	−10.097	−8.9248	−6.6897	5.7766	10.4834
10	F2PFL	−3.5597	4.6824	3.2367	9.7284	10.6049	22.008
11	F2DFL	34.4015	39.7102	40.997	45.2537	10.9272	20.2423
12	F3MFL	9.9423	15.3421	14.7695	20.1967	10.8546	16.7196
13	F3MAB	−4.4742	−2.074	−1.1116	1.8662	4.5849	9.2891
14	F3PFL	13.4975	19.0985	18.7881	24.4648	13.8742	20.386
15	F3DFL	34.5147	40.9176	46.2534	51.7569	20.6108	39.154
16	F4MFL	12.0715	17.0942	17.0932	20.9885	11.2158	14.8464
17	F4MAB	4.0431	5.8001	6.4979	8.7263	3.5539	7.1952
18	F4PFL	11.4181	17.6159	18.963	23.794	15.7028	25.6548
19	F4DFL	41.6329	49.6022	57.4888	68.3254	25.9015	49.3497
20	F5MFL	−17.2533	−12.9177	−11.5781	−9.3199	13.7938	17.6025
21	F5MAB	−3.3143	−0.22806	0.46729	4.4013	5.6831	11.5326
22	F5PFL	13.4233	16.8724	17.6013	20.296	9.1738	13.4868
23	F5DFL	46.786	52.6077	61.2375	62.227	29.8424	34.9421

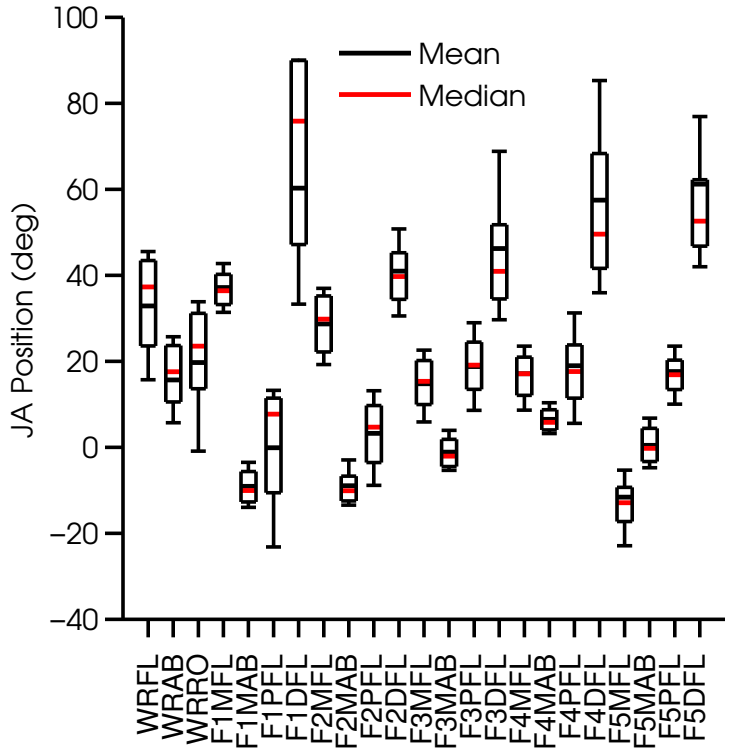

Figure 3.10: **Summary statistics boxplot: monkey E:** for JAs from a full session of monkey E. The boundaries of the boxes are the 1^{st} and 3^{rd} quartiles. The mean and median are indicated by horizontal lines. The whiskers extend to the minimal and maximal values, after removing outliers.

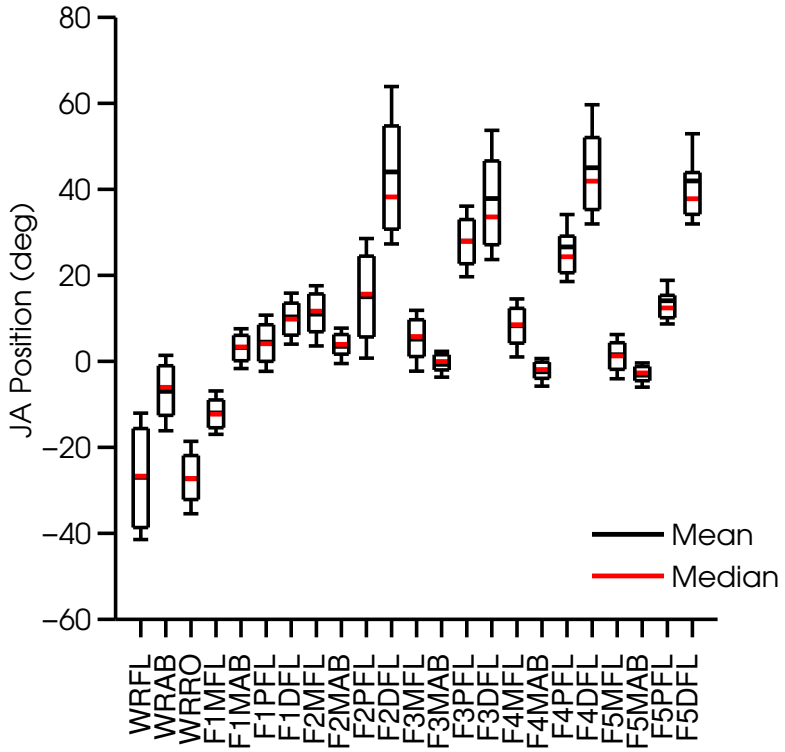

Figure 3.11: **Summary statistics boxplot: monkey B:** for JAs from a full session of monkey E. The boundaries of the boxes are the 1^{st} and 3^{rd} quartiles. The mean and median are indicated by horizontal lines. The whiskers extend to the minimal and maximal values, after removing outliers.

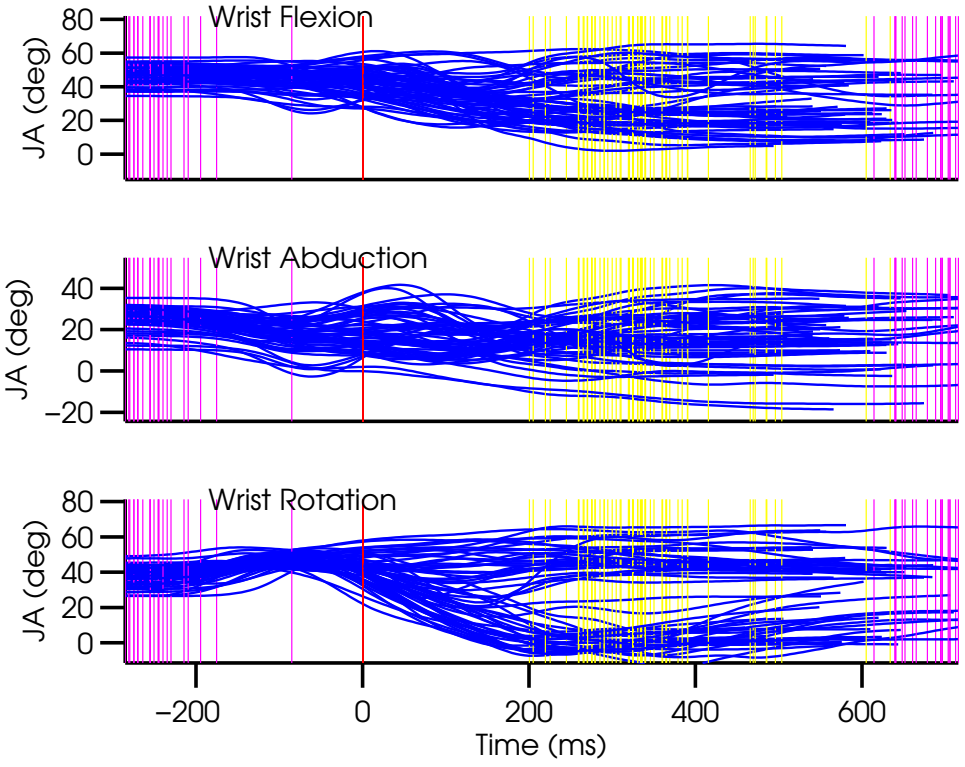

Figure 3.12: Wrist joint angles from 60 randomly selected trials, for monkey E, are superimposed (blue traces). Time zero represents the time of maximal end-point velocity during the reach, also indicated by a red vertical line. The beginning of MoveA and the end of the static grasp epoch, for every trial, are indicated by magenta vertical lines. The beginning of the static grasp epoch is indicated by a yellow vertical line.

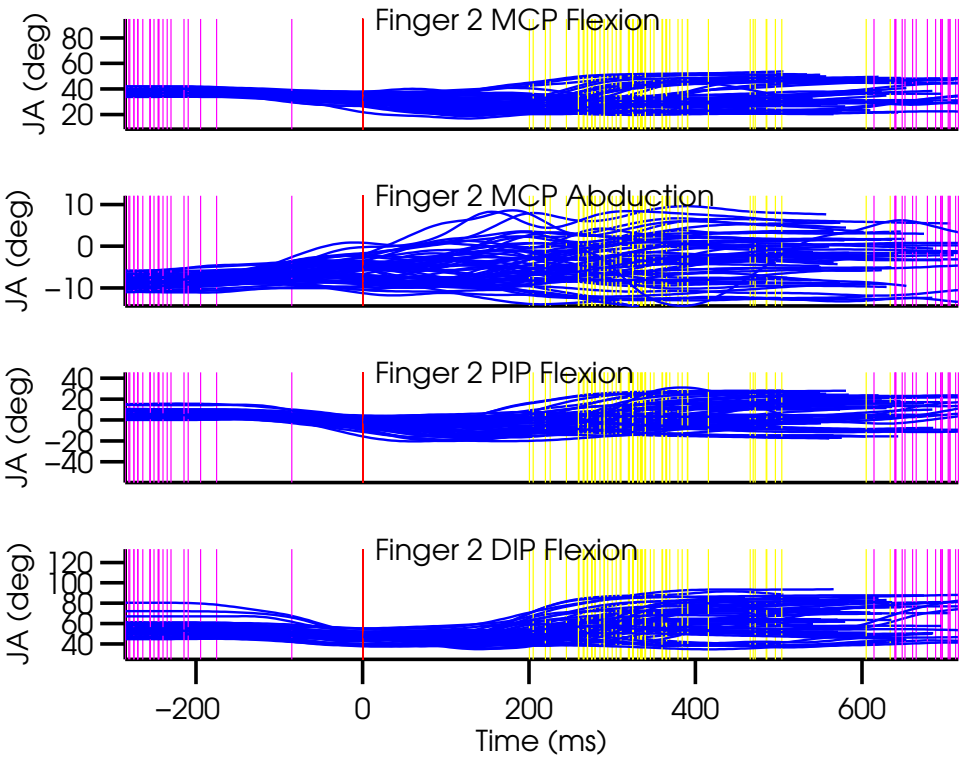

Figure 3.13: Finger 2 joint angles from 60 randomly selected trials, for monkey E, are superimposed (blue traces). Time zero represents the time of maximal end-point velocity during the reach, also indicated by a red vertical line. The beginning of MoveA and the end of the static grasp epoch, for every trial, are indicated by magenta vertical lines. The beginning of the static grasp epoch is indicated by a yellow vertical line.

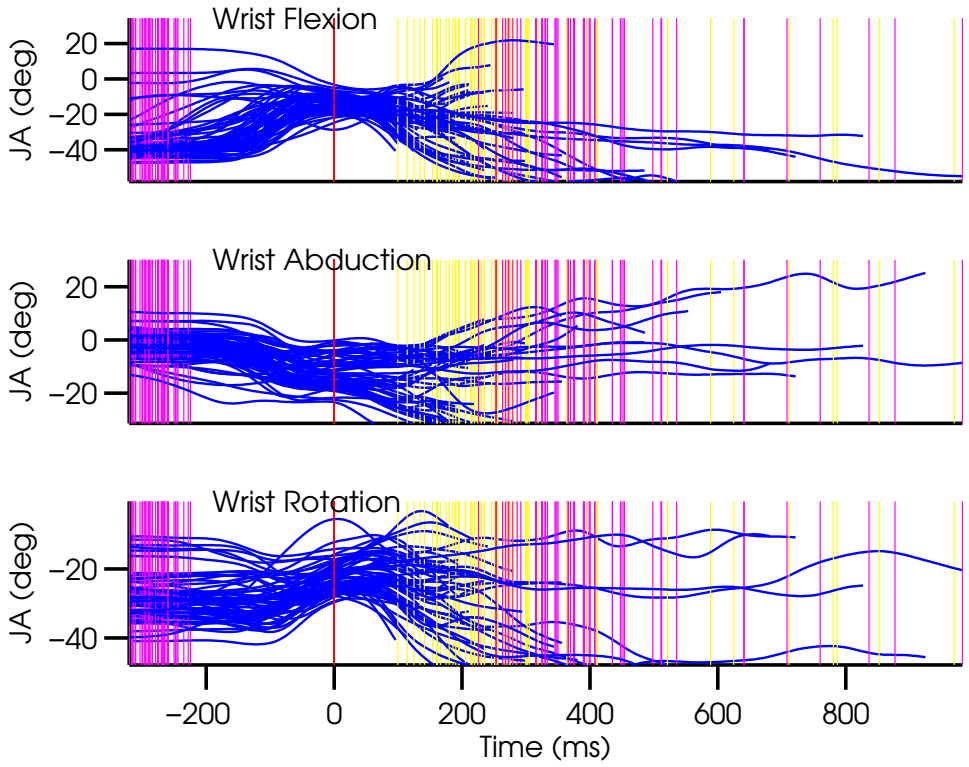

Figure 3.14: Wrist joint angles from 60 randomly selected trials, for monkey B, are superimposed (blue traces). Time zero represents the time of maximal end-point velocity during the reach, also indicated by a red vertical line. The beginning of MoveA and the end of the static grasp epoch, for every trial, are indicated by magenta vertical lines. The beginning of the static grasp epoch is indicated by a yellow vertical line.

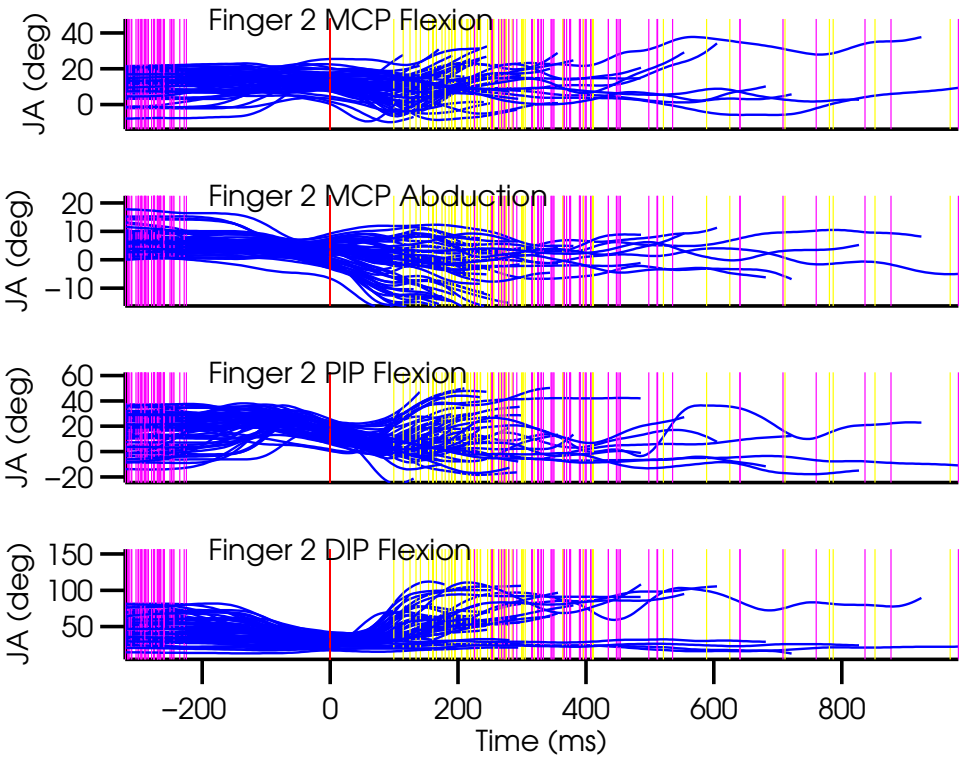

Figure 3.15: Finger 2 joint angles from 60 randomly selected trials, for monkey B, are superimposed (blue traces). Time zero represents the time of maximal end-point velocity during the reach, also indicated by a red vertical line. The beginning of MoveA and the end of the static grasp epoch, for every trial, are indicated by magenta vertical lines. The beginning of the static grasp epoch is indicated by a yellow vertical line.

3.1.3 SIGNAL TO NOISE ANALYSIS

To compare the quality of the EMG and JA data, we examined their signal to noise ratios. Signal to noise ratio compares the signal power to the noise power, and is defined as:

$$SNR = (P_{signal}/P_{noise}) = (A_{signal}/A_{noise})^2 \tag{3.1}$$

where P represents average power and A represents the amplitude. Since many signals have large dynamic ranges, SNR is usually expressed in logarithmic units (dB) and computed according to:

$$SNR_{dB} = 20log_{10}(A_{signal}/A_{noise}) \tag{3.2}$$

There are various ways to compute the amplitude of a signal. In electrical engineering, root-mean-square (RMS) amplitude is used for non-repeating signals. Given N samples from signal x, its RMS amplitude is computed using:

$$A_{RMS} = \sqrt{\frac{1}{n}(x_1^2 + x_2^2 + \cdots + x_N^2)} \tag{3.3}$$

Another commonly used way to compute the amplitude of a signal is the peak-to-peak (PP) amplitude, which is the change between the highest and lowest values of a signal.

The EMG data contained raw voltage recordings from 16 bi-polar electrodes, but was rectified in all subsequent analyses. Hence we followed the same procedure here, and used rectified EMG data, which contained zero and positive values. It was then appropriate to compute the EMG RMS amplitude to determine the SNR. The kinematic data contained the 3D spatial locations of 23 reflective markers, with both negative and positive values, hence it was appropriate to compute its peak-to-peak amplitude.

To compute the signal amplitude of both EMG and kinematic data, we used 4 minutes of data from trials in which the monkey reached to different attitudes. To compute the noise amplitude for both EMG and kinematic data, we used 1 minute of data in which the monkey sat in its chair and rested its hand on the start button, without producing any visible EMG. Figure 3.16 shows the SNR for the EMG data, and Figure 3.17 shows the SNR for the kinematic data. The kinematic data had significantly higher SNR compared to EMG, probably due to its nature (a deterministic signal compared to EMG which is a stochastic signal), and due to the fact that we used significantly more

sensors to collect the kinematic data (12 cameras) compared to the EMG data (a single bi-polar electrode per muscle). Hence, the spatial location of the markers was measured with sub-millimeter accuracy.

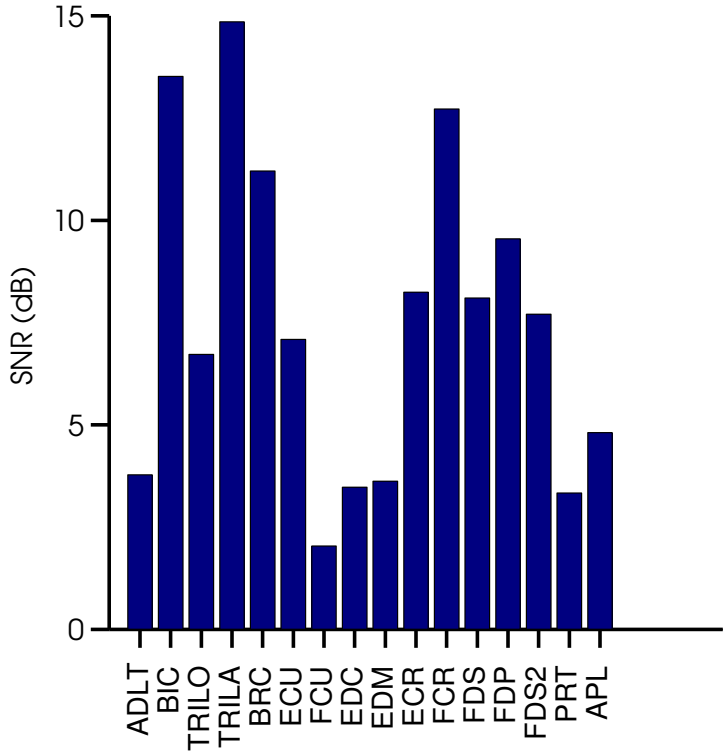

Figure 3.16: **EMG signal-to-noise ratio for** 16 **muscles: monkey E:** 4 minutes of reaching data were used to compute the EMG signal RMS amplitude. 1 minute during which the monkey rested its hand on the start button was used to compute the noise RMS amplitude. Some muscles show higher SNR than others, indicating the recording electrode might have been closer to the neuro-muscular junction for those muscles.

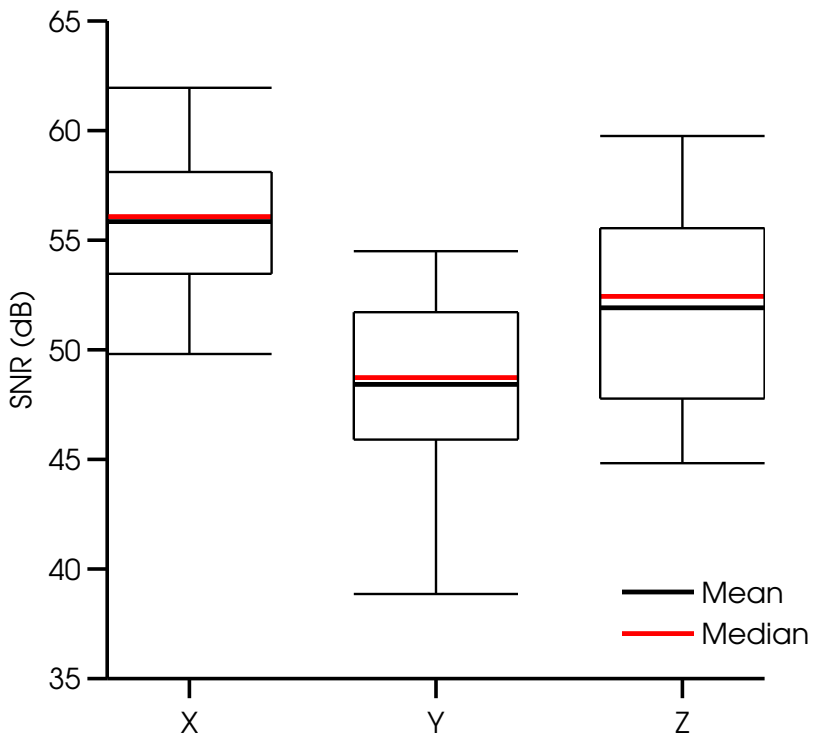

Figure 3.17: **Kinematics signal-to-noise ratio for** 23 **markers: monkey E:** 4 minutes of reaching data were used to compute the kinematics peak-to-peak amplitude. 1 minute during which the monkey rested its hand on the start button was used to compute the noise peak-to-peak amplitude. For every marker, the data contained 3 measurements: its x,y and z spatial location. We computed the SNR for all markers, and show a box-plot summarizing the SNR for all markers, separated to x,y and z measurements. The x direction represented forwards-backwards movements and had higher SNR compared to the other directions.

3.1.4 PERFORMANCE ACROSS SESSIONS

Figures 3.18 and 3.19 show histograms of reaction times for monkeys E and B. Reaction times were computed as the time between the lights on event (”Go“ cue) and the time when the hand reached 20% of its maximal speed. Mean reaction times for both monkeys are within a reasonable range. Some trials have reaction times shorter than 100*ms*, suggesting both monkeys sometimes tended to guess when the lights would go on. Monkey B tended to do that more than monkey E.

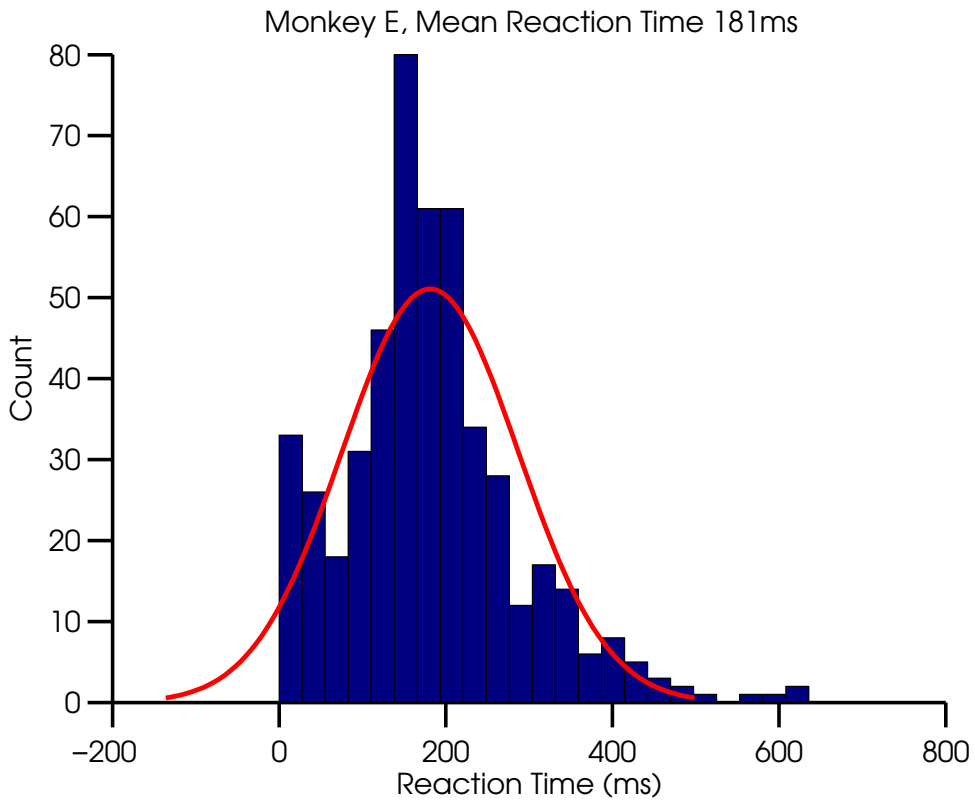

Figure 3.18: Histogram of reaction times, computed as the duration from the lights on event to the time at which the hand reached 20% of its maximal speed. Data combined from 495 trials is shown, with a normal fit to the histogram. Reaction times close to zero indicate trials where the monkey started moving prior to the ”go“ cue.

Figures 3.20 and 3.21 show the number of total trials and the number of successful trials for every recording session for both monkeys. Figures 3.22 and 3.23 summarize that information by plotting the success rate for every recording session. The majority of failed trials, for both monkeys, were caused by a MoveA timeout, often late in the recording session. This was caused by the monkeys initiating trials by placing their hands on the start pad without reaching for the objects, which often happened late in the session, when the animals were satiated and wanted to rest. Success rates are shown after removing trials failed due to a MoveA timeout at the last portion of every recording session.

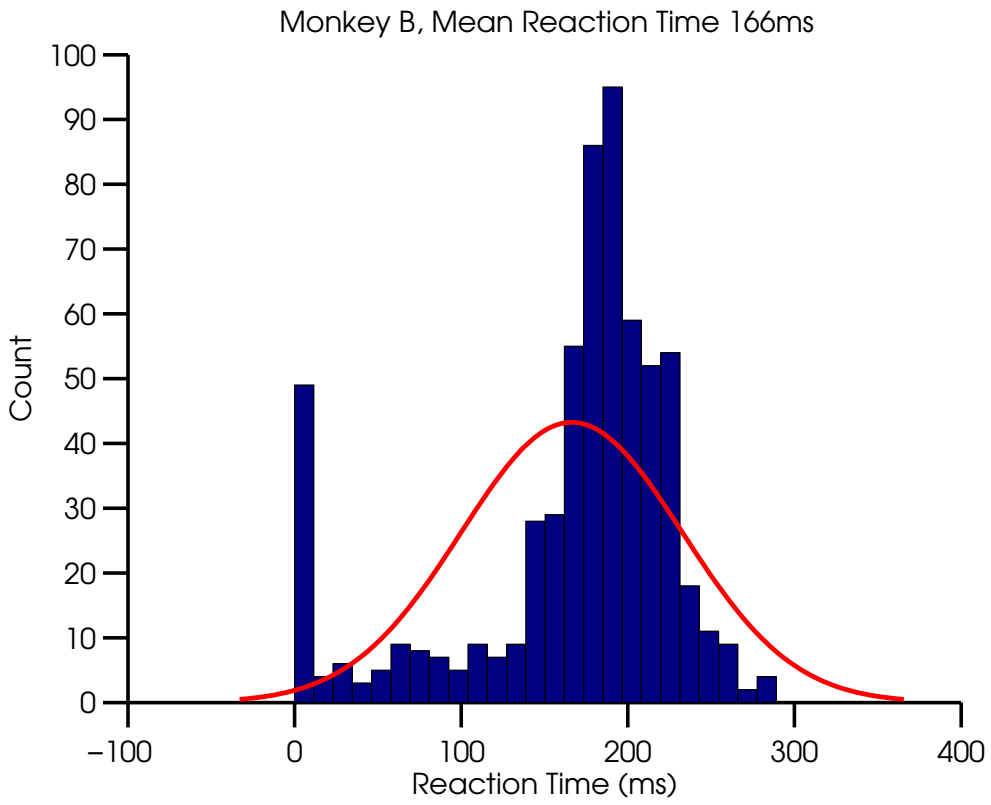

Figure 3.19: Histogram of reaction times, computed as the duration from the lights on event to the time at which the hand reached 20% of its maximal speed. Data combined from 633 trials is shown, with a normal fit to the histogram. Reaction times close to zero indicate trials where the monkey started moving prior to the ”go“ cue.

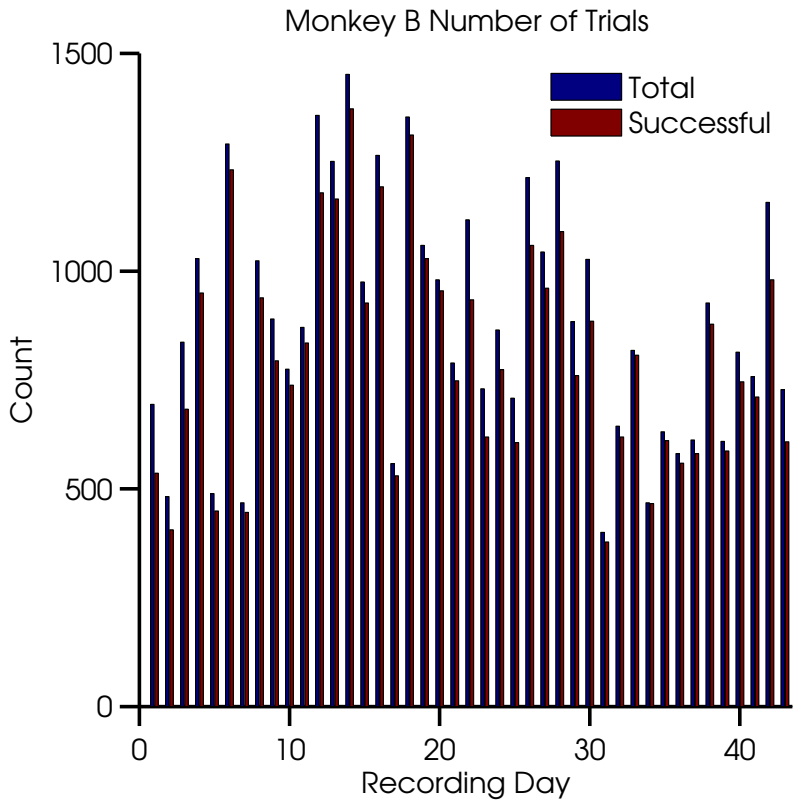

Figure 3.20: Histograms of the number of total trials and successful trials for every recording session for monkey B.

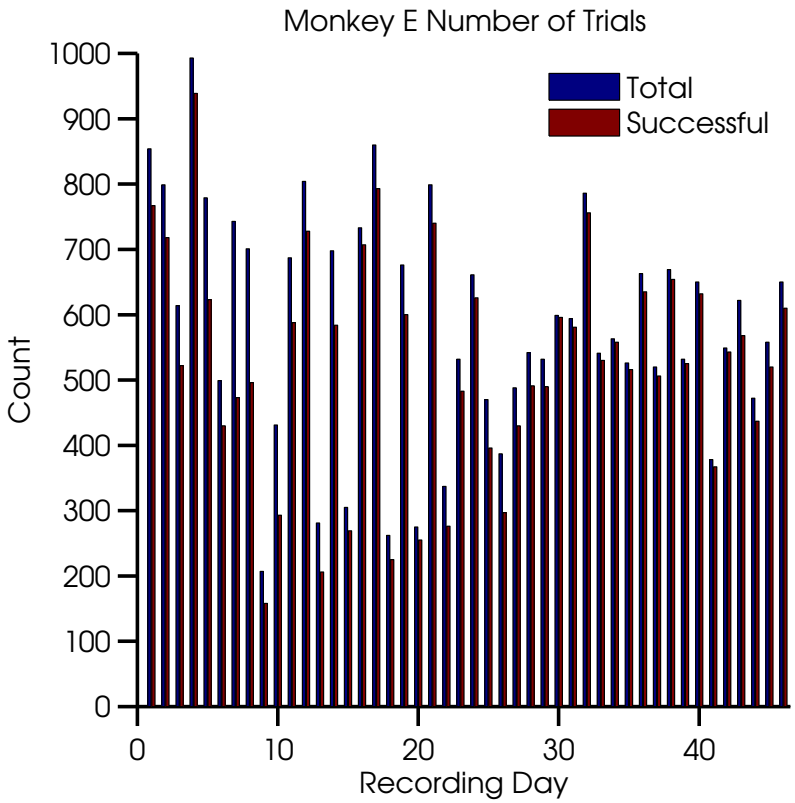

Figure 3.21: Histograms of the number of total trials and successful trials for every recording session for monkey E.

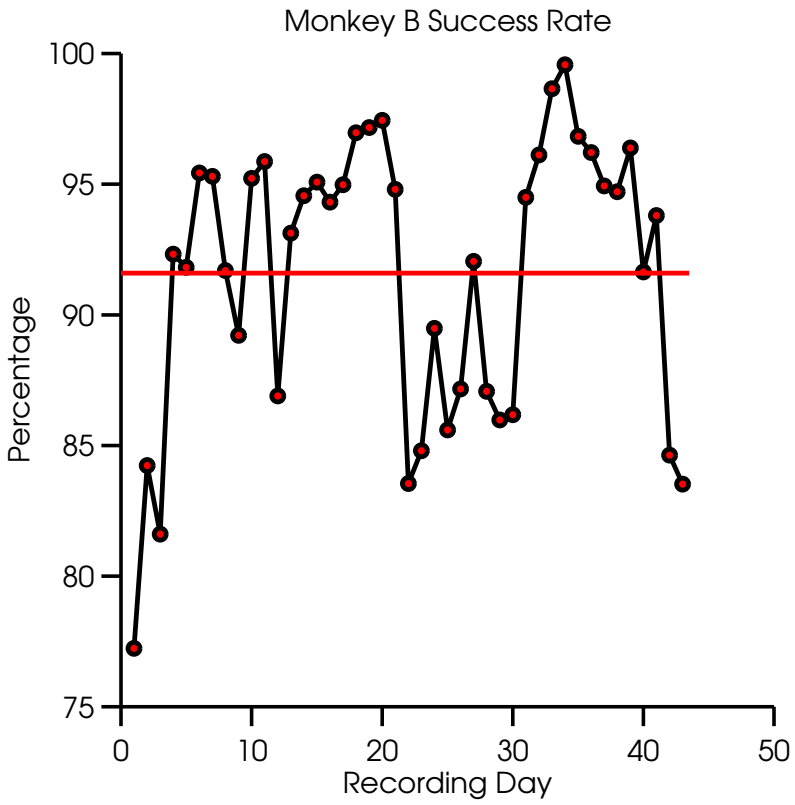

Figure 3.22: Success rate for every recording session (monkey B), computed as the number of successful trials divided by the number of total trials. The average success rate is plotted as a red horizontal line.

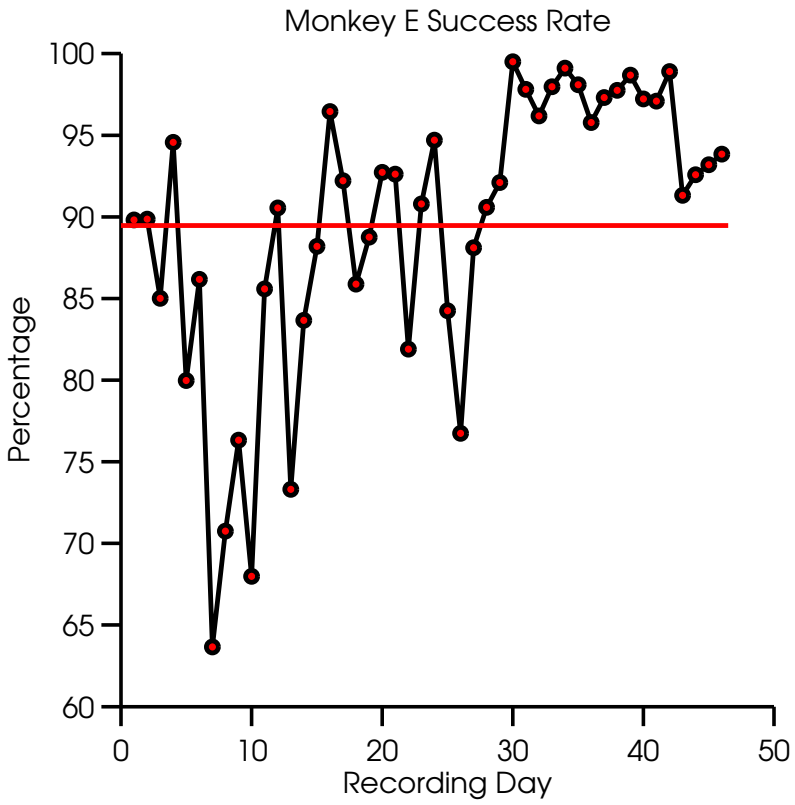

Figure 3.23: Success rate for every recording session (monkey E), computed as the number of successful trials divided by the number of total trials. The average success rate is plotted as a red horizontal line.

3.2 CLASSIFICATION OF TASK COVARIATES USING EMG AND JA

Previous studies have suggested that hand kinematics and EMG activity during reach-to-grasp movements show distinct activity patterns for different objects (Brochier et al. [4],Santello et al. [60]). We tested those hypotheses on our data, and extended them by testing selectivity of both EMG activity and hand kinematics to objects, targets and attitudes (combinations of objects and targets).

3.2.1 CLASSIFICATION OF ATTITUDES

When selecting the objects and targets to be used in this task, a main goal was the ability to record a rich set of hand shapes and EMG, where correlation patterns between JAs and muscles would be as different as possible between attitudes. This would enable us to more accurately associate neural firing rates with EMG and JAs, compared to a degenerate task design with a small number of attitudes. We asked whether the objects and targets shown in Table 1 and Figure 2.1 elicited different hand shapes and EMG patterns, by classifying the attitudes using the recorded EMG or JAs.

We used a linear discriminant analysis (LDA) classifier, designed to find a linear combination of features that best separates the classes, which in our case are attitudes [26]. LDA belongs to a class of methods which models discriminant functions for each class, and then classifies features to the class with the largest discriminant function value. It uses linear decision boundaries, defined as hyperplanes when the data dimensionality is more than two. If we denote the attitudes by G (class label taking values from a discrete set of values), and the EMG or JAs by $\vec{X}$ (features, with p dimensions), according to the decision theory for classification, we need to know the class posteriors $P(G|X)$ for optimal classification. Let $f_k(x)$ be the class conditional density of X in class $G = k$, and π_k the prior probability of class k, where $\sum_{k=1}^{K} \pi_k = 1$, estimated from a training set. According to Bayes theorem:

$$Pr(G = k|X = x) = \frac{f_k(x)\pi_k}{\sum_{l=1}^{K} f_l(x)\pi_l} \tag{3.4}$$

LDA models each class conditional density as a multivariate Gaussian

$$f_k(x) = \frac{1}{(2\pi)^{p/2}|\Sigma_k|^{1/2}} e^{-\frac{1}{2}(x-\mu_k)^T\Sigma_k(x-\mu_k)} \tag{3.5}$$

with the relaxing assumption that all classes have a common covariance matrix $\Sigma_k = \Sigma, \forall k$. It then performs two-class classification by examining the log ratio:

$$log\frac{Pr(G=k|X=x)}{Pr(G=l|X=x)} = log\frac{f_k(x)}{f_l(x)} + log\frac{\pi_k}{\pi_l} = -\frac{1}{2}(\mu_k+\mu_l)^T\Sigma^{-1}(\mu_k-\mu_l) + x^T\Sigma^{-1}(\mu_k-\mu_l) + log\frac{\pi_k}{\pi_l} \tag{3.6}$$

which is linear in x. Multi-class classification is achieved by dividing the feature plane to regions which are separated by hyperplanes.

We can also describe the LDA decision rule by using linear discriminant functions

$$\delta_k(x) = -\frac{1}{2}\mu_k^T\Sigma^{-1}\mu_k + x^T\Sigma^{-1}\mu_k + log\pi_k \tag{3.7}$$

where $G(x) = argmax_k\delta_k(x)$.

In practice, we estimate the parameters of the Gaussian distributions from our training data:
$\hat{\pi}_k = N_k/N$ where N_k is the number of occurrences of class k (a uniform distribution in our case)
$\hat{\mu_k} = \sum x_i/N_k$ for all features assigned class k
$\hat{\Sigma} = \sum_{k=1}^{K}\sum_{g_i=k}(x_i-\hat{\mu_k})(x_i-\hat{\mu_k})^T/(N-K)$

We selected average muscle activation levels as features, computed using all samples from the beginning of MoveA epoch to the end of the static grasp epoch. These features ignored temporal correlations between muscles. For every trial, we calculated a 16 dimensional feature vector, containing means of rectified EMG for every muscle. LDA classification error rate was estimated using 10-fold cross-validation. Average confusion matrices for monkeys B and E are shown in Figures 3.24 and 3.25. The mean classification error rates were 25% (B) and 31% (E). These results indicate that mean EMG activation is sufficiently different between attitudes, since the classification rate is well above chance. Incorporating temporal structure should increase the classification rate even more.

We investigated whether mean EMG data calculated over different epochs reduced the classification error, by repeating the above analysis using only samples which occurred between specific

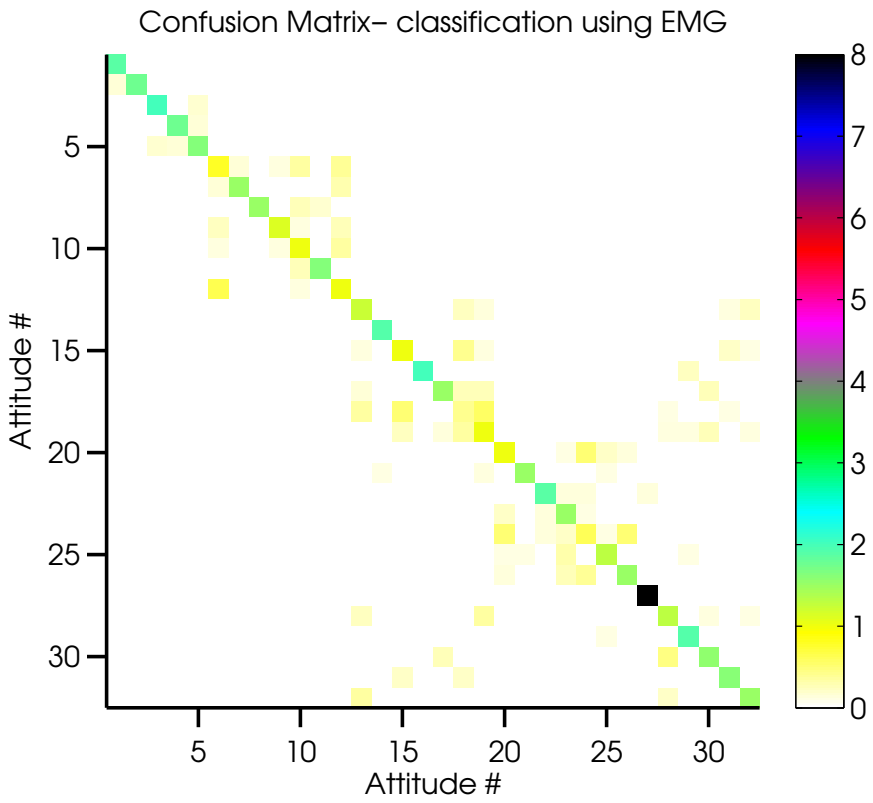

Figure 3.24: **Monkey B**: Average confusion matrix for classifying attitudes using EMG features. Features contained mean EMG from the beginning of MoveA epoch to the end of the static grasp epoch, for all muscles, for every trial. The matrix was averaged from 10-fold cross-validation results. The mean classification error rate was 25%.

task events. The following events were used for this analysis: *Reach Start* was the time the hand speed reached ($5\% \times MaxSpeed$) before the maximal speed; *Reach End* was the time the hand speed reached ($5\% \times MaxSpeed$) after the maximal speed; *Grasp Start* was the time the monkey started pressing the object; *Grasp End* was *HoldB* milliseconds after *Grasp Start* (this value was determined from the recorded real-time value for HoldB for every trial).

The results, presented in Table 7, suggest that there was no advantage to calculating the mean EMG from specific task epochs. This indicates that information contained in the correlation of EMGs is spread throughout the task, which is reasonable, since arm muscles are activated prior to

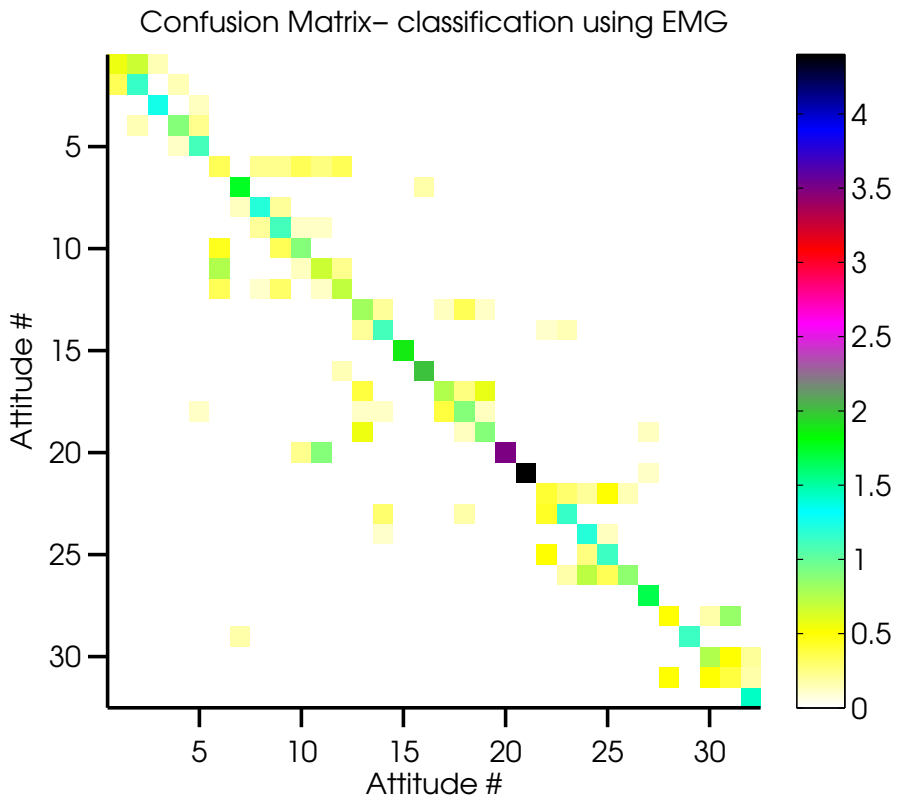

Figure 3.25: **Monkey E**: Average confusion matrix for classifying attitudes using EMG features. Features contained mean EMG from the beginning of MoveA epoch to the end of the static grasp epoch, for all muscles, for every trial. The matrix was averaged from 10-fold cross-validation results. The mean classification error rate was 31%.

wrist muscles at the beginning of the reach, followed by wrist and hand muscles at the end of the reach (see Figure 3.3).

Since the monkeys reached to objects of different shapes at different targets, requiring different wrist orientations, one would expect JAs to be a better predictor of attitude than EMG. We therefore repeated the attitude classification using mean JAs as the features. When using data from the entire task (beginning of MoveA to the end of the static grasp), classification rates were low for monkey B (59%, Figure 3.26), but better for monkey E (80%, Figure 3.27). We suspect this was a result of monkey E maintaining similar hand shape and wrist orientation between trials, causing the

Table 7: **Attitude classification mean error rates**: features contained mean EMGs of samples which occurred between the specified task events. The mean error rates were calculated from the results of 10-fold cross-validation.

			Monkey B	**Monkey E**
	Start Event	**End Event**	**Error Mean±SD**	**Error Mean±SD**
1	N/A	N/A	25.20 ± 4.74	31.84 ± 7.34
2	Reach Start	Reach End	52.96 ± 6.16	32.65 ± 7.33
3	Reach Start	Max Speed	73.98 ± 6.59	64.69 ± 6.01
4	Max Speed	Reach End	51.21 ± 8.40	36.12 ± 5.70
5	Max Speed	Grasp Start	33.69 ± 5.35	32.24 ± 6.44
6	Reach End	Grasp Start	40.62 ± 5.66	46.33 ± 8.17
7	Reach End	Grasp End	29.67 ± 6.51	37.14 ± 6.86
8	Grasp Start	Grasp End	42.38 ± 5.75	35.31 ± 5.45

JA features to be more informative of the hand shape at the end of the trial. On the other hand, monkey B tended to use variable hand shapes between trials, so JA features were less informative of the hand shape at the end of the trial (see Figures 3.14,3.15 compared to Figures 3.12,3.13). Knowing that both monkeys tended to preshape their hand and wrists towards the end of the reach, we repeated the classification using only JA samples collected between specific task events. The results, listed in Table 8 indicated that using samples from the preshape phase, usually occurring after the hand has reached its maximal speed, significantly reduced the classification error rate.

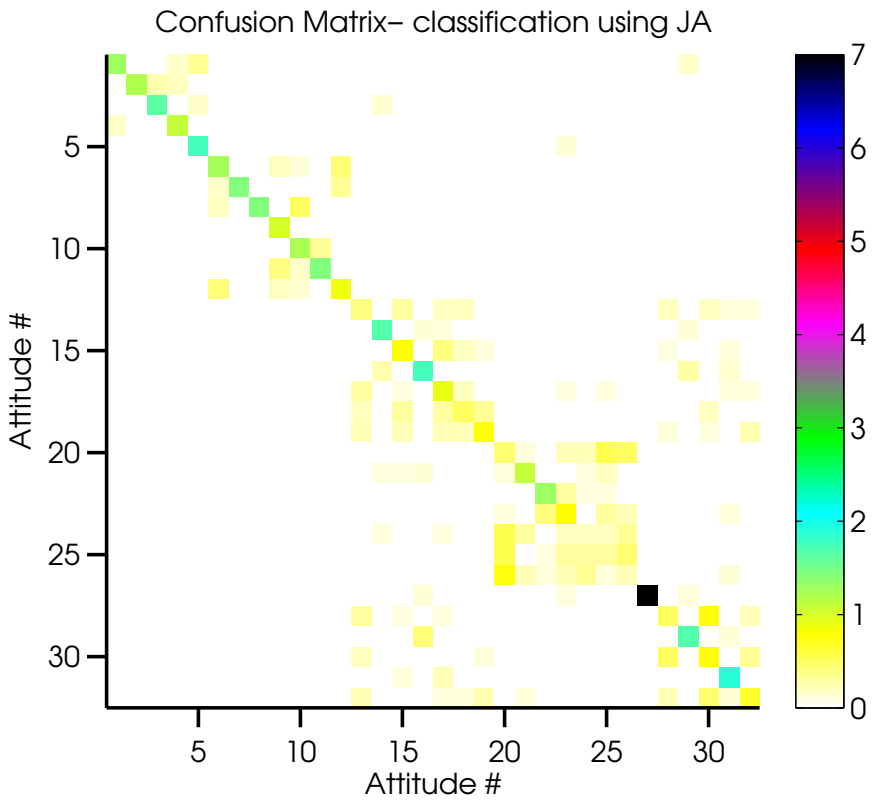

Figure 3.26: **Monkey B**: Average confusion matrix for classifying attitudes using JA features, defined as the mean JA from the beginning of MoveA epoch to the end of the static grasp epoch. The matrix was averaged from 10-fold cross-validation results. The mean classification error rate using 10-fold cross-validation was 41%.

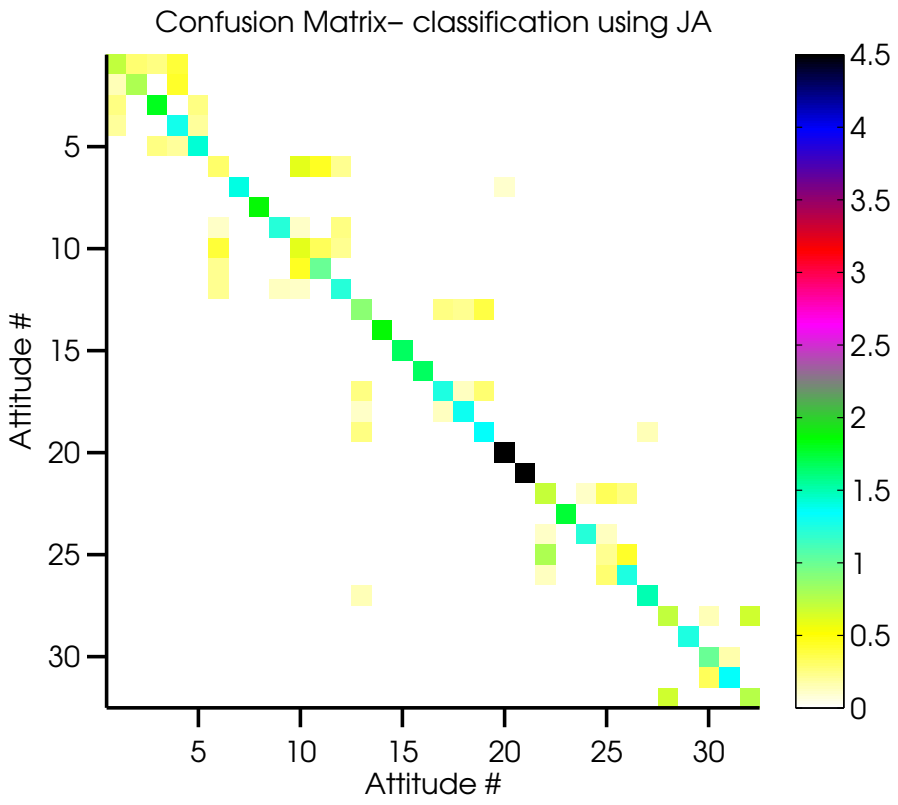

Figure 3.27: **Monkey E**: Average confusion matrix for classifying attitudes using JA features, defined as the mean JA from the beginning of MoveA epoch to the end of the static grasp epoch. The matrix was averaged from 10-fold cross-validation results. The mean classification error rate using 10-fold cross-validation was 20%.

Table 8: **Attitude classification mean error rates**: features contained mean JAs of samples which occurred between the specified task events. The mean error rates were calculated from the results of 10-fold cross-validation.

			Monkey B	**Monkey E**
	Start Event	**End Event**	**Error Mean±SD** (%)	**Error Mean±SD** (%)
1	N/A	N/A	40.72 ± 7.05	20.32 ± 6.16
2	Reach Start	Reach End	34.97 ± 6.02	27.77 ± 6.16
3	Reach Start	Max Speed	51.97 ± 7.97	60.66 ± 5.55
4	Max Speed	Reach End	25.91 ± 5.85	23.28 ± 7.64
5	Max Speed	Grasp Start	18.94 ± 3.92	17.54 ± 6.74
6	Reach End	Grasp Start	14.54 ± 4.38	15.70 ± 6.12
7	Reach End	Grasp End	14.58 ± 4.46	15.70 ± 4.12

3.2.2 IMPORTANT FEATURES FOR CLASSIFICATION OF ATTITUDES

LDA uses a covariance matrix computed from the training data (Σ in Eq. 3.7) for classification, which we can inspect to determine which EMGs and JAs were most helpful in classification. We stored the Σ matrices used by LDA in the cross-validation process, and computed their eigenvalues and eigenvectors. This process is almost identical to principal-component-analysis (PCA), in which an orthogonal rotation of the data is performed to convert the correlated observations to *principal components*, or orthogonal linearly uncorrelated variables. The main difference is that LDA performs a rotation which best separates observations belonging to different input classes, essentially maximizing the inter-class variability, while minimizing the within-class variability in the transformed data. The eigenvectors are usually called the principal-component-coefficients (PCs), and the eigenvalues represent the variances accounted for by the PCs.

We first examined how many PCs were required to account for most of the variance in the EMG features. Figure 3.28 shows superimposed results computed from covariance matrices used by LDA in 10 cross-validation runs. For every cross-validation run, we computed the proportion of the variance accounted for by 1 to 16 PCs. The results are almost identical, suggesting that 7 PCs are sufficient to account for 90% of the variance in the data.

The first 7 PC coefficients for monkey B are plotted in Figure 3.29, and the first 6 PC coefficients for monkey E are plotted in Figure 3.30. It is usually hard to attribute physiological meaning to any of the PCs, since they do not necessarily represent any real physiological phenomena, but are rather the results of mathematical decomposition. However, some similarities are evident between the coefficients calculated for both monkeys: the wrist and finger muscles have higher coefficients in the first PC, while the arm muscles has higher coefficients in PC2 (both monkeys) and PC3 (only monkey B). We can therefore conclude that all three muscle groups (arm, wrist, hand) are important for optimal classification.

We computed the eigenvectors and eigenvectors from the covariance matrices used in the 10 cross-validations, where attitudes were classified from JAs, using only samples occurring between *Reach End* and *Grasp End*. Figure 3.31 shows that for both monkeys, 8 PCs were required to account for 90% of the variance. Figures 3.32 and 3.33 show the PC coefficients for one of the cross-validation runs. Only the first PC coefficients are similar between the two monkeys, where

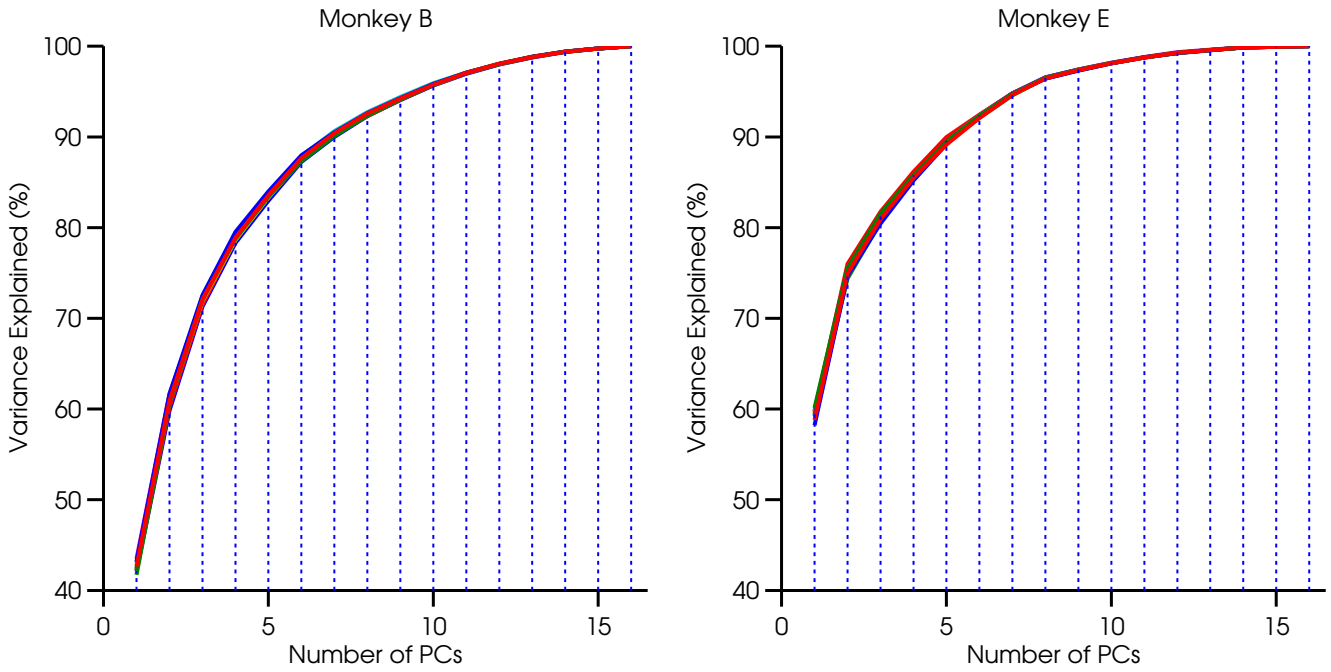

Figure 3.28: Superimposed curves specifying the amount of explained variance as a function of number of PCs, computed from 10 cross-validation Σ matrices, where attitudes were classified using mean EMG. The results are almost identical across all matrices. For monkey B (Left), 7 PCs were required to account for 90% of the variance. For monkey E (Right), 6 PCs were required to account for 90% of the variance.

fingers $3,4$ MCP flexion, fingers $4,5$ PIP flexion and fingers $3,4,5$ DIP flexion receive high coefficients for monkey B; and fingers $2,3,4,5$ PIP and DIP flexion receive high coefficients for monkey E. It is not surprising that the finger JAs account for a large proportion of the variance, since they measure hand shape, which differentiates objects best. The wrist flexion JA receives high coefficients in the first three PCs.

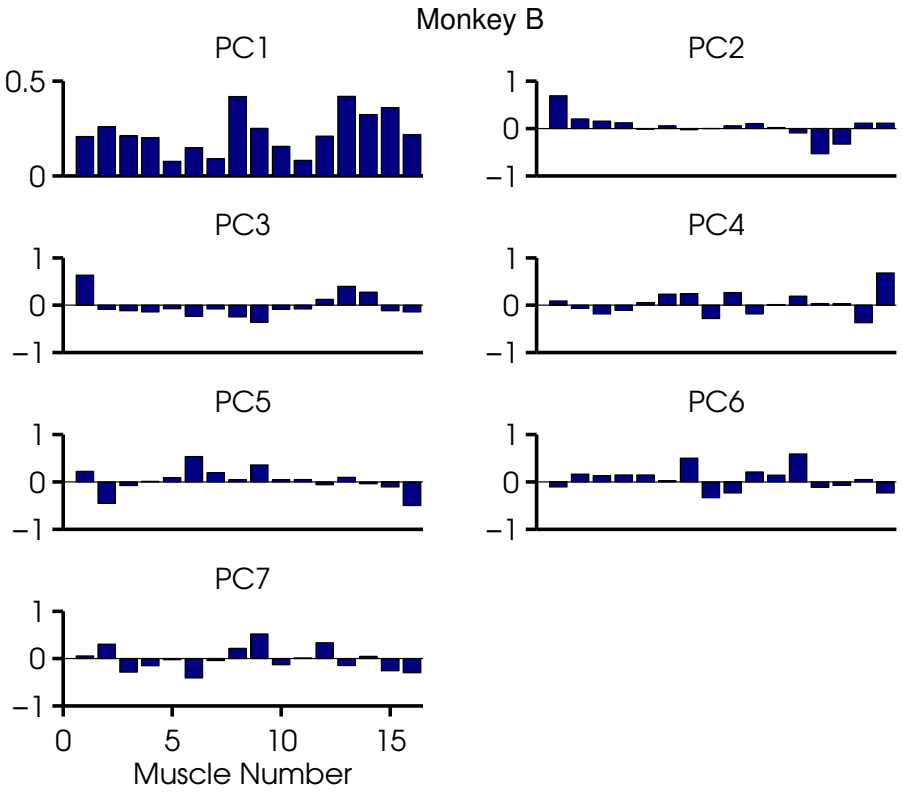

Figure 3.29: The first 7 PC coefficients (the eigenvectors of the covariance matrix) from one of the cross-validation runs, where attitudes were classified using mean EMG. Results for other cross-validation runs were similar (not shown).

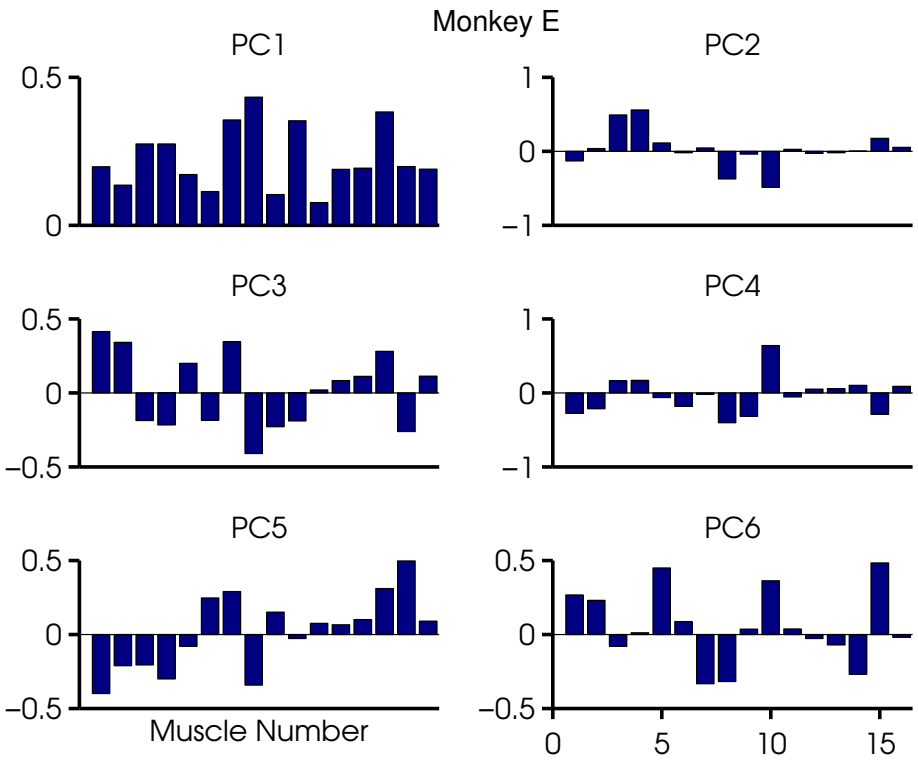

Figure 3.30: The first 6 PC coefficients (the eigenvectors of the covariance matrix) from one of the cross-validation runs, where attitudes were classified using mean EMG. Results for other cross-validation runs were similar (not shown).

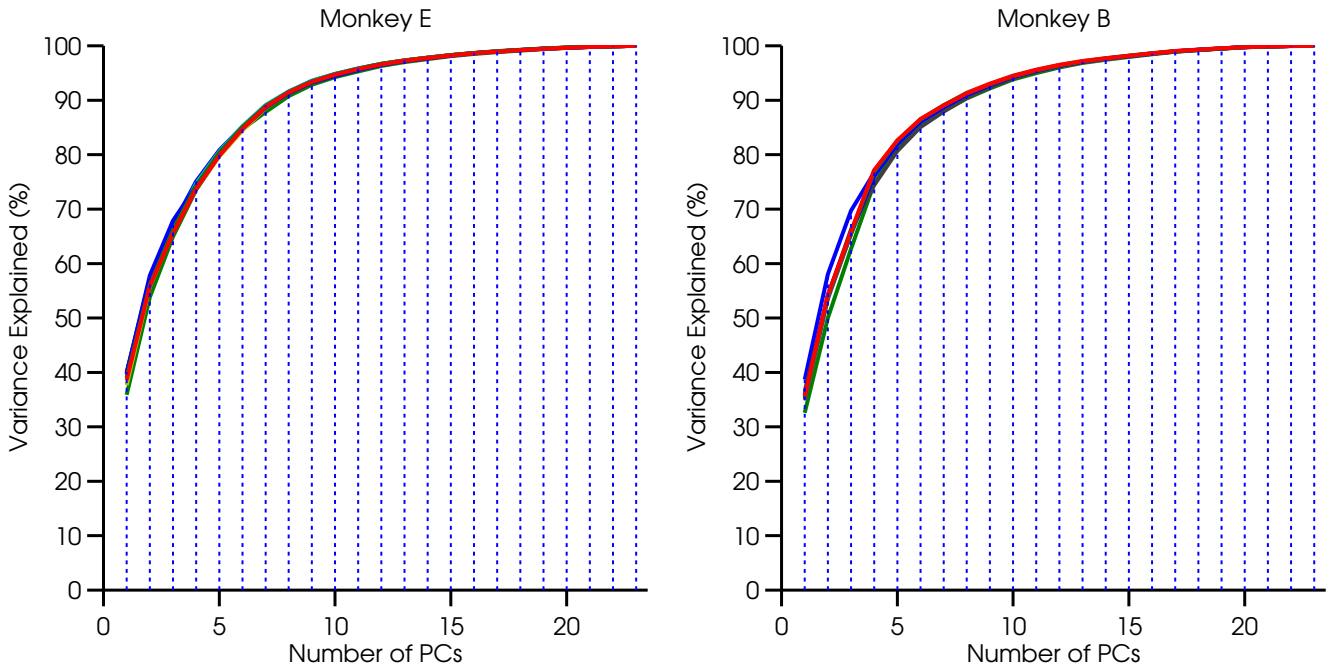

Figure 3.31: Superimposed curves specifying the amount of explained variance as a function of number of PCs, computed from 10 cross-validation Σ matrices, where attitudes were classified using mean JA. The results are almost identical across all matrices. For both monkeys, 8 PCs were required to account for 90% of the variance.

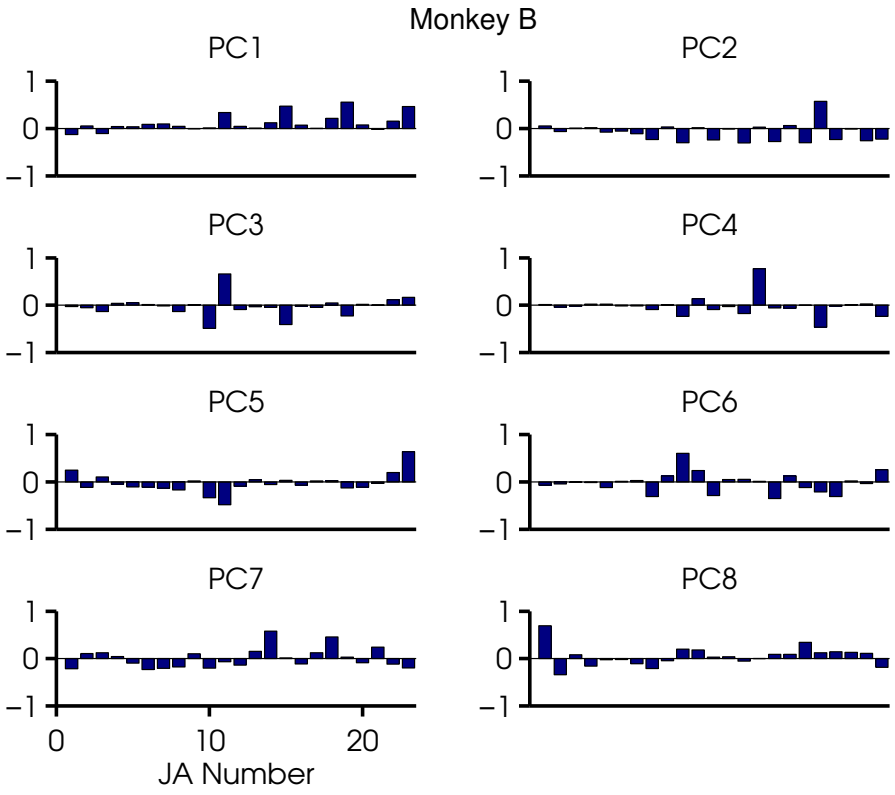

Figure 3.32: The first 8 PC coefficients (the eigenvectors of the covariance matrix) from one of the cross-validation runs, where attitudes were classified using mean JA. Results for other cross-validation runs were similar.

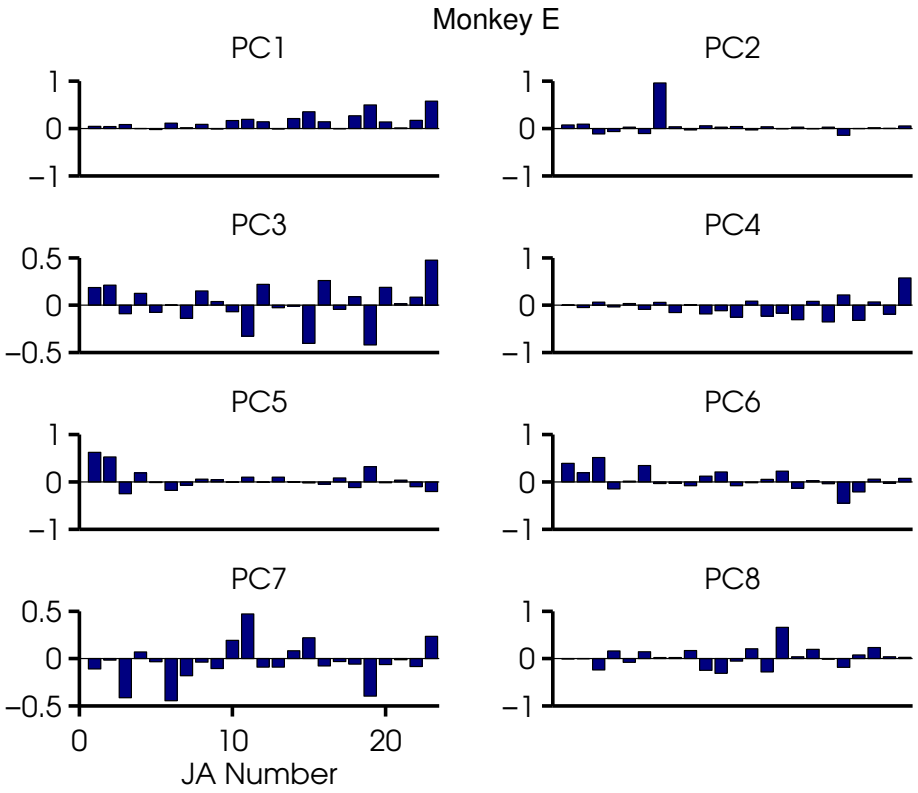

Figure 3.33: The first 8 PC coefficients (the eigenvectors of the covariance matrix) from one of the cross-validation runs, where attitudes were classified using mean JA. Results for other cross-validation runs were similar.

3.2.3 CLASSIFICATION OF OBJECTS

When examining reconstructions of the monkey's arm and hand movements using the marker data, it is easy to guess the object the monkey was reaching to, based solely on the hand shape. One would expect the LDA classifier to exhibit better classification rates then those in Table 8. We repeated the analysis once more, but this time classified objects, instead of attitudes, using the JA features. Table 9 shows the object classification mean error rates. As expected, the classification error rate for objects was much lower than for attitudes. For monkey E, objects were classified with 99% accuracy, when using either all available samples to compute the JA features, or when including samples from the preshape epoch (*Reach End* to *Grasp Start*). An example confusion matrix for object classification (monkey E) is shown in Figure 3.34. Classification accuracy was 97%, for monkey B, using samples from the preshape epoch.

Table 9: **Object classification mean error rates**: features contained mean JAs of samples which occurred between the specified task events. The mean error rates were calculated from the results of 10-fold cross-validation.

			Monkey B	**Monkey E**
	Start Event	**End Event**	**Error Mean±SD (%)**	**Error Mean±SD (%)**
1	N/A	N/A	12.00 ± 5.20	0.82 ± 1.43
2	Reach Start	Reach End	11.76 ± 3.44	3.75 ± 3.11
3	Reach Start	Max Speed	17.03 ± 3.74	11.57 ± 3.73
4	Max Speed	Reach End	7.39 ± 1.98	5.60 ± 2.55
5	Max Speed	Grasp Start	3.11 ± 3.25	0.62 ± 1.00
6	Reach End	Grasp Start	4.64 ± 3.54	0.20 ± 0.65
7	Reach End	Grasp End	3.88 ± 3.45	1.43 ± 2.56

Examining the PCs computed from the LDA covariance matrix, only 5 PCs were required to account for 90% of the variance, compared to 8 PCs when classifying attitudes (Figure 3.35). Finger JAs received high coefficients, but surprisingly so did the wrist JAs for some PCs (Figure

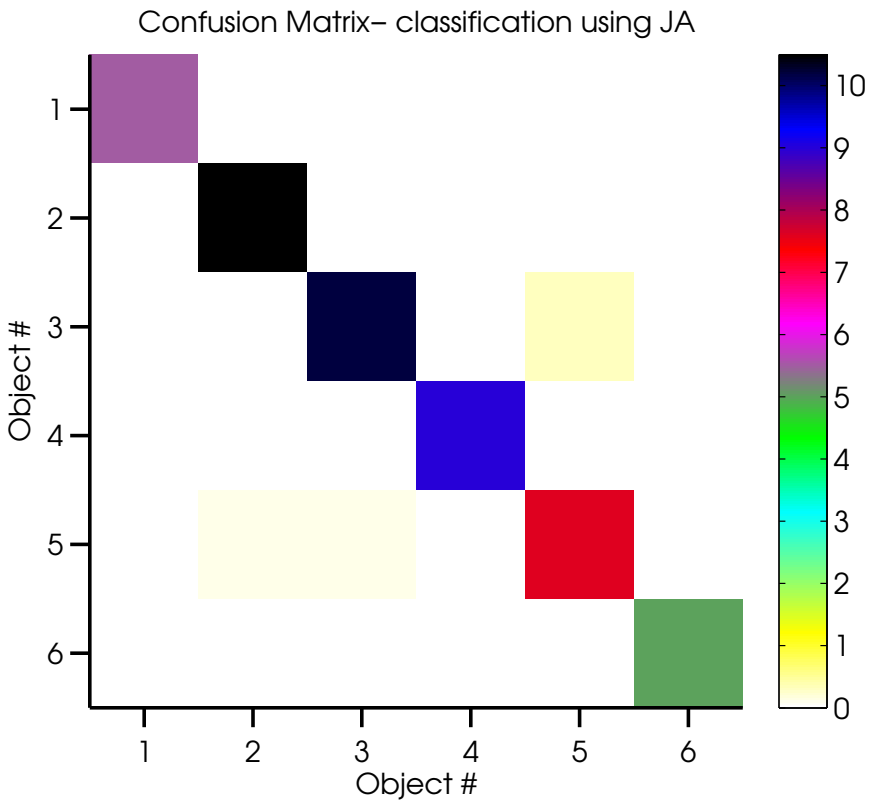

Figure 3.34: **Monkey E**: Average confusion matrix for classifying objects using JA features, defined as the mean JA from the beginning of MoveA epoch to the end of the static grasp epoch. The matrix was averaged from 10-fold cross-validation results. The mean classification error rate using 10-fold cross-validation was 1%.

3.36), indicating that some object specific wrist-finger correlation is present in the dataset. We explore that further in Section 3.3.

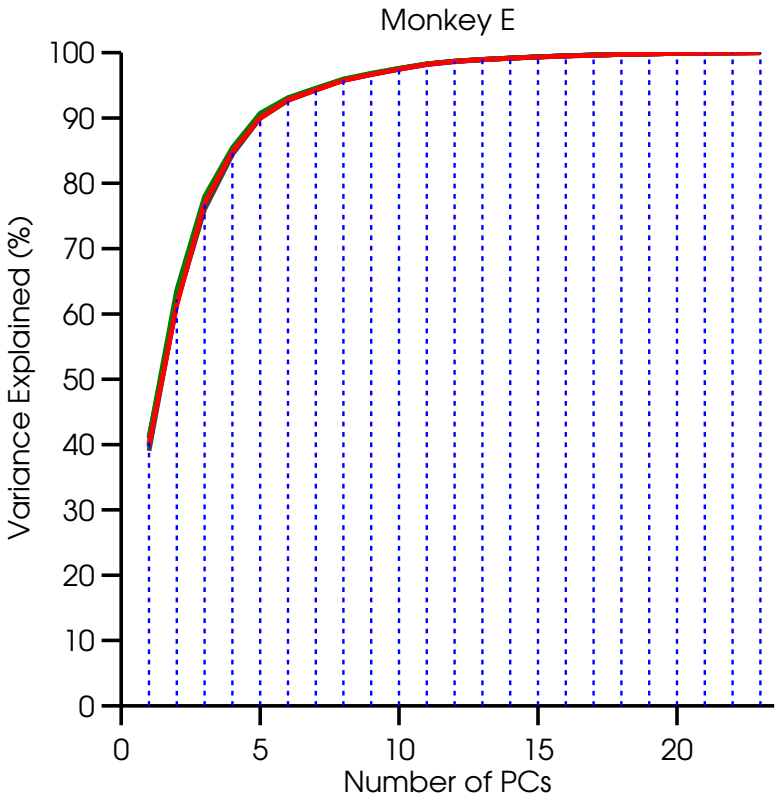

Figure 3.35: Superimposed curves specifying the amount of explained variance as a function of number of PCs, computed from 10 cross-validation Σ matrices, where objects were classified using mean JA. The results are almost identical across all matrices. For both monkeys, 5 PCs were required to account for 90% of the variance (monkey B not shown).

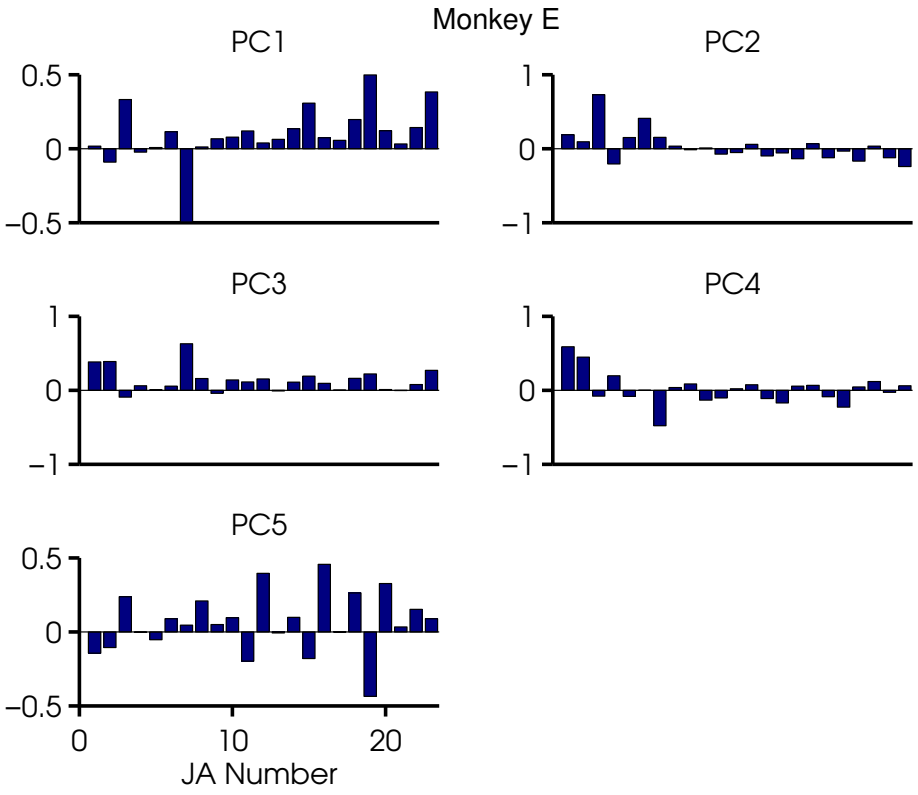

Figure 3.36: The first 5 PC coefficients (the eigenvectors of the covariance matrix) from one of the cross-validation runs, where objects were classified using mean JA. Results for other cross-validation runs were similar.

We expected the classification rate to improve when using EMG features to classify objects, so the analysis was repeated using EMG features (compare Table 7 to Table 8). Table 10 shows the results, and it is clear that is indeed the case: objects can be classified with 94% accuracy for monkey E, and with 88% accuracy for monkey B, when using all available samples. The best classification rates were obtained using data from the preshape/static-grasp epochs (monkey E); or all samples/preshape-epoch (monkey B). However, monkey E classification rates were two to four times better than monkey B. The difference probably results from the fact that monkey E showed more consistent hand shapes and EMG patterns than monkey B across specific epochs in repeat trials.

Table 10: **Object classification mean error rates**: features contained mean EMGs of samples which occurred between the specified task events. The mean error rates were calculated from the results of 10-fold cross-validation.

			Monkey B	**Monkey E**
	Start Event	**End Event**	**Error Mean±SD (%)**	**Error Mean±SD (%)**
1	N/A	N/A	12.17 ± 5.49	8.16 ± 4.41
2	Reach Start	Reach End	31.32 ± 6.31	20.61 ± 5.65
3	Reach Start	Max Speed	47.68 ± 5.14	33.27 ± 8.05
4	Max Speed	Reach End	31.64 ± 5.16	20.41 ± 4.08
5	Max Speed	Grasp Start	17.85 ± 5.87	14.29 ± 4.51
6	Reach End	Grasp Start	21.19 ± 6.05	19.39 ± 4.33
7	Reach End	Grasp End	15.41 ± 3.23	5.51 ± 1.68
8	Grasp Start	Grasp End	21.19 ± 4.52	6.12 ± 4.19

Figure 3.37 shows that 4 PCs are required to account for 90% of the variance, compared to 6 PCs when classifying attitudes using EMG. Figure 3.38 includes the first 4 PC coefficients. All muscles, including arm and wrist muscles have high coefficient values in one of the PCs, suggesting that similar to JAs, some object-specific arm-wrist-finger muscle correlation is present in the dataset as well.

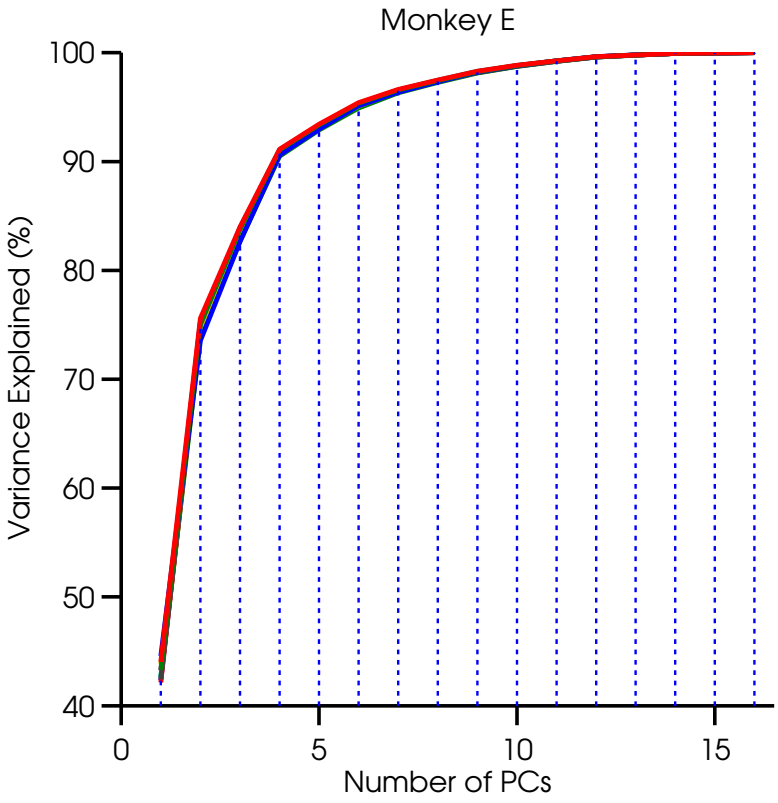

Figure 3.37: Superimposed curves specifying the amount of explained variance as a function of number of PCs, computed from 10 cross-validation Σ matrices, where objects were classified using mean EMG. The results are almost identical across all matrices. For both monkeys, 4 PCs were required to account for 90% of the variance (monkey B not shown).

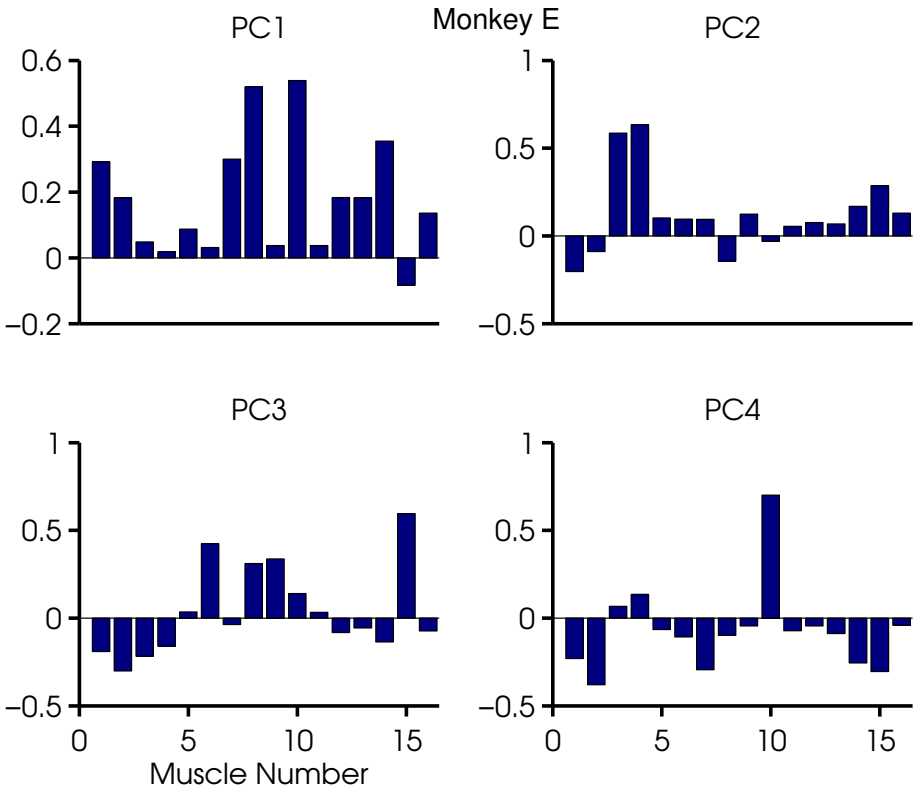

Figure 3.38: The first 4 PC coefficients (the eigenvectors of the covariance matrix) from one of the cross-validation runs, where objects were classified using mean EMG. Results for other cross-validation runs were similar.

3.2.4 CLASSIFICATION OF TARGETS

When an object was grasped at different targets, the hand shape was always similar, due to the constraint imposed by the force sensors location on each object. However, similar targets for different objects, for example the flexion target for the small handle and the small rectangle, did not necessarily require the same wrist orientation. We should therefore not expect the JAs or the EMGs to be good predictors of the target. We verified this was indeed the case, by classifying targets using either JA or EMG features. Targets with the same anatomical orientation were considered to be the same target across the different objects. Tables 11 and 12 show that indeed, classification rates for targets were around chance level.

Table 11: **Target classification mean error rates**: features contained mean JAs of samples which occurred between the specified task events. The mean error rates were calculated from the results of 10-fold cross-validation.

			Monkey B	**Monkey E**
	Start Event	**End Event**	**Error Mean±SD** (%)	**Error Mean±SD** (%)
1	N/A	N/A	58.52 ± 4.22	42.49 ± 7.15
2	Reach Start	Reach End	61.10 ± 3.59	46.46 ± 7.23
3	Reach Start	Max Speed	65.50 ± 6.17	66.00 ± 6.63
4	Max Speed	Reach End	54.28 ± 6.09	43.89 ± 5.53
5	Max Speed	Grasp Start	43.29 ± 3.48	41.33 ± 7.59
6	Reach End	Grasp Start	40.96 ± 4.38	34.80 ± 7.15
7	Reach End	Grasp End	40.54 ± 7.06	33.11 ± 6.75

Table 12: **Target classification mean error rates**: features contained mean EMGs of samples which occurred between the specified task events. The mean error rates were calculated from the results of 10-fold cross-validation.

			Monkey B	**Monkey E**
	Start Event	**End Event**	**Error Mean±SD (%)**	**Error Mean±SD (%)**
1	N/A	N/A	51.82 ± 6.72	46.53 ± 8.15
2	Reach Start	Reach End	65.82 ± 4.76	51.43 ± 7.25
3	Reach Start	Max Speed	74.33 ± 4.65	64.08 ± 8.45
4	Max Speed	Reach End	68.84 ± 6.00	50.00 ± 6.33
5	Max Speed	Grasp Start	56.34 ± 5.31	44.49 ± 9.94
6	Reach End	Grasp Start	59.88 ± 5.13	52.86 ± 5.65
7	Reach End	Grasp End	58.44 ± 7.21	49.39 ± 8.43
8	Grasp Start	Grasp End	65.45 ± 9.14	48.37 ± 5.86

3.2.5 SUMMARY OF CLASSIFICATION RESULTS

We can conclude that attitude and object classification rates was similar across the two monkeys, with slightly better object classification rates for monkey E. When classifying either attitudes or objects from JA or EMG features, classification using JA features was always better than classification using EMG features. We found two potential explanations for this discrepancy. First, JAs change much more slowly throughout trials compared to EMGs, so that the EMG has more variance. Therefore, using the mean as a feature provides a better description of the JAs than the EMGs. Second, different muscle activation patterns can lead to similar joint movements. The task required consistent hand shapes but not consistent EMG patterns. EMGs were therefore more variable across repeat trials, compared to JAs.

3.3 SELECTIVITY OF EMG AND JA

In Section 3.2, we used classification of attitudes and objects to show that EMG was more variable than JAs across repeat trials. The features we used consisted of one mean value per trial for every EMG or JA. Here, we extend that analysis to study the tuning of EMG and JA to different attitudes, objects and targets across trial epochs.

We divided each trial into 5 epochs, occurring *between* the following events: *Trial Start*, *Reach Start*, *Max Speed*, *Reach End*, *Grasp Start*, *Grasp End*. As in Section 3.2, *Reach Start* was the time the hand speed reached $(5\% \times MaxSpeed)$ before the maximal speed, *Reach End* was the time the hand speed reached $(5\% \times MaxSpeed)$ after the maximal speed, *Grasp Start* was the time the monkey started pressing the object, *Grasp End* was *HoldB* milliseconds after *Grasp Start* (this value was determined from the recorded real-time value for HoldB for every trial). Figure 3.39 shows a typical example of the temporal relationship of these events. The figure contain plots of the hand end-point velocity and speed. The events are marked by filled circles on the different traces. For some attitudes, the Reach End event occurred simultaneously with the Grasp Start event, and this task epoch was not used.

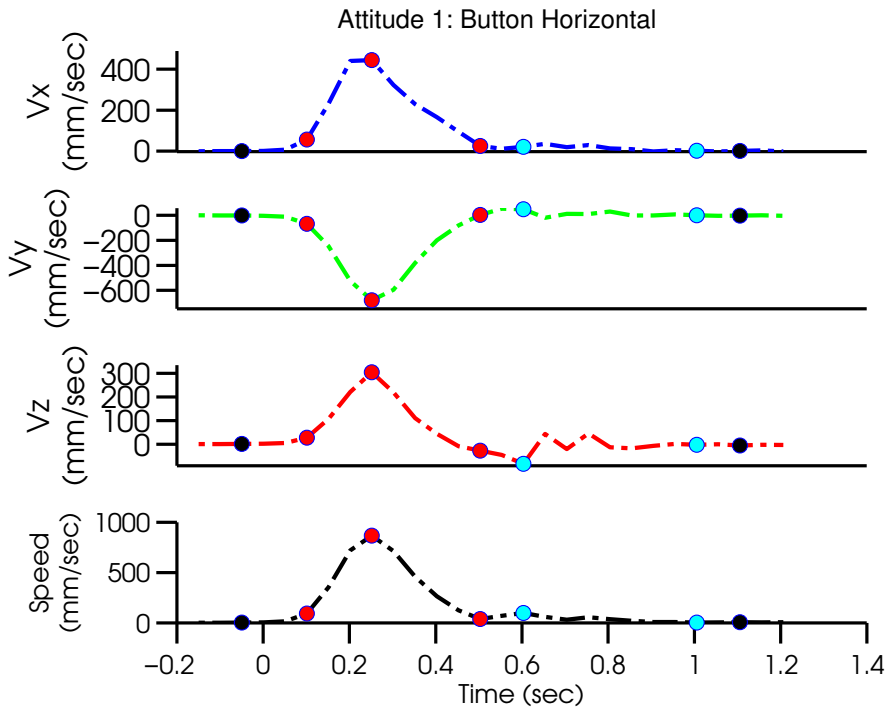

Figure 3.39: Hand end point velocity and speed for one trial. Time zero indicates the beginning of the trial. Monkey E reached to the button in the horizontal target. Trial events are marked by filled circles: black for the Trial Start/End, red for the Reach Start/MaxSpeed/End events, and blue for the Grasp Start/End.

3.3.1 EMG TUNING TO OBJECTS

We first investigated how EMG activation levels changed between task epochs for different objects. Figure 3.40 shows mean EMG activation levels for arm muscles, computed across all trials where the monkey reached to grasp each object, regardless of the target. Every curve includes 5 data points, corresponding to 5 task epochs (see Figure 3.40 caption for details). All muscles show almost identical activity levels during the first 2 epochs, corresponding to the first part of the reach (until the hand reaches maximal speed), across all objects, thus suggesting there was no object specific difference in arm muscle activity in the first part of the reach.

The triceps, brachioradialis and pronator-teres showed similar activity levels during the deceleration phase of the reach (past maximal speed). However, deltoid, biceps and pectorialis, had selective activity during the deceleration phase of the reach . Most muscles showed object-differentiated activity levels for the preshape and static grasp task epochs. Two conclusions can be drawn: first, not only did the monkeys use object-specific hand shapes, they also used object-specific arm postures. Table 11 supports this conclusion, since we see that JAs were not a good predictor of targets. If the monkeys used object-specific hand postures, the elbow and shoulder JAs should have been similar across objects. Unfortunately, we did not record those JAs, due to the limited number of cameras available for tracking, and the narrow workspace of each camera. The second conclusion we can draw is that arm muscles activity was object-specific activity during the static-grasp epoch.

Two interesting atypical examples can be seen in the activity of the arm muscles when monkey E reached to grasp the bar and button objects. Only monkey E was presented with the bar object, a rectangular bar, fitted with force sensors only on one face. The bar was presented at two targets: one requiring the monkey to push the bar downward with the hand pronated, and the other requiring the monkey to push the bar upward with the hand supinated. As a result, we see that the biceps, triceps and brachioradialis, showed relatively higher activity levels for this object (Figure 3.40**B**). A higher activity level was observed for both targets, with the supination target the highest of the two (see Figure. 3.43**B**). This is expected, as these muscles are used to either supinate the hand or support the arm when the hand is supinated. A second interesting example is seen in the activity of pronator-teres for monkey E (Figure 3.40**B**). This muscle was highly active when monkey E reached to push the button (a "null" grasp object). The button was presented at the edge of the monkey E's workspace, forcing the monkey to fully extend its arm. Monkey B did not show high pronator-teres activity levels for the button object. This difference may have been due to monkey E's shorter arm length. While monkey B was able to reach the button without fully extending the arm, monkey E had to extend fully its arm to exert enough force to push the button.

Figure 3.41 shows how wrist muscles were tuned for different objects. Similarly to the arm muscles, wrist muscles also show similar activity during the first 2 epochs, in line with the observation that during the acceleration phase of the reach, the monkeys tended to extend both their wrist and fingers (Figures 3.14, 3.12,3.15,3.13). Monkey B (Figure 3.41**A**) shows both higher activity levels and more variability in the wrist muscles during the 3*rd* epoch (the deceleration phase of the

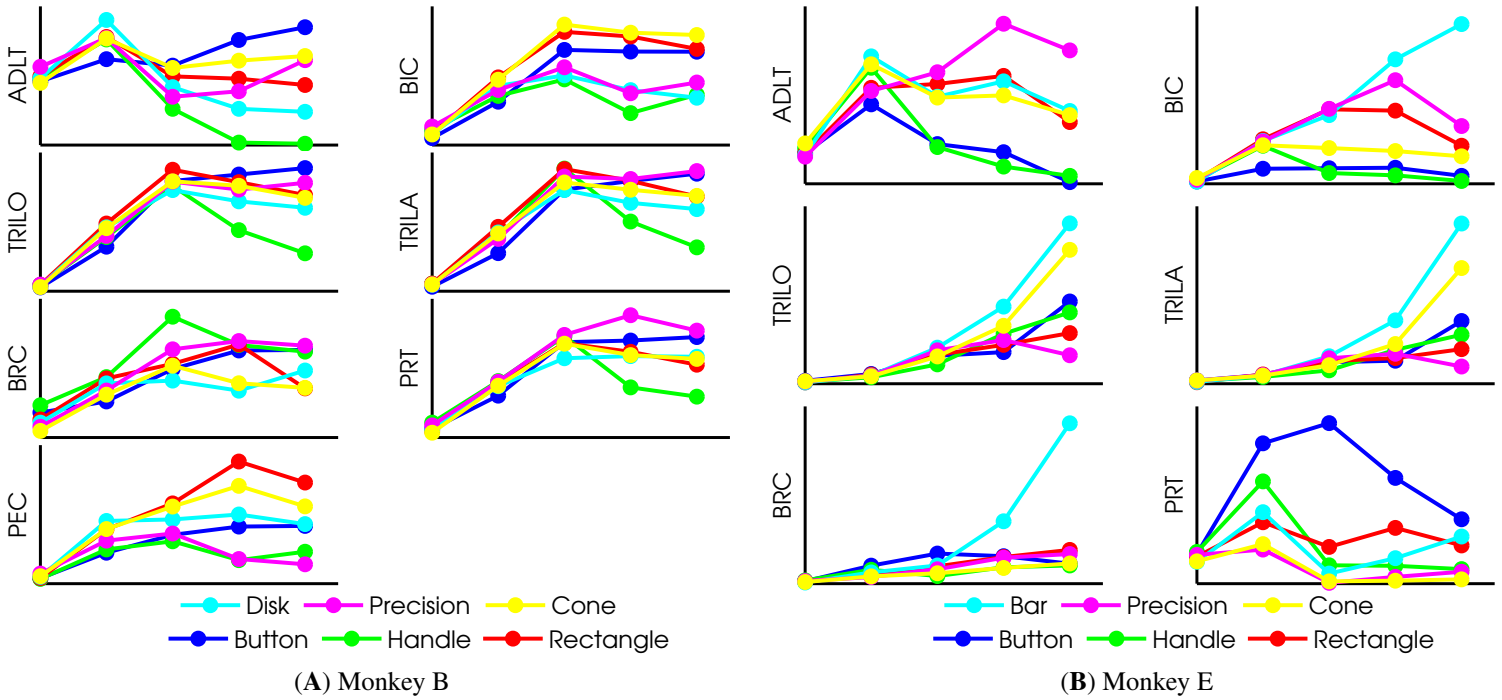

Figure 3.40: **Arm muscles tuning to objects:** Mean EMG levels during 5 task epochs (X-axis). Means were computed across all trials where the monkey reached to grasp a certain object, regardless of the target. Objects are the same for both monkeys, except for the disk and bar. Panels were scaled vertically to fit the axis, hence values are not comparable *across* panels. The 5 task epochs shown are: (1) *Trial Start* to *Reach Start*, (2) *Reach Start* to *Max Speed*, (3) *Max Speed* to *Reach End*, (4) *Reach End* to *Grasp Start*, (5) *Grasp Start* to *Grasp End*.

reach), compared to the static grasp epoch, for all muscles but extensor carpi radialis (ECR). This suggests that the wrist was oriented during the deceleration phase of the reach, but after that, the wrist muscles were not used to stabilize the hand. ECR showed object-specific activity during the static grasp phase, suggesting that monkey B maintained an extended and abducted wrist orientation in an object-specific manner. Monkey B activated the wrist flexors more (FCU, FCR) for the handle object compared to the other objects, to slightly pull the handle and press the force sensors more efficiently. Monkey E (Figure 3.41**B**) showed object specific activation of all wrist muscles, due to its shorted arm, when pressing the button object. This monkey tended to extend the wrist,

place its middle finger on the button force sensor, and flex the wrist to press the button. This can be seen by the increased activity of ECU, FCU and FCR. Figure 3.41 also supports the conclusion that the monkeys used object-specific arm-wrist-hand postures.

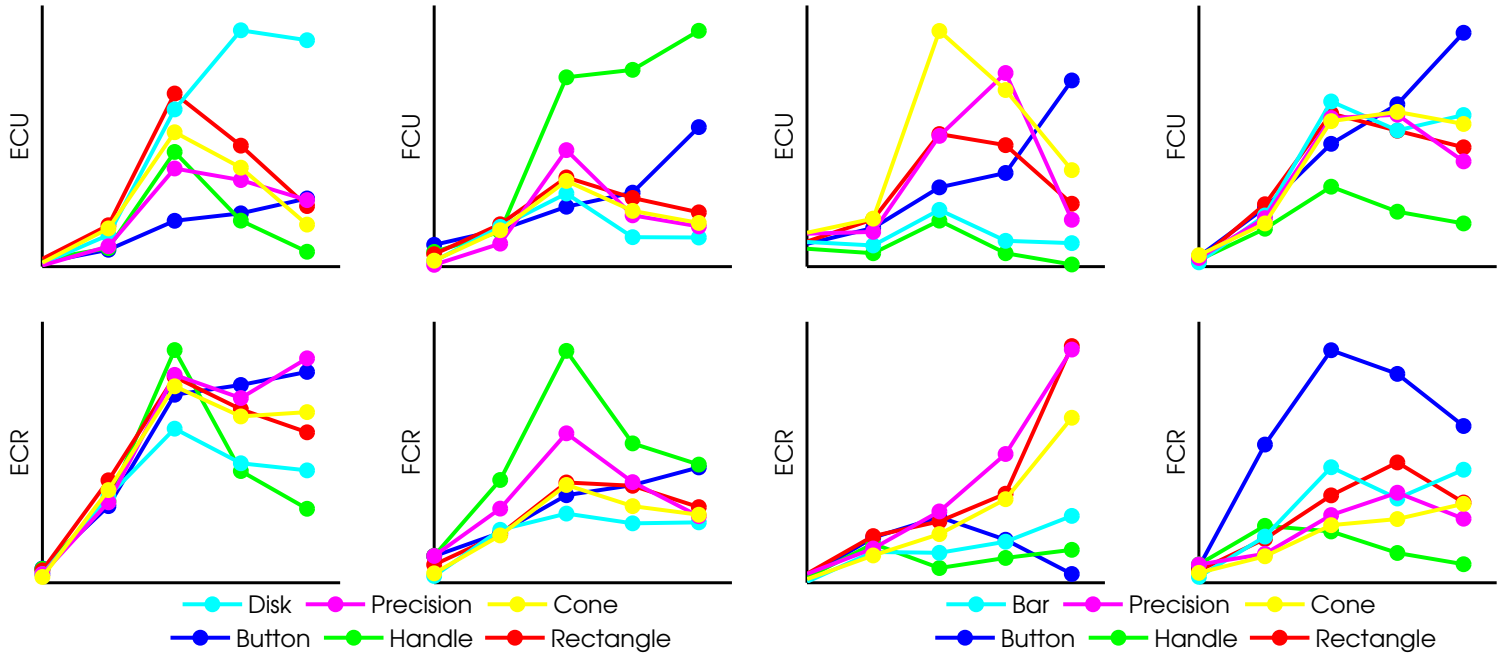

(**A**) Monkey B (**B**) Monkey E

Figure 3.41: **Wrist muscles tuning to objects:** Mean EMG levels during 5 task epochs (X-axis). Means were computed across all trials where the monkey reached to grasp a certain object, regardless of the target. Objects are the same for both monkeys, except for the disk and bar. Panels were scaled vertically to fit the axis, hence values are not comparable *across* panels. The 5 task epochs shown are: (1) *Trial Start* to *Reach Start*, (2) *Reach Start* to *Max Speed*, (3) *Max Speed* to *Reach End*, (4) *Reach End* to *Grasp Start*, (5) *Grasp Start* to *Grasp End*.

Figure 3.42 shows finger muscles EMG object tuning. As expected, EMG levels are object-specific for both monkeys from the 3*rd* epoch onwards, suggesting that object-specific hand shaping starts in the deceleration phase of the reach and is maintained through the static grasp.

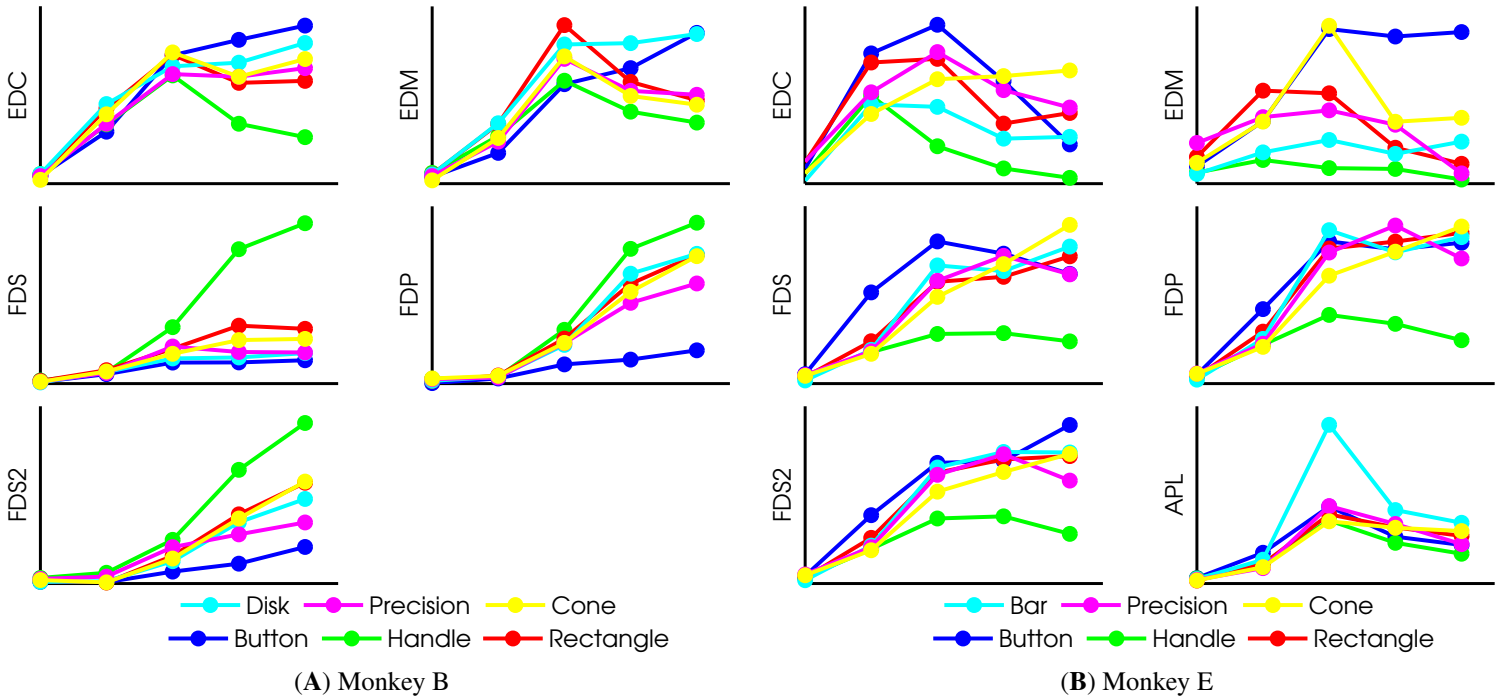

(**A**) Monkey B

(**B**) Monkey E

Figure 3.42: **Finger muscles tuning to objects:** Mean EMG levels during 5 task epochs (X-axis). Means were computed across all trials where the monkey reached to grasp a certain object, regardless of the target. Objects are the same for both monkeys, except for the disk and bar. Panels were scaled vertically to fit the axis, hence values are not comparable *across* panels. The 5 task epochs shown are: (1) *Trial Start* to *Reach Start*, (2) *Reach Start* to *Max Speed*, (3) *Max Speed* to *Reach End*, (4) *Reach End* to *Grasp Start*, (5) *Grasp Start* to *Grasp End*.

3.3.2 EMG TUNING TO TARGETS

Targets varied slightly across the different objects due to different object sizes and the different orientations required to comfortably grasp each object. Thus, different amounts of wrist flexion were required to grasp different objects at their flexion targets. However, variability within targets was smaller than variability across targets. For example, flexion targets generally required more flexion than extension targets.

Figure 3.43 shows mean EMG activation levels for the arm muscles, computed across all trials where the monkey reached to grasp objects at a certain target, regardless of the object. Every curve includes 5 data points, corresponding to 5 task epochs (see Figure 3.43 caption for details). While monkey B shows almost identical EMG activation levels for all targets across all task epochs, monkey E shows target-specific activity for most arm muscles. The difference might, again, be due to the difference in arm lengths between both monkeys: monkey E had to orient its arm differently for different targets, to efficiently grasp the objects; whereas monkey B kept its arm in a rather similar configuration across targets, except for slight differences at the shoulder (note the slight variability in ADLT and PEC in Figure 3.43**A**). For example, monkey E activated its triceps more for the flexion targets, probably because the elbow was more extended for these targets. As seen in Figure 3.40**B**, biceps and brachioradialis show higher activation levels for the supination target, which was unique to the bar object.

Figure 3.44 shows wrist muscles activation levels for the different targets. As expected, wrist muscles show target-specific activations, beginning at the deceleration phase of the reach. Monkey E shows clearer target-specific activations compared to monkey B. Generally, muscles show high activation levels for targets requiring movements in their anatomical pulling directions. For example, for monkey E, ECU is mostly active for the 45°-left target. A 45°-left movement of the hand corresponds to adduction of the wrist, which is one of the roles of ECU. For monkey B, ECU is active for the adduction target, which requires more extreme adduction compared to the 45°-left target.

Figure 3.45 shows mean finger muscle EMG levels for different targets. Not surprisingly, monkey B shows almost no target-specific activation for the finger muscles. Monkey E shows slight variability, mostly due to activity at the supination target, compared to the other targets. The supination target was unique in that it did not require flexion of fingers, although sometimes monkey E tended to flex its fingers around the bar to press the force sensors more efficiently. In addition, this target required activation of muscles when the ulna and radius were not crossed, so muscle lengths were different for this target compared to all other targets.

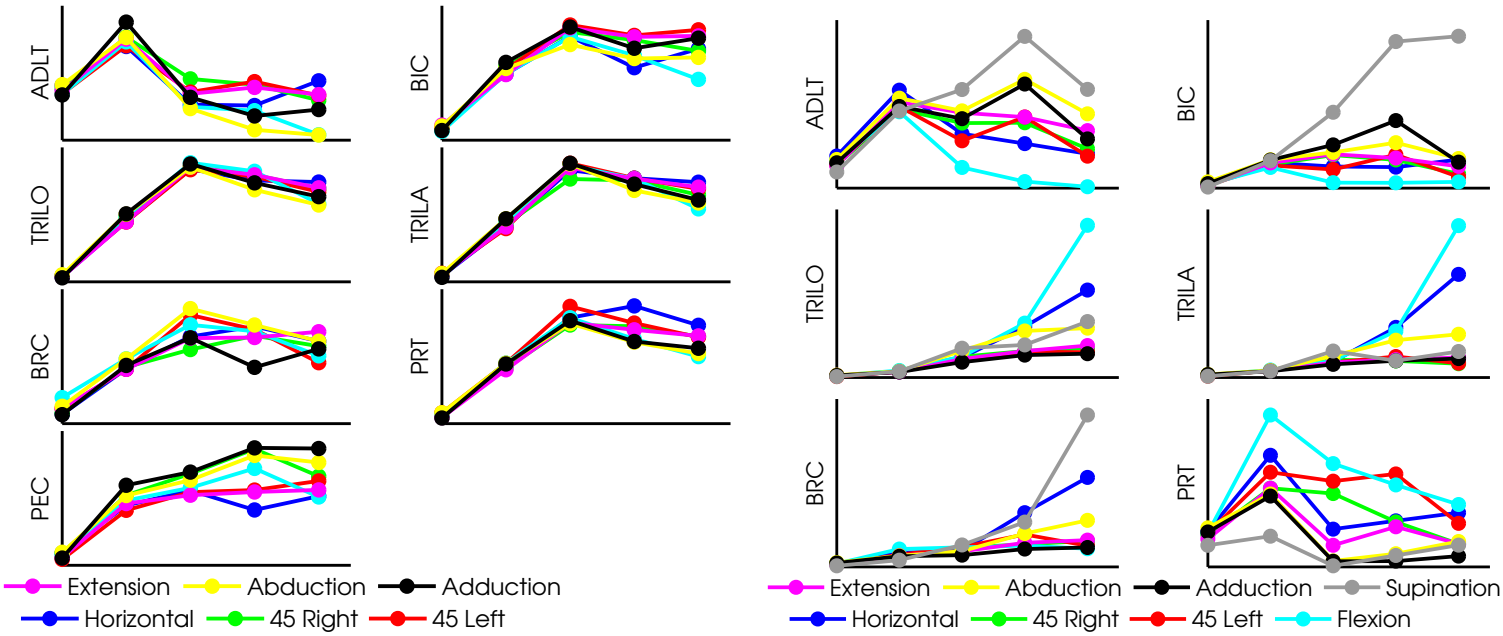

(**A**) Monkey B

(**B**) Monkey E

Figure 3.43: **Arm muscles tuning to targets:** Mean EMG levels during 5 task epochs (X-axis). Means were computed across all trials where the monkey reached to grasp a certain target, regardless of the object. Panels were scaled vertically to fit the axis, hence values are not comparable *across* panels. The 5 task epochs shown are: (1) *Trial Start* to *Reach Start*, (2) *Reach Start* to *Max Speed*, (3) *Max Speed* to *Reach End*, (4) *Reach End* to *Grasp Start*, (5) *Grasp Start* to *Grasp End*.

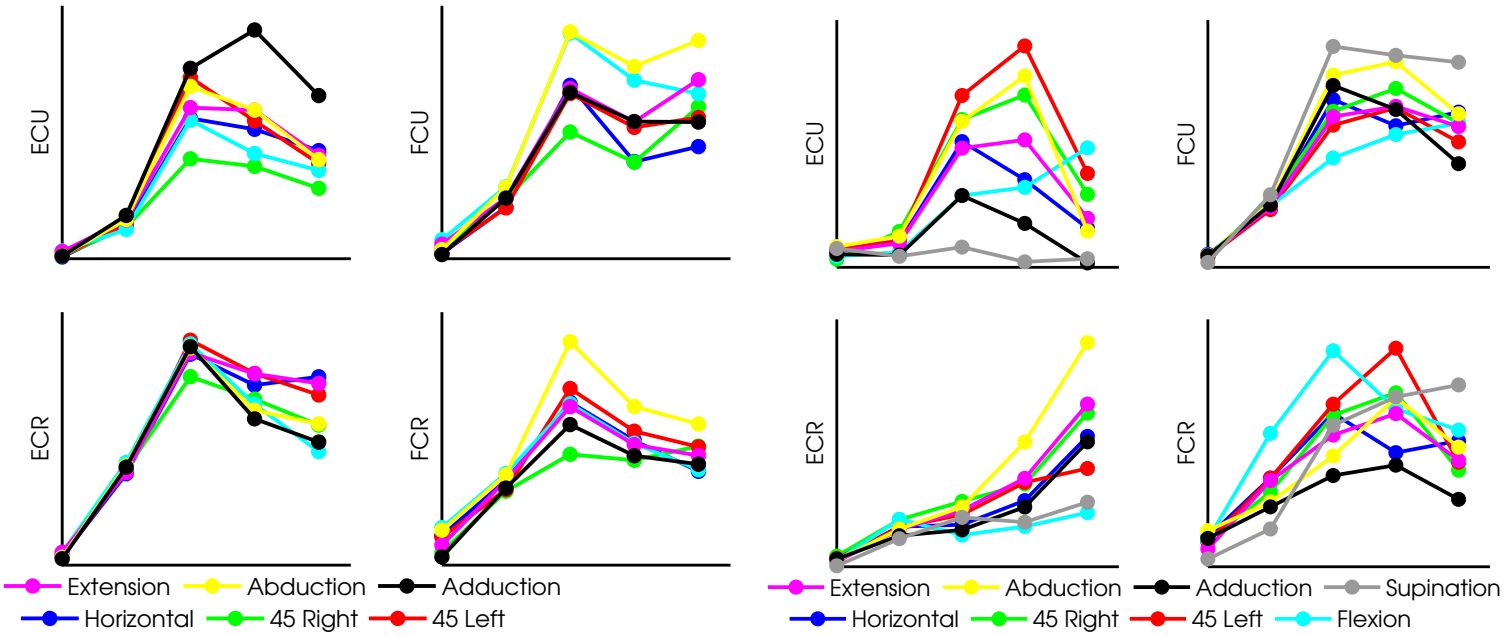

(**A**) Monkey B

(**B**) Monkey E

Figure 3.44: **Wrist muscles tuning to targets:** Mean EMG levels during 5 task epochs (X-axis). Means were computed across all trials where the monkey reached to grasp a certain target, regardless of the object. Panels were scaled vertically to fit the axis, hence values are not comparable *across* panels. The 5 task epochs shown are: (1) *Trial Start* to *Reach Start*, (2) *Reach Start* to *Max Speed*, (3) *Max Speed* to *Reach End*, (4) *Reach End* to *Grasp Start*, (5) *Grasp Start* to *Grasp End*.

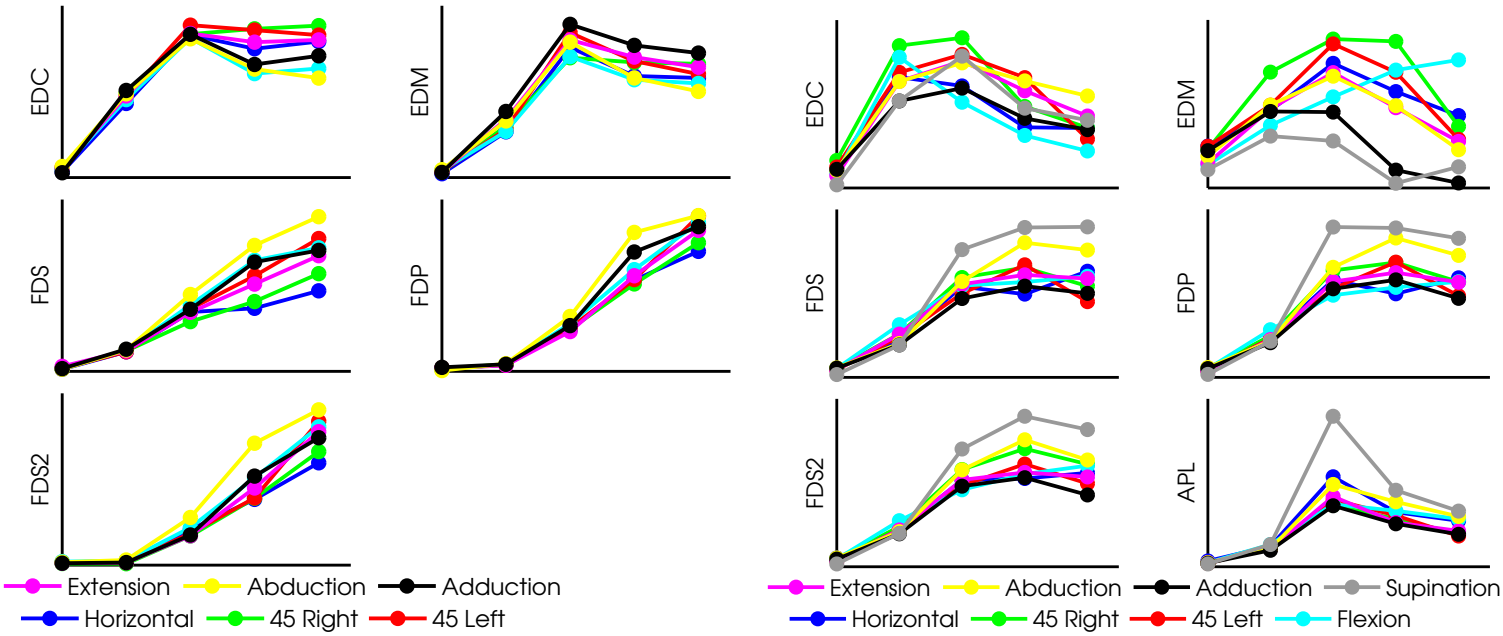

(**A**) Monkey B

(**B**) Monkey E

Figure 3.45: **Finger muscles tuning to targets:** Mean EMG levels during 5 task epochs (X-axis). Means were computed across all trials where the monkey reached to grasp a certain target, regardless of the object. Panels were scaled vertically to fit the axis, hence values are not comparable *across* panels. The 5 task epochs shown are: (1) *Trial Start* to *Reach Start*, (2) *Reach Start* to *Max Speed*, (3) *Max Speed* to *Reach End*, (4) *Reach End* to *Grasp Start*, (5) *Grasp Start* to *Grasp End*.

3.3.3 EMG TUNING TO ATTITUDES

Both monkeys showed object- and target-specific mean EMG activation levels for different muscle groups. To examine whether specificity for objects was stronger than specificity for targets, we plotted mean activation levels for every attitude, and colored the data curves according to objects or targets. In one plot, all attitudes where the monkey reached to grasp a certain object would have the same color, regardless of the target. On the other plot, all attitudes where the monkey reached to a certain target would have the same color, regardless of the object.

Figures 3.46, 3.47 and 3.48 show arm, wrist and finger muscles mean activation levels for all attitudes, for monkey E. The left panels color the attitudes by objects, the right panels by target. For all muscle groups, coloring by object produces color bands, whereas coloring by target produces a mix of colors. We concluded that muscle activation was more object specific, than target specific, for arm, wrist and finger muscles. Figures 3.49, 3.50 and 3.51 show similar figures for monkey B.

It is interesting to note that some attitudes caused high activation in specific muscles. For monkey E, the bar at the supination target corresponded to BIC, and BRC activation at both targets (Figure 3.46). PRT (Figure 3.46), ECU and FCR (Figure 3.47) were mostly active for the rectangle at the 45°-left target. For monkey B, ADLT was active for the button at the 45°-right target, and BRC (Figure 3.49) was active for the handle at the 45°-left target. Several factors could contribute to such specific activation. First, muscles have several compartments and the placement of the EMG electrode relative to the compartments determines which compartment's activation will be recorded as higher voltage levels. Second, it is possible that some attitudes required specific arm-wrist-hand configurations corresponding to muscle patterns.

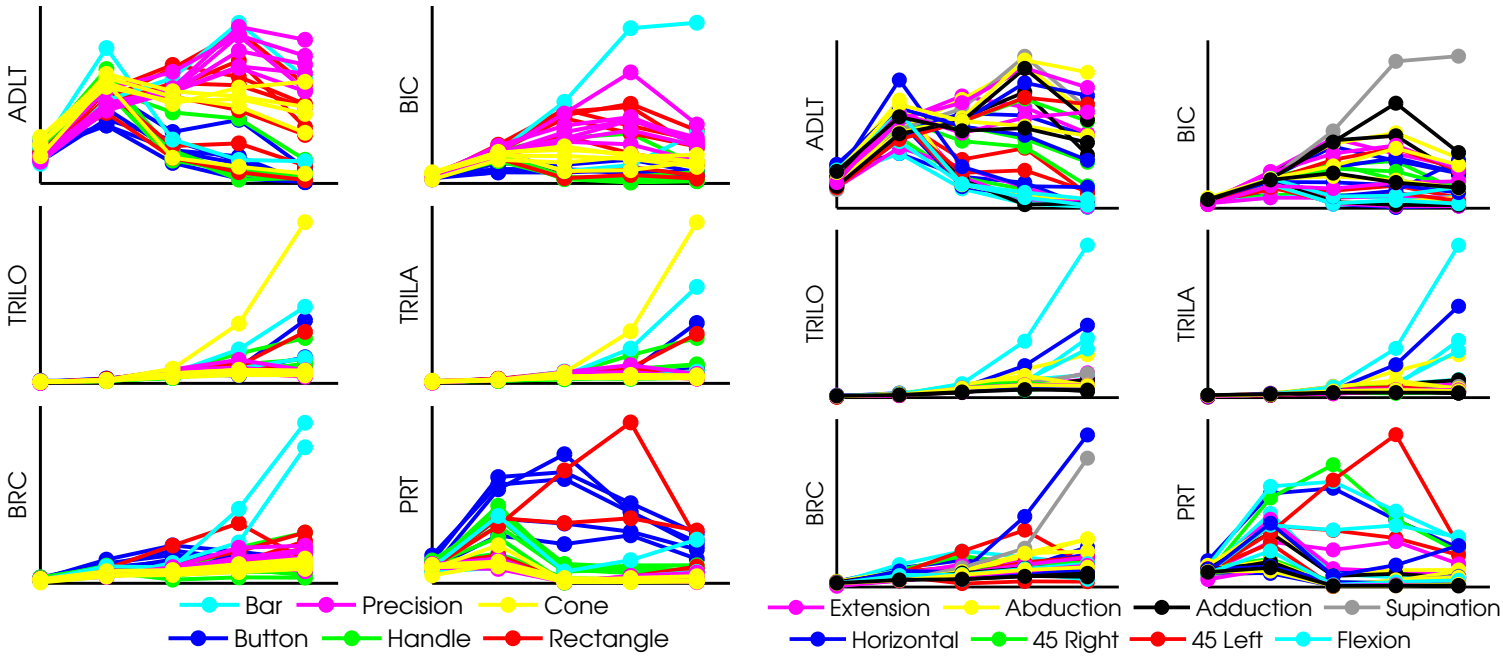

(**A**) Colored by object

(**B**) Colored by target

Figure 3.46: **Arm muscles tuning to attitudes: Monkey E:** Mean EMG levels during 5 task epochs (X-axis). Means were computed across all trials from a certain attitude. Attitudes are colored by objects **(A)** or targets **(B)**. Panels were scaled vertically to fit the axis, hence values are not comparable *across* panels. The 5 task epochs shown are: (1) *Trial Start* to *Reach Start*, (2) *Reach Start* to *Max Speed*, (3) *Max Speed* to *Reach End*, (4) *Reach End* to *Grasp Start*, (5) *Grasp Start* to *Grasp End*.

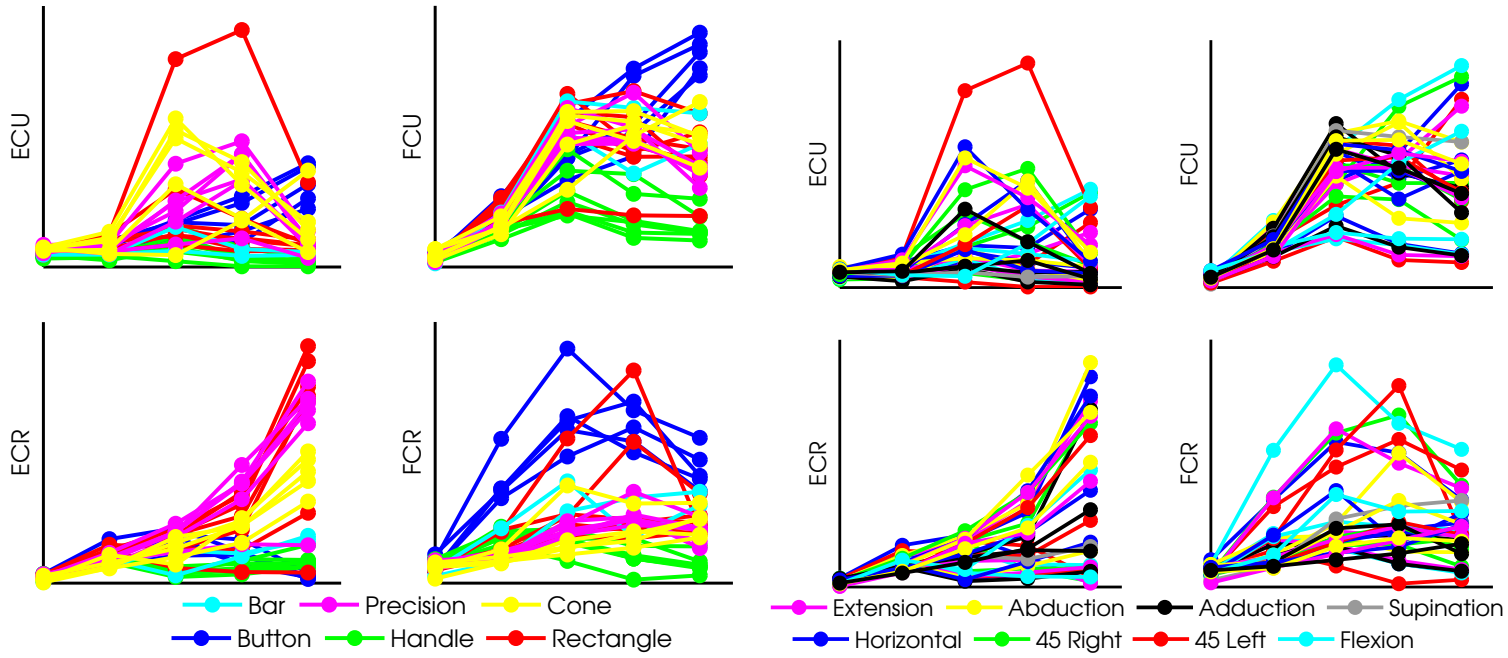

(**A**) Colored by object

(**B**) Colored by target

Figure 3.47: **Wrist muscles tuning to attitudes: Monkey E:** Mean EMG levels during 5 task epochs (X-axis). Means were computed across all trials from a certain attitude. Attitudes are colored by objects **(A)** or targets **(B)**. Panels were scaled vertically to fit the axis, hence values are not comparable *across* panels. The 5 task epochs shown are: (1) *Trial Start* to *Reach Start*, (2) *Reach Start* to *Max Speed*, (3) *Max Speed* to *Reach End*, (4) *Reach End* to *Grasp Start*, (5) *Grasp Start* to *Grasp End*.

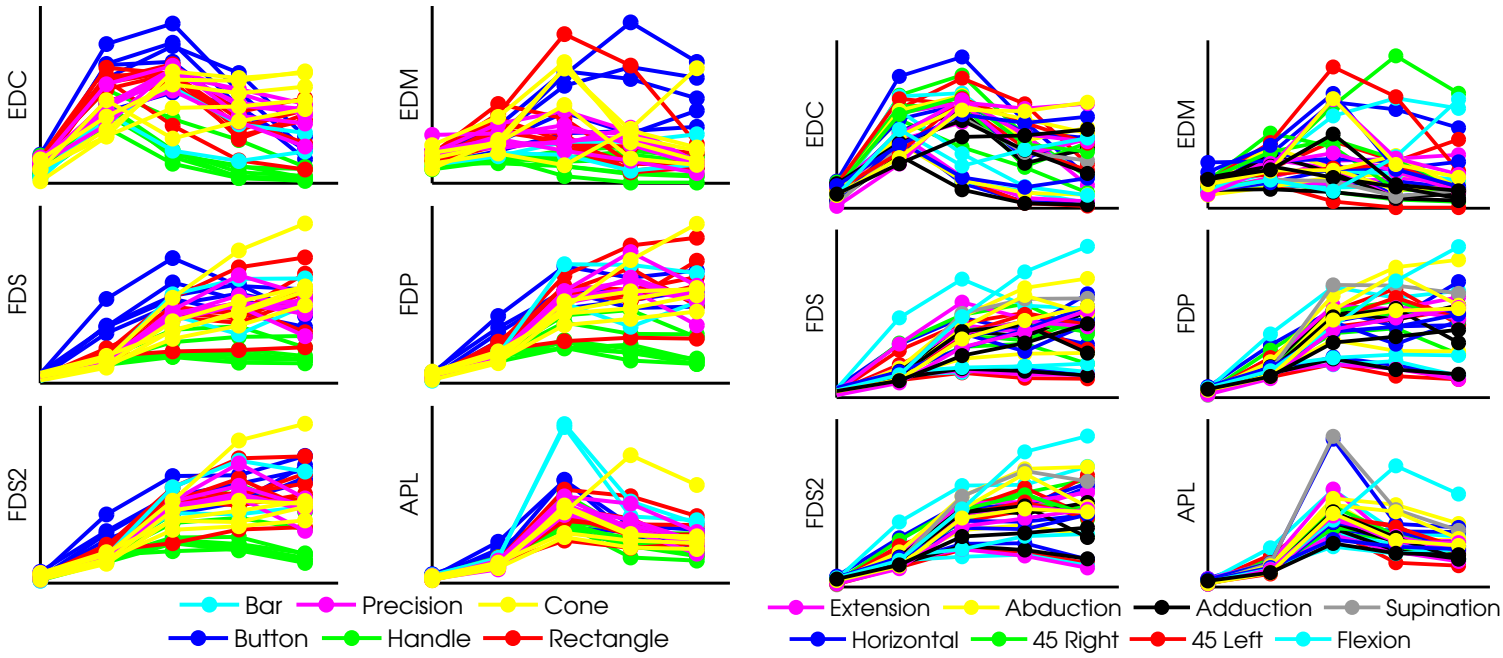

(**A**) Colored by object

(**B**) Colored by target

Figure 3.48: **Finger muscles tuning to attitudes: Monkey E:** Mean EMG levels during 5 task epochs (X-axis). Means were computed across all trials from a certain attitude. Attitudes are colored by objects **(A)** or targets **(B)**. Panels were scaled vertically to fit the axis, hence values are not comparable *across* panels. The 5 task epochs shown are: (1) *Trial Start* to *Reach Start*, (2) *Reach Start* to *Max Speed*, (3) *Max Speed* to *Reach End*, (4) *Reach End* to *Grasp Start*, (5) *Grasp Start* to *Grasp End*.

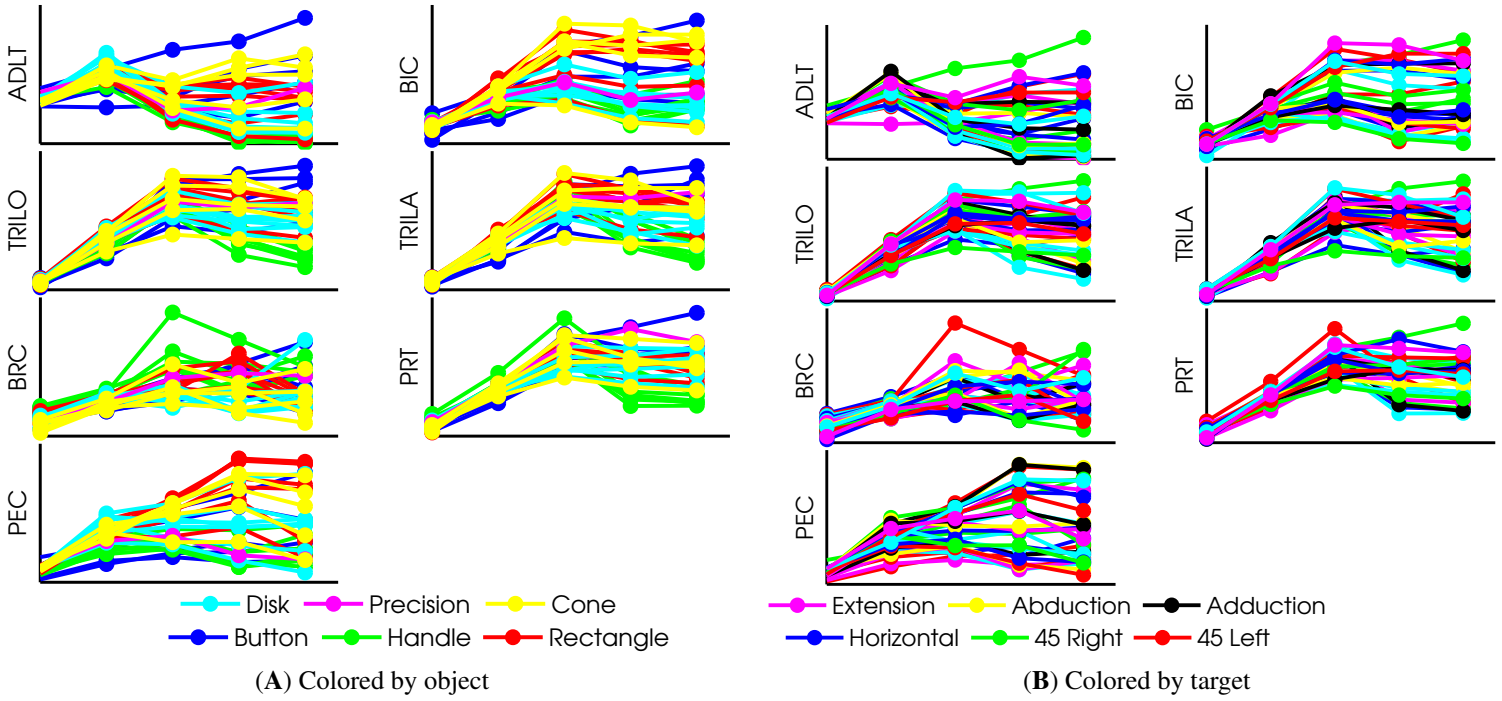

(**A**) Colored by object

(**B**) Colored by target

Figure 3.49: **Arm muscles tuning to attitudes: Monkey B:** Mean EMG levels during 5 task epochs (X-axis). Means were computed across all trials from a certain attitude. Attitudes are colored by objects **(A)** or targets **(B)**. Panels were scaled vertically to fit the axis, hence values are not comparable *across* panels. The 5 task epochs shown are: (1) *Trial Start* to *Reach Start*, (2) *Reach Start* to *Max Speed*, (3) *Max Speed* to *Reach End*, (4) *Reach End* to *Grasp Start*, (5) *Grasp Start* to *Grasp End*.

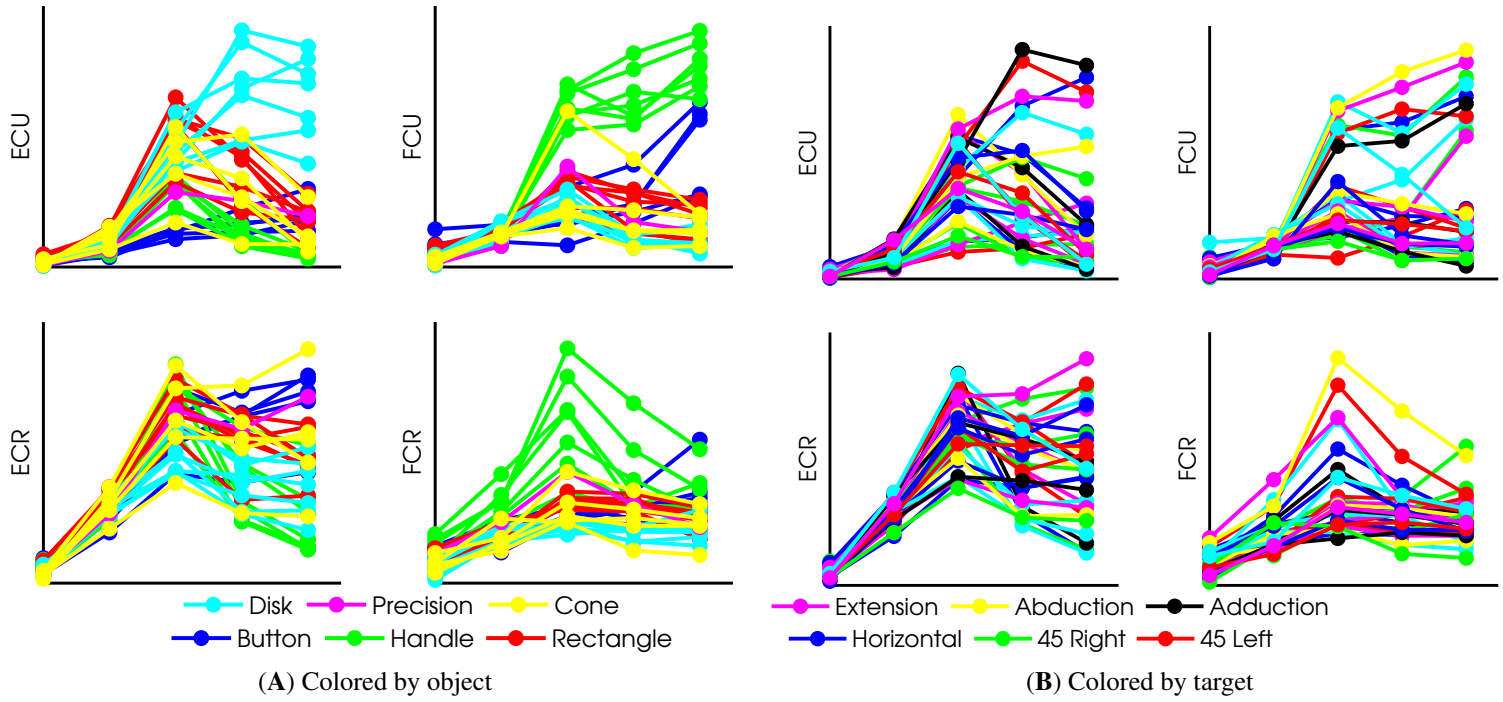

(**A**) Colored by object

(**B**) Colored by target

Figure 3.50: **Wrist muscles tuning to attitudes: Monkey B:** Mean EMG levels during 5 task epochs (X-axis). Means were computed across all trials from a certain attitude. Attitudes are colored by objects **(A)** or targets **(B)**. Panels were scaled vertically to fit the axis, hence values are not comparable *across* panels. The 5 task epochs shown are: (1) *Trial Start* to *Reach Start*, (2) *Reach Start* to *Max Speed*, (3) *Max Speed* to *Reach End*, (4) *Reach End* to *Grasp Start*, (5) *Grasp Start* to *Grasp End*.

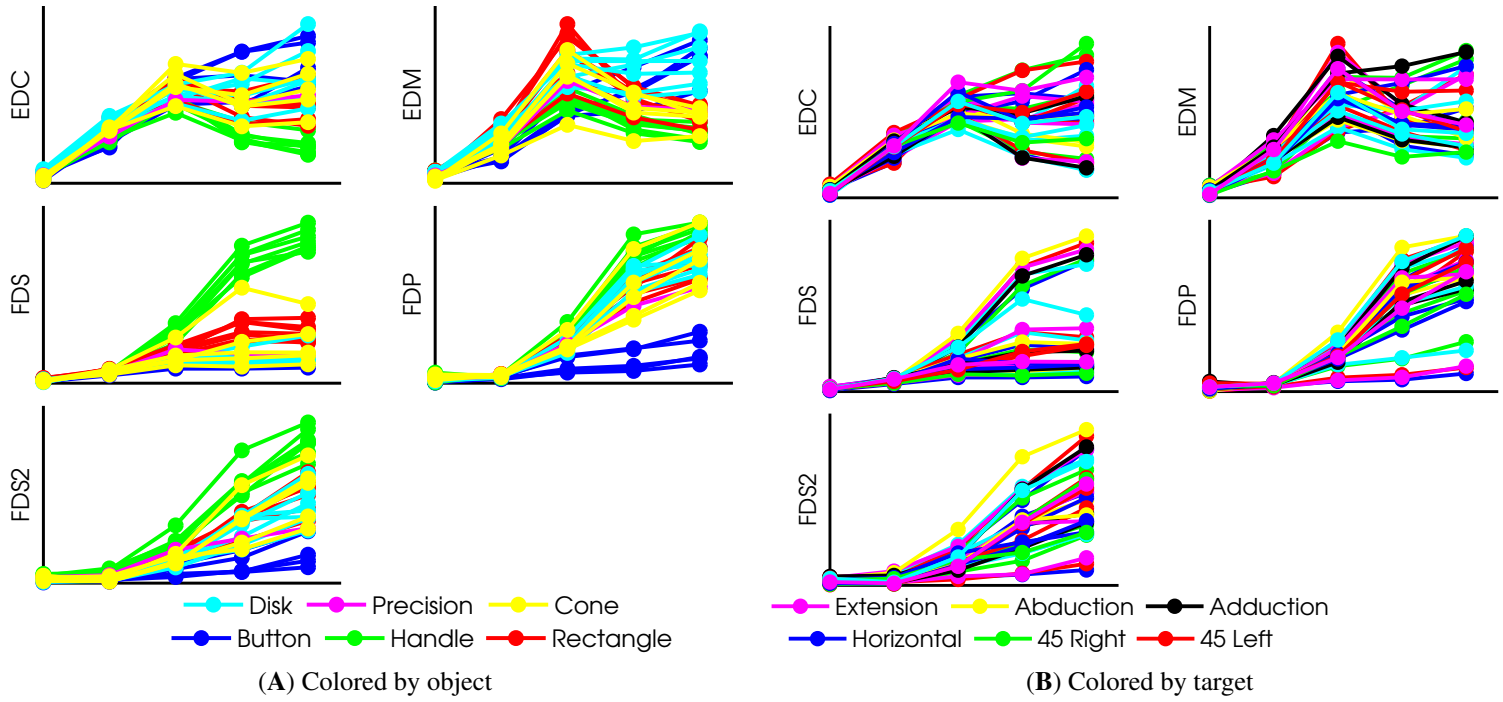

(**A**) Colored by object

(**B**) Colored by target

Figure 3.51: **Finger muscles tuning to attitudes: Monkey B:** Mean EMG levels during 5 task epochs (X-axis). Means were computed across all trials from a certain attitude. Attitudes are colored by objects **(A)** or targets **(B)**. Panels were scaled vertically to fit the axis, hence values are not comparable *across* panels. The 5 task epochs shown are: (1) *Trial Start* to *Reach Start*, (2) *Reach Start* to *Max Speed*, (3) *Max Speed* to *Reach End*, (4) *Reach End* to *Grasp Start*, (5) *Grasp Start* to *Grasp End*.

3.3.4 JA TUNING TO OBJECTS

In the previous sections, we concluded that the muscles showed mainly object-specific differential EMG. In other words, EMG activity was tuned to objects more than to targets. We examined whether this translated to object-specific tuning for JAs. We calculated the mean JA in every one of the 5 task epochs (see Figure 3.52 caption for details), and plotted them as a function of task epoch, and colored by object. We separated the JAs into 5 groups by anatomical joints. The first group included all the wrist JAs (flexion/extension, abduction/adduction, rotation; see Figure 3.52). The other 4 groups included the MCP flexion/extension JAs, MCP abduction/adduction JAs, PIP flexion/extension JAs and DIP flexion/extension JAs (see Figures 3.53, 3.54).

The results indicate that most wrist JAs have object-specific mean values to some degree, beginning at the deceleration phase of the reach. However, overlaps exist for some objects: for example, wrist rotation values are similar between the button and the disk (Figure 3.52**A**) and between the bar and the rectangle (Figure 3.52**B**). Wrist JAs differ most in the static grasp epoch, where there is no movement.

Figures 3.54 and 3.53 show that mean finger JAs are rather well differentiated between objects, supporting our finding that objects can be accurately classified using mean JAs. We also see that JAs are better differentiated beginning at the deceleration phase of the reach; and that JAs of matching anatomical segments are well correlated across the different fingers.

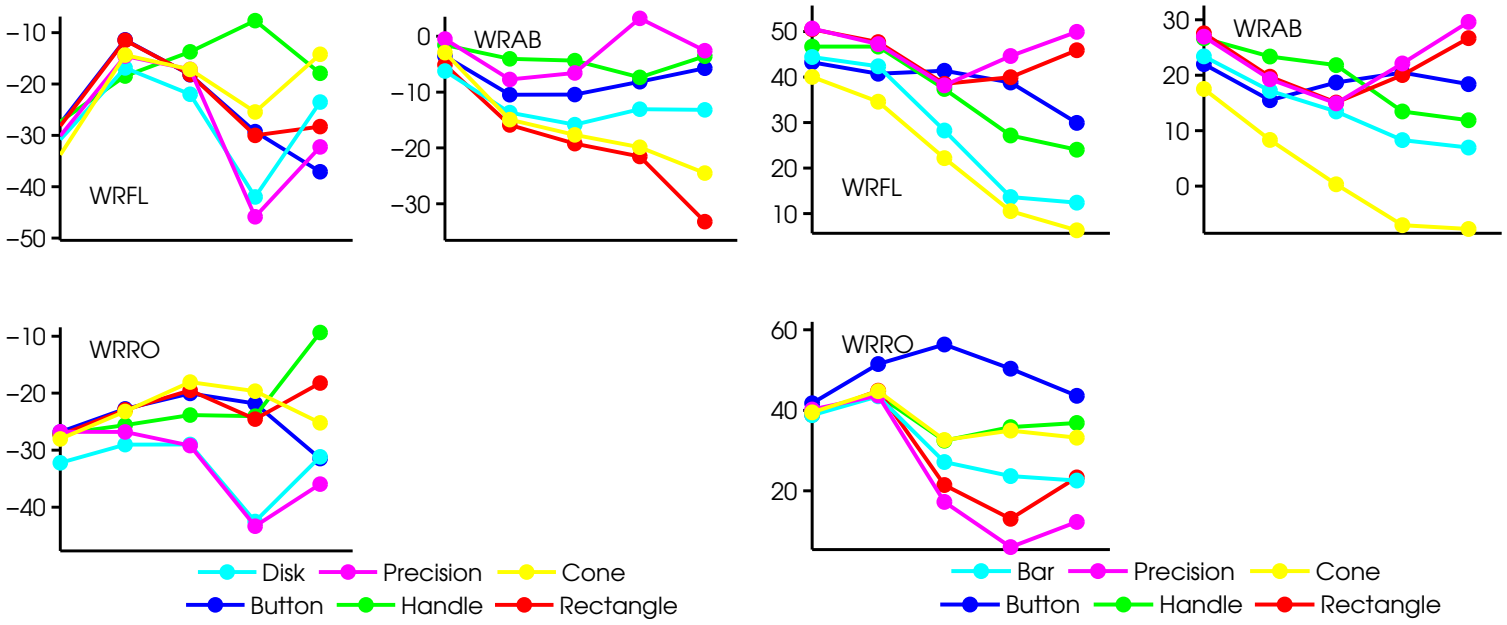

(**A**) Monkey B

(**B**) Monkey E

Figure 3.52: **Wrist JA tuning to objects:** Mean JAs during 5 task epochs (X-axis). Means were computed across all trials where the monkey reached to grasp a certain object, regardless of the target. Objects are the same for both monkeys, except for the disk and bar. Panels were scaled vertically to fit the axis, hence values are not comparable *across* panels. Wrist JAs signs are different between the two monkeys, due to a sign convention used in our software and the fact that monkey B reached with its right hand, and monkey E reached with its left hand. The 5 task epochs shown are: (1) *Trial Start* to *Reach Start*, (2) *Reach Start* to *Max Speed*, (3) *Max Speed* to *Reach End*, (4) *Reach End* to *Grasp Start*, (5) *Grasp Start* to *Grasp End*.

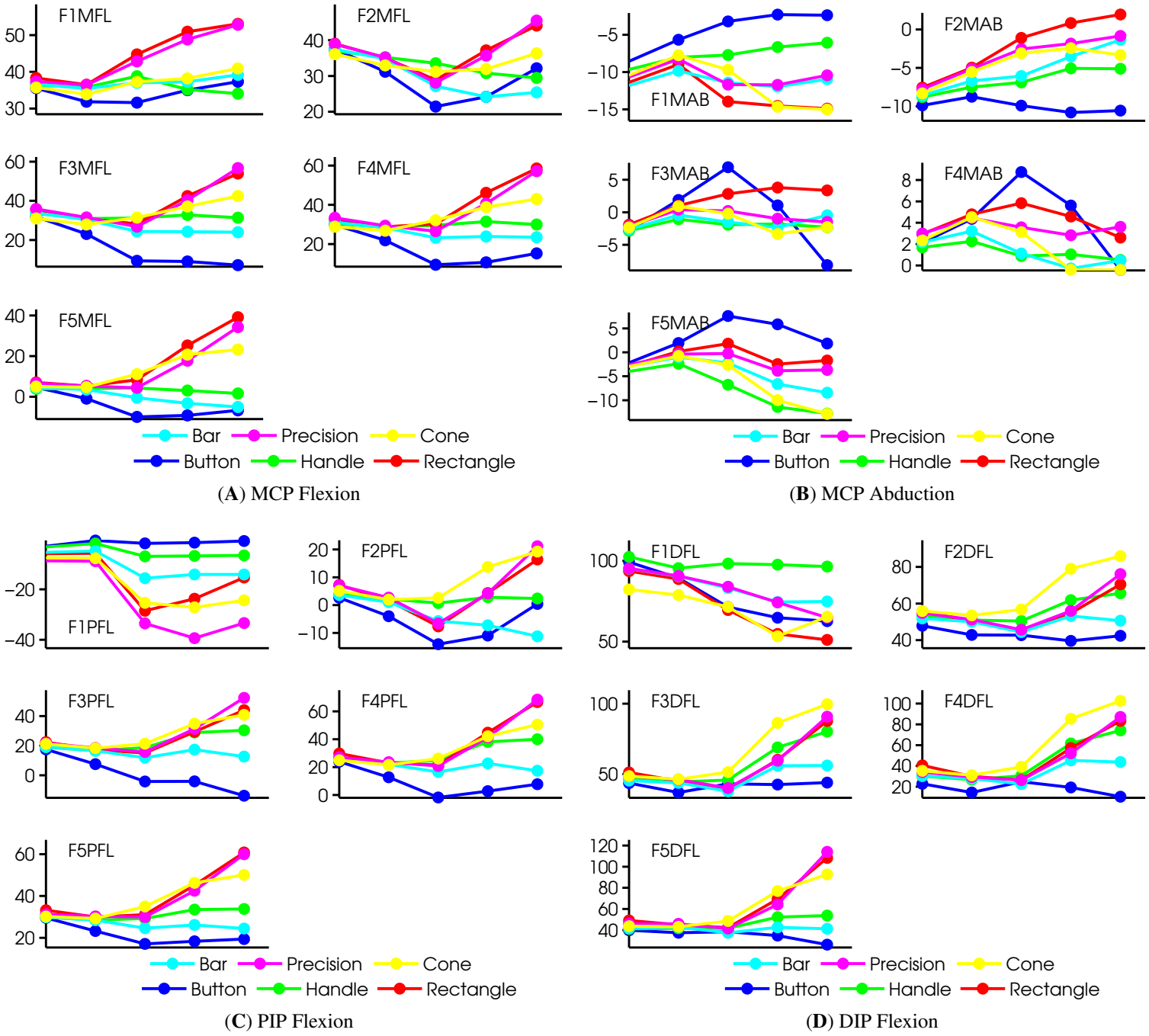

(**A**) MCP Flexion

(**B**) MCP Abduction

(**C**) PIP Flexion

(**D**) DIP Flexion

Figure 3.53: **Finger JA tuning to objects: Monkey E:** Mean JAs during 5 task epochs (X-axis). Means were computed across all trials where the monkey reached to grasp a certain object, regardless of the target. Objects are the same for both monkeys, except for the disk and bar. Panels were scaled vertically to fit the axis, hence values are not comparable *across* panels. The 5 task epochs shown are: (1) *Trial Start* to *Reach Start*, (2) *Reach Start* to *Max Speed*, (3) *Max Speed* to *Reach End*, (4) *Reach End* to *Grasp Start*, (5) *Grasp Start* to *Grasp End*.

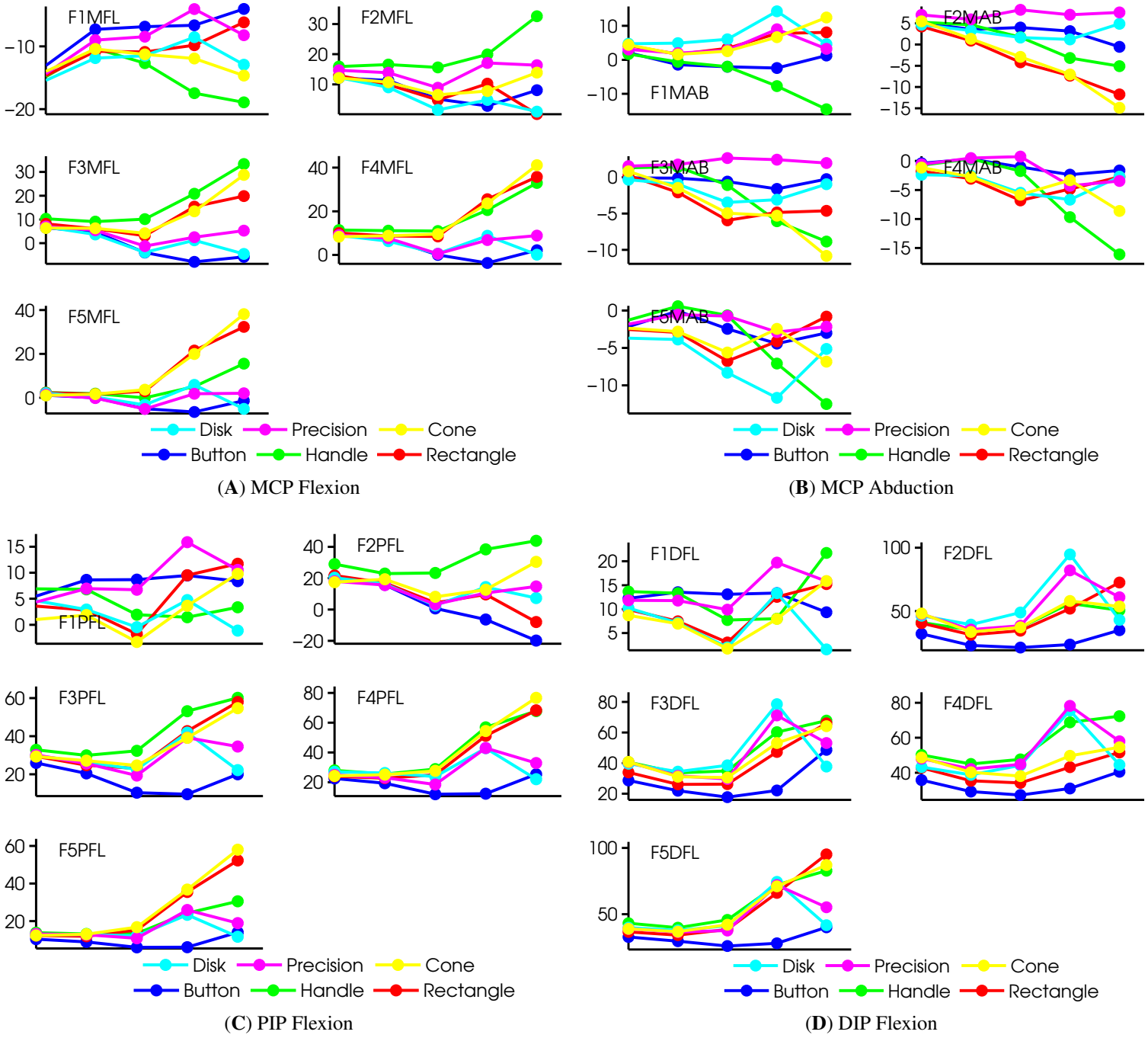

(**A**) MCP Flexion

(**B**) MCP Abduction

(**C**) PIP Flexion

(**D**) DIP Flexion

Figure 3.54: **Finger JA tuning to objects: Monkey B:** Mean JAs during 5 task epochs (X-axis). Means were computed across all trials where the monkey reached to grasp a certain object, regardless of the target. Objects are the same for both monkeys, except for the disk and bar. Panels were scaled vertically to fit the axis, hence values are not comparable *across* panels. The 5 task epochs shown are: (1) *Trial Start* to *Reach Start*, (2) *Reach Start* to *Max Speed*, (3) *Max Speed* to *Reach End*, (4) *Reach End* to *Grasp Start*, (5) *Grasp Start* to *Grasp End*.

3.3.5 JA TUNING TO TARGETS

In Figure 3.52, we observed some object-specific mean JA values, mostly in the static grasp phase. Figure 3.55 shows that mean JA values are also well differentiated by targets, beginning at the deceleration phase of the reach. We compare the two in the next section. On the other hand, finger JAs are not as well differentiated by targets, especially for monkey B (Figures 3.56,3.57).

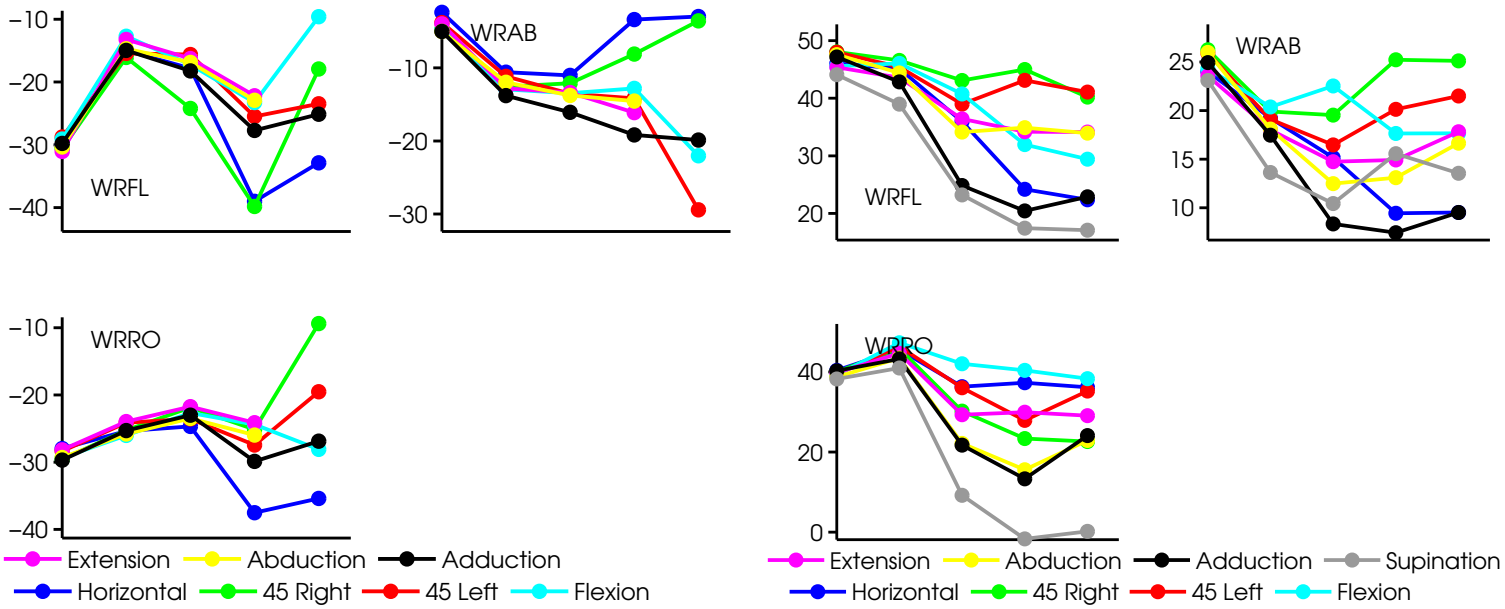

(**A**) Monkey B

(**B**) Monkey E

Figure 3.55: **Wrist JA tuning to targets:** Mean JAs during 5 task epochs (X-axis). Means were computed across all trials where the monkey reached to a certain target, regardless of the object. Panels were scaled vertically to fit the axis, hence values are not comparable *across* panels. The 5 task epochs shown are: (1) *Trial Start* to *Reach Start*, (2) *Reach Start* to *Max Speed*, (3) *Max Speed* to *Reach End*, (4) *Reach End* to *Grasp Start*, (5) *Grasp Start* to *Grasp End*.

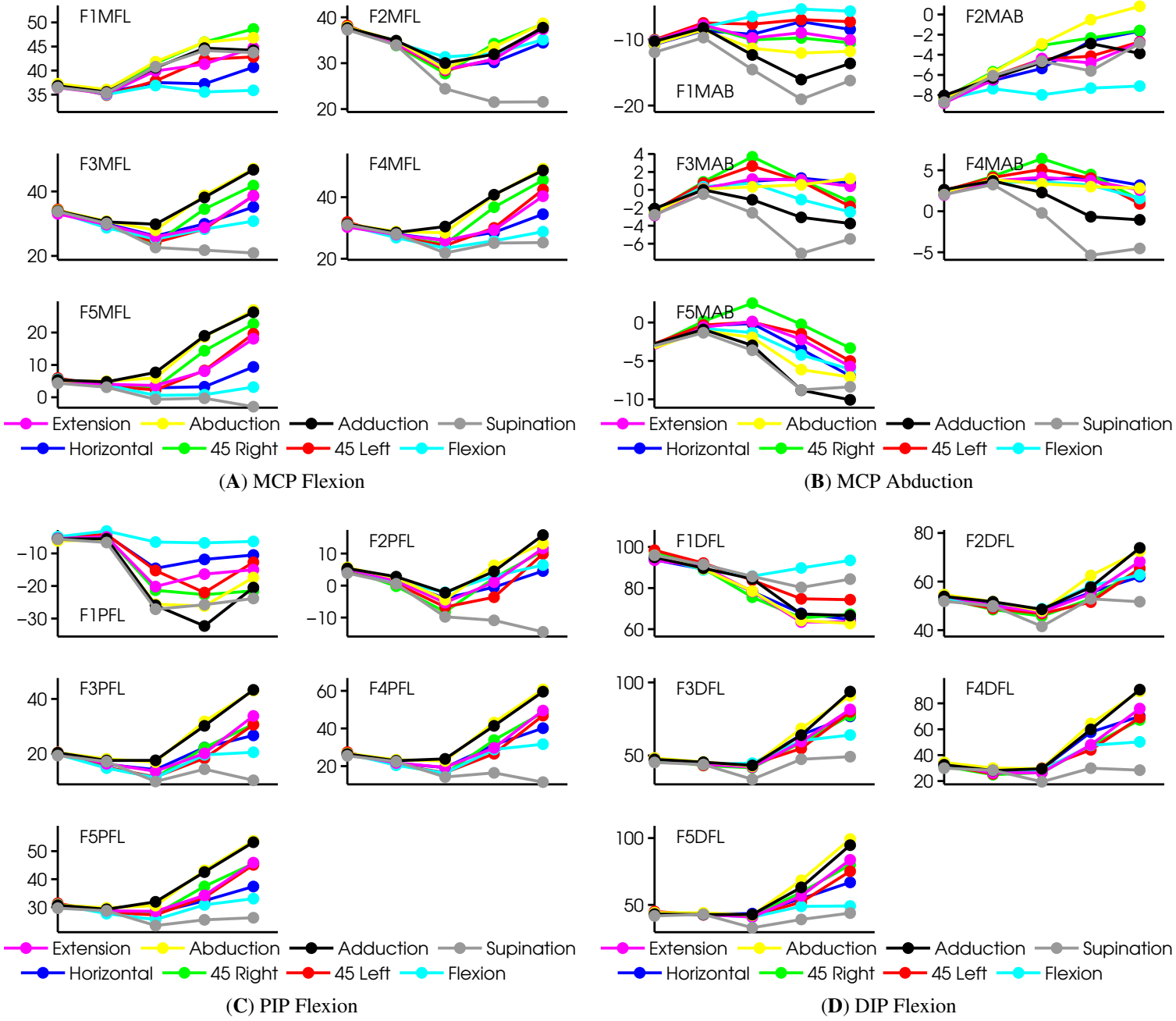

(**A**) MCP Flexion

(**B**) MCP Abduction

(**C**) PIP Flexion

(**D**) DIP Flexion

Figure 3.56: **Finger JA tuning to targets: Monkey E:** Mean JAs during 5 task epochs (X-axis). Means were computed across all trials where the monkey reached to a certain target, regardless of the object. Panels were scaled vertically to fit the axis, hence values are not comparable *across* panels. The 5 task epochs shown are: (1) *Trial Start* to *Reach Start*, (2) *Reach Start* to *Max Speed*, (3) *Max Speed* to *Reach End*, (4) *Reach End* to *Grasp Start*, (5) *Grasp Start* to *Grasp End*.

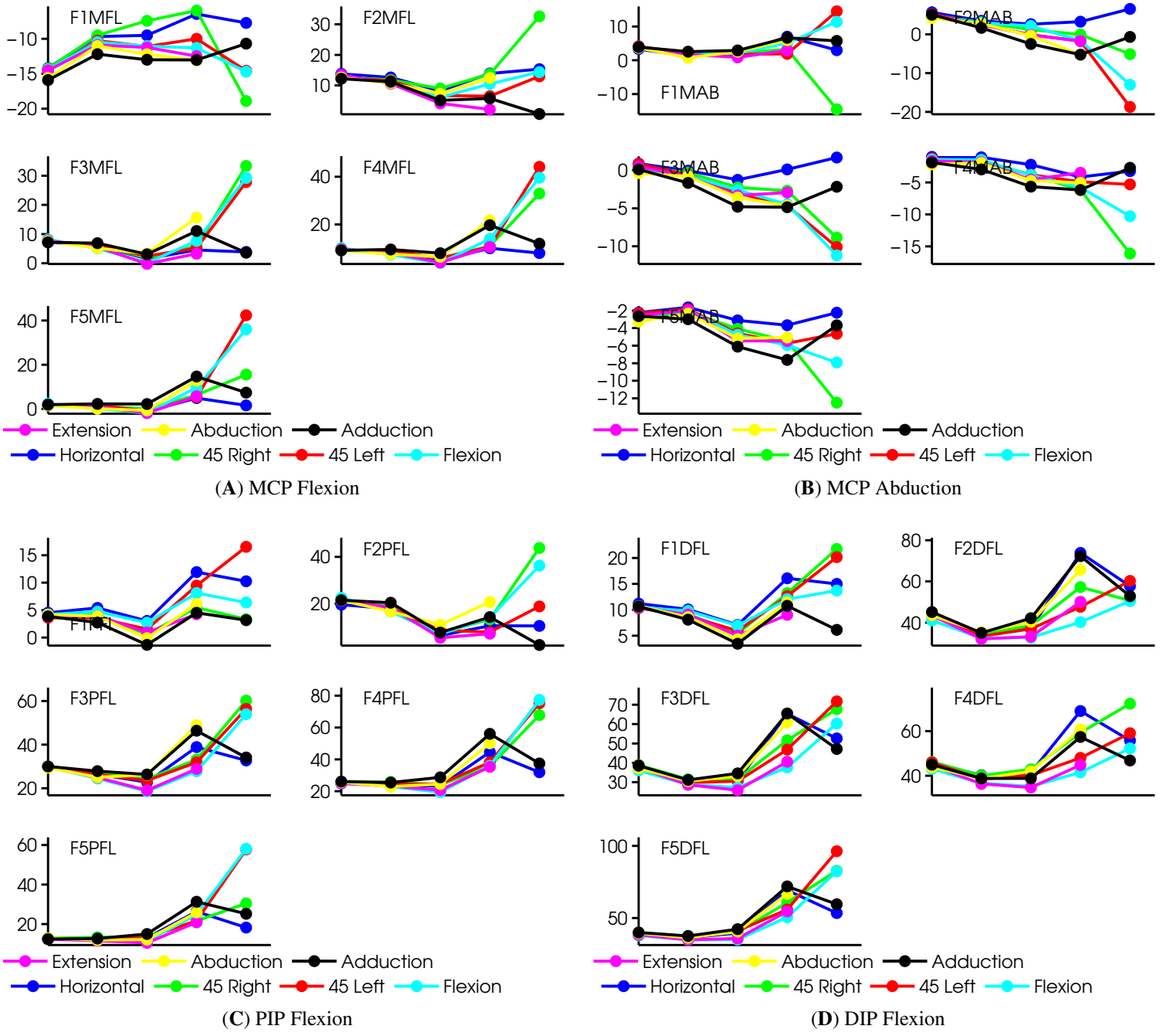

(**A**) MCP Flexion

(**B**) MCP Abduction

(**C**) PIP Flexion

(**D**) DIP Flexion

Figure 3.57: **Finger JA tuning to targets: Monkey B:** Mean JAs during 5 task epochs (X-axis). Means were computed across all trials where the monkey reached to a certain target, regardless of the object. Panels were scaled vertically to fit the axis, hence values are not comparable *across* panels. The 5 task epochs shown are: (1) *Trial Start* to *Reach Start*, (2) *Reach Start* to *Max Speed*, (3) *Max Speed* to *Reach End*, (4) *Reach End* to *Grasp Start*, (5) *Grasp Start* to *Grasp End*.

3.3.6 JA TUNING TO ATTITUDES

In the previous sections, we observed both object and target differentiation in mean wrist JAs (Figures 3.52, 3.55). It is hard to compare the figures, since both show the mean JA values, without a measure of variance (such as SD). We opted not to plot error bars on these figures, since they would become hard to read. Instead, we used the same approach as in Section 3.3.3, and plotted the mean JA values for all attitudes, colored by either the object or target, for every attitude. We show results only for monkey E in Figure 3.58, since results for monkey B were similar. The figure shows clearer differentiation by objects than targets, although some degree of grouping can be seen when attitudes are colored by targets. We concluded that wrist JAs are better differentiated by objects, which coincides with the classification results in Section 3.2.4.

Based on Figures 3.53 and 3.56, we expected to find better differentiation of finger JAs by object, than by target. Figure 3.59 shows the mean JAs for every attitude, colored by object or target, and it confirms that finger JAs are better differentiated by objects than by targets. Results for monkey B were similar (not shown).

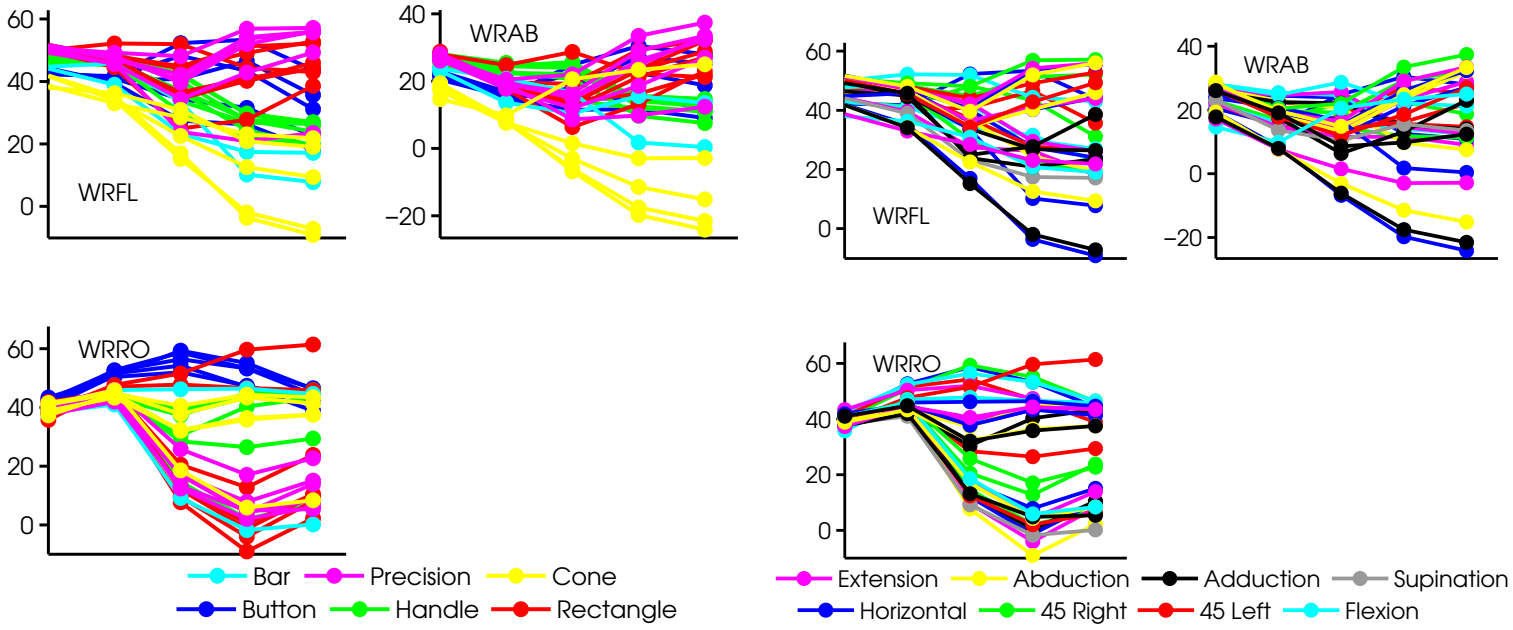

(**A**) Colored by object

(**B**) Colored by target

Figure 3.58: **Wrist JA tuning to attitudes: Monkey E:** Mean JAs during 5 task epochs (X-axis). Means were computed across all trials from a certain attitude. Attitudes are colored by objects **(A)** or targets **(B)**. Panels were scaled vertically to fit the axis, hence values are not comparable *across* panels. The 5 task epochs shown are: (1) *Trial Start* to *Reach Start*, (2) *Reach Start* to *Max Speed*, (3) *Max Speed* to *Reach End*, (4) *Reach End* to *Grasp Start*, (5) *Grasp Start* to *Grasp End*.

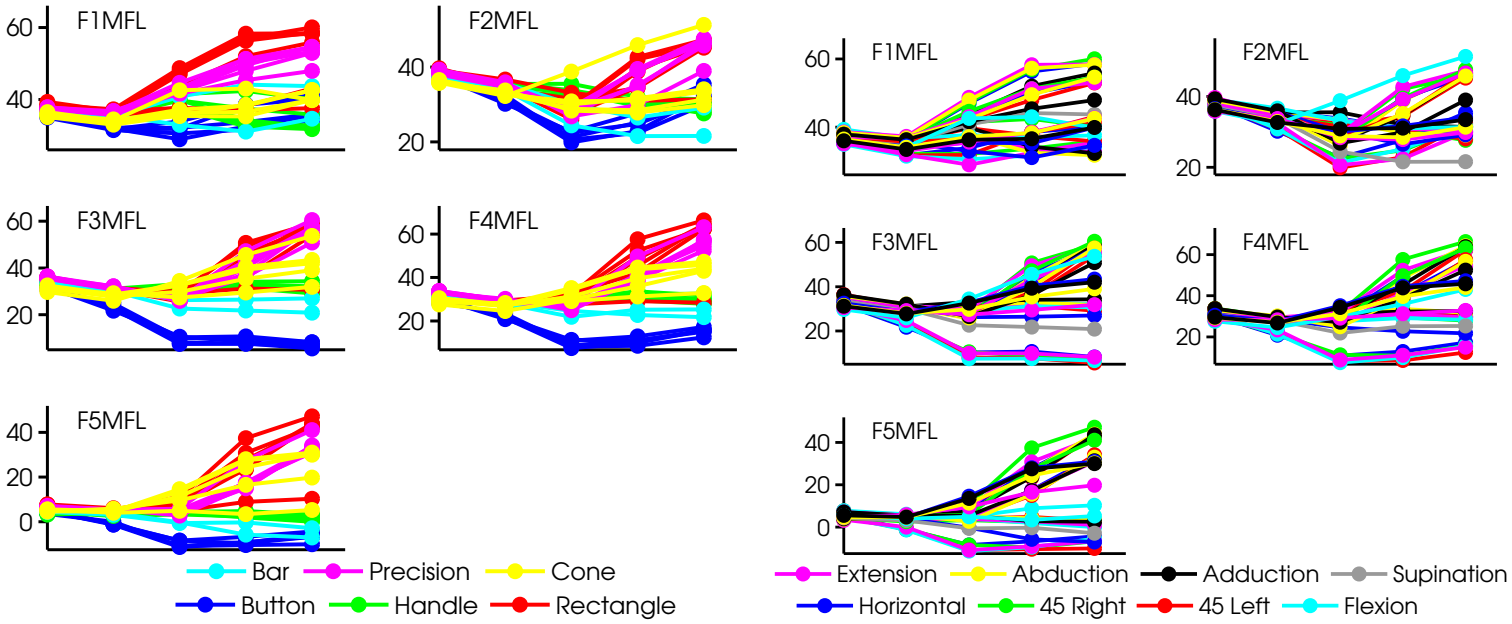

(**A**) MCP Flexion colored by object

(**B**) MCP Flexion colored by target

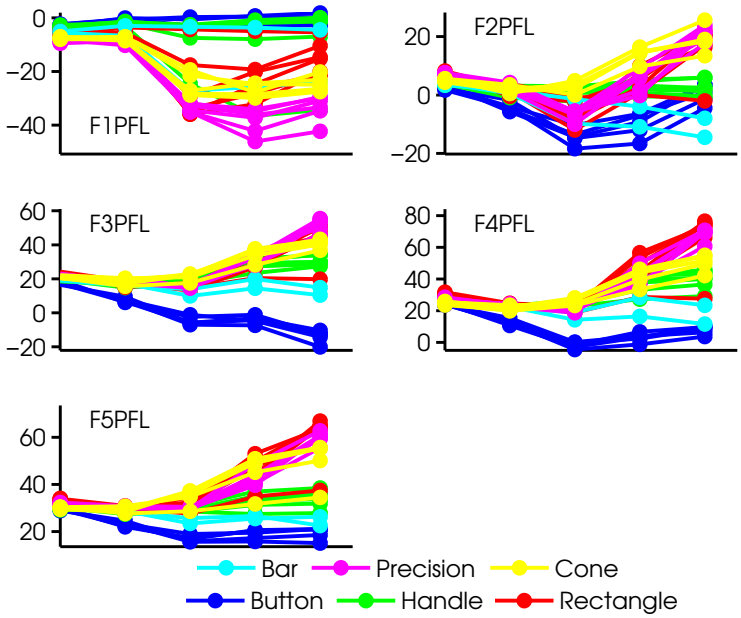

(**C**) PIP Flexion colored by object

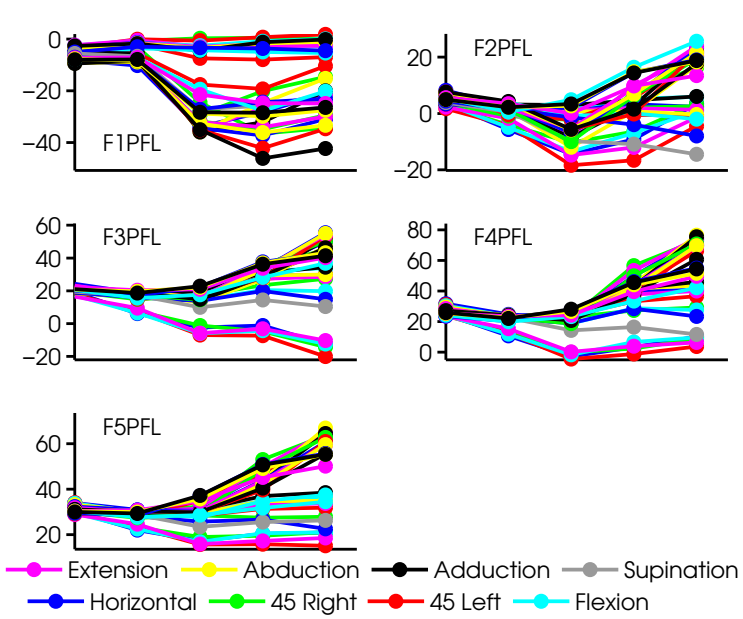

(**D**) PIP Flexion colored by target

Figure 3.59: **Finger JA tuning to attitudes: Monkey E:** Mean JAs during 5 task epochs (X-axis). Means were computed across all trials from a certain attitude. Attitudes are colored by objects **(A)**,**(C)** or targets **(B)**,**(D)**. Panels were scaled vertically to fit the axis, hence values are not comparable *across* panels. The 5 task epochs shown are: (1) *Trial Start* to *Reach Start*, (2) *Reach Start* to *Max Speed*, (3) *Max Speed* to *Reach End*, (4) *Reach End* to *Grasp Start*, (5) *Grasp Start* to *Grasp End*.

3.4 CORRELATION BETWEEN MUSCLES

As mentioned in Section 3.2, when selecting the objects and targets to be used in this task, our main goal was to record a rich set of EMG patterns, where correlation patterns between muscles would be as different as possible between attitudes. We have already shown that using the mean trial EMG activity, it is possible to classify what attitude the monkey was reaching to. In this section, we examine changes in correlation *between* EMGs across attitudes.

For every attitude, we computed the sample correlation coefficients between all pairs of muscles, using all available trials. Data from the beginning of the MoveA epoch to the end of the static grasp were used. The *sample correlation coefficient* between two EMGs (x, y), each with n samples is

$$r_{xy} = \frac{\sum_{i=1}^{n}(x_i - \bar{x})(y_i - \bar{y})}{(n-1)s_x s_y} = \frac{\sum_{i=1}^{n}(x_i - \bar{x})(y_i - \bar{y})}{\sqrt{\sum_{i=1}^{n}(x_i - \bar{x})^2 \sum_{i=1}^{n}(y_i - \bar{y})^2}} \tag{3.8}$$

Figure 3.60 shows 4 representative correlation matrices for monkey E, each computed using data from a different attitude. The 4 attitudes differed by both object and target. Some correlations are common across all 4 attitudes. First, the finger flexors (FDS,FDS2,FDP) are well correlated. This is expected, since FDS and FDS2 were recorded from two compartments of the same muscle, mainly flexing the PIP joints. FDP flexes the DIP joints, so that its activation usually follows that of FDS. Second, the two heads of the triceps (TRILA, TRILO) are well correlated, which is expected since they have similar roles. Third, the wrist flexors (FCU, FCR) correlate well with the finger flexors, since the wrist flexors are usually active during the static grasp to stabilize the wrist, while the finger flexors help perform the grasp.

Most other correlations changed between attitudes, in a manner consistent with the task requirements. Monkey E tended to grasp the cone at the flexion target with its wrist flexed in the ulnar direction, using all fingers. The cone required the monkey to exert a lot of force, in order to successfully press all force sensors. Figure 3.60**B** shows that the finger flexors and extensors are strongly correlated, as well the wrist muscles, the triceps and brachioradialis (which support the arm and bring it to the midprone position). The bar at the supination target, required the monkey the supinate the hand and press the object upwards. Figure 3.60**A** shows strong correlation between the finger flexors, and also between the finger flexors and the deltoid, biceps the long head of the

triceps. In contrast to Figure 3.60**B**, pronator teres and extensor carpi-ulnaris are anti-correlated with most other muscles. The triceps are anti-correlated with the deltoid and the biceps in Figure 3.60**C**, but positively correlated with them for the other attitudes. After examining the correlation matrices for all attitudes, for both monkey B and E, we concluded that correlation structure between EMGs changed between attitudes, in a task-related manner. In Section 3.6, we explore correlation features further, using dimensionality reduction methods.

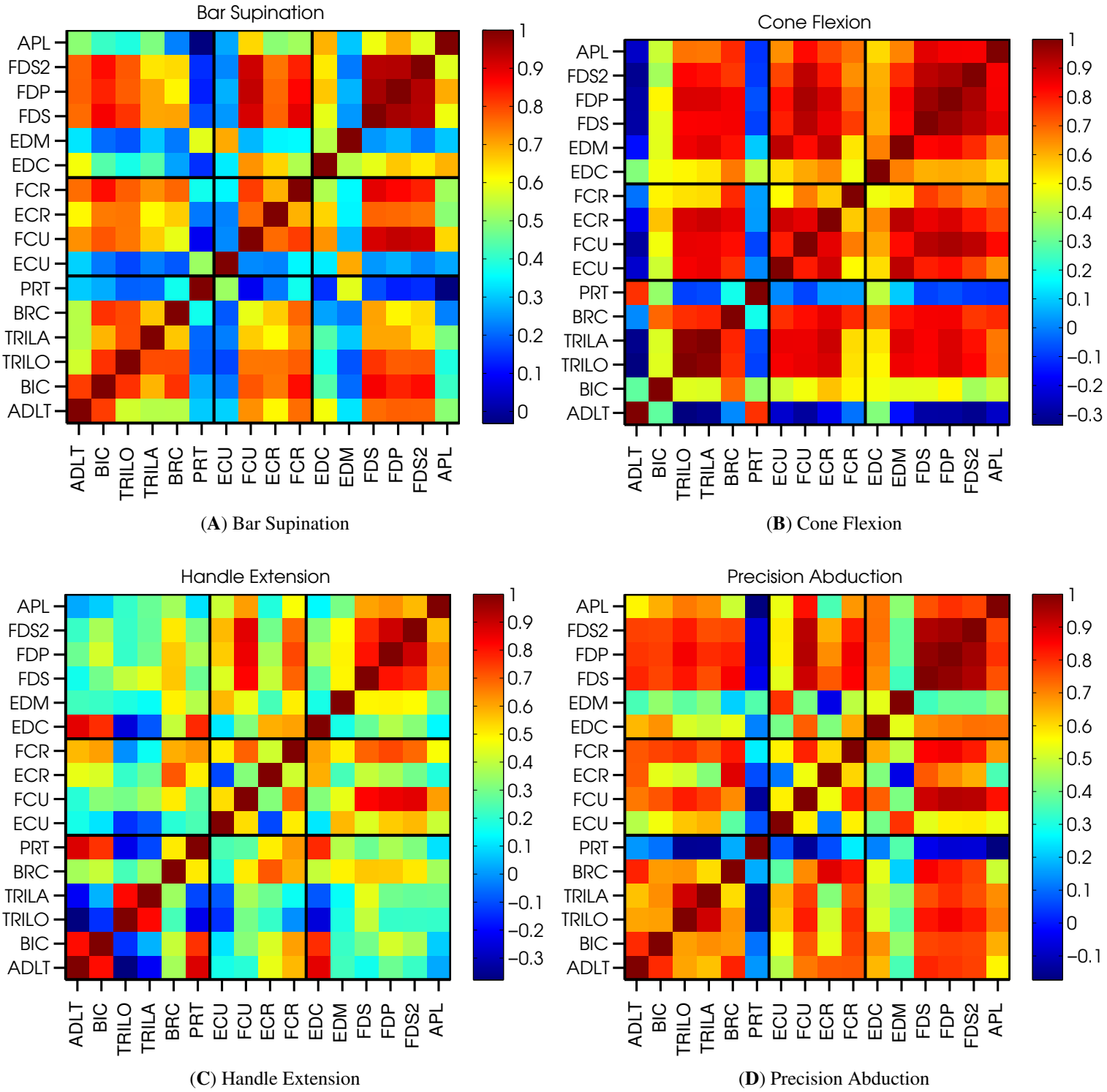

(**A**) Bar Supination

(**B**) Cone Flexion

(**C**) Handle Extension

(**D**) Precision Abduction

Figure 3.60: **EMG correlation across attitudes: Monkey E:** Representative EMG correlation matrices for 4 attitudes. EMGs are grouped by arm, wrist and hand muscles; separated by black lines.

3.5 CORRELATION BETWEEN JOINT ANGLES

We found that objects could be almost perfectly classified using the mean JAs at the preshape and static grasp epochs (Section 3.2). Based on these results, we expected to see a clear difference in the correlation structure between JAs across attitudes. We therefore computed the sample correlation coefficients (Eq. 3.8) between the JAs and between JA velocities for every attitude, using all samples from repeat trials, from the beginning of MovaA epoch to the end of the static grasp epoch. Within-object correlation matrices were more similar than across objects, and the correlation structure changed as a function of object, rather than a function of target, supporting our finding that individual JAs tend to change as a function of object, rather than target (Section 3.3).

Figure 3.61 shows 4 typical correlation matrices, for the same attitudes as Figure 3.60. One common feature across attitudes was the correlation between PIP and DIP joints, although its magnitude was variable. Examining individual correlation matrices, we found high correlation between the MCP and PIP joints, but not the DIP joints (Figure 3.61**A**). This was likely due to the monkey pushing the bar instead of grasping it. When the monkey grasped the cone object, it tended to curl its fingers around it, which is evident in the negative correlation between the abduction and flexion joint angles in Figure 3.61**B**. Monkey E tended to perform a power grip on the handle using only 3 fingers, in order to press the force sensors more efficiently. This can be seen in the high correlation between the PIP flexion of fingers $3-5$, in Figure 3.61**C**.

While the average correlation between hand shapes across attitudes was used in Figure 3.61, Figure 3.62 measures the average correlation between joint angles across attitudes. Joint angular velocities were obtained from the joint angles, and the sample correlation coefficients between all pairs were computed. Similarities between correlation structures across attitudes can be seen here as well: the PIP and DIP joints tend to flex together, and MCP joints tend to abduct together. For some attitudes, the MCP joints flexion was correlated with both PIP and DIP joints flexion (Figures 3.62**B**,3.62**D**), only with PIP joints flexion (Figure 3.62**A**), or neither (Figure 3.62**C**). The object size and shape relative to the monkey hand size were key factors in determining the correlation between finger joints.

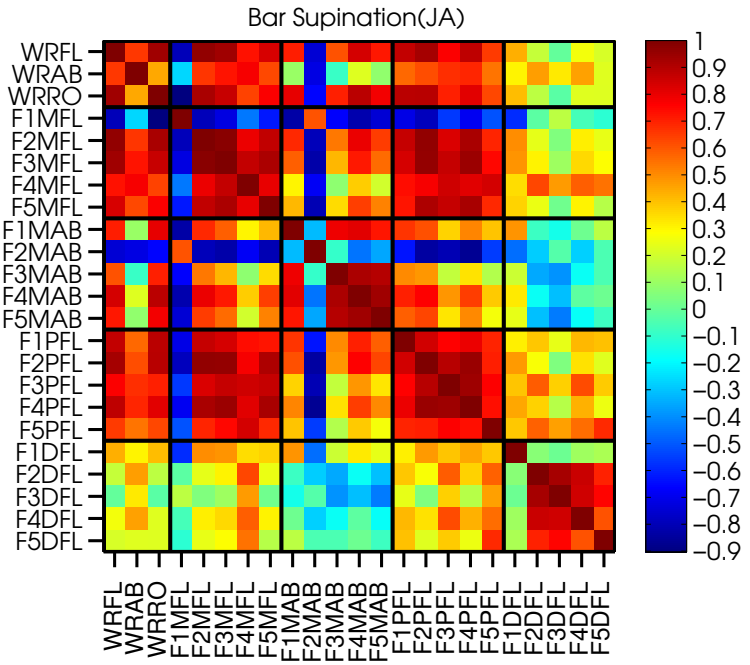

(**A**) Bar Supination

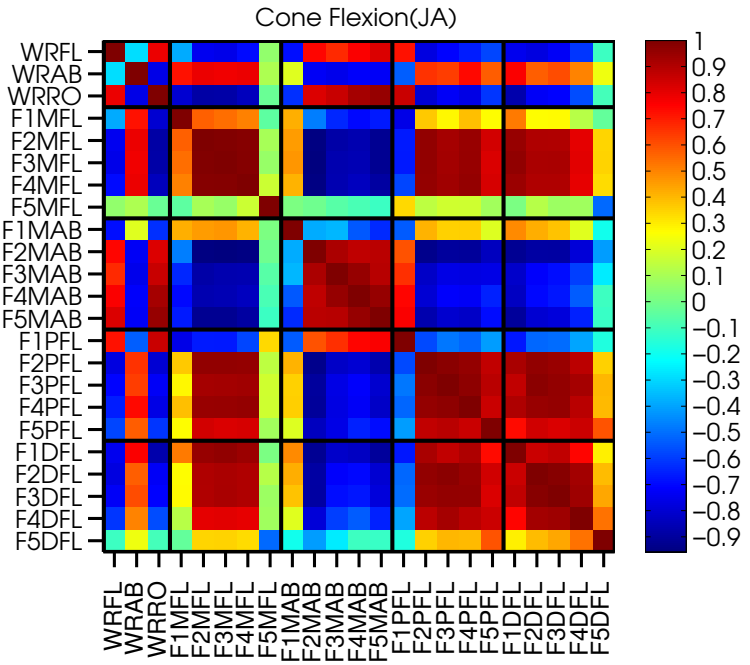

(**B**) Cone Flexion

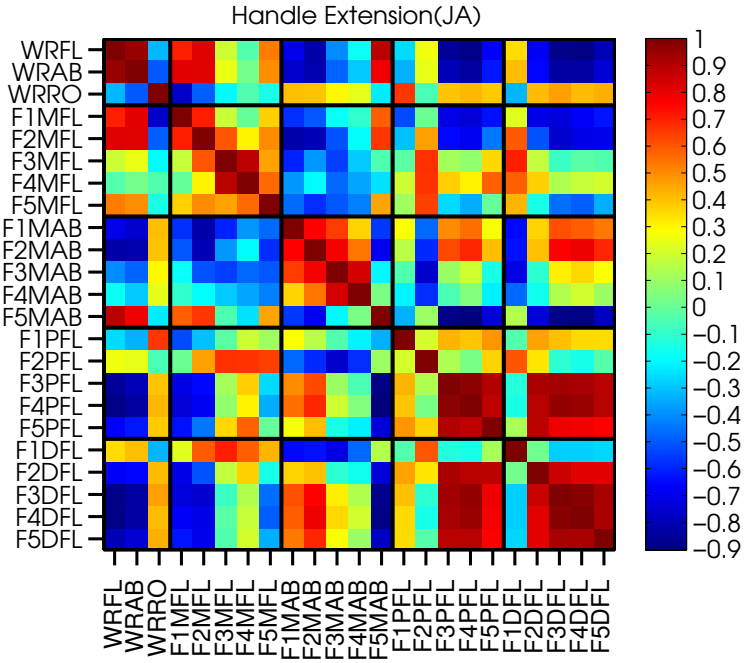

(**C**) Handle Extension

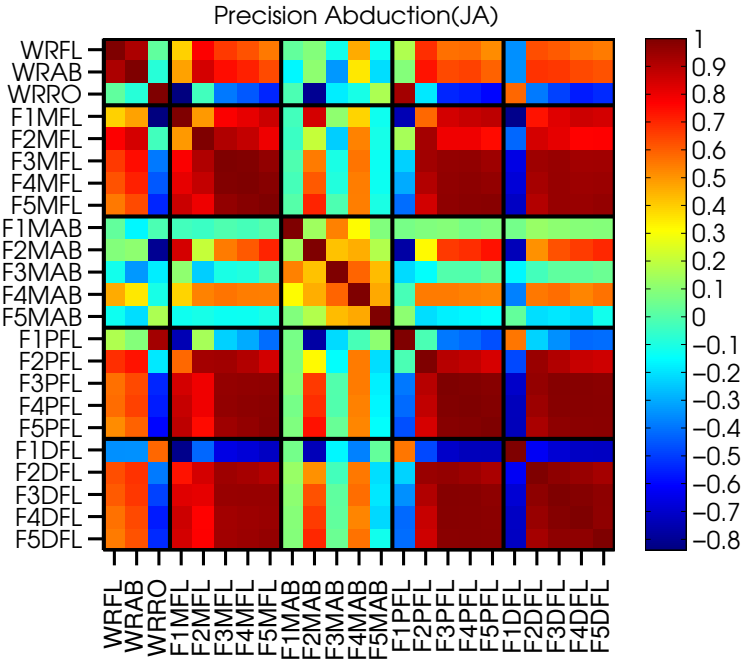

(**D**) Precision Abduction

Figure 3.61: **JA correlation across attitudes: Monkey E:** Representative JA correlation matrices for 4 attitudes. JAs are grouped by anatomical joints; separated by black lines.

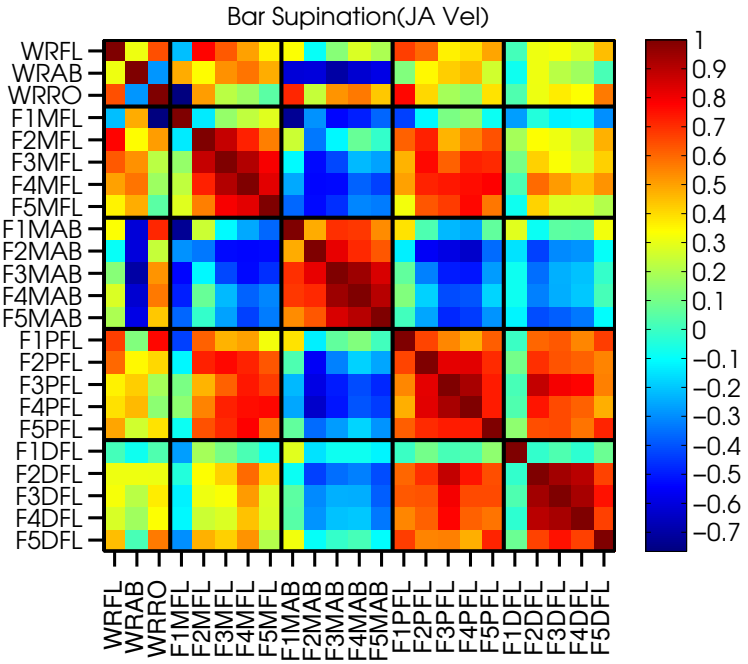

(**A**) Bar Supination

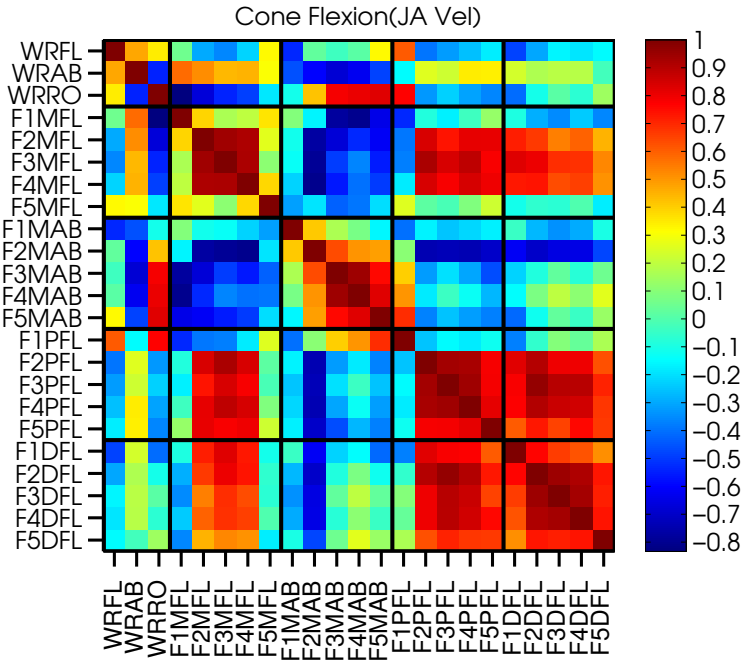

(**B**) Cone Flexion

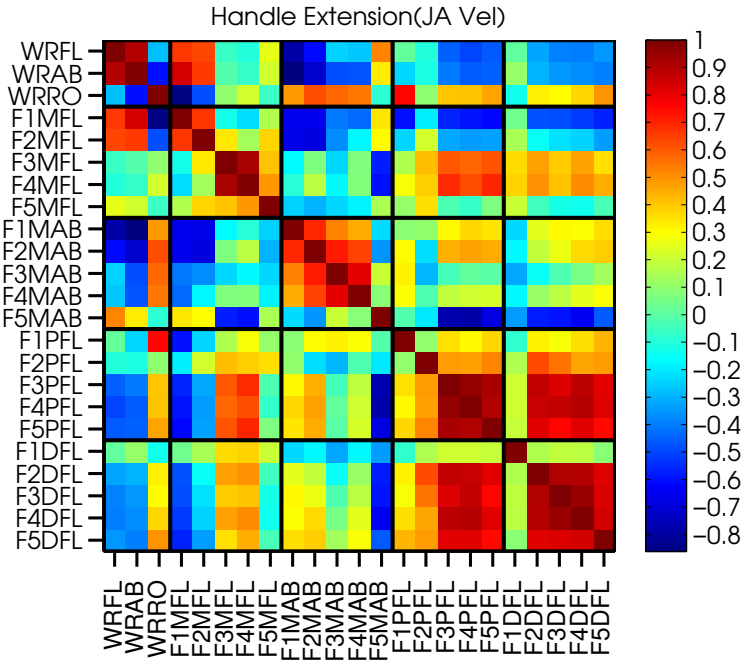

(**C**) Handle Extension

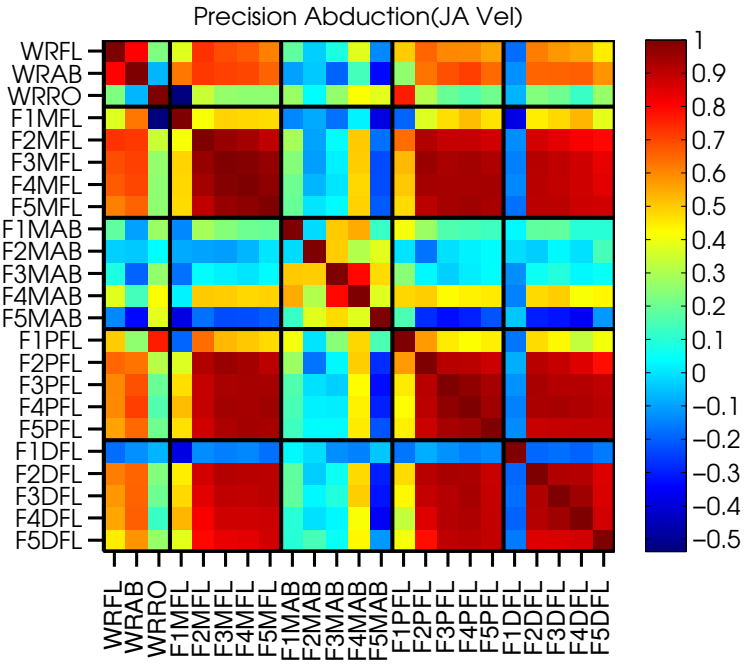

(**D**) Precision Abduction

Figure 3.62: **JA velocity correlation across attitudes: Monkey E:** Representative JA velocity correlation matrices for 4 attitudes. JA velocities are grouped by anatomical joints; separated by black lines.

3.6 MUSCLE SYNERGIES

In Section 3.4, we examined the pairwise correlations between EMGs across attitudes. Some of the correlations were attitude dependent, while others were more consistent across attitudes. In this section, we explore multivariate relationships between EMGs, using dimensionality reduction techniques.

Muscle synergies have been suggested as a possible way for the central nervous system to control a complicated construct like the hand with its 23 degrees-of-freedom (DOF). Instead of directly controlling over 40 individual muscles, the motor cortex could plan movements or muscle activations in a reduced dimensionality space; and utilize downstream structures, perhaps located in the spinal-cord, implementing muscle synergies. Every muscle synergy activates different muscles in a certain proportion, and the combined activation of all synergies determines the activation of individual muscles.

We have reviewed different dimensionality-reduction techniques (PCA, ICA, FA, ICA-PCA) for extracting muscle synergies, and concluded that they usually tend to provide similar results (see Section 1.5 for details). Therefore, we used ICA to compute *muscle synergies* from our data.

As a pre-processing step, EMG is usually smoothed to produce estimates of its non-stationary baseline, but there is no consensus as to the most appropriate amount of smoothing. A common smoothing method is a $20Hz$ low-pass filter, which tends to provide a reasonable estimate of the EMG baseline. We have computed muscle synergies using both low-pass filtered and spline-smoothed EMG data. Due to its more flexible nature, spline smoothing tends to capture more high-frequency changes in EMG, often missed by low-pass filtering. We used a cubic smoothing spline with a fixed smoothing parameter (csaps in Matlab with $p = 1e^{-5}$). Figure 3.63 shows a comparison of low-pass filtered EMG to spline smoothed EMG, for two muscles. Spline-smoothing follows the original EMG baseline better.

Given an $N \times M$ data matrix X, of N rectified EMG samples from M muscles,the first step in the ICA computation is to compute Σ, the sample covariance matrix of mean-centered X, according to $\Sigma = X^T X/N$; later used in the whitening process (see below). Then, the eigenvalues and eigenvectors (the *principal components directions*) of Σ are computed. We implemented that using singular value decomposition (SVD).

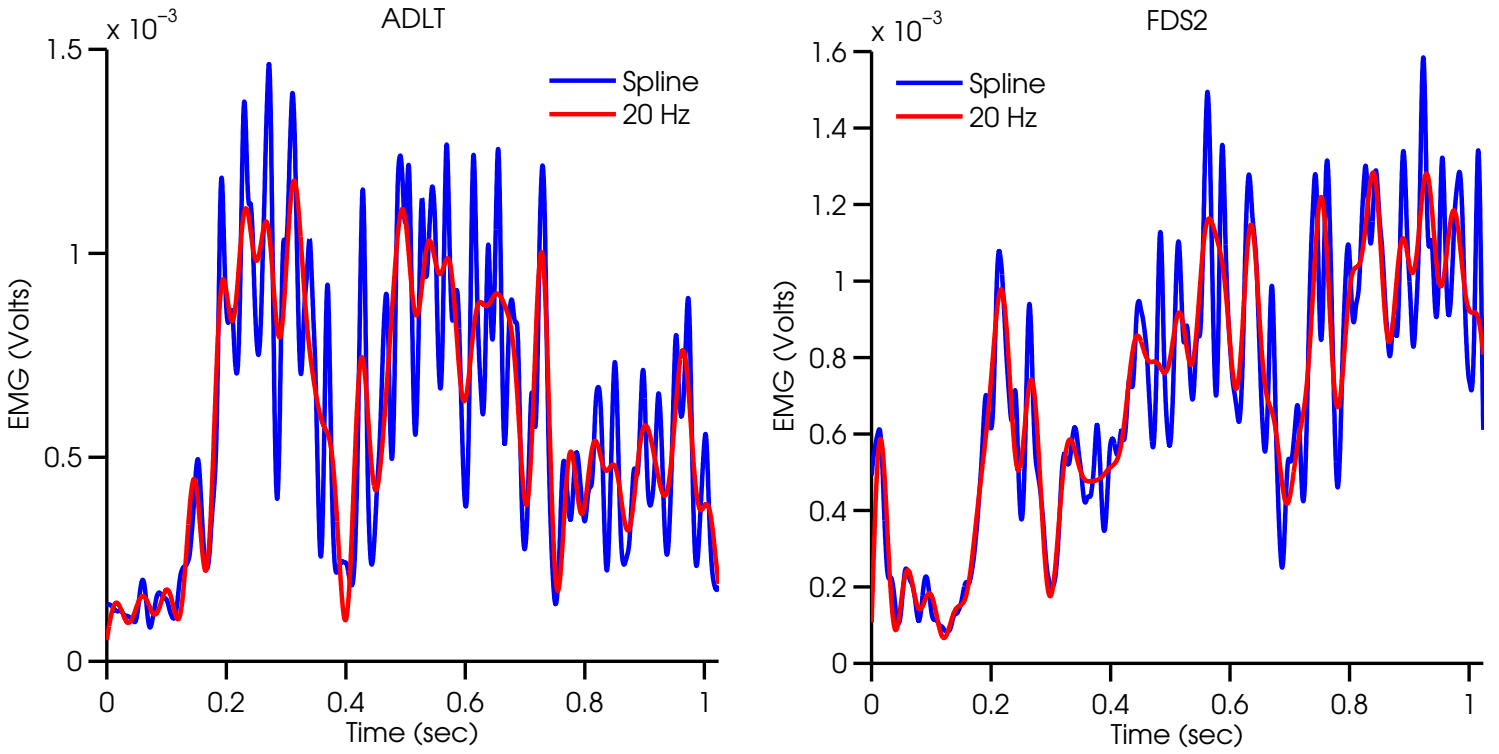

(**A**) Anterior Deltoid

(**B**) Flexor Digitorium Superficialis

Figure 3.63: **Comparison of EMG smoothing: Monkey E:** Raw rectified EMG was smoothed using both a $20Hz$ low-pass FIR filter, and a smoothing-spline. Results are superimposed for two muscles. Note how spline-smoothing captures high-frequency features, which are missed by the low-pass filter.

The SVD of an $N \times M$ matrix X has the form $X = UDV^T$, where U is a $N \times M$ and V is $M \times M$, with the columns of U spanning the column space of X, and the columns of V spanning the row space of X. D is a $M \times M$ diagonal matrix, with diagonal values $d_1 \geq d_2 \geq \cdots \geq d_M \geq 0$. These are the singular values of X, and if one or more d values are equal to zero, then X is singular.

We can express $X_T X$ in terms of the SVD of X

$$X^T X = (UDV^T)^T UDV^T =^{[1]} VD^T U^T UDV^T =^{[2]} VD^T U^{-1} UDV^T =^{[3]} VD^2 V^T \tag{3.9}$$

[1] used $(AB)^T = B^T A^T$; [2] used the fact that U is orthonormal so $U^{-1} = U^T$; [3] used $U^{-1}U = I$.

Then, the SVD of mean centered X is a way of expressing the principal components of its columns

$$X^T X = V D^2 V^T \tag{3.10}$$

This is the eigen decomposition of $X^T X$ (and of Σ, up to a factor N): the columns of orthonormal V are the eigenvectors (the principal components), and the diagonal matrix D^2 contains the eigenvalues on its diagonal, ordered in descending order. The first principal, v_1, has the property that Xv_1 has the largest sample variance among all normalized linear combinations of the columns of X, equal to ${d_1}^2/N$. The implementation we used, limited the number of retained principal components to the maximal number of eigenvalues which kept D^2 non-singular (assuming some numerical tolerance around zero); and not based on the amount of variance explained by each PC. This prevented convergence problems in the ICA computation.

X was then whitened and simultaneously reduced (if needed) using

$$X_w = \Sigma^{-1/2} X \tag{3.11}$$

where $\Sigma = \Sigma^{-1/2}(\Sigma^{-1/2})^T$ and $\Sigma^{-1/2} = VD^{-\frac{1}{2}}$. Dimensionality reduction was achieved by using only subsets of the columns in V and the diagonal elements of D. The columns of X_w are uncorrelated and $COV(X_w) = I$ (in PCA, the covariance matrix of the scores has the eigenvalues in its diagonal).

We then computed the ICA as

$$X_w = AS \tag{3.12}$$

where A is the *mixing matrix* (defining the synergies) and S is the *sources matrix* (defining the activation of synergies). We used the FastICA package for Matlab, which looks for orthogonal non-normal projections, with maximally non-Gaussian distributions, using a fixed-point algorithm.

We used EMG data from an entire session, including all attitudes, to compute the muscle synergies using the ICA algorithm described above, for both sets of smoothed EMG. 5 synergies extracted from the $20Hz$ low-pass filtered EMG are shown in Figure 3.64, along with their activation coefficients in Figure 3.65. The EMG activity of 16 muscles, was reduced to a 5-dimensional space, due to correlations between muscle activations (the maximal number of synergies that kept D^2 non-singular was 5).

Interpretation of synergies in a meaningful way is not straight forward. First, rectified EMG does not contain negative values, whereas some of the synergies have both negative and positive muscle coefficients. A solution could be to interpret positive coefficients as facilitation of muscle activity, and negative coefficients as inhibition of muscle activity. Second, synergies and their activation coefficients are only defined up to a sign, that is, we can invert the sign of a synergy and its activation coefficients. For example, synergies 1 and 2 contain mainly negative coefficients, and negative activation coefficients, which we would probably want to invert for easy interpretation. Third, the synergy activation coefficients are almost always different than zero during the entire trial (Figure 3.65), which makes interpretation harder. Synergy 4 contains higher coefficients for muscles mainly active during the reach epoch, yet it is active throughout the entire trial; and we cannot label it as a ”reaching synergy“.

Figures 3.66 and 3.67 show the synergies and activation coefficients, extracted from spline-smoothed EMG data. The ICA algorithm extracted 6 synergies, probably due to the higher frequency content compared with the low-pass filtered EMG. Most synergies are similar to those in Figure 3.64, up to a sign difference, except for synergy 3, confirming that the ICA algorithm was consistent, regardless of the smoothing method used. That the amount of smoothing has an effect on the number of extracted synergies is not surprising, but provides another obstacle in interpreting the results in a meaningful physiological manner.

The number of EMG synergies we extracted was slightly higher than published numbers in the literature ($3-4$ synergies), presumably due to the richer set of EMG activations we collected. Nevertheless, our results support previous studies reporting that multi-muscle EMG collected during grasping movements can be represented using a small number of muscle synergies. In Chapter 4, we look for evidence of neural correlates to the muscles synergies we extracted.

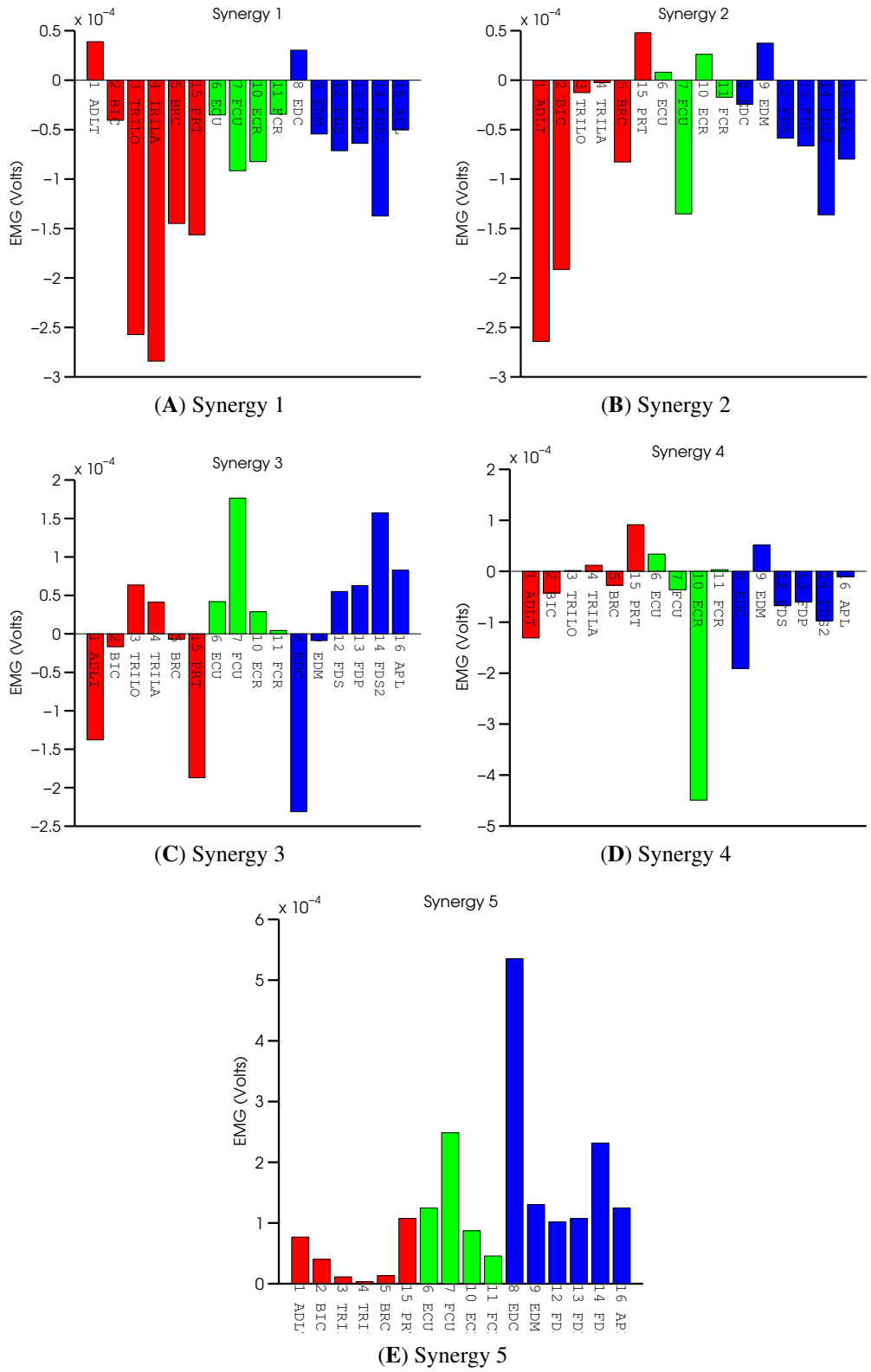

Figure 3.64: **EMG synergies computed using ICA: Monkey E:** EMG was low-pass filtered with a $20Hz$ FIR filter prior to computing the synergies. Arm muscles are colored red, wrist muscles are colored green, and finger muscles are colored blue.

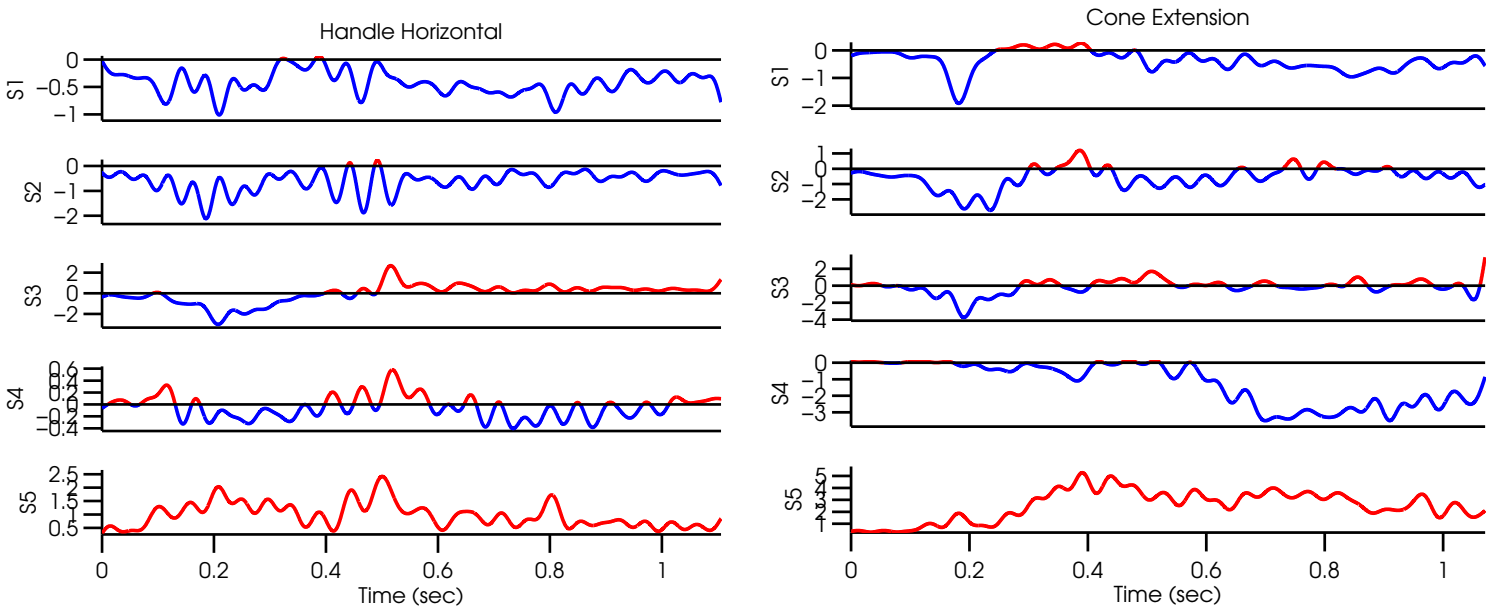

(**A**) Handle Horizontal

(**B**) Cone Extension

Figure 3.65: **LPF EMG synergy activation coefficients computed using ICA: Monkey E:** EMG was low-pass filtered with a 20Hz FIR filter prior to computing the synergies. Negative values are blue, positive values are red.

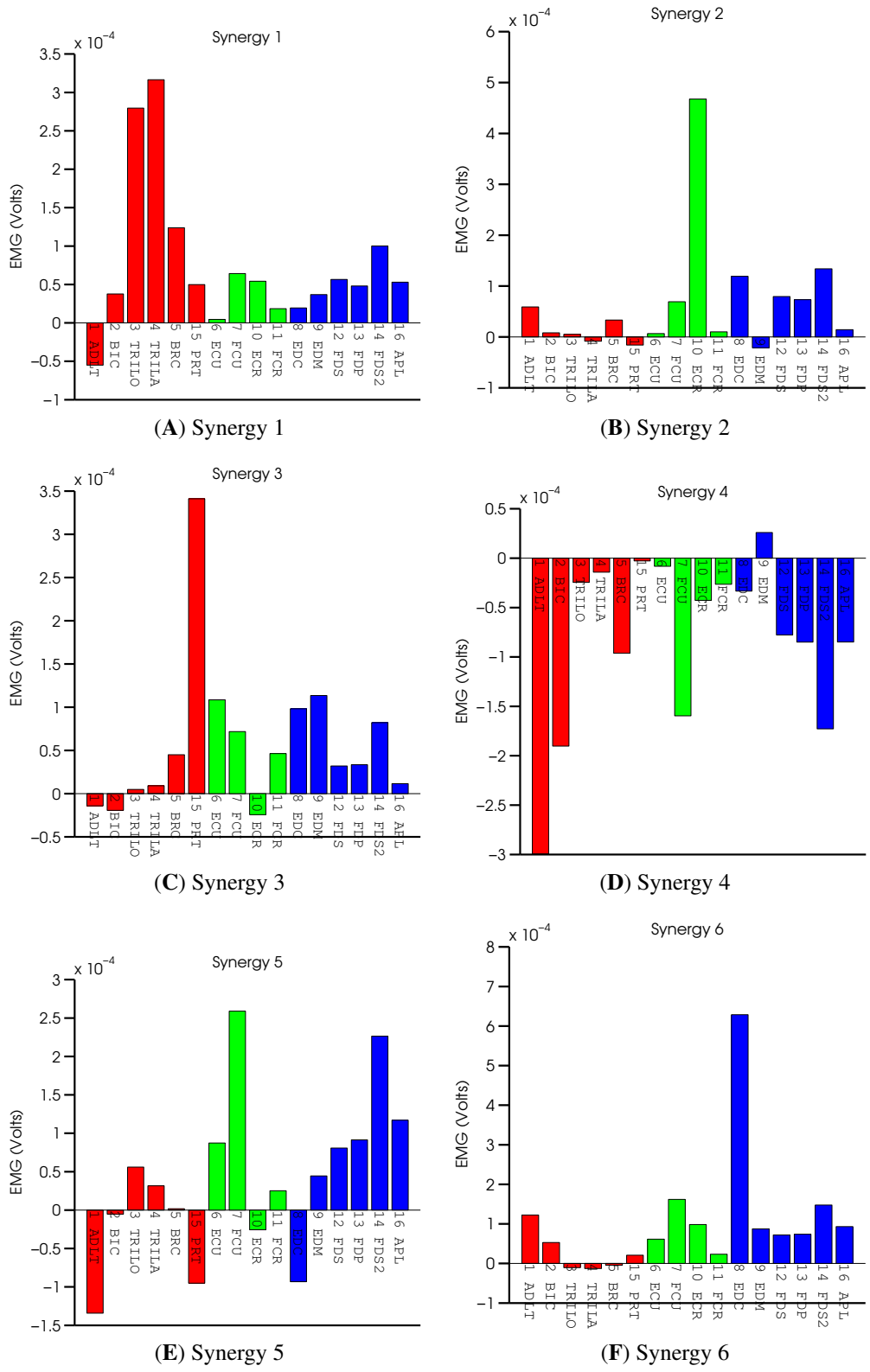

(**A**) Synergy 1

(**B**) Synergy 2

(**C**) Synergy 3

(**D**) Synergy 4

(**E**) Synergy 5

(**F**) Synergy 6

Figure 3.66: **EMG synergies computed using ICA: Monkey E:** EMG was spline-smoothed prior to computing the synergies. Arm muscles are colored red, wrist muscles are colored green, and finger muscles are colored blue.

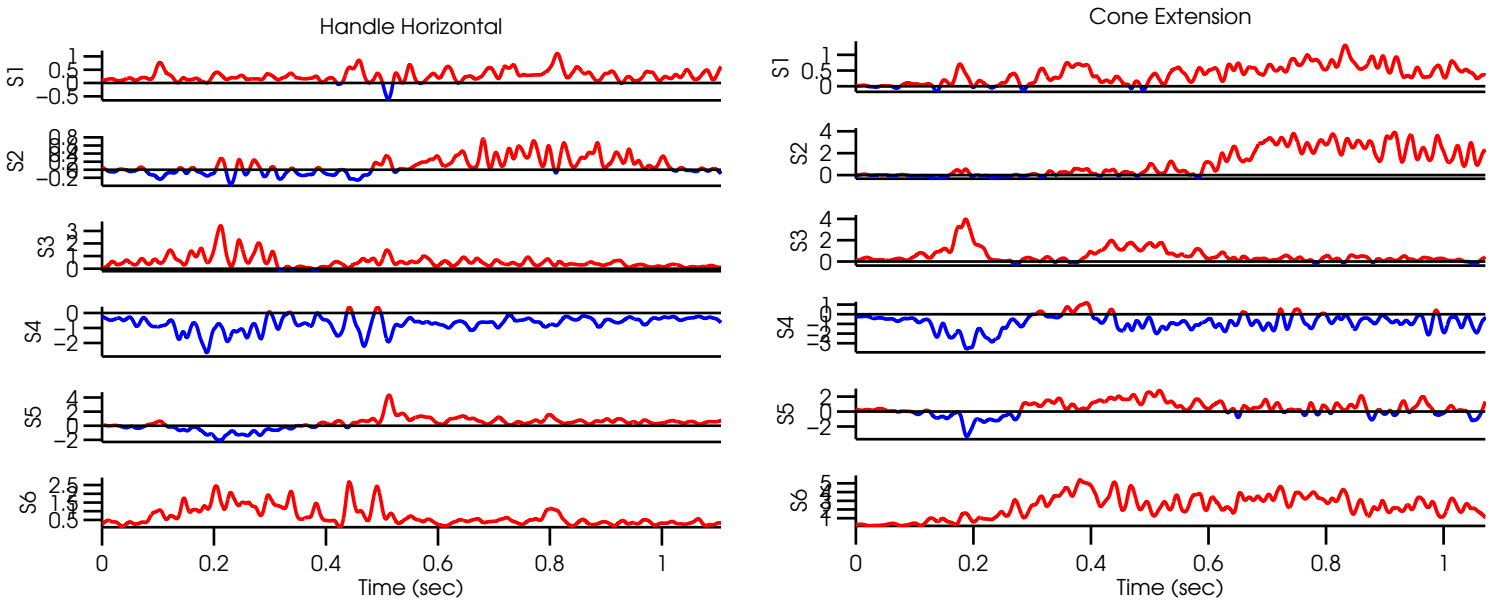

(**A**) Handle Horizontal

(**B**) Cone Extension

Figure 3.67: **EMG synergy activation coefficients computed using ICA: Monkey E:** EMG was spline-smoothed prior to computing the synergies. Negative values are blue, positive values are red.

3.7 KINEMATIC SYNERGIES

We have examined the pairwise correlations between JAs across attitudes in Section 3.5, and found that most correlations were attitude dependent, with the exception of the PIP-DIP JAs. In this section, we explore multivariate relationships between JAs using PCA and ICA (presented in Section 3.6).

PCA is usually assumed to capture the important correlation features in the JA data, since it finds orthogonal rotations in directions which maximize the amount of variance explained, and digit JAs usually correlate to some degree during grasping movements. Principal components (PCs) are sorted according to the variance explained by each, in descending order, so the first PCs account for more variance and are assumed to represent correlated movements of the digits, whereas the higher order PCs are assumed to represent fine movements, including individual finger movements.

We first extracted kinematic synergies using JA data from an entire session, including all attitudes. Figure 3.68 shows that 5 PCs were required to account for 90% of the variance in the JA data. Figure 3.69 shows the PC coefficients for the first 5 PCs. While the first PC's coefficients represent simultaneous flexion of the MCP, PIP and DIP joints, or a power grasp, interpreting the other PCs in a meaningful way is hard. Figure 3.70 shows the PCs, which are the JA data projected unto the dimensions defined by the PC coefficients, for two trials. Most of the changes in the PCs occur around the preshape epoch, as expected.

We also extracted kinematic synergies using ICA, but selected the number of ICs based on the PCA results. Figure 3.71 shows 5 synergies extracted using ICA. Only synergy 2 (Figure 3.71**B**) resembled PC 1 (Figure 3.69**A**) and the rest of the ICA synergies did not match the PCA synergies. The ICA synergy activation coefficients for two trials are shown in Figure 3.72, all different from the PC scores shown in Figure 3.70. This demonstrates potential problems of using dimensionality reduction techniques to compute meaningful kinematic synergies. PCA looks for orthogonal rotations which result in uncorrelated projections of the JA data, while ICA looks for orthogonal rotations which result in uncorrelated projections that are maximally non-Gaussian and therefore assumed to be independent. The two might differ, depending on the nature of the JA data; and it is hard to infer either of them in a meaningful physiological way.

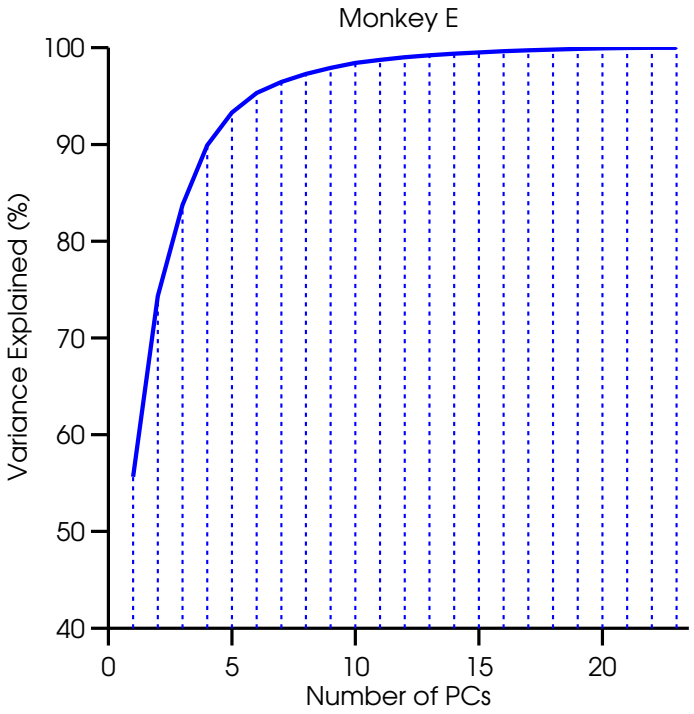

Figure 3.68: The amount of explained variance in the JA data, as a function of number of PCs. 5 PCs are required to account for 90% of the variance.

The number of kinematic synergies we extracted corresponded to those in the literature for similar tasks. However, most of the studies in the literature extracted kinematic synergies using PCA, and did not compare them to synergies extracted using other dimensionality-reduction methods. We have shown that

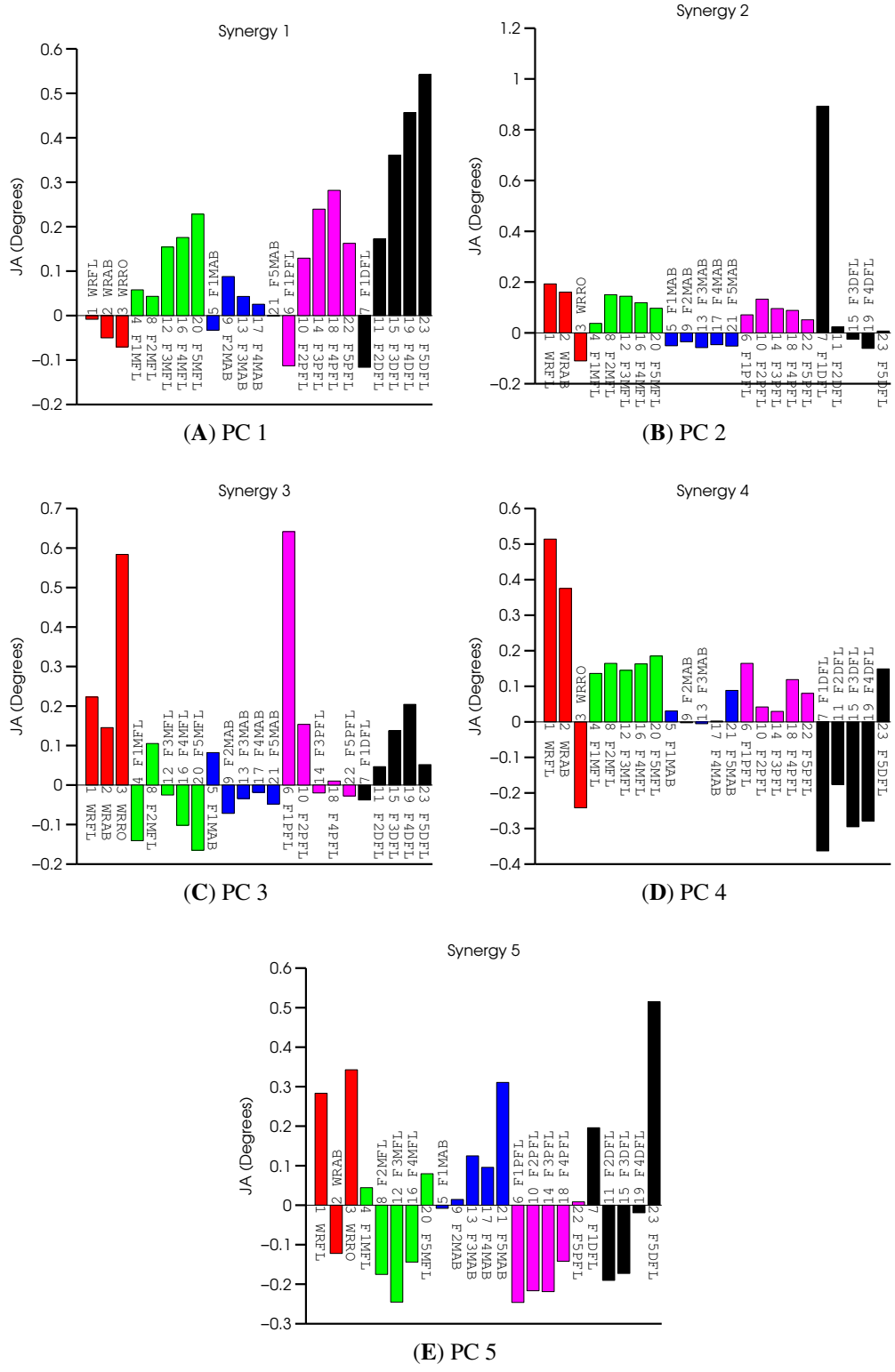

(**A**) PC 1

(**B**) PC 2

(**C**) PC 3

(**D**) PC 4

(**E**) PC 5

Figure 3.69: **Kinematic synergies computed using PCA: Monkey E:** JAs are grouped by anatomical joints: wrist, MCP flexion, MCP abduction, PIP flexion and DIP flexion.

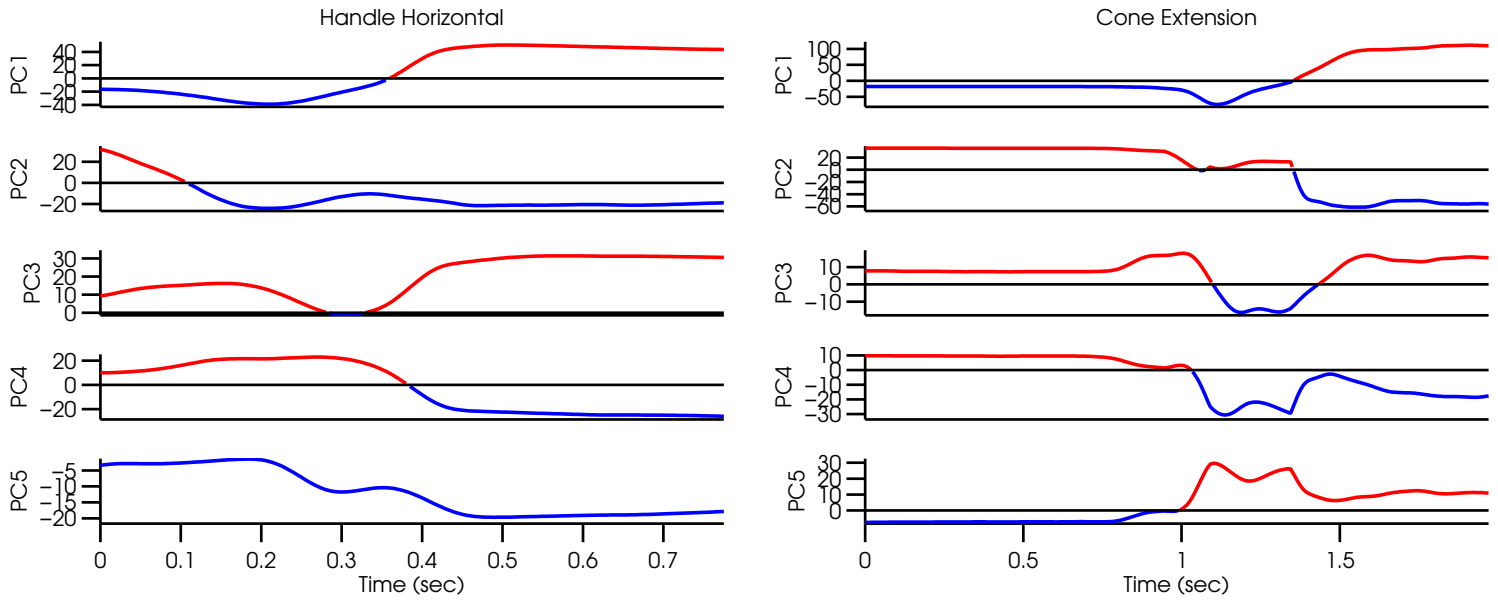

(**A**) Handle Horizontal

(**B**) Cone Extension

Figure 3.70: **Principal components computed from JA data: Monkey E:** The projected JA data to each one of the first 5 PCs. Negative values are blue, positive values are red.

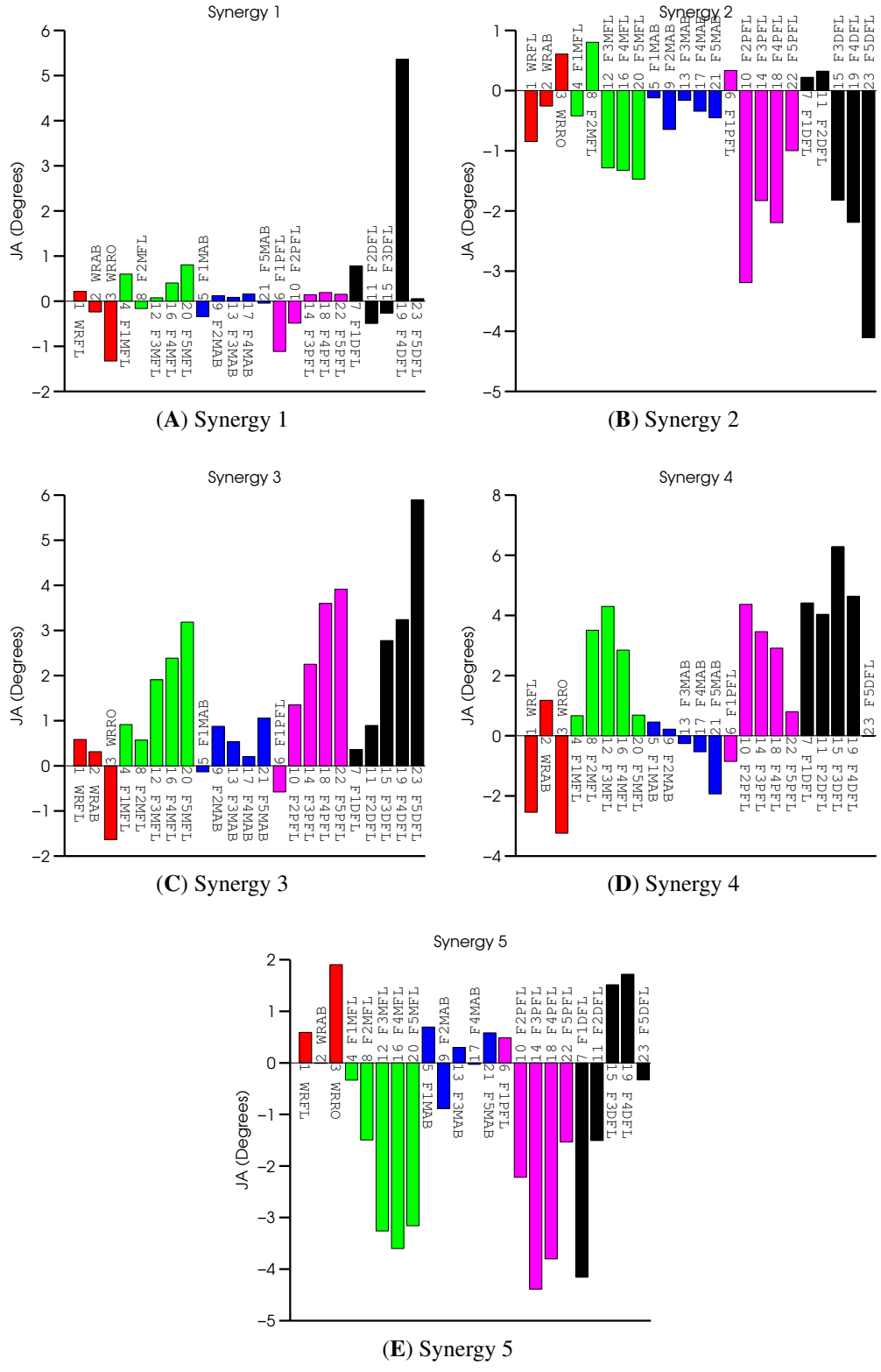

(**A**) Synergy 1

(**B**) Synergy 2

(**C**) Synergy 3

(**D**) Synergy 4

(**E**) Synergy 5

Figure 3.71: **Kinematic synergies computed using ICA: Monkey E:** JAs are grouped by anatomical joints: wrist, MCP flexion, MCP abduction, PIP flexion and DIP flexion.

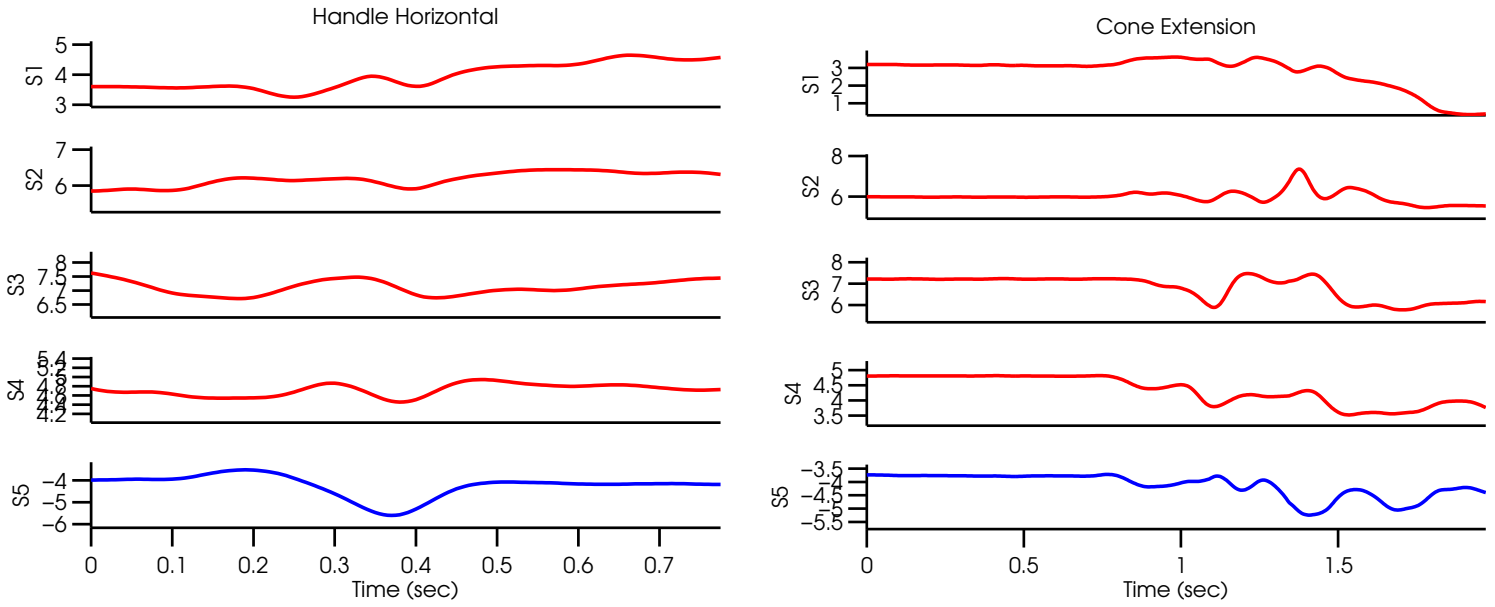

(**A**) Handle Horizontal

(**B**) Cone Extension

Figure 3.72: **Independent components computed from JA data: Monkey E:** JA data separated to independent components. Negative values are blue, positive values are red.

4.0 MOTOR-CORTICAL TUNING TO MUSCLES AND KINEMATICS

4.1 NEURONAL CORRESPONDENCE TO TASK PARAMETERS

Figure 4.1 shows a penetration map summarizing all the locations where neural activity was recorded from monkey E's right hemisphere. We estimated that the majority of neurons were recorded from the caudal bank of the pre-central gyrus. Only units that were modulated during at least one task epoch (reach, static grasp) or the retrieval epoch were studied. Figures 4.2 and 4.3 show box-plots with the mean, median and extremum firing rates for neurons collected from each monkey. All available trials, for every neuron, were used to calculate these values. Most neurons modulated their activity within $\pm 20 - 30 Hz$ around the mean firing rate. Neurons recorded from monkey E had higher mean firing rates, compared to monkey B.

Although an effort was made to record from areas of the motor cortex more likely to be involved with digit manipulation, the fact that somatotopic organization in the motor-cortex is coarse, and combined with the need to record from areas separated by at least a few mm on subsequent recording day, to minimize brain damage, resulted in a very heterogeneous population of neuronal reponses. Some neurons were mainly active during the reach epoch, or both the reach and retrieval epochs. A raster plot for a "reach" neuron is shown in Figure 4.4. The neuron increased its firing rate after the beginning of MoveA (indicated by blue horizontal lines around $-800 ms$), and decreased its firing rate at the beginning of the static grasp phase (indicated at time zero). The neuron increased its firing rate again after the trials were over and the monkey moved its hand back to the pad (blue horizontal lines around $1000 ms$). The firing rate of this neuron remained high across different attitudes.

Other neurons, such as the one in Figure 4.5, were active during both the reach and static grasp epochs. However, this neuron did not maintain a high firing rate for all attitudes: for example, it

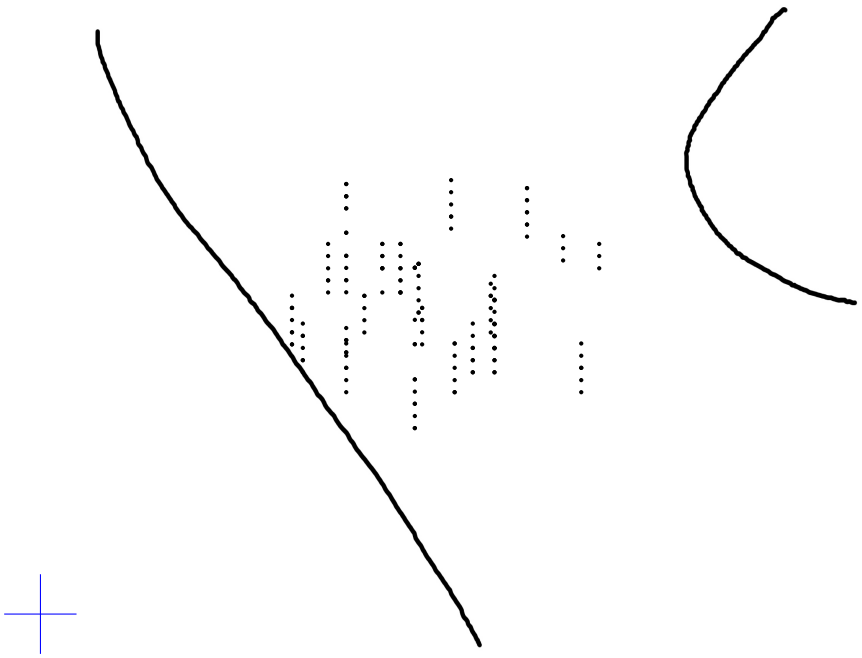

Figure 4.1: **Penetration map: monkey E, right hemisphere:** Landmarks, as identified from photos of the recording chamber on the day of surgery, are overlaid on the map of penetration sites. The vertical and horizontal lines at the bottom left are 1*mm* long.

hardly spiked for attitudes $6-12$, corresponding to the presentations of the small handle object. Figures 4.6 and 4.7 show raster plots for the same neuron, with trials sorted by object or target. It is clear that this neuron is selective for objects and not targets: it did not fire when the monkey reached and grasped objects 2 (small handle) and 5 (small bar), but fired for all other objects.

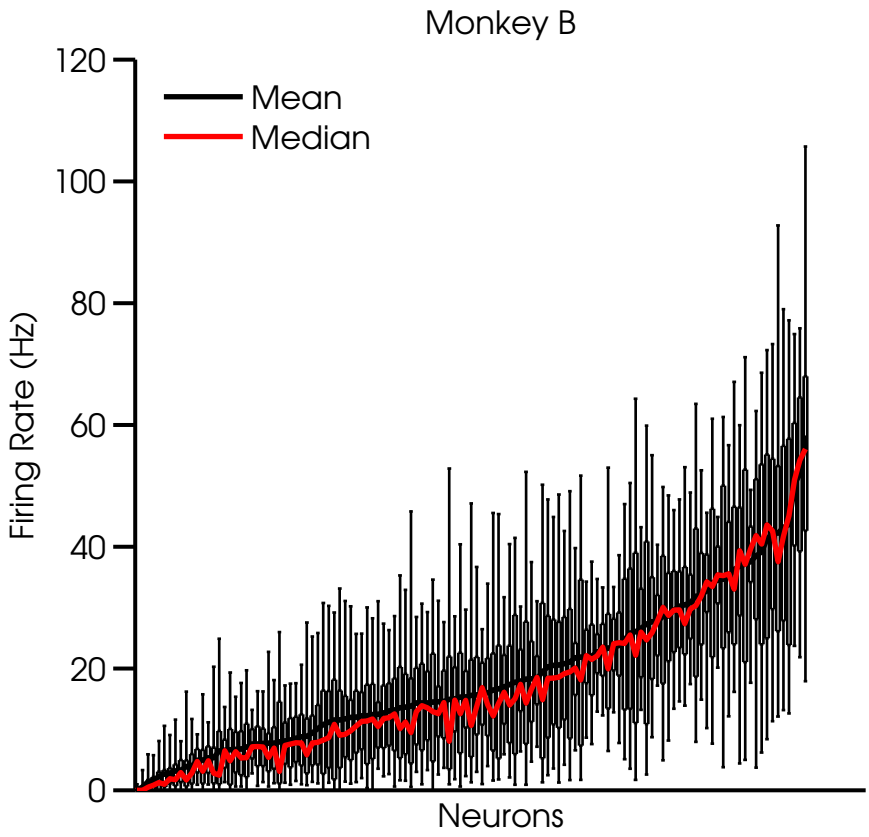

Figure 4.2: **Monkey B Neuronal firing rate:** Box-plot showing the mean, median and extremum firing rates for 125 neurons. Neurons were sorted by ascending mean firing rate.

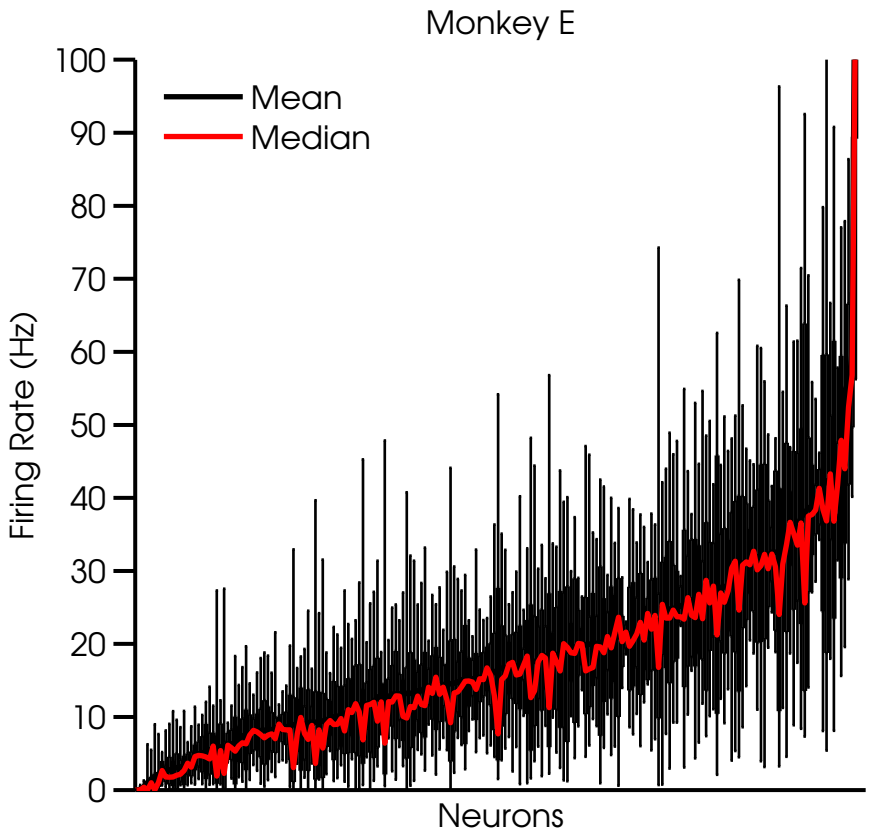

Figure 4.3: **Monkey E Neuronal firing rate:** Box-plot showing the mean, median and extremum firing rates for 200 neurons. Neurons were sorted by ascending mean firing rate.

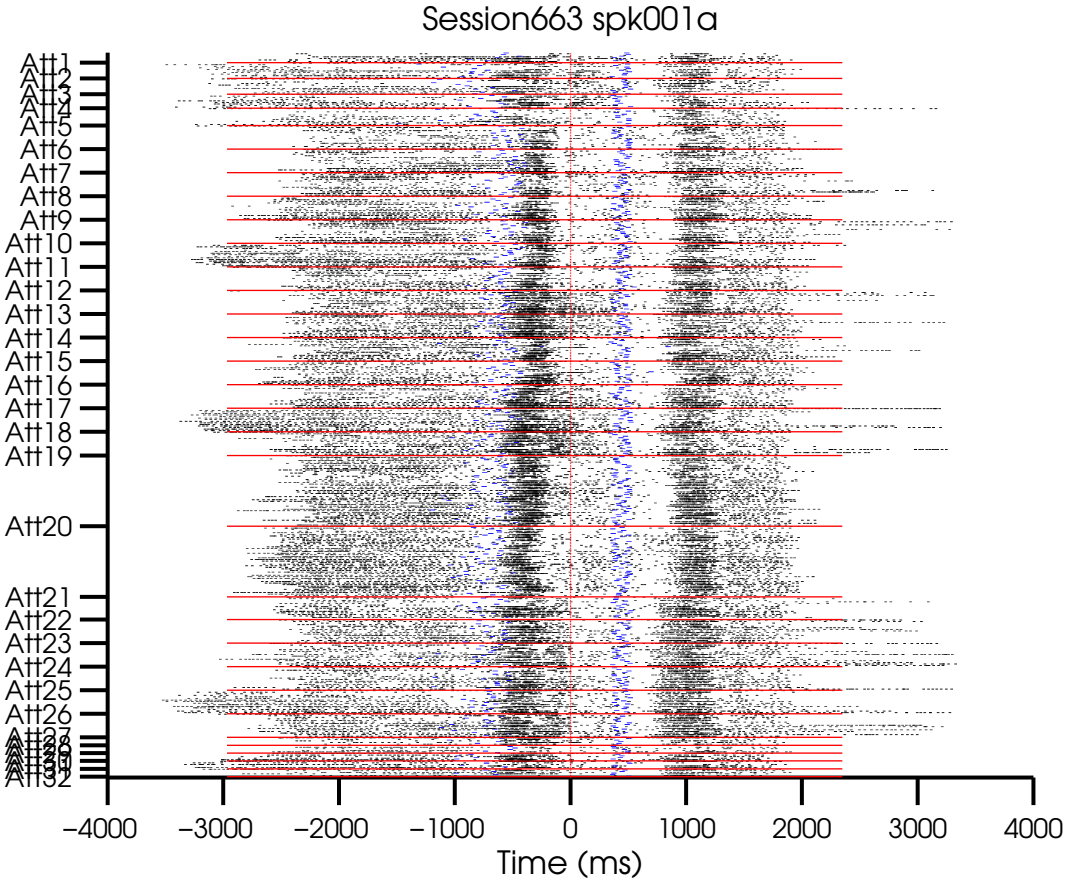

Figure 4.4: **Raster plot for session 663, spk002a:** Reach and retrieval modulated neuron. Every row represents one trial. Trials were sorted by attitudes: all trials belonging to the same attitude were grouped together and separated by red horizontal lines. All trials were aligned by the beginning of the static grasp epoch, indicated by time zero. The beginning of the MoveA and the end of the static grasp epochs, for every trial, are indicated by blue vertical lines. Spikes are colored black.

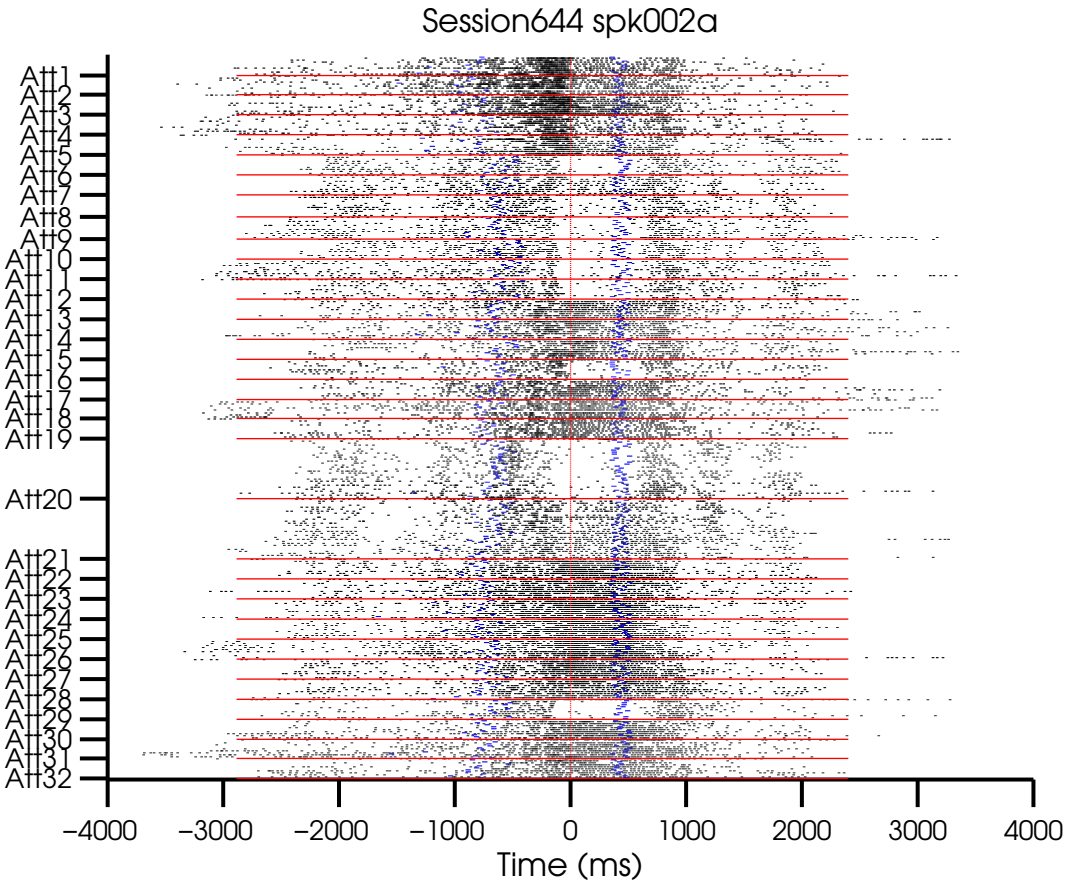

Figure 4.5: **Raster plot for session 644, spk002a:** Reach and grasp modulated neuron, selective for certain attitudes. Every row represents one trial. Trials were sorted by attitudes: all trials belonging to the same attitude were grouped together and separated by red horizontal lines. All trials were aligned by the beginning of the static grasp epoch, indicated by time zero. The beginning of the MoveA and the end of the static grasp epochs, for every trial, are indicated by blue vertical lines. Spikes are colored black.

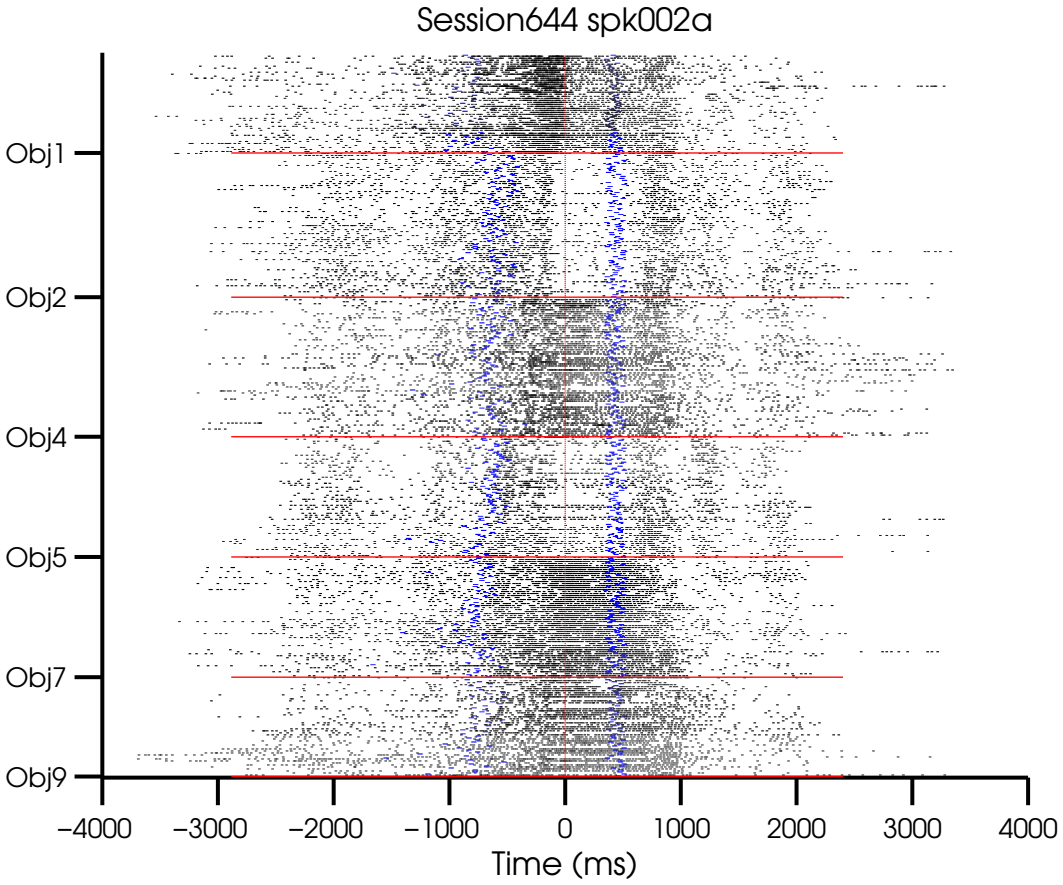

Figure 4.6: **Raster plot for session 644, spk002a:** Reach and grasp modulated neuron, selective for certain attitudes. The plot contains the same data as Figure 4.5, with trials sorted by objects. The attitude selectivity is due to object selectivity. Every row represents one trial. Trials were sorted by objects: all trials belonging to the same object were grouped together and separated by red horizontal lines. All trials were aligned by the beginning of the static grasp epoch, indicated by time zero. The beginning of the MoveA and the end of the static grasp epochs, for every trial, are indicated by blue vertical lines. Spikes are colored black.

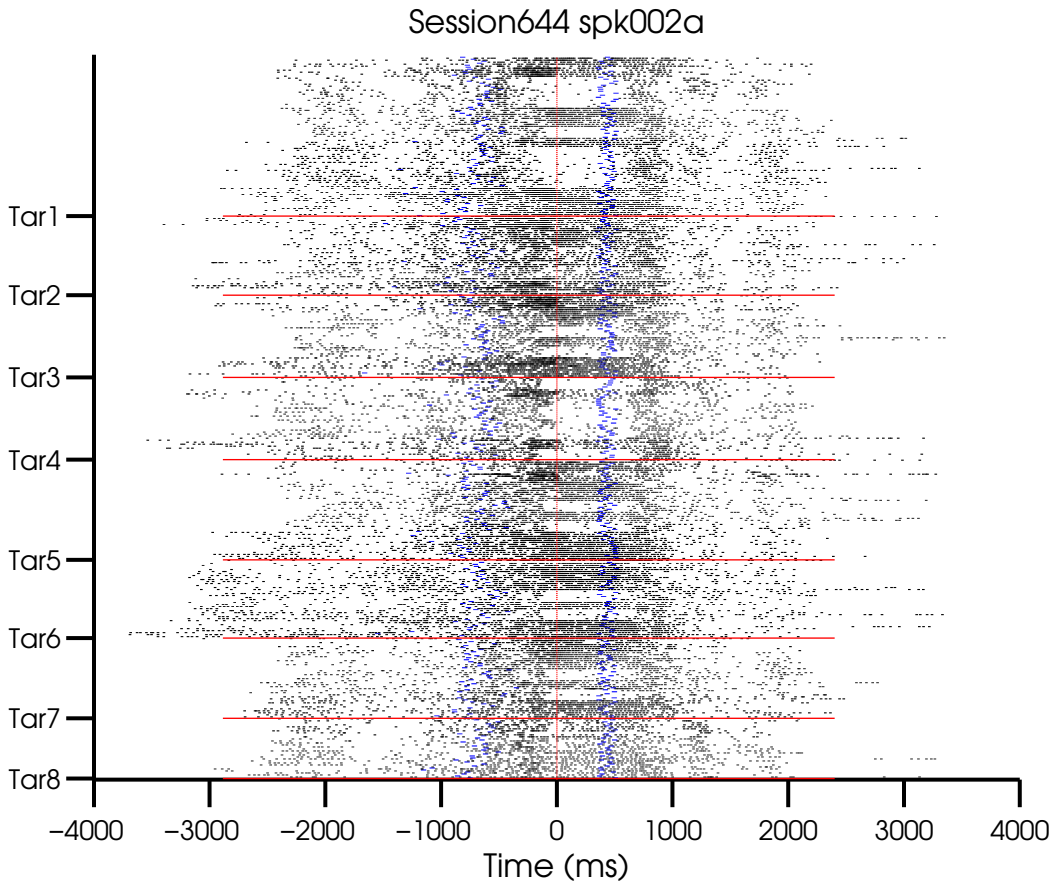

Figure 4.7: **Raster plot for session 644, spk002a:** Reach and grasp modulated neuron, selective for certain attitudes. The plot contains the same data as Figure 4.5, with trials sorted by targets. The attitude selectivity does not seem to relate to target selectivity. Every row represents one trial. Trials were sorted by targets: all trials belonging to the same object were grouped together and separated by red horizontal lines. All trials were aligned by the beginning of the static grasp epoch, indicated by time zero. The beginning of the MoveA and the end of the static grasp epochs, for every trial, are indicated by blue vertical lines. Spikes are colored black.

To classify neurons by their activity related to reach and grasp, we computed, for every trial, the mean fractional firing rate during 3 epochs (see Section 2.2 for details about fractional firing rates): **(1)** Inter-trial (all data prior to the beginning of MoveA), **(2)** Reach (beginning of MoveA to the beginning of the static grasp), **(3)** Static grasp,

We used multiple comparisons analysis of variance (ANOVA, Tukey's honestly significant difference criterion for every pair, $\alpha = 5\%$) to determine which neurons fired significantly more (or less) during the reach or grasp epochs relative to the inter-trial epoch; and out of those, which neurons fired more during the reach or grasp epochs. The procedure compared the mean firing rates during the reach epoch to the inter-trial epoch; the mean firing rates during the grasp epoch to the inter-trial epoch; and the mean firing rates between the reach and grasp epochs. Tables 13 and 14 summarize the results. Only neurons which fired at a significantly different rate during the reach or grasp epochs, compared to the inter-trial epoch, were considered as modulated. The majority of modulated neurons, for both monkeys, fired during both the reach and grasp epochs. For monkey B, neurons active during both reach and grasp divided to 3 similar sized groups: the first fired more during the reach compared to the grasp epoch (41%), the second fired more during the grasp compared to the reach epoch (25%), and the third fired at similar rates for both the reach and grasp epochs (34%). For monkey E, the majority of neurons active during both reach and grasp, fired more during the reach (66%) compared to the grasp epoch (20%).

We also classified neurons according to their object and target selectivity, by finding neurons whose firing rates were better differentiated when grouping the trials by objects, rather than by targets. We first computed every neuron's mean firing rate during an entire trial, for all trials. We then formed two test datasets: one where mean trial firing rates were grouped by objects and another where mean trial firing rates were grouped by targets. For each dataset, we used a multiple comparisons algorithm, which returned a list of all possible pairs, specifying for each pair whether the neuron's mean firing rate was significantly different between the two objects or targets. Neurons with a larger percentage of significant pairs in the object groups relative to the target groups, were classified as object selective; and neurons with a larger percentage of significant pairs in the target groups, were classified as target selective. For both monkeys, 90% of the neurons ($112/125$, monkey B; $179/200$, monkey E) showed object selectivity. This means that

Table 13: **Neural tuning to task epochs: Monkey B:** Multiple comparisons ANOVA was used to classify neurons using mean firing rates

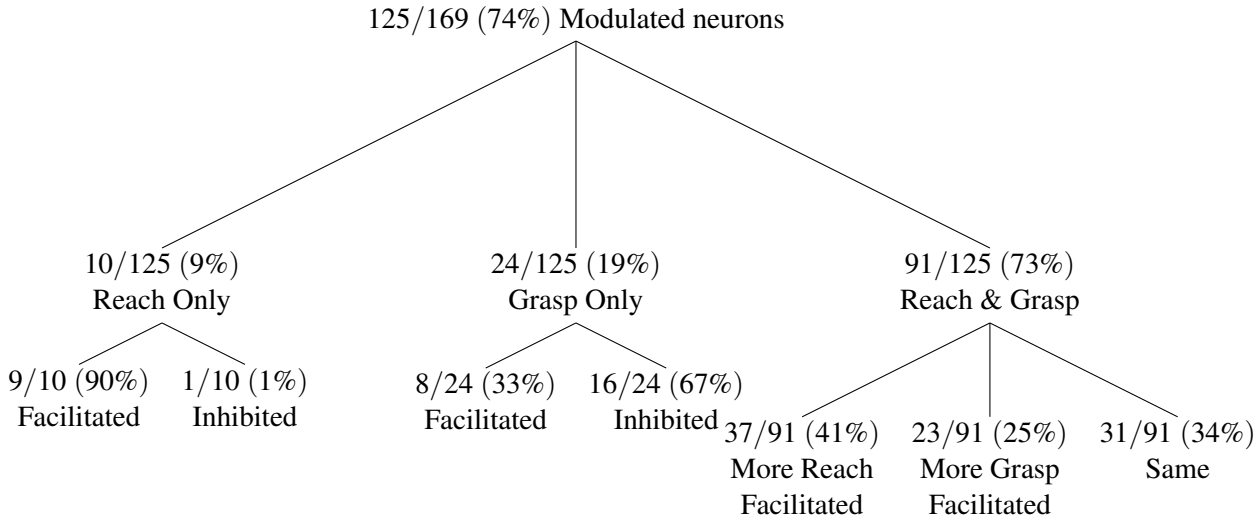

Table 14: **Neural tuning to task epochs: Monkey E:** Multiple comparisons ANOVA was used to classify neurons using mean firing rates

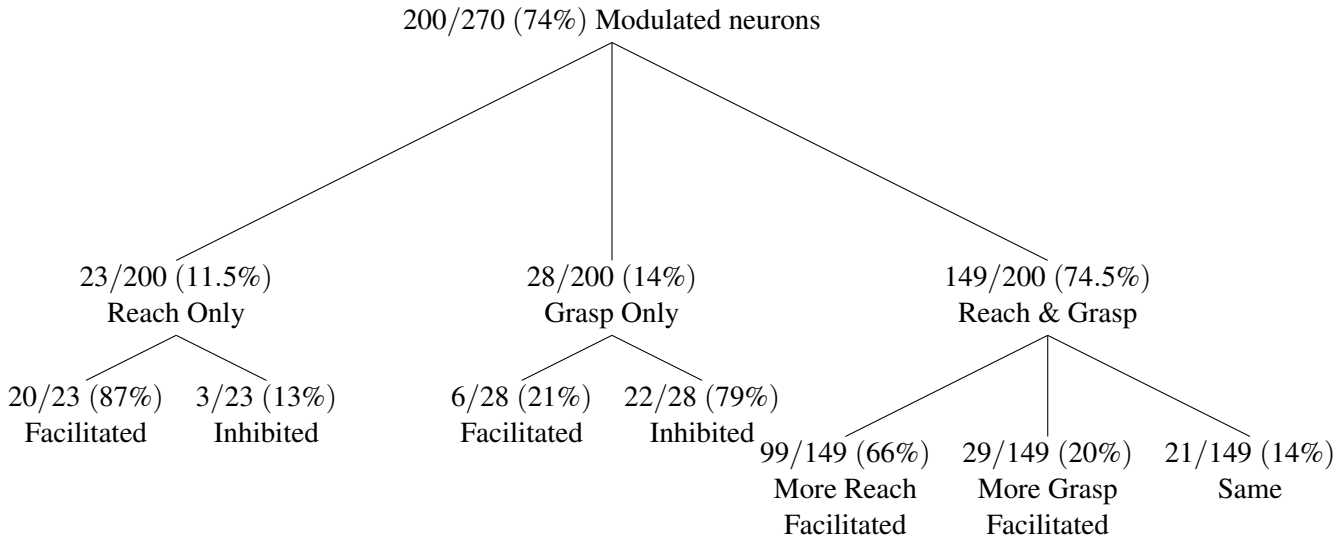

most neurons changed their firing rate based on the object being grasped, rather than its location and orientation. These results are consistent with previous studies [66, 27].

4.2 NEURAL TUNING TO EMG

In Section 1.4, we described the study by Townsend et al. [64], where individual neural firing rates were predicted from the EMG activity of 9 muscles during a precision grip task with a compliant load. They concluded that for their data, there was no difference between a non-linear model and a linear model, when predicting firing rates from EMG. They reported that firing rates were predicted equally well by the finger JA and JA velocity; and that the non-linear model showed improvement over the linear one, for predicting firing rates from the kinematic data. They also found that including spike history in the models, did not improve firing rate predictions.

In this section, we predict individual neuronal firing rates from the EMG activity of 16 muscles; and in the next section we predict firing rates from the joint angle values and velocities of 23 joints. We could then compare our results to those of Townsend et al. [64].

We used the following linear model to relate neural firing rate to EMG:

$$\lambda_{50} = b_0 + \sum_{m=1}^{16} b_m EMG_m \tag{4.1}$$

where λ_{50} is the fractional firing rate for an individual neuron, computed using adjusted $50ms$ bins (see Section 2.2 for details); EMG_m is the rectified EMG for muscle m, averaged in the same adjusted $50ms$ bins as the neural data, but lagged by one bin width ($50ms$ on average). We did not calculate an optimal lag for every neuron and muscle, since previous studies have shown minor improvement in predictive power, and in addition, the results presented here are unlikely to change when using optimal lags. We also chose not to incorporate spike history in both models, since we are not interested in obtaining the best possible fit to the firing rates, but rather in comparing fits using different covariates.

For every neuron, we fitted the model using data from all attitudes, over 4 different epochs: (1) *All Trial Data*, (2) *Reach Start* to *Reach End*, (3) *Reach End* to *Grasp Start*, (4) *Grasp Start* to *Grasp End*. As in Section 3.2, *Reach Start* was the time the hand speed reached $(5\% \times MaxSpeed)$ before the maximal speed, *Reach End* was the time the hand speed reached $(5\% \times MaxSpeed)$ after the maximal speed, *Grasp Start* was the time the monkey started pressing the object, *Grasp End* was *HoldB* milliseconds after *Grasp Start* (this value was determined from the recorded real-time value for HoldB for every trial). Figure 3.39 shows an example of these trial epochs.

Figure 4.8 shows results from 258 neurons (monkey E), in the form of regression R^2 histograms, from all neurons, for all 4 task epochs. The firing rate fits of very few neurons showed R^2 values higher than 0.5. The median R^2 values are shown in the figure. We investigated whether neurons recorded on the same sessions, or at close spatial locations, tended to show similar R^2 values; and have found no significant relationships. Neurons with high R^2 values were spread across recording sessions and cortical spatial locations. We tested whether neurons with higher firing rates tended to have better linear relationship to EMG, by plotting the R^2 values from Figure 4.8 against the mean normalized firing rate for all neurons; shown in Figure 4.9. It can be seen that the linear relationship between the mean firing rate and the regression R^2 is weak.

We also tested whether firing rate predictions from multiple EMGs are better when no grasp is involved. For that, we only used data from the button attitudes (see Table 1), where the monkey reached to press a button, and minimal finger flexion was involved (the monkeys tended to extend the index or middle finger to press the button, with minimal movement of the other fingers). The button attitudes are therefore similar to a classic reaching task. We repeated the regression analysis, using the model in Equation 4.1 and only data from the button attitudes. Only 212 neurons had a satisfactory number of trials after combining the button attitudes, and their regression R^2 values are shown in Figure 4.10. These histograms are similar to the ones in Figure 4.8, suggesting that even when the task consists mostly of reaching, firing rates are not predicted well by multiple EMGs. A more direct comparison is shown in Figure 4.11. An ANOVA test showed that the differences in R^2 values between using all VS button-only attitudes, are statistically significant for all epochs, especially for the preshape epoch (p-values were: All Data 0.03, Reach 0.006, Preshape $4.19e^{-4}$, Grasp 0.03). However, these differences might arise from an overfitted model when using only one task attitude, as observed in some studies reviewed in Section 1.4.

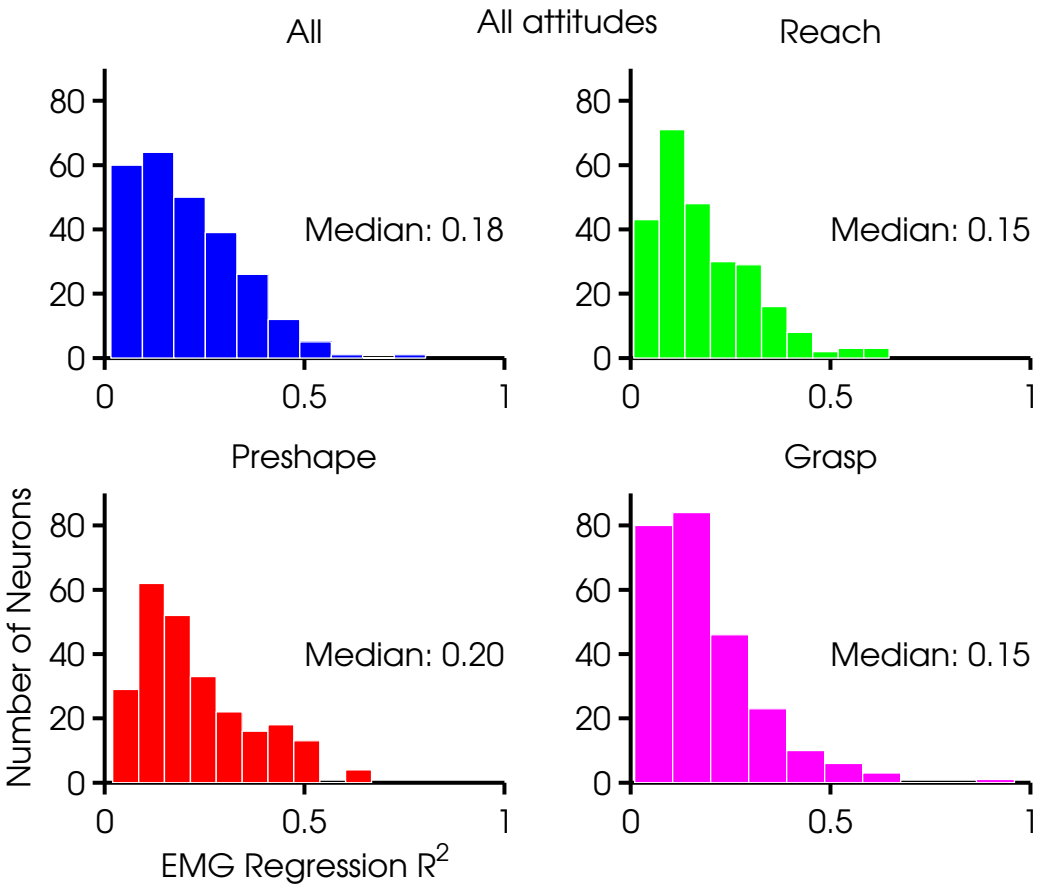

Figure 4.8: **EMG regression R^2 histograms: All attitudes: Monkey E:** Histograms of regression R^2 values for 258 neurons. The regression model in Equation 4.1 was computed using data from all attitudes, over 4 task epochs: (1) *All Trial Data*, (2) *Reach Start* to *Reach End*, (3) *Reach End* to *Grasp Start*, (4) *Grasp Start* to *Grasp End*.

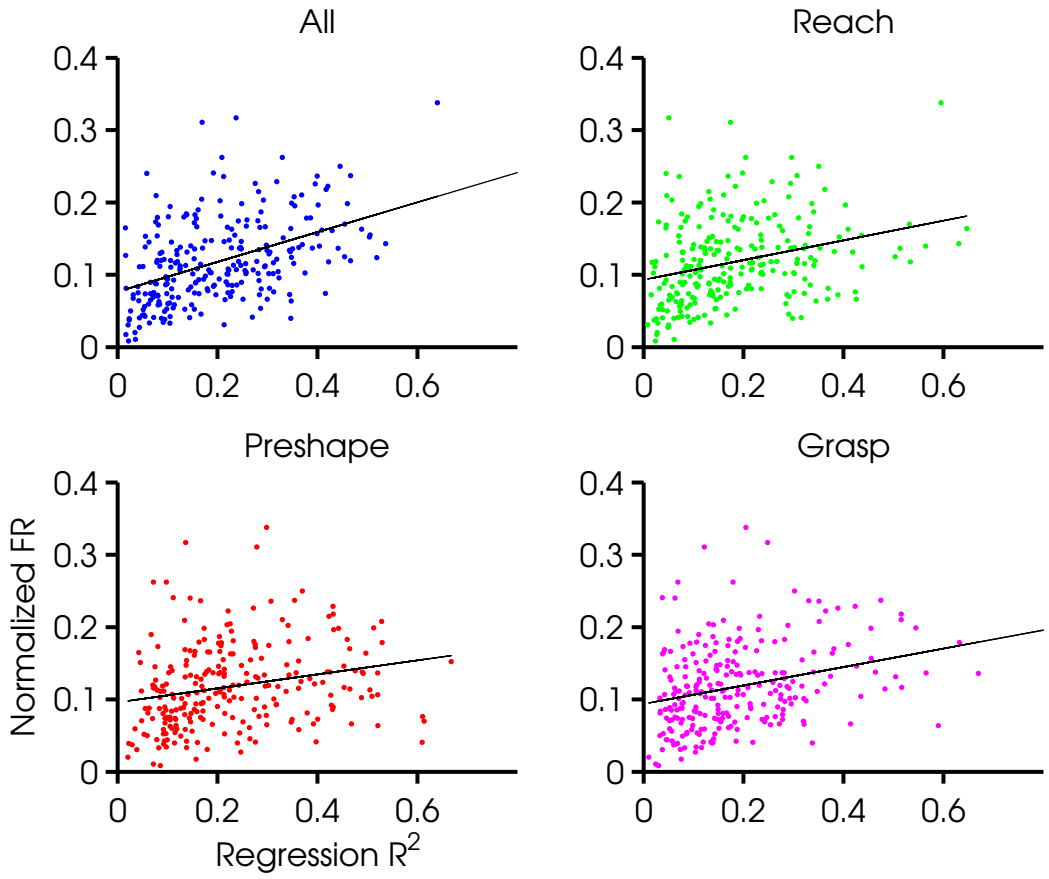

Figure 4.9: **EMG regression R^2 VS normalized firing rate: Monkey E:** Scatter plots of regression R^2 values VS the mean normalized firing rate for all neurons (normalized by the maximal firing rate for the session), for 258 neurons. Data for regression was taken from all attitudes, and histograms of the corresponding R^2 values are shown in Figure 4.8. Linear fits are shown on top, with R^2 values of 0.21, 0.08, 0.05, 0.09 (all significant); suggesting there is no good correspondence between a high firing rate and better linear relationship to muscles. The comparison is shown over 4 task epochs: (1) *All Trial Data*, (2) *Reach Start* to *Reach End*, (3) *Reach End* to *Grasp Start*, (4) *Grasp Start* to *Grasp End*.

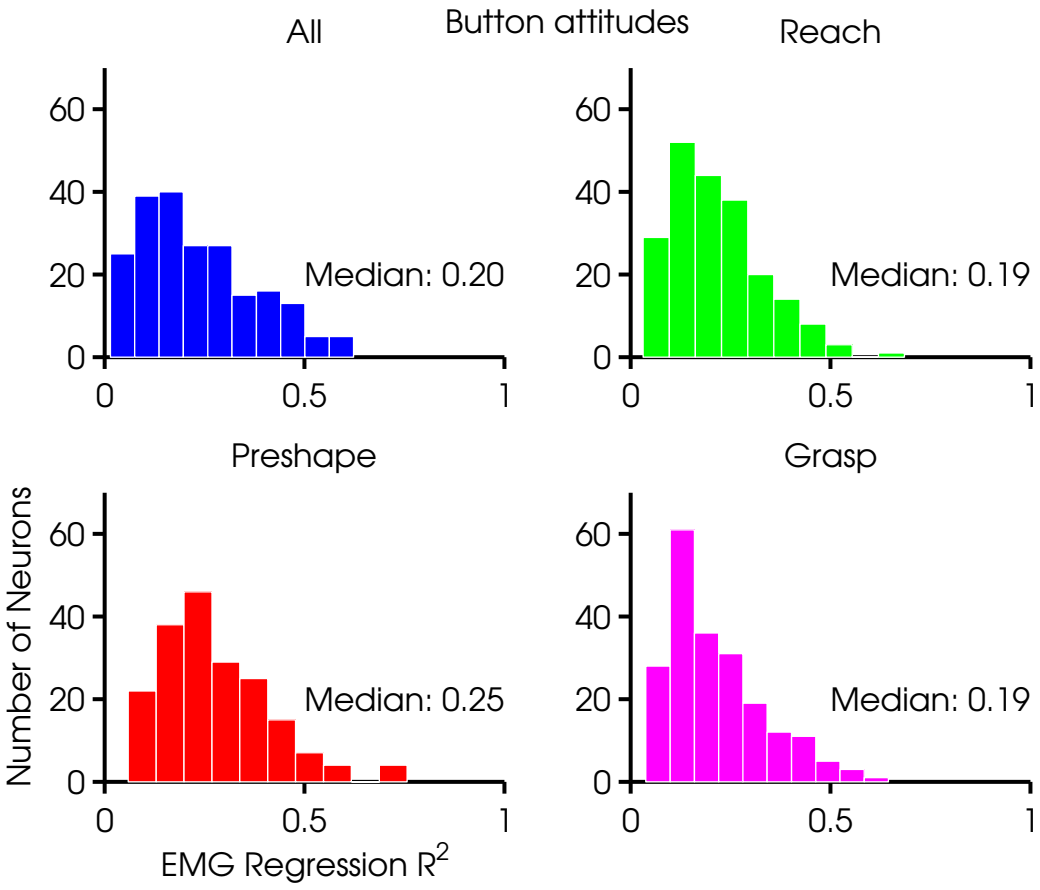

Figure 4.10: **EMG regression R^2 histograms: Button attitudes: Monkey E:** Histograms of regression R^2 values for 212 neurons. The regression model in Equation 4.1 was computed using data from button attitudes, over 4 task epochs: (1) *All Trial Data*, (2) *Reach Start* to *Reach End*, (3) *Reach End* to *Grasp Start*, (4) *Grasp Start* to *Grasp End*.

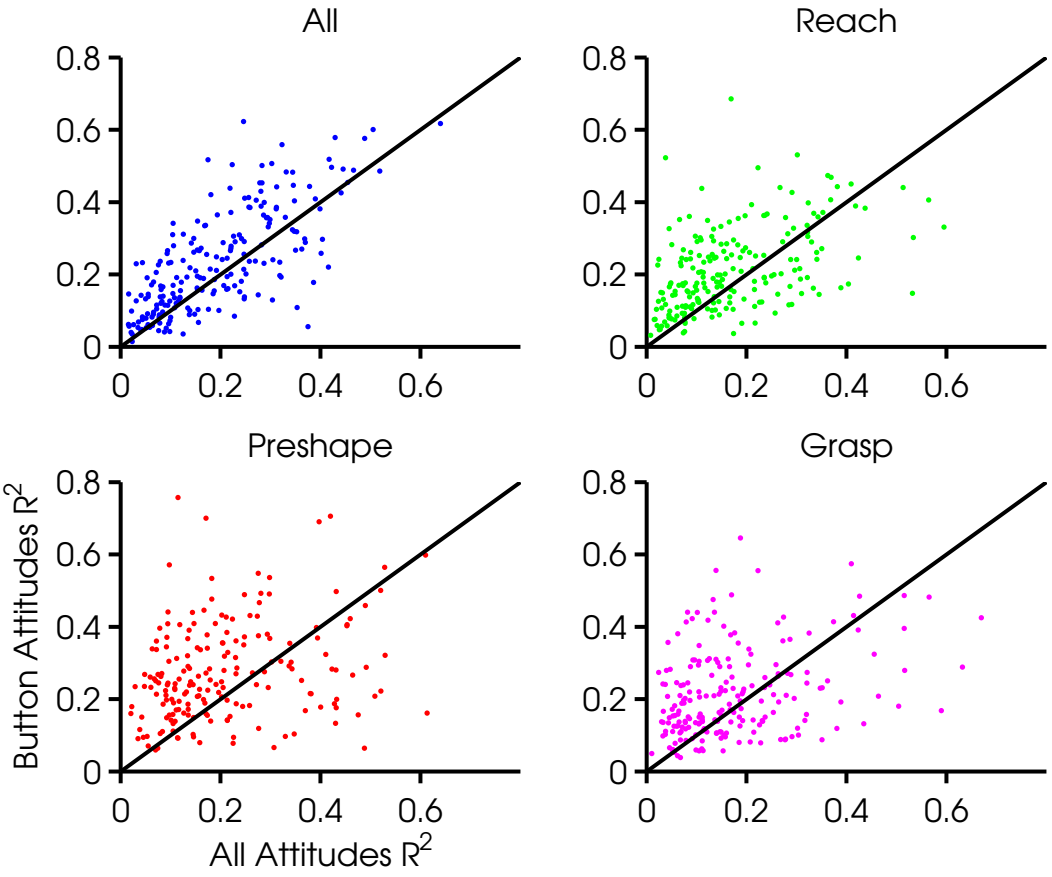

Figure 4.11: **EMG regression R^2 comparison: Monkey E:** Scatter plots of regression R^2 values for 212 neurons, when data from all attitudes was used versus data from button attitudes only. The equality line is superimposed. Histograms of the corresponding R^2 values are shown in Figures 4.8 and 4.10. The comparison is shown over 4 task epochs: (1) *All Trial Data*, (2) *Reach Start* to *Reach End*, (3) *Reach End* to *Grasp Start*, (4) *Grasp Start* to *Grasp End*.

4.3 NEURAL TUNING TO JA

We next predicted individual neuronal firing rates from 23 joint angle values and velocities, using the model:

$$\lambda_{50} = c + \sum_{j=1}^{23} a_j JA_j + \sum_{j=1}^{23} b_j JAV_j \tag{4.2}$$

where λ_{50} is the fractional firing rate for an individual neuron, computed using adjusted $50ms$ bins (see Section 2.2 for details); JA_j and JAV_j are the joint angle value and velocity for joint j, averaged in the same adjusted $50ms$ bins as the neural data, but lagged by two bins ($100ms$ on average).

Figure 4.12 shows the R^2 values for 152 neurons, for the 4 task epochs described in the previous section. Only neurons with complete kinematic data, and at least 10 repetitions per attitude were used in this analysis. Comparing Figure 4.12 to Figure 4.8, we can conclude that firing rates are predicted better by joint angle values and velocities, than EMGs. Figure 4.13 compares the EMG and JA regression R^2 values directly. It is evident that JA R^2 values are higher, and also that neurons with high EMG R^2 values tend to have high JA R^2 values; therefore the neurons do not seem to divide to distinct groups modulated with either kinematics or muscles. These results contrast the ones from Townsend et al. [64], where regression fits to EMG and kinematics were similar. Several reasons could account for this difference: First, the kinematic data used in Townsend et al. [64] was very limited (JA and JA velocity of one finger, not separated to joints), whereas we used a richer description of the hand and wrist. Second, Townsend et al. [64] studied only precision grip, whereas our dataset is much richer. Our results indicate that the neural relationship to kinematics is more stable than the relationship to EMG, when examined over a rich set of reach and grasp behaviors.

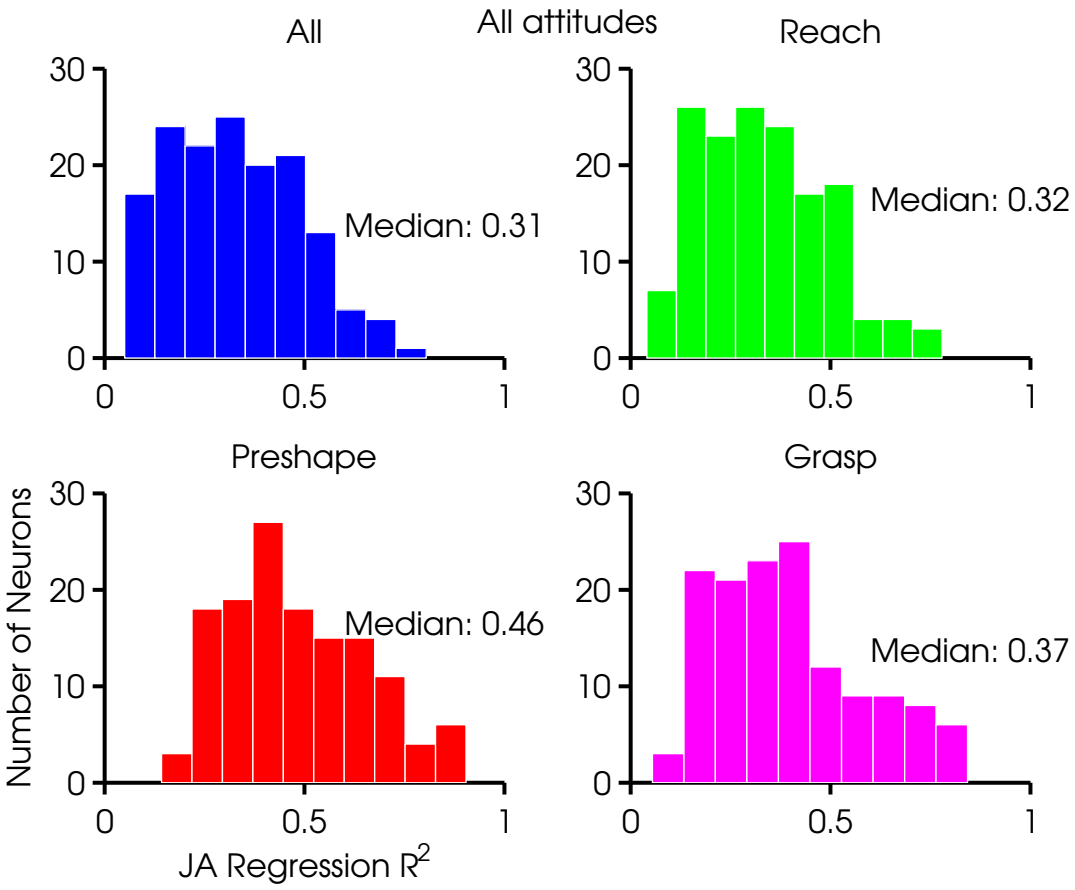

Figure 4.12: **JA regression R^2 histograms: All attitudes: Monkey E:** Histograms of regression R^2 values for 152 neurons. The regression model in Equation 4.2 was computed using data from all attitudes, over 4 task epochs: (1) *All Trial Data*, (2) *Reach Start* to *Reach End*, (3) *Reach End* to *Grasp Start*, (4) *Grasp Start* to *Grasp End*.

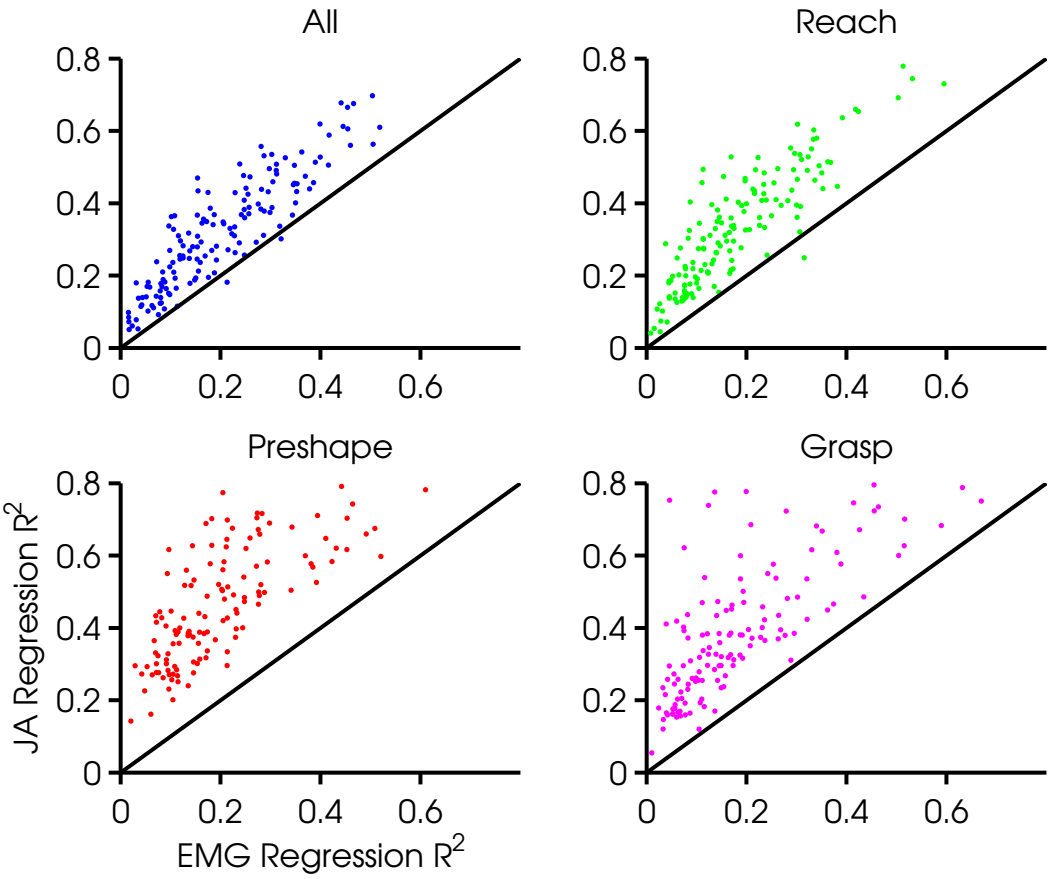

Figure 4.13: **EMG regression R^2 VS JA regression R^2: Monkey E:** Scatter plots of EMG regression R^2 values VS JA regression R^2 for 152 neurons. Data for regression was taken from all attitudes, and histograms of the corresponding R^2 values are shown in Figures 4.8. and 4.12. It is clear that JA R^2 values are higher, and also that neurons with high EMG R^2 values tend to have high JA R^2 values. The comparison is shown over 4 task epochs: (1) *All Trial Data*, (2) *Reach Start* to *Reach End*, (3) *Reach End* to *Grasp Start*, (4) *Grasp Start* to *Grasp End*.

4.4 NEURAL TUNING TO EMG AND JA

In Section 1.4, we have reviewed studies relating the activity of motor cortical neurons to muscles or kinematics, in separate experiments, mostly during simple behavioral tasks (e.g. reaching, one type grasp, single joint movements). We have also listed some more recent studies relating motor-cortical activity to kinematics during reach to grasp movements. Those studies suggested that tuning of individual neurons spanned a continuum of arm, wrist and hand kinematics combinations, represented as extensive temporal combinations of joint angle values and velocities. However, to our knowledge, no published study has examined how motor-cortical activity *simultaneously* relates to both muscles and kinematics during reach-to-grasp movements.

We used the following linear model to relate neural firing rate to both EMG and kinematics:

$$\lambda_{50} = d + \sum_{m=1}^{16} a_m EMG_m + \sum_{j=1}^{23} b_j JA_j + \sum_{j=1}^{23} c_j JAV_j \tag{4.3}$$

where λ_{50} is the fractional firing rate for an individual neuron, computed using adjusted $50ms$ bins (see Section 2.2 for details); EMG_m is the rectified EMG for muscle m, averaged in the same adjusted $50ms$ bins as the neural data, lagged by one bin ($50ms$ on average); JA_j and JAV_j are the joint angle value and velocity for joint j, averaged in the same adjusted $50ms$ bins as the neural data, lagged by two bins ($100ms$ on average).

Figure 4.14 shows the regression R^2 values for 152 neurons. As expected, combining the EMG and JA data improved the firing rate fits compared to the two individual models. Figures 4.15 and 4.16 directly compare the combined model fits (Equation 4.3) to the EMG only model (Equation 4.1) and JA only model (Equation 4.2). Although the difference between the combined model and the JA only model were small, an ANOVA analysis showed that they were still statistically significant. This indicates that the EMG data still contributed some information which was encoded in the firing rates, and not present in the JA data.

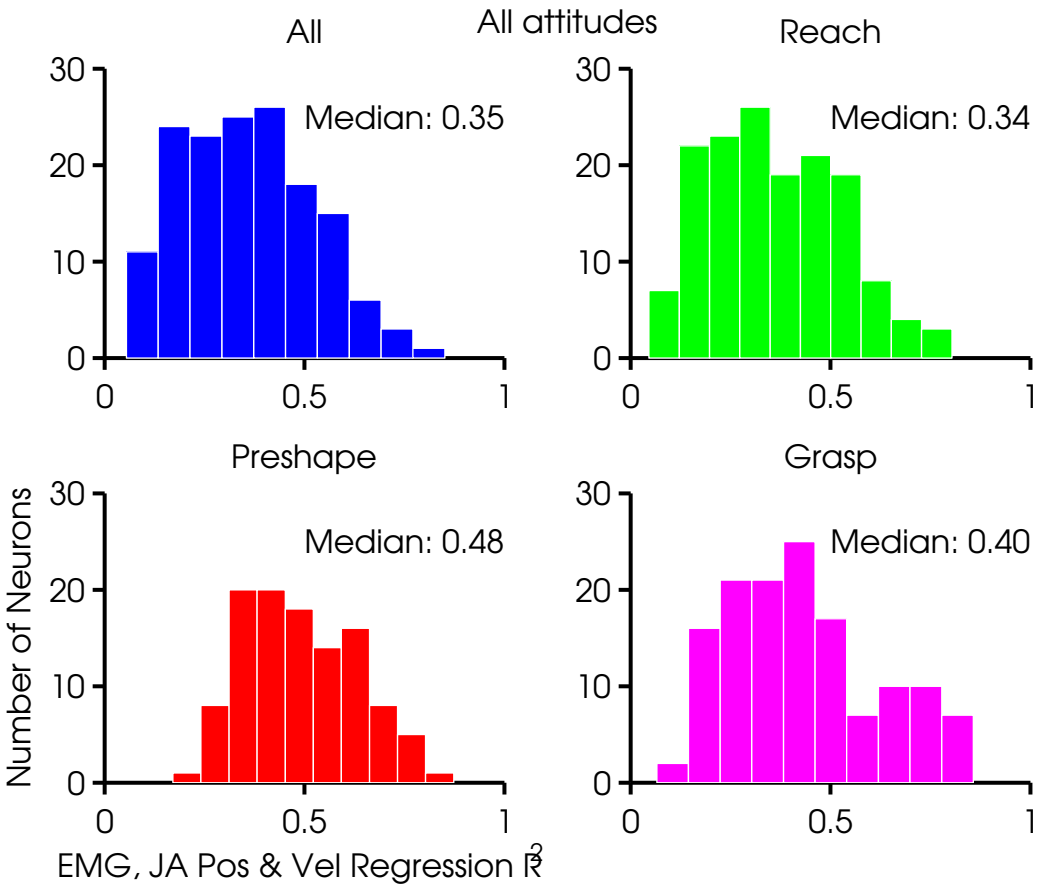

Figure 4.14: **EMG & JA regression R^2 histograms: All attitudes: Monkey E:** Histograms of regression R^2 values for 152 neurons. The regression model in Equation 4.3 was computed using data from all attitudes, over 4 task epochs: (1) *All Trial Data*, (2) *Reach Start* to *Reach End*, (3) *Reach End* to *Grasp Start*, (4) *Grasp Start* to *Grasp End*.

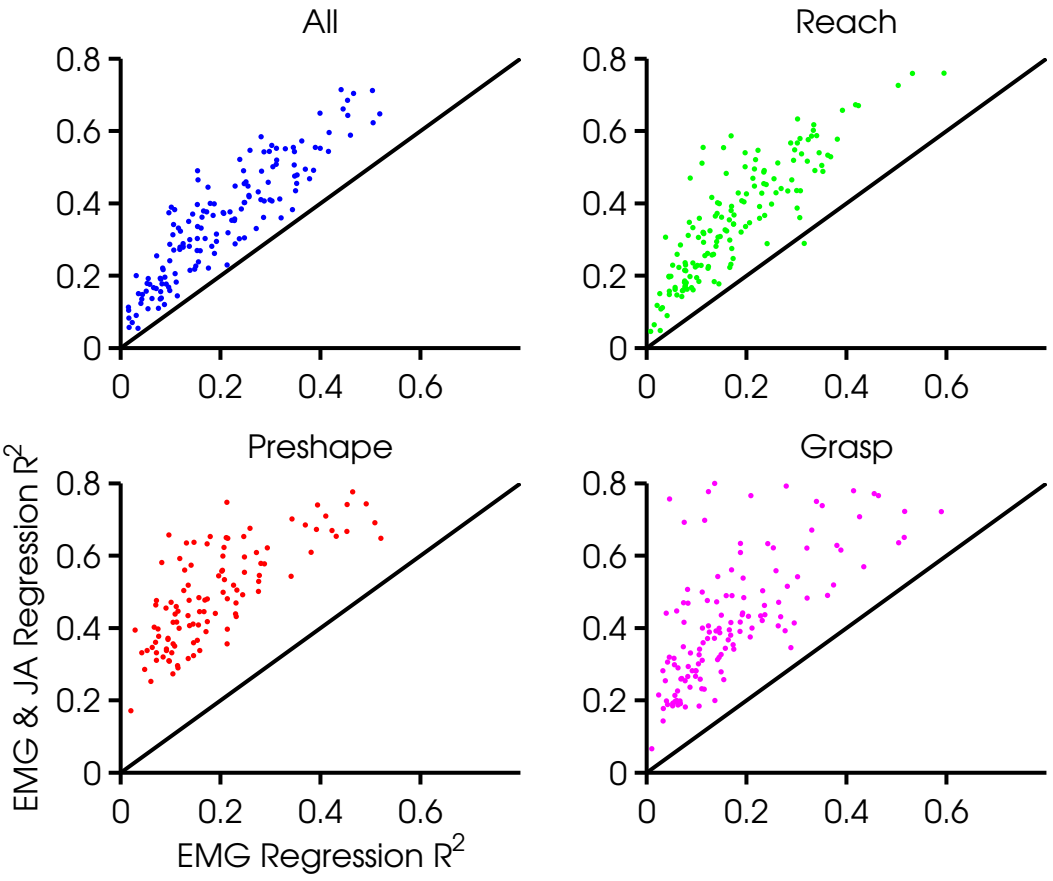

Figure 4.15: **EMG & JA regression R^2 VS EMG regression R^2: Monkey E:** Scatter plots of EMG & JA regression R^2 values VS EMG regression R^2 for 152 neurons. Data for regression was taken from all attitudes, and histograms of the corresponding R^2 values are shown in Figures 4.14 and 4.8. It is clear that the combined model R^2 values are higher, and also that neurons with high combined R^2 values tend to have high EMG R^2 values. The comparison is shown over 4 task epochs: (1) *All Trial Data*, (2) *Reach Start* to *Reach End*, (3) *Reach End* to *Grasp Start*, (4) *Grasp Start* to *Grasp End*.

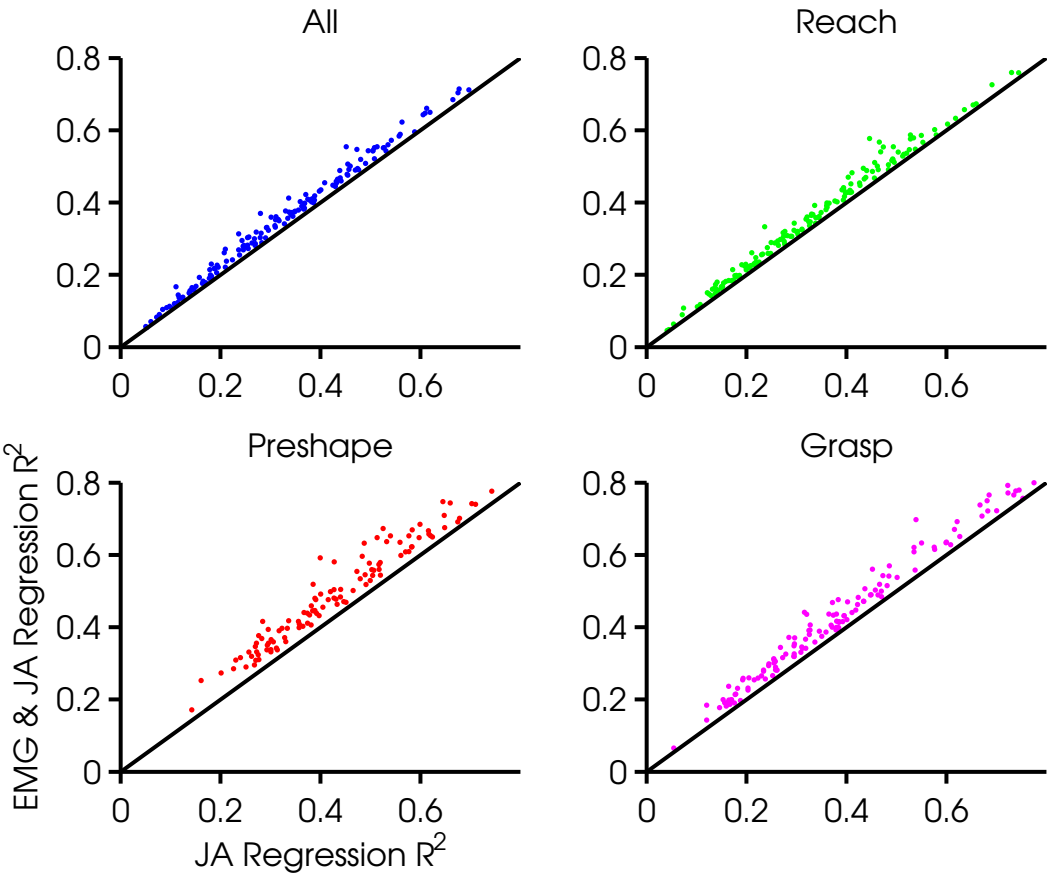

Figure 4.16: **EMG & JA regression R^2 VS JA regression R^2: Monkey E:** Scatter plots of EMG & JA regression R^2 values VS JA regression R^2 for 152 neurons. Data for regression was taken from all attitudes, and histograms of the corresponding R^2 values are shown in Figures 4.14 and 4.12. The combined model R^2 values are higher by a statistically significant difference. Also, neurons with high combined R^2 values tend to have high JA R^2 values. The comparison is shown over 4 task epochs: (1) *All Trial Data*, (2) *Reach Start* to *Reach End*, (3) *Reach End* to *Grasp Start*, (4) *Grasp Start* to *Grasp End*.

4.4.1 TUNING FEATURES I

The results in Sections 4.2, 4.3 and 4.4 indicate that the kinematic data are better linear predictors of neural firing rates compared to EMG. Previous studies have suggested that firing rates of individual neurons represent a continuum of arm, wrist and hand kinematics combinations; and most neurons were not preferential to subsets of kinematics (see Section 1.4). We investigated if this was the case in our data as well by using model selection techniques with the model defined in Equation 4.3.

Model selection is often used in the context of linear regression to improve prediction accuracy by using only a subset of the covariates. Regression predictions using a small number of covariates have low variance, but high bias. Conversely, regression predictors using a large number of covariates have low bias, but high variance. One of the goals of model selection is to balance the bias-variance trade off. We were interested in finding out if certain kinematic or EMG covariates contributed more to prediction of firing rates, to determine whether the neurons were preferentially related to subsets of covariates.

Given a linear regression model with d covariates $Y = X^T\beta = \sum_{j=1}^{d} \beta_j X_j$, the *coefficient of multiple determination*, denoted R^2, measures the proportion of the variance of a dependent variable Y explained by a set of d explanatory variables $X_j, j = 1,\ldots,d$. There are several ways to compute R^2, all equivalent for a linear model where X includes a constant term, but not equivalent otherwise. If $\hat{Y} = X^T\hat{\beta}$ is a linear predictor, where $\hat{\beta}$ is the least squares estimator, then the *error sum of squares* of the residuals $res = Y - \hat{Y}$, is given by $SSE = \sum res^2 = \sum (Y - \hat{Y})^2$; and the *total sum of squares* is given by $TSS = \sum (Y - \bar{Y})^2$. The R^2 is then computed by $R^2 = 1 - \frac{SSE}{TSS}$.

We chose to use a related measure, *coefficients of partial determination*, to measure the *marginal* contribution of one or more covariates to the variance of the dependent variable Y, when all other covariates were already included in the model. For a simple model with $d = 2$, the coefficient of partial determination between Y and X_1, given that X_2 is already included in the model is

$$r^2_{Y,1|2} = \frac{SSE(X_2) - SSE(X_1, X_2)}{SSE(X_2)} = \frac{SSR(X_1|X_2)}{SSE(X_2)} \tag{4.4}$$

$r^2_{Y,1|2}$ measures the proportionate unexplained variance of Y that becomes explained after adding X_1 to a model that already included X_2. This measure readily extends to three or more covariates.

For example, if $d = 3$ then

$$r^2_{Y,1|2,3} = \frac{SSR(X_1|X_2,X_3)}{SSE(X_2,X_3)} \tag{4.5}$$

is the coefficient of partial determination for X_1, when X_2, X_3 are already included in the model.

First, we computed the coefficients of partial determination for every one of the 62 covariates in Equation 4.3. Figure 4.17 shows a heat map with all coefficients of partial determination for all neurons. Around 10 neurons show higher coefficients for the first few JAs, which include the wrist JA and the thumb MCP/PIP flexion and thumb MCP abduction. However, most neurons do not show high coefficients for any individual covariate, indicating that neurons were usually not preferential for individual muscles or JAs / JA velocities.

Next, we computed the coefficients of partial determination for subsets of covariates from Equation 4.3. We chose 44 subsets, corresponding to functional groups of muscles or joints: (1) all EMG, (2) all JAs, (3) all JA velocities, (4) all kinematics (JAs and JA velocities), (5) arm muscles, (6) wrist muscles, (7) finger muscles, (8) wrist extensors, (9)wrist flexors, (10) finger extensors, (11) finger flexors, (12) wrist JA (angle & angular velocity), (13)finger JA (angle & angular velocity), (14-18) individual finger JA (angle & angular velocity), (19) MCP flexion JA (angle & angular velocity), (20) MCP abduction JA (angle & angular velocity), (21) PIP flexion JA (angle & angular velocity), (22) DIP flexion JA (angle & angular velocity); and the same kinematics subsets as groups 12-22 corresponding only to JAs or JA velocities (groups 23-44). Figure 4.18 shows a heat map of coefficients of partial determination for the various groups. Seven groups show high coefficients across neurons: (1) all EMG, (2) all JAs, (3) all JA velocities, (4) all Kinematics, (13) all finger JA values and velocities, (24) all finger JAs, (35) all finger JA velocities. Out of those, the groups which contained all kinematics and all finger JA values & velocities showed the highest coefficients. The group which included all EMGs showed the lowest coefficients compared to the other six groups. Figure 4.19 shows a more quantitative analysis in the form of a boxplot for the values from Figure 4.18; demonstrating that covariate groups containing only kinematic features had higher coefficients of partial determination than covariate groups containing only EMGs.

We concluded that motor-cortical neurons tended to be most linearly related to hand kinematics; and that finger JA values and velocities were best represented in their firing rates. Very few neurons showed preference to wrist, rather than hand, JA value and velocity. EMGs were not as well linearly related to the neural firing rates, even during the static grasp epoch, where no move-

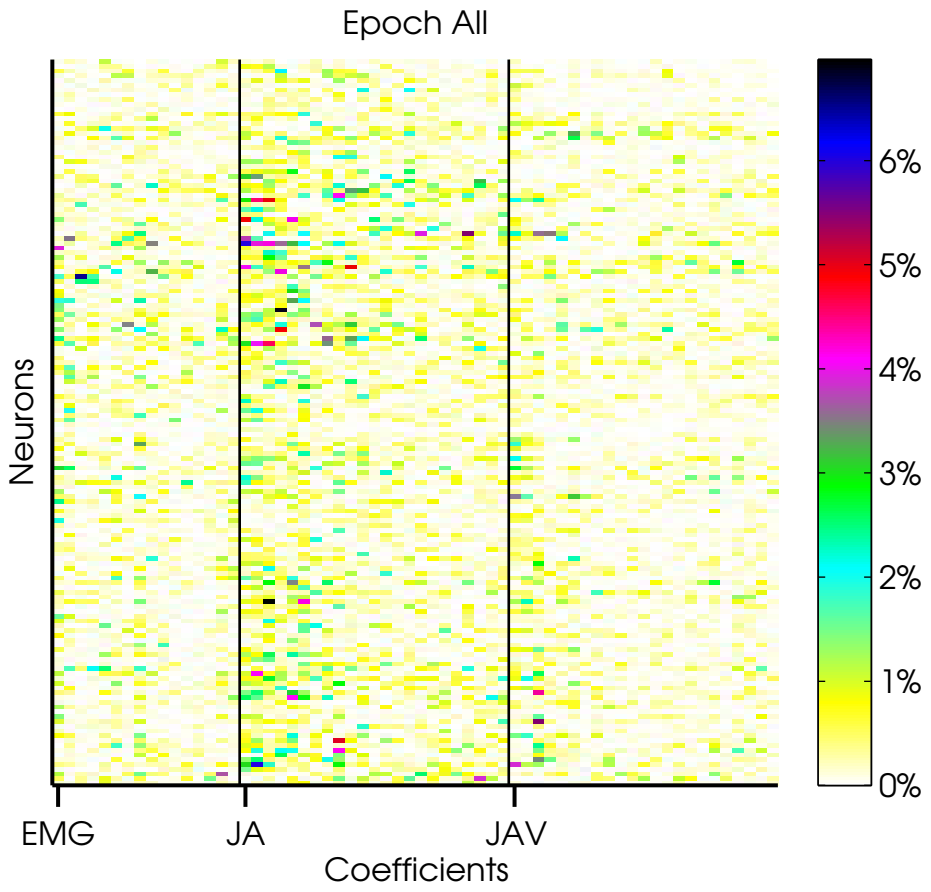

Figure 4.17: **Coefficients of partial determination for all covariates: Monkey E:** Heat map of coefficients of partial determination computed for the 62 covariates in Equation 4.3. Y-axis represent 152 neurons, x-axis represent the regression covariates, ordered by EMG, JA, JAV. The data used here included all samples for trials, from *Reach Start* to *Grasp End*.

ment occurred and the monkey only exerted force on the object. Neurons were not preferential to individual muscles, joint angle values/velocities, or any of the functional groups we examined. Hand shape and multiple finger movements accounted (linearly) for most of the variance in the firing rates, strengthening our conclusion from Section 4.1, that neural firing rates were better differentiated by objects than by targets.

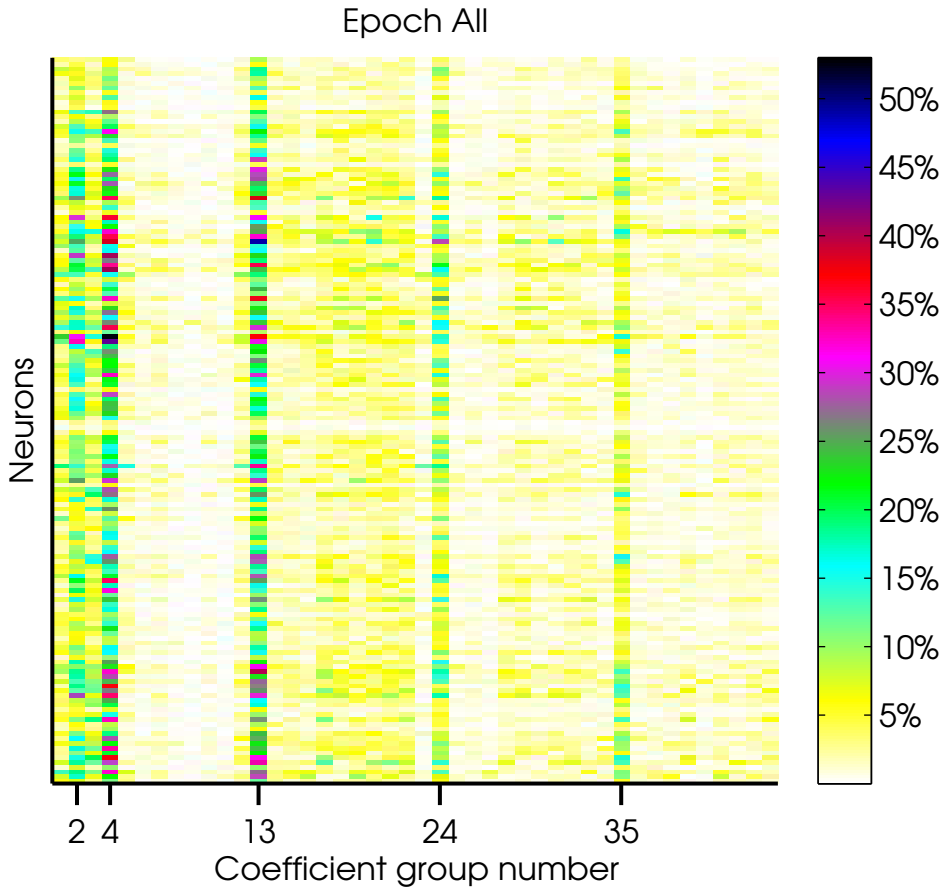

Figure 4.18: **Coefficients of partial determination of covariate groups: Monkey E:** Heat map of coefficients of partial determination computed for 44 subsets of the 62 covariates in Equation 4.3. Y-axis represent 152 neurons, x-axis represent the regression covariate groups. The groups with especially high coefficients across neurons are: (1) all EMG, (2) all JA, (3) all JA velocities, (4) all Kinematics, (13) all finger JA and JA velocities, (24) all finger JA, (35) all finger JA velocities. The data used here included all samples for trials, from *Reach Start* to *Grasp End*.

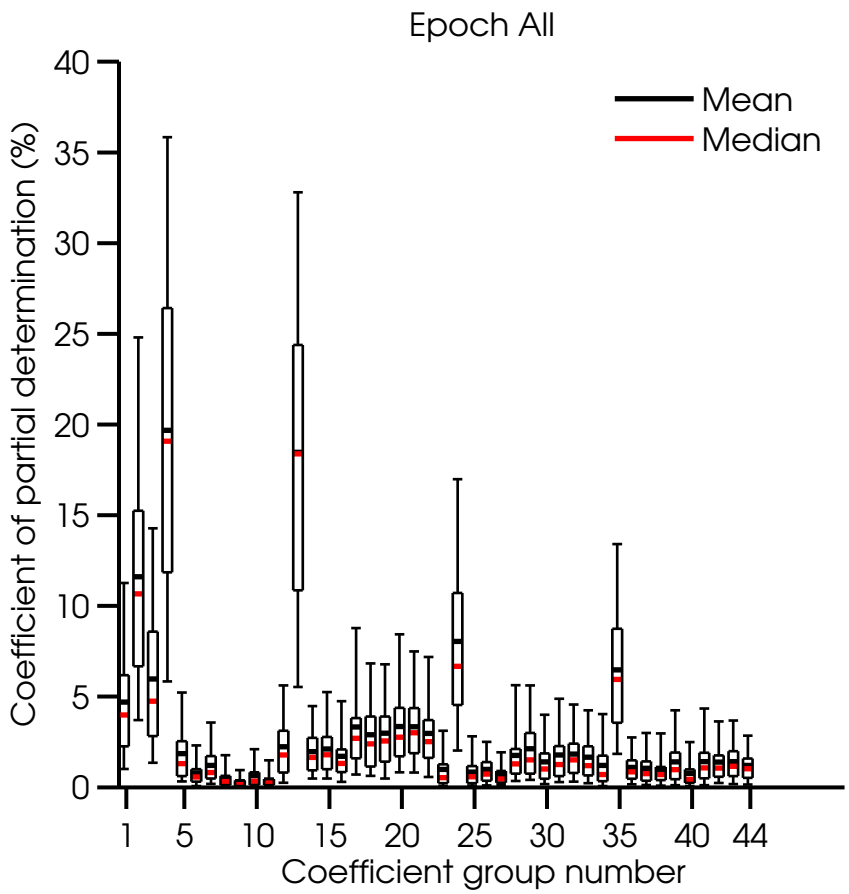

Figure 4.19: **Boxplot of coefficients of partial determination for covariate groups: Monkey E:** Boxplot of coefficients of partial determination computed for 44 subsets of the 62 covariates in Equation 4.3. Data for this figure is also plotted in Figure 4.18. The groups with especially high coefficient medians are: (1) all EMG, (2) all JA, (3) all JA velocities, (4) all Kinematics, (13) all finger JA and JA velocities, (24) all finger JA, (35) all finger JA velocities.

4.4.2 TUNING FEATURES II

Model selection using partial coefficients of determination enabled us to determine which general subsets of covariates (kinematics, JAs, JA velocities) were best represented in the neural firing rates. However, none of the more specific functional groups we tested seemed to be well represented in the firing rates: for example, neurons did not seem preferential to finger flexion/extension, or MCP flexion; although finger flexion is a main component of the reach to grasp task (see Figure 3.69**A**). Testing every possible subset of covariates is not feasible, therefore we required a different model selection method that would inherently perform model selection, and select an optimal subset of covariates by minimizing some cost function.

Least absolute shrinkage and selection operator (LASSO), is a variable selection method which avoids the extensive combinatorial search over the whole model space, and performs estimation and model selection simultaneously [69]. The LASSO estimator $\hat{\beta}(\lambda)$ is the value of β which minimizes

$$\frac{1}{2}\sum_{i=1}^{n}(y_i - X^T\beta)^2 + \lambda\|\beta\|_1 \tag{4.6}$$

where $\lambda > 0$ and $\|\beta\|_1 = \sum_{j=1}^{d}|\beta_j|$ is the ℓ_1-norm of β. Some of the β estimators are set zero, which corresponds to dropping them from the regression model. In this regards, LASSO is different than rigde or multiple linear regressions, which would set some estimators to low values, instead of zero. λ was chosen using cross-validation, as illustrated in Figure 4.20. Any model between the minimal λ to the lse λ is a valid model to use. We chose the largest λ with a mean squared error smaller than the standard error of the minimal λ. This corresponds to picking the model with the smallest number of nonzero coefficients within the uncertainty of the model with the minimal cross validation error. All data was normalized prior to fitting the LASSO regressions.

We fit LASSO regressions to the 152 neurons from Figure 4.14, and the resulting coefficients are shown in Figures 4.21 (for all task epochs), 4.22 (for the reach epoch), 4.23 (for the preshape epoch) and 4.24 (for the static grasp epoch). When using data from all task epochs, it is clear that JAs receive the highest coefficients compared to JA velocities or EMG (Figure 4.21). Also, neurons with the largest absolute coefficients are not necessarily the ones with the highest mean normalized firing rate (shown on the bottom heat map). Similar conclusions can be drawn for the reach epoch (Figure 4.22). During the preshape epoch, which is the shortest epoch, only 111 neurons had

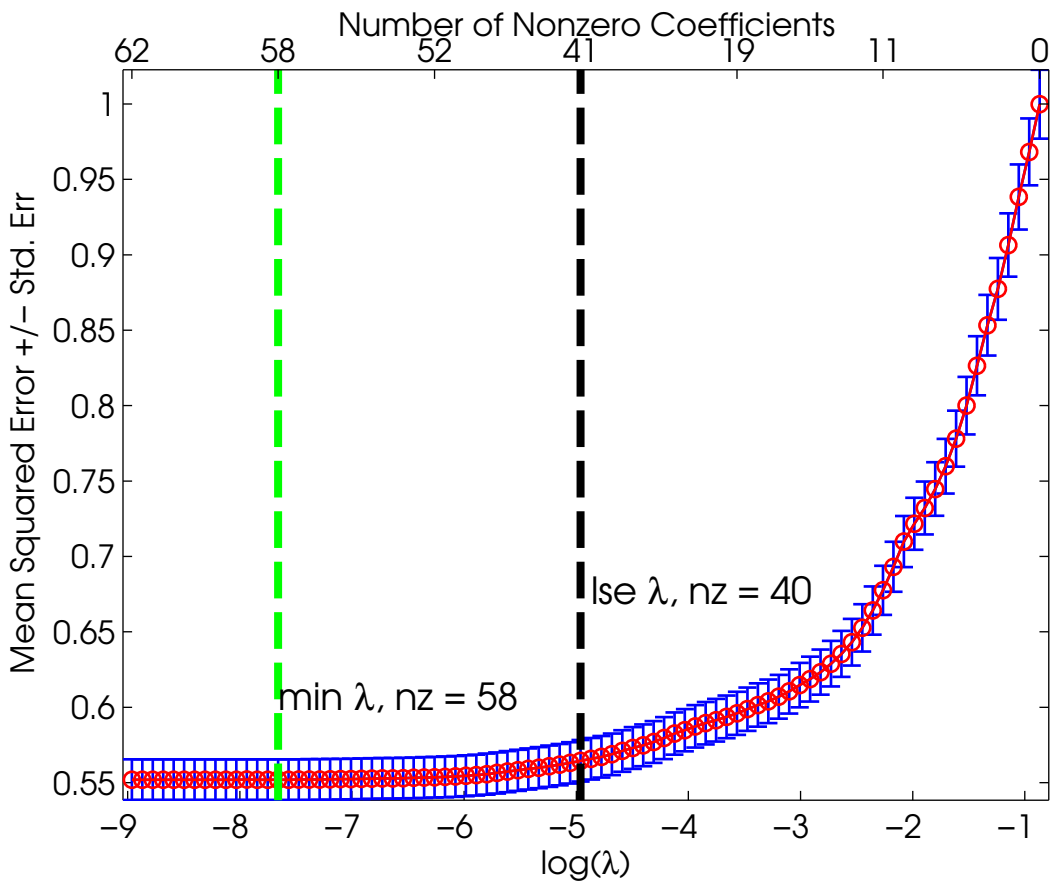

Figure 4.20: **Selection of LASSO λ using cross-validation:** An example of how λ was chosen using cross validation, for the model in Equation 4.3. 88 values of lambda were used here, represented on the x-axis. For each λ, 100-fold cross-validation was performed, and the mean squared error was computed; shown on the y-axis, along with the standard error. The minimal λ was the largest λ with the minimal mean cross-validation error, and is shown as a dashed green line, where 58 coefficients are non-zero. We chose the lse λ, defined as the largest λ with a mean squared error smaller than the standard error of the minimal λ; which in this case corresponded to 40 non-zero coefficients.

sufficient data to compute the regression against. The coefficients heat map is sparse, probably due to the small number of available samples, but the JA coefficients are still higher compared to JA velocity or EMG coefficients. During the static grasp epoch (Figure 4.24), 136 neurons had

sufficient data to compute the regression against; and there are no apparent differences between the coefficients for JA, JA velocity or EMG.

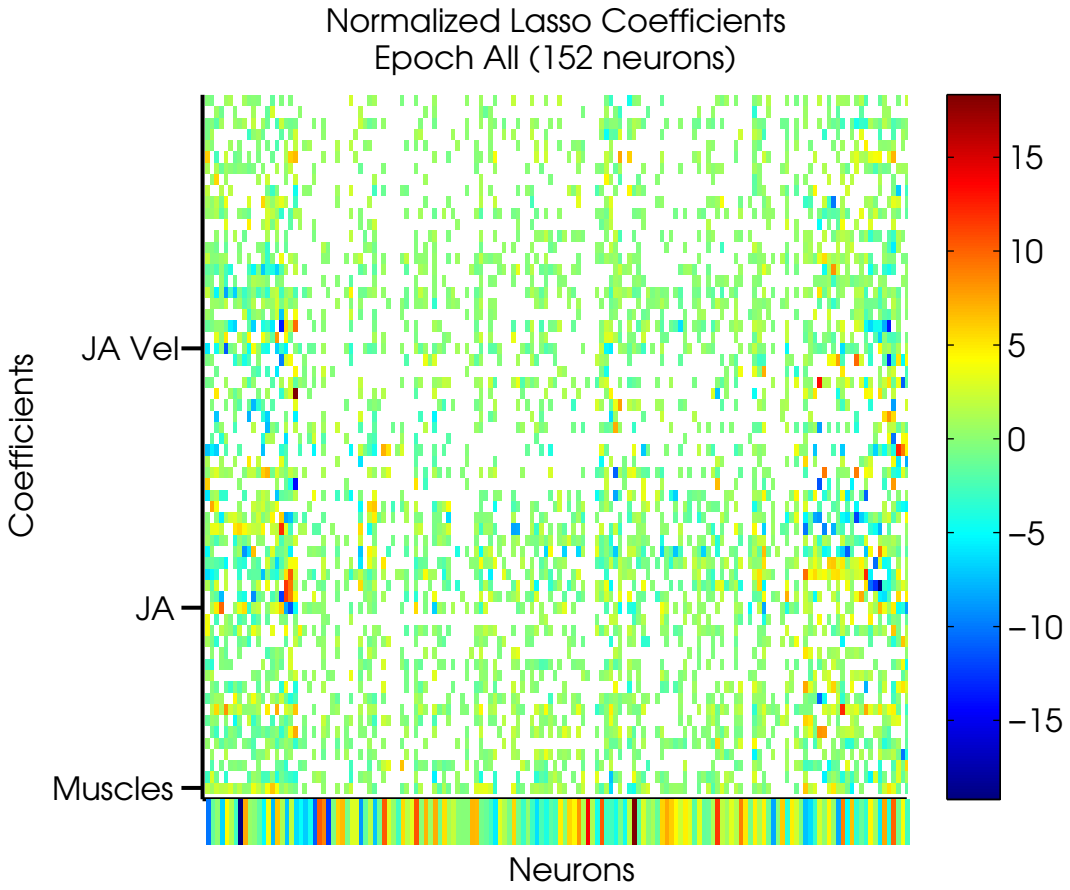

Figure 4.21: **Heat map of LASSO coefficients: monkey E:** Heat map of LASSO coefficients for 152 neurons, using the model in Equation 4.3. Neurons with similar coefficients were clustered together. The mean normalized firing rate for every neuron is shown on the bottom heat map. The data used here included all samples for trials, from *Reach Start* to *Grasp End*. Coefficients are represented on the y-axis, bottom-up: 16 EMG coefficients, 23 JA coefficients and 23 JA velocity coefficients; a total of 62 coefficients.

Based on Figure 4.21, we concluded that both kinematics and EMGs are represented in the neural firing rates; since the proportion of nonzero EMG coefficients is similar to that of the kinematic coefficients. Comparing the results of the LASSO regression to those obtained using the partial coefficients of determination, we concluded that JAs are best linearly represented in the

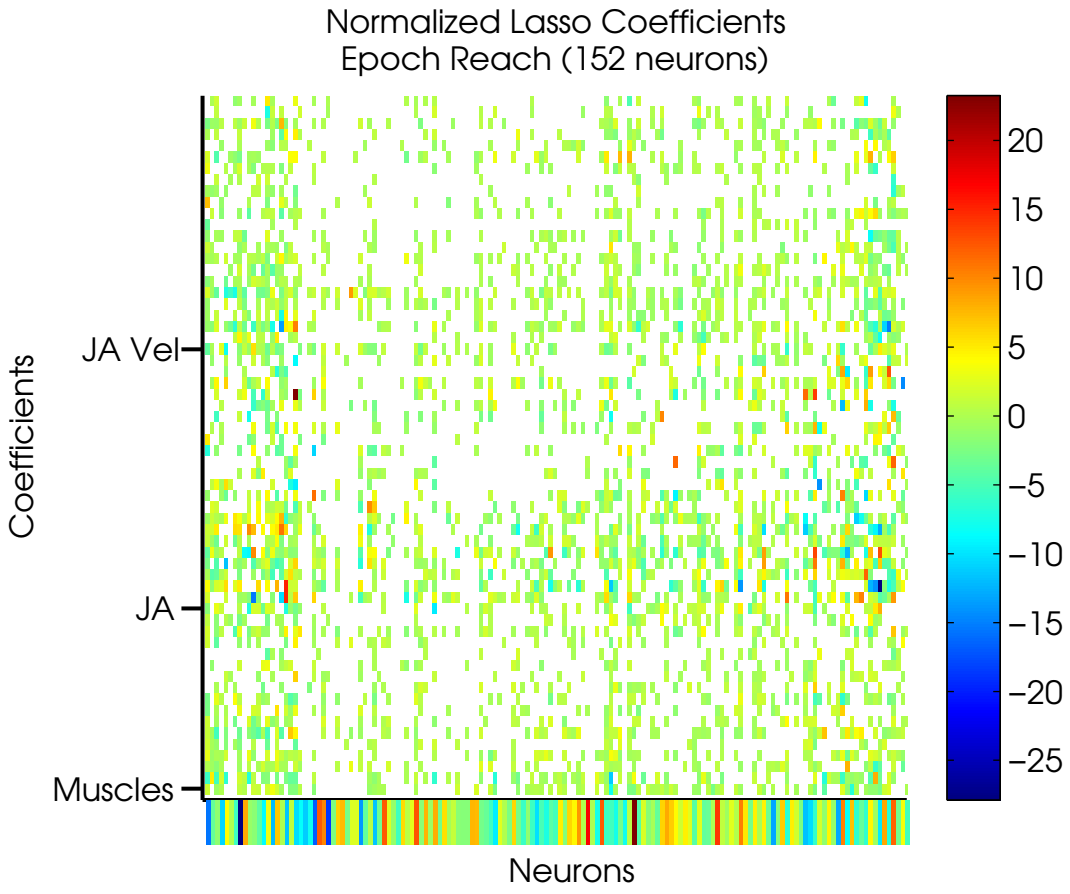

Figure 4.22: **Heat map of LASSO coefficients: monkey E:** Heat map of LASSO coefficients for the model in Equation 4.3. Neurons are in the same order as in Figure 4.21. The mean normalized firing rate for every neuron is shown on the bottom heat map. The data used here included all samples for trials, from *Reach Start* to *Reach End*. Coefficients are represented on the y-axis, bottom-up: 16 EMG coefficients, 23 JA coefficients and 23 JA velocity coefficients; a total of 62 coefficients.

neural firing rates. Neurons were not preferential to functional groups of joints or muscles, but rather to a distributed mixture of all covariates.

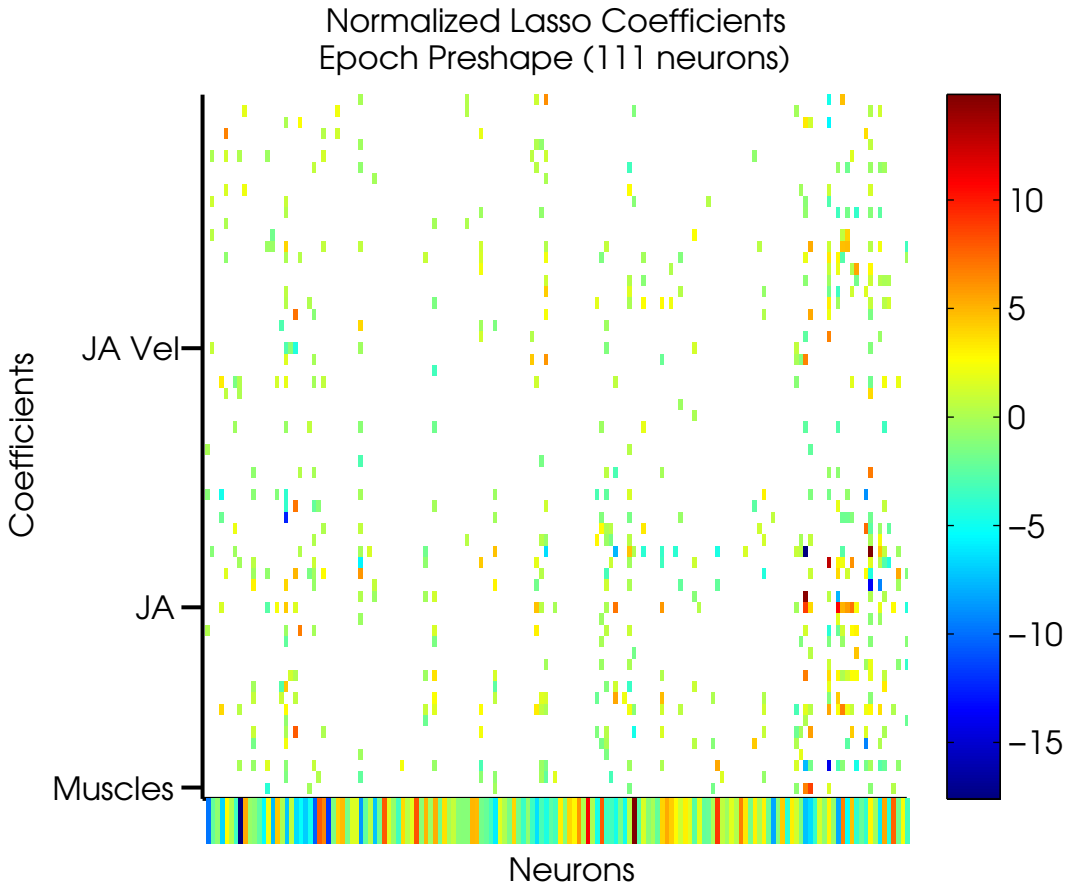

Figure 4.23: **Heat map of LASSO coefficients: monkey E:** Heat map of LASSO coefficients for the model in Equation 4.3. Neurons are in the same order as in Figure 4.21. The mean normalized firing rate for every neuron is shown on the bottom heat map. The data used here included all samples for trials, from *Reach End* to *Grasp Start*. Coefficients are represented on the y-axis, bottom-up: 16 EMG coefficients, 23 JA coefficients and 23 JA velocity coefficients; a total of 62 coefficients.

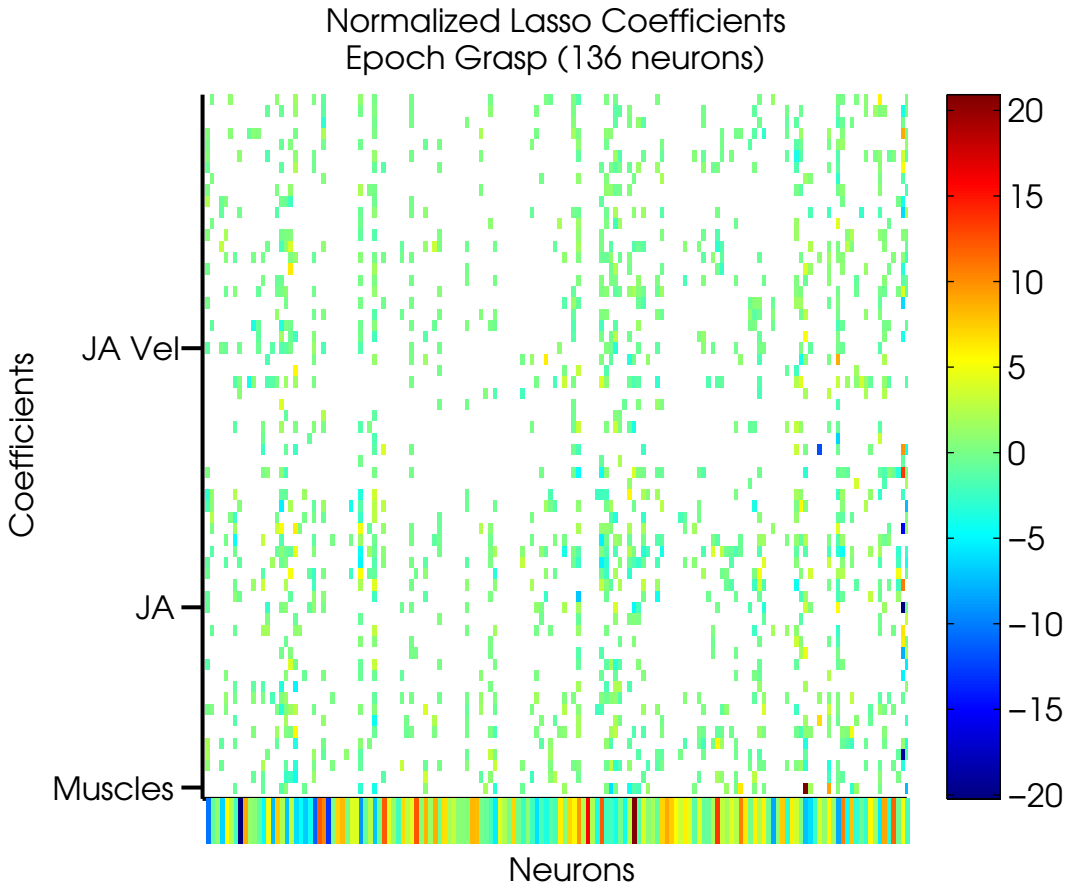

Figure 4.24: **Heat map of LASSO coefficients: monkey E:** Heat map of LASSO coefficients for the model in Equation 4.3. Neurons are in the same order as in Figure 4.21. The mean normalized firing rate for every neuron is shown on the bottom heat map. The data used here included all samples for trials, from *Grasp Start* to *Grasp End*. Coefficients are represented on the y-axis, bottom-up: 16 EMG coefficients, 23 JA coefficients and 23 JA velocity coefficients; a total of 62 coefficients.

4.5 NEURAL TUNING TO EMG AND JA SYNERGIES

We have shown in Sections 3.6 and 3.7, that EMG and kinematic data can be represented in lower dimensional spaces, while preserving their correlation structures. These lower dimensionality representations are often referred to as *muscle synergies* and *kinematic synergies*. We investigated whether motor cortical activity was related to EMG or kinematic synergies.

We used the following linear model to relate neural firing rate to the simultaneous activation of both EMG and kinematic synergies:

$$\lambda_{50} = d + \sum_{d=1}^{D_{EMG}} a_d EMG\_PC_d + \sum_{d=1}^{D_{JA}} b_d JA\_PC_d + \sum_{d=1}^{D_{JAV}} c_d JAV\_PC_d \tag{4.7}$$

where λ_{50} is the fractional firing rate for an individual neuron, computed using adjusted $50ms$ bins (see Section 2.2 for details); EMG_PC_d is the d^{th} EMG synergy activation, averaged in the same $50ms$ bins as the neural data, lagged by one bin ($50ms$ on average); JA_PC_d and JAV_PC_d are the d^{th} joint angles and velocity synergies, averaged in the same $50ms$ bins as the neural data, lagged by two bins ($100ms$ on average). To compute this model, we first used data from an entire session to compute the EMG and kinematic synergies using PCA (similarly to Sections 3.6 and 3.7). Synergies for JAs and JA velocities were computed separately. We then determined the number of PCs required to account for 90% of the variance in the EMG or kinematic data, denoted in the model as D_{EMG}, D_{JA} and D_{JAV}; and regressed the neural firing rates against the data projected to the appropriate D^{th} dimensional space, for each synergy type. Figure 4.25 shows the distribution of D_{EMG}, D_{JA} and D_{JAV} values across neurons.

Figure 4.26 shows a comparison of R^2 values between the full model previously used to relate neural firing rates to EMG and kinematics (Equation 4.3); and the PC model (Equation 4.7). For all 152 neurons, the R^2 values were better for the full model, compared to the PC model. Figure 4.27 indicates that the difference was $13 \pm 6\%$, on average, across all neurons. Reducing data dimensionality using PCA, necessarily involves losing information, hence it is not surprising that the fits are worse for the PC model. If, however, the neurons use some type of reduced dimensionality to control muscles or joints, we would expect the fits to be almost identical, when comparing the full and the PC models.

To clarify this further, we examined which synergies were best represented in the neural firing rates. We used LASSO regression (see Section 4.4.2 for information about LASSO), with the same model structure as Equation 4.7; but we set D_{EMG}, D_{JA} and D_{JAV} to the number of EMGs, JAs and JA velocities accordingly. Therefore, the LASSO model contained the same data as the full model (Equation 4.3), only linearly transformed to the spaces defined by the EMG and kinematic synergies. Instead of always using the first few PCs to predict the neural firing rates, we let the LASSO model select the appropriate PCs for every neuron; or a specific set of synergies most appropriate for every neuron.

We set λ to zero, as a sanity check, and as expected, the LASSO solution was identical to the multiple linear regression solution, the model fits were identical to the ones from the full model. We then selected λ using cross-validation: as in Sec. 4.4.2, we chose the largest λ with a mean squared error smaller than the standard error of the minimal λ. Figure 4.28 shows the LASSO R^2 values compared with the full model and PC model R^2 values. For all 3 models, R^2 were calculated between the neural firing rate and the regression firing rate predictions. For most neurons, the LASSO fits were close to the full model fits; and were better than the PC model fits. Figure 4.29 shows that the average difference in fits between LASSO and the full model, was smaller than 5%, for 70% of the neurons.

These results indicate that the firing rate of most neurons did not correspond to the subspaces defined by PCA. Figure 4.30 shows a heat map of LASSO coefficients for all 152 neurons. While the lower-order synergies, accounting for most variance, receive higher coefficients compared to the higher-order ones; for most neurons, the coefficients for the higher-order synergies are not zero; indicating some contribution to the prediction of firing rate. We concluded that correlated joint movement and correlated muscle activation were strongly represented in the neural firing rate of many neurons. At the same time, features corresponding to finer and individuated joint movements, as well as individuated muscle activations, were also represented in the neural firing rates; although to a lesser extent. Therefore, there is not strong evidence in favor of a reduced set of synergies being used by motor cortical neurons. By employing dimensionality reduction techniques which take into account the neural activity, we might be able to find some synergy space, for either EMG or kinematics, in use by motor cortical neurons.

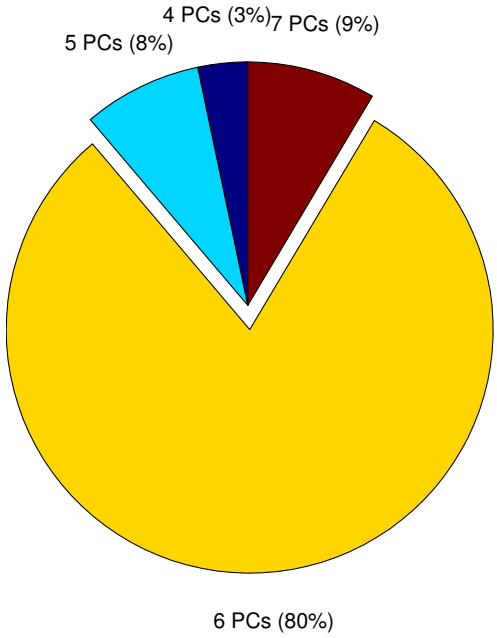

(**A**) Number of EMG PCs Used

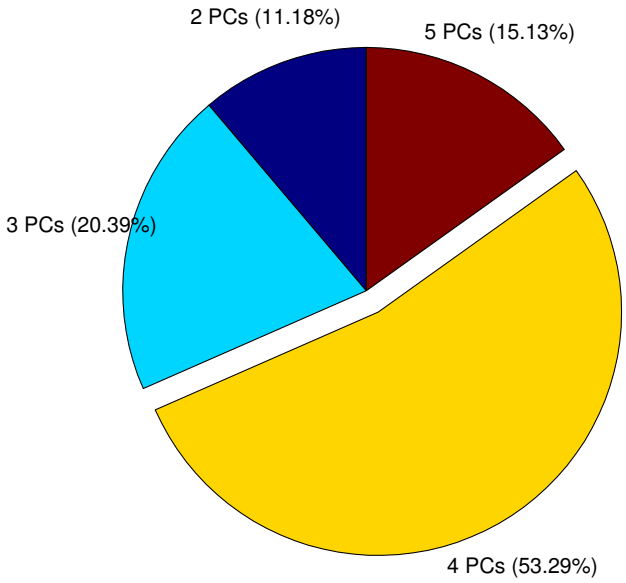

(**B**) Number of JA Pos PCs Used

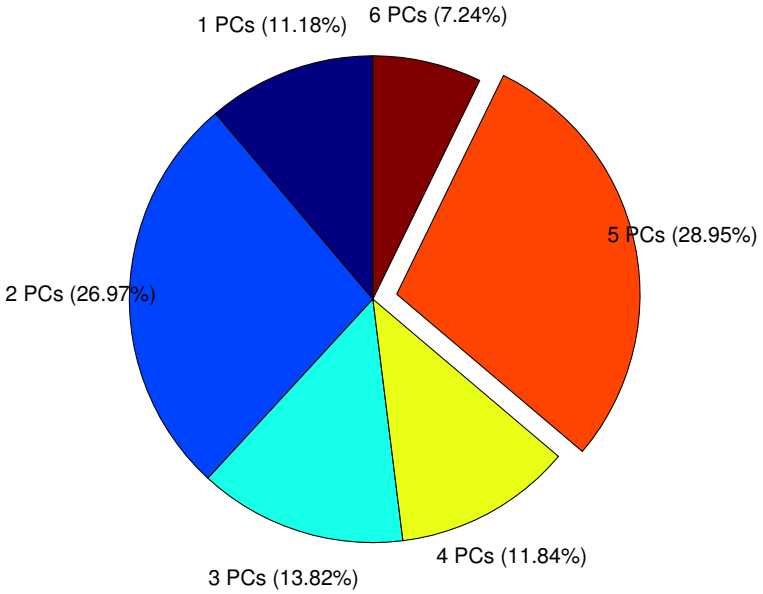

(**C**) Number of JA Vel PCs Used

Figure 4.25: **Number of PCs used in the reduced model: Monkey E:** The number of PCs used to reduce the EMG and kinematic data in the PC model (D_{EMG}, D_{JA} and D_{JAV} in Equation 4.7). Percentages of neurons for which that number of PCs was used are indicated in parenthesis.

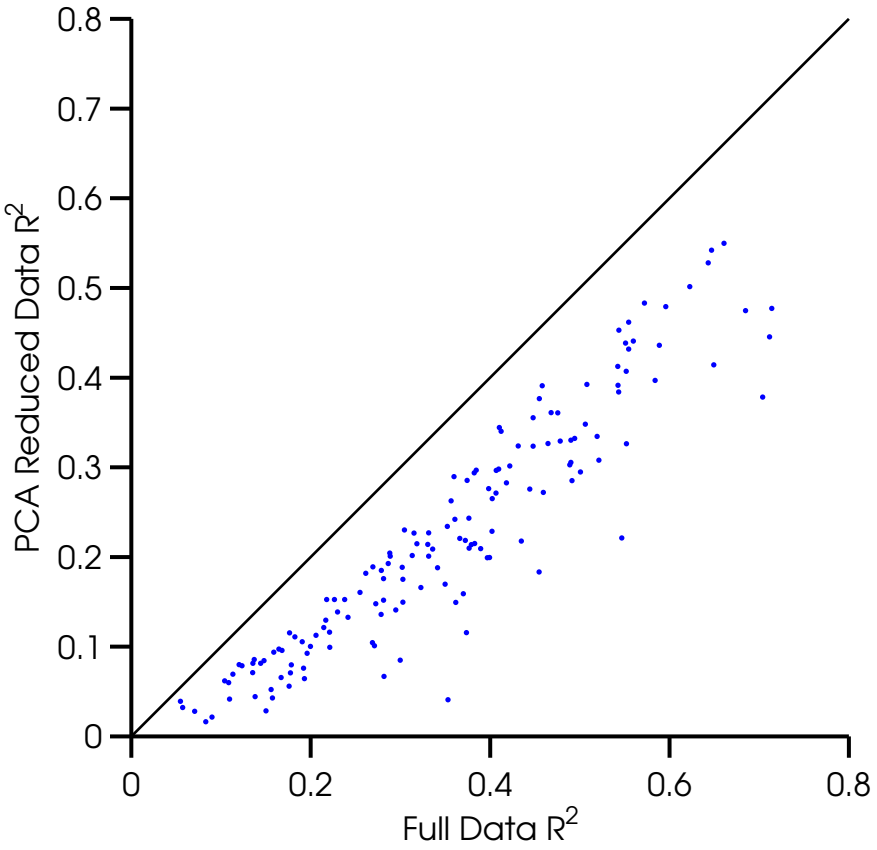

Figure 4.26: **Comparison of R^2 between full and reduced data regressions: monkey E:** Comparison of R^2 values between the PC model in Equation 4.7, to the full model in Equation 4.3. A histogram of R^2 values for the full model is shown in Figure 4.14. R^2 values for the full model are better than the PC model, for all 152 neurons.

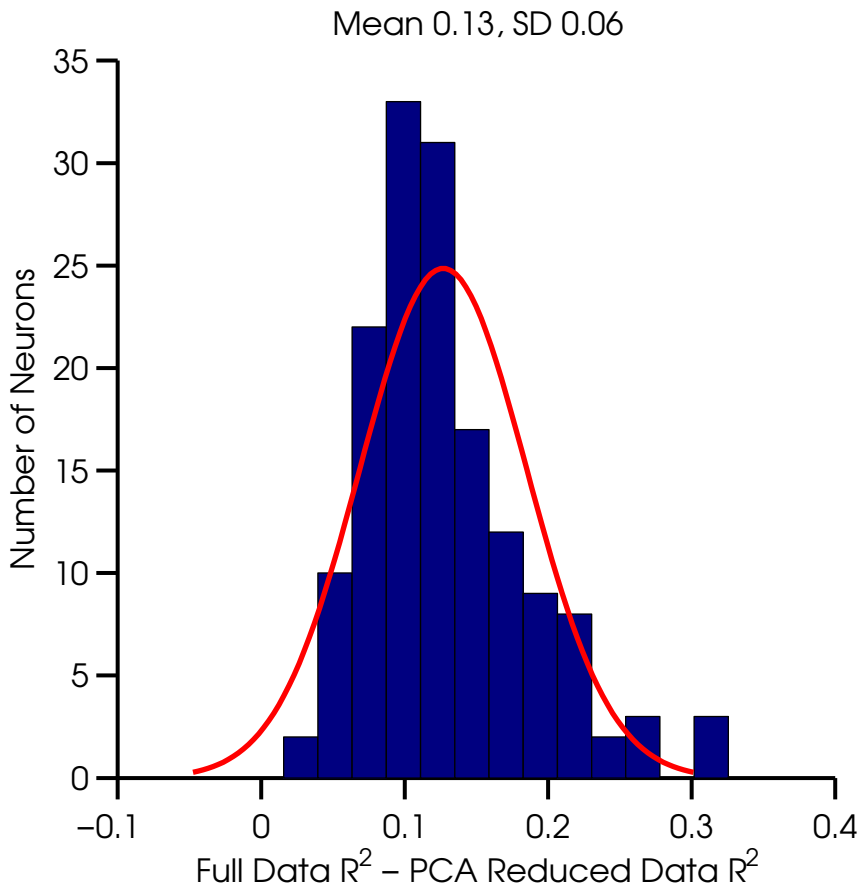

Figure 4.27: **Differences in R^2 between full and reduced data regressions: monkey E:** A histogram of R^2 values between the PC model in Equation 4.7, to the full model in Equation 4.3. A histogram of R^2 values for the full model is shown in Figure 4.14. R^2 values for the full model are better than the PC model, for all 152 neurons.

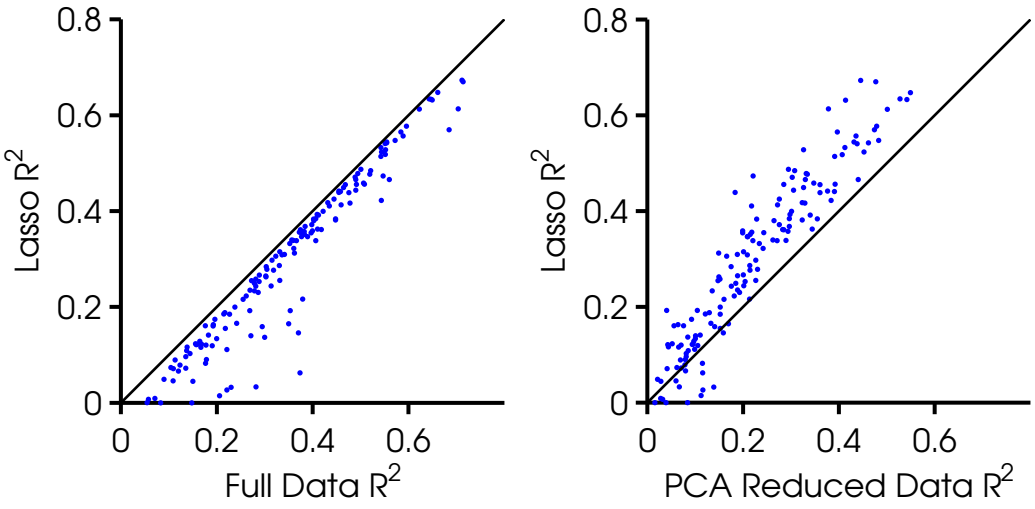

Figure 4.28: **Comparison of R^2 between full and LASSO regressions: monkey E:** Comparison of R^2 values between the LASSO model based on Equation 4.7, to the full model in Equation 4.3. The LASSO model used values of D_{EMG}, D_{JA} and D_{JAV} set to the number of EMG, JA and JA velocity variables. A histogram of R^2 values for the full model is shown in Figure 4.14. For 70% of the neurons (107/152), the difference in R^2 between the LASSO model and the full model was smaller than 5%.

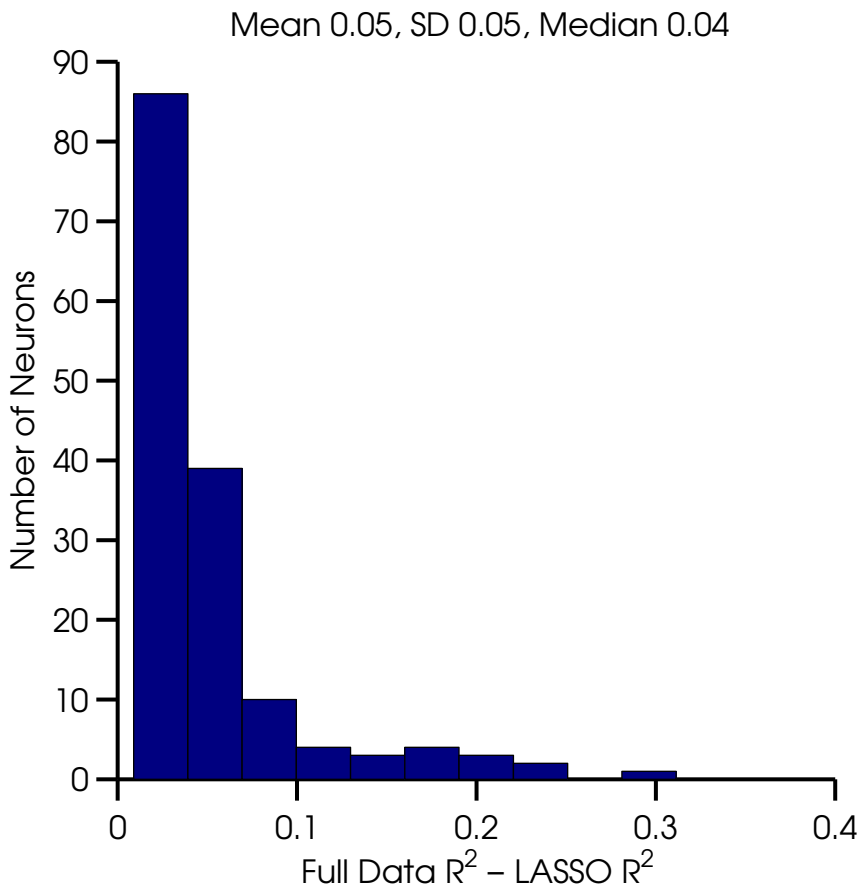

Figure 4.29: **Differences in R^2 between full and LASSO regressions: monkey E:** A histogram of R^2 values between the LASSO model based on Equation 4.7, to the full model in Equation 4.3. The LASSO model used values of D_{EMG}, D_{JA} and D_{JAV} set to the number of EMG, JA and JA velocity variables. A histogram of R^2 values for the full model is shown in Figure 4.14. For 70% of the neurons (107/152), the difference in R^2 between the LASSO model and the full model was smaller than 5%.

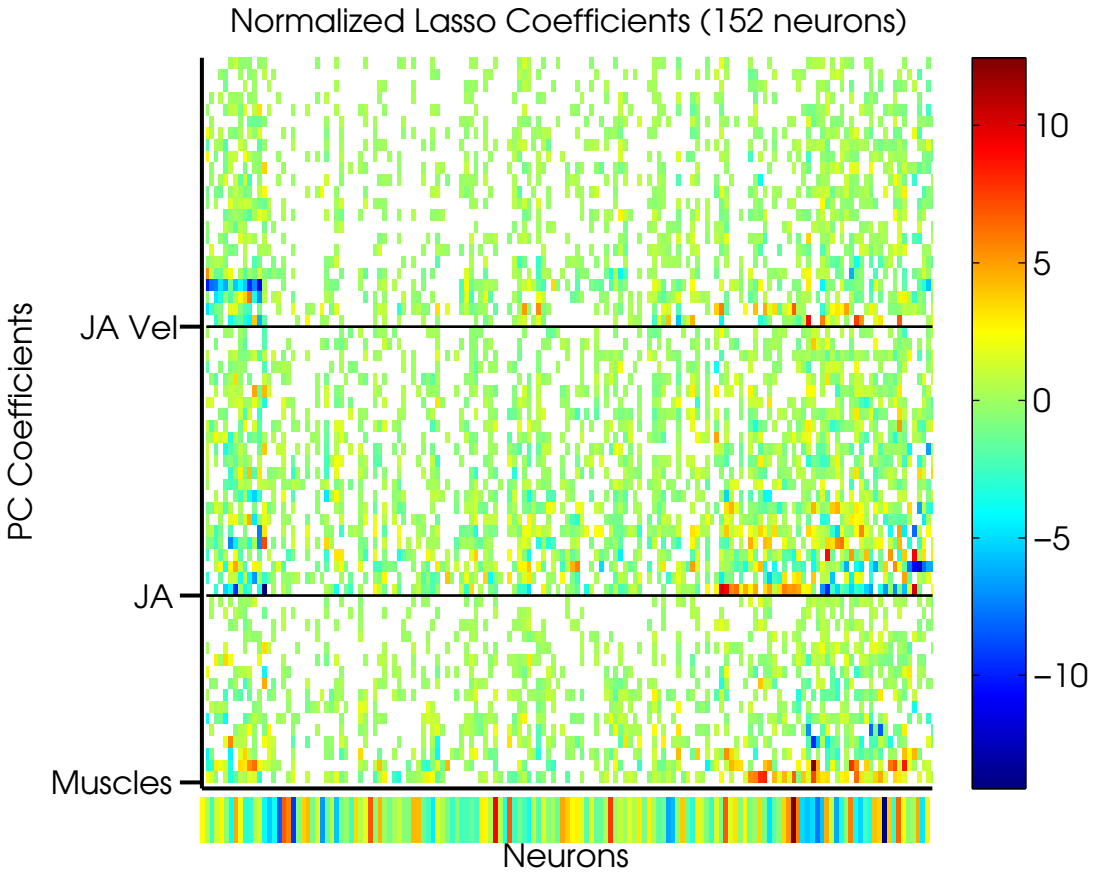

Figure 4.30: **Reduced data LASSO regression coefficients: monkey E:** Heat map of LASSO regression coefficients for a model based on Equation 4.7 with values of D_{EMG}, D_{JA} and D_{JAV} set to the number of EMG, JA and JA velocity variables. Synergy coefficients are arranged by EMG, JA and JA velocity groups. Within each group, the synergies are ordered by decreasing amounts of variance accounted bottom-up: so the lower-order synergies within each group are closer to the bottom, and the high-order synergies are closer to the top.

4.6 DECODING EMG AND JA USING A POPULATION OF NEURONS

In Section 1.4, we have listed previous studies in which the activity of sequentially (Morrow and Miller [44]) or simultaneously (Pohlmeyer et al. [52]) recorded motor-cortical neurons was used to predict the envelope of muscle activity. The authors of both studies concluded that mainly EMG is represented in the firing rates of motor cortical neurons. Other studies (Hamed et al. [24], Vargas-Irwin et al. [67], Saleh et al. [58, 59]) have shown that the population activity of motor-cortical neurons can be used to predict joint angles values and velocities; concluding that kinematic features are well represented in the neural firing rates.

We investigated whether the activity of our neural population could be used to predict either EMG or JAs. Only neurons which had valid data for at least 70% of the repetitions to all attitudes (corresponding to at least 14 repetitions per attitude), were considered in this analysis. Therefore, neurons from sessions that did not include all possible attitudes were excluded. Neurons which did not fire any spikes during more than 30% of the repeat trials to any attitude were also excluded. Using these criteria, we made sure that our decoding model was trained on the same number of samples from every attitude, minimizing bias to attitudes with more repetitions. 64 neurons met all these requirements and were subjected to this analysis.

We used the following model to predict the EMG activity of every muscle:

$$\overline{EMG_m} = b_0 + \sum_{n=1}^{N} b_n \overline{\lambda_n^{50}} \tag{4.8}$$

where

- $\overline{\lambda_n^{50}}$ is the fractional firing rate for neuron n, computed using adjusted $50ms$ bins (see Section 2.2 for details), and averaged over all repeat trials
- $\overline{EMG_m}$ is the EMG for muscle m, averaged over all repeat trials to every attitude, computed using the same bins as the firing rates, and lagged by one bin ($50ms$ on average)

Because our neural population was sequentially recorded, we averaged the firing rate of every neuron, and the EMG of every muscle, across all repeat trials to every attitude. EMG was averaged across trials in multiple sessions, while firing rates were averaged across trials in the same session, since neurons were only recorded for the duration of one session. To eliminate bias for longer

trials, we computed the adjusted bin widths using the average trial duration across all sessions, which resulted in the same number of bins to all trials across all sessions.

We used 50% hold-out cross validation to evaluate the predictive power of our model, that is, we used 50% of our data for training, and 50% for testing. The samples were selected at random from all trials, across all attitudes. Figure 4.31 shows the cross-validation prediction, with the R^2 goodness-of-fit, for all 16 EMGs; demonstrating that average EMGs across multiple attitudes can be reconstructed using average firing rates from neurons which **were not** simultaneously recorded. The mean$\pm$SD R^2 value was $77 \pm 7\%$. The mean$\pm$SD R^2 values for the 3 functional muscle groups were: Arm $75 \pm 8\%$, Wrist $76 \pm 6\%$ and Fingers $79 \pm 7\%$. Figure 4.32 shows an example of the best (4.32**A**) and worst (4.32**B**) predictions.

We used a similar model to predict the JAs from the neural firing rates:

$$\overline{JA_j} = b_0 + \sum_{n=1}^{N} b_n \overline{\lambda_n^{50}} \tag{4.9}$$

where

- $\overline{\lambda_n^{50}}$ is the fractional firing rate for neuron n, computed using adjusted $50ms$ bins (see Section 2.2 for details), and averaged over all repeat trials
- $\overline{JA_j}$ is the $j-th$ JA, averaged over all repeat trials to every attitude, computed using the same bins as the firing rates, and lagged by two bins ($100ms$ on average)

Firing rates were averaged across all repeat trials to every attitude; and similarly to the EMG data, the JAs were averaged across all repeat trials to every attitude, across sessions. Adjusted bin widths were computed using the average trial duration across all sessions. Again, we used 50% hold-out cross validation to evaluate the predictive power of our model. Figure 4.33 shows the cross-validation prediction, with the R^2 goodness-of-fit, for all 23 JAs; demonstrating that average JAs, across multiple attitudes, can be reconstructed using average firing rates from neurons which **were not** simultaneously recorded. The mean$\pm$SD R^2 value across all joints was $70 \pm 10\%$, slightly lower than that for the EMG predictions. The JAs are divided to 5 functional groups in the rows of Figure 4.33, and the mean$\pm$SD R^2 value per group are: Wrist $72 \pm 6\%$, MCP Flexion $76 \pm 9\%$, MCP Abduction $61 \pm 18\%$, PIP Flexion $79 \pm 6\%$, DIP Flexion $74 \pm 3\%$. Predictions for MCP

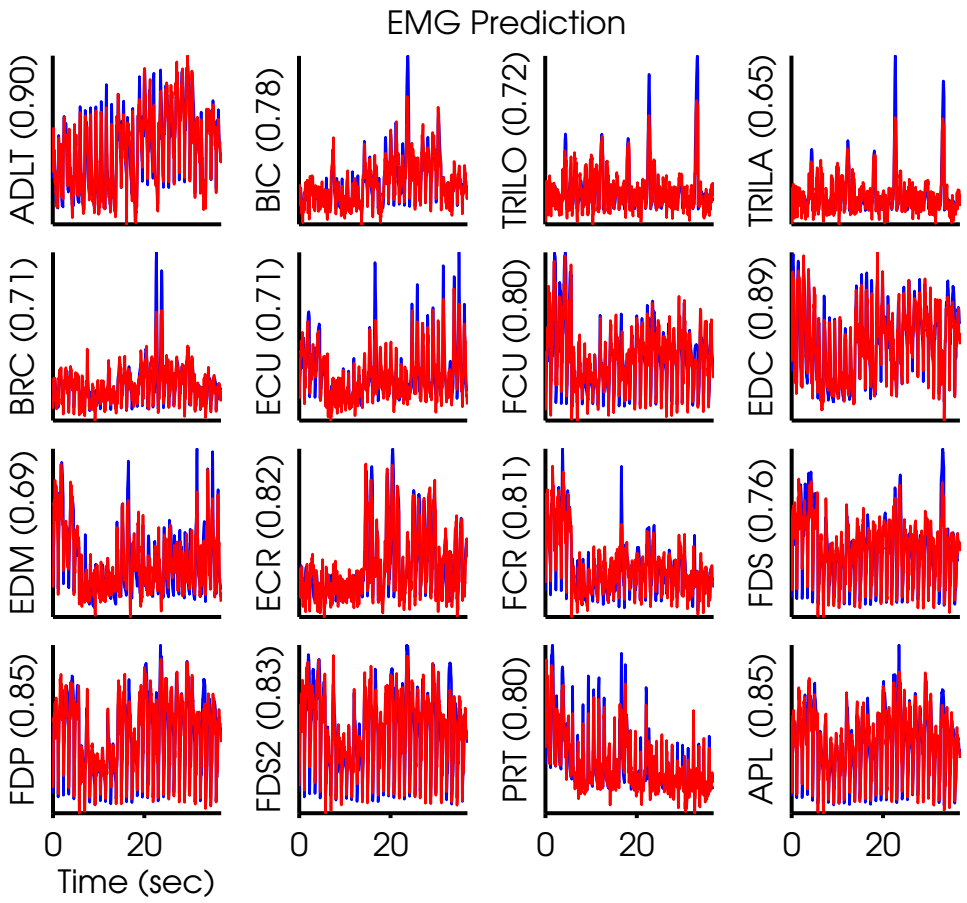

Figure 4.31: **Prediction of EMG from a neural population: monkey E:** Cross-validation predictions of average EMG activity for 16 muscles, using the averaged firing rates of 64 neurons. The R^2 for every muscle is specified on the y-axis.

Abduction were the worst, whereas predictions for the PIP flexion were the best. Figure 4.34 shows an example of the best (4.34**A**) and worst (4.34**B**) predictions.

We have shown in Sections 4.2, 4.3, and 4.4, that JA values and velocities were better predictors of individual neural firing rates, than EMG. However, here we found that the combined activity of 64 sequentially recorded neurons predicted JAs and EMG equally well. We concluded that single-unit activity contained synergistic information related to EMG, not independently present in individual neurons, and independent information related to kinematics. An additional explanation

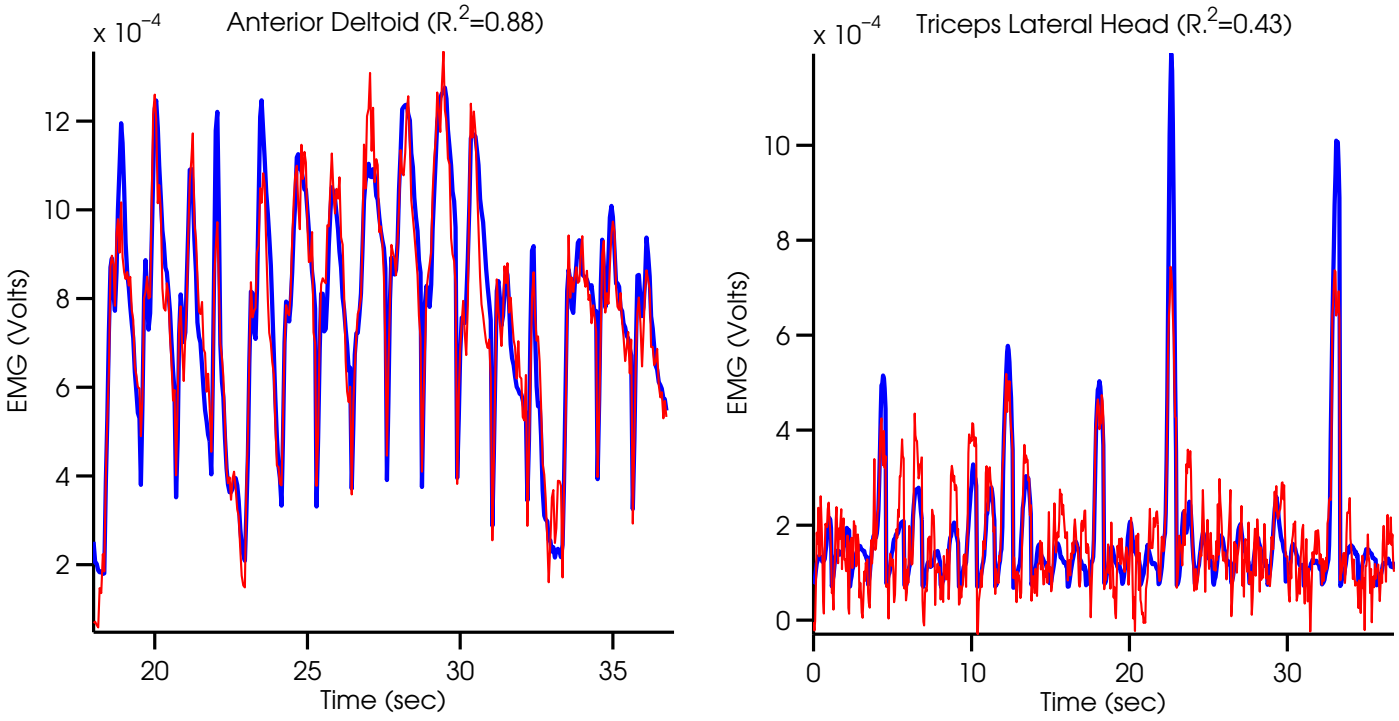

(**A**) Best Prediction

(**B**) Worst Prediction

Figure 4.32: **Best and worst EMG prediction: monkey E:** Taken from Figure 4.31.

could be that neurons facilitate different muscles in different task epochs, suggesting that their functional connectivity to muscles is dynamic. We investigate that further in Chapter 6.

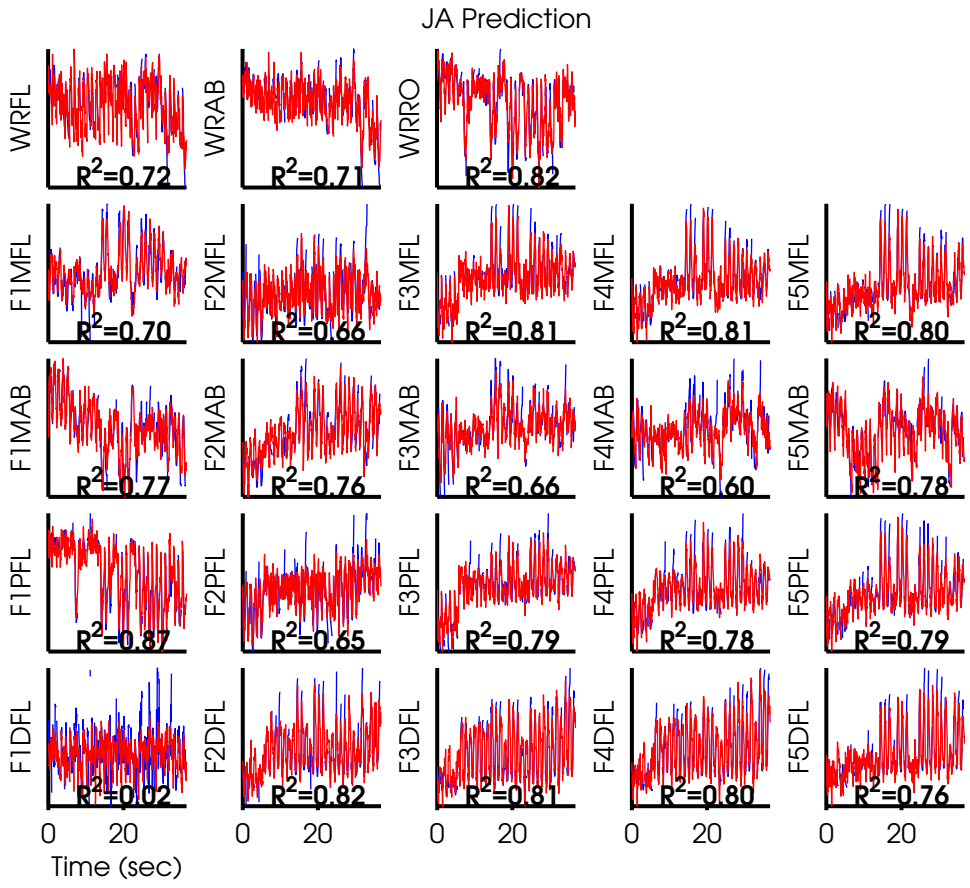

Figure 4.33: **Prediction of JA from a neural population: monkey E:** Cross-validation predictions of 23 mean JA, using the averaged firing rates of 49 neurons. The R^2 for every JA is specified on the plot.

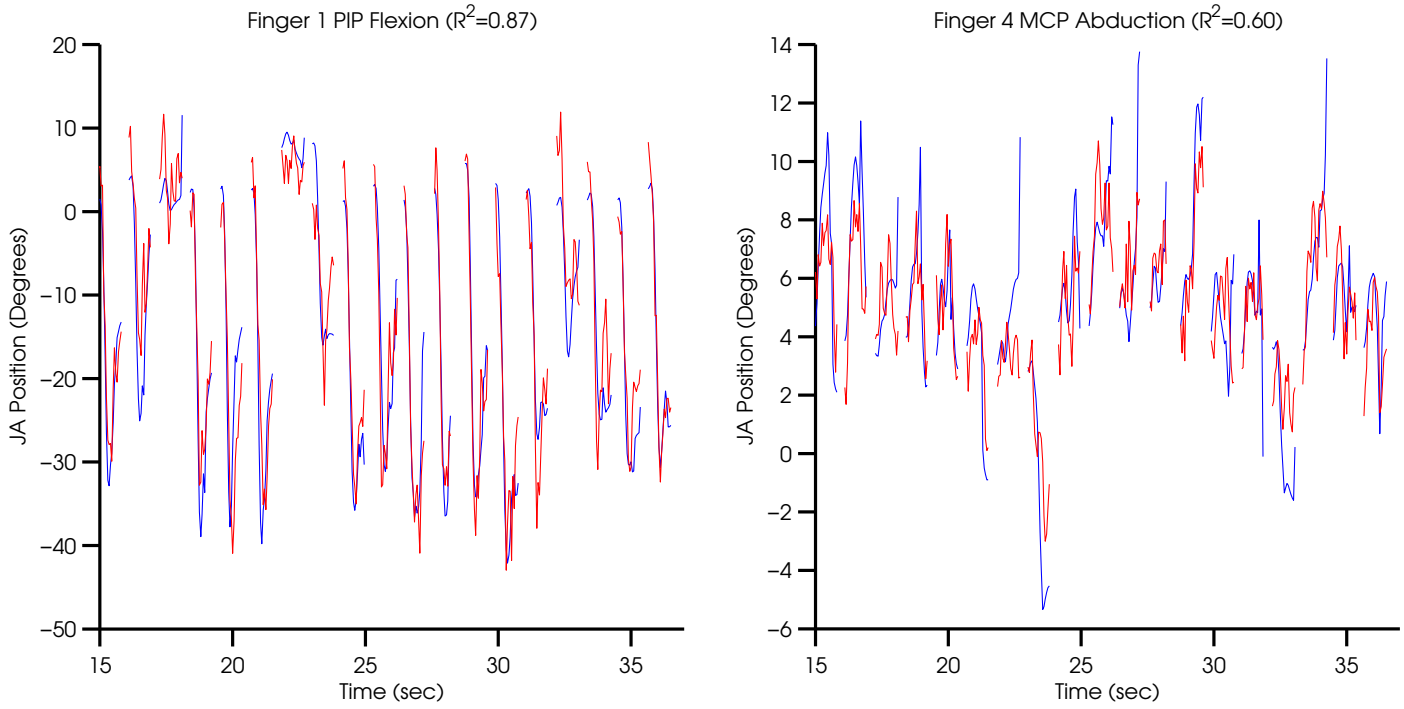

(**A**) Best Prediction

(**B**) Worst Prediction

Figure 4.34: **Best and worst JA prediction: monkey E:** Taken from Figure 4.33.

5.0 NOVEL METHODS FOR DETECTION OF FUNCTIONAL CONNECTIVITY

In Chapter 6, we investigate long- and short-time scale functional connectivity between cortex and muscles. Short time-scale connectivity is detected as post-spike effects (PSEs), which are brief changes in EMG, time-locked to spikes from a cortical neuron. The methods presented in this chapter, allowed us to perform objective and automatic PSE detection in our datasets, which contained a small number of spike-triggers for every attitude.

This chapter has been submitted as a paper titled: "Methods for detection of functional connectivity between cortex and muscles", by Sagi Perel, Andrew B. Schwartz, Valérie Ventura.

5.1 ABSTRACT AND KEYWORDS

Direct, monosynaptic cortical output to motoneurons originates from corticomotoneuronal cells (CMN), located predominantly in the primary motor cortex. Post-spike effects (PSEs) in averages of spike-triggered EMG snippets provide physiological evidence of connectivity between CMN cells and spinal motoneurons innervating skeletal muscles. PSEs within a narrow window following the trigger are currently detected using either a visual inspection of a spike-triggered average (SpTA) or the Multiple-Fragments-Analysis test (MFA, Poliakov and Schieber [53]). SpTA requires a large number of spikes to clearly visualize the PSE and lacks a statistical significance measure, so it cannot be automated easily. More formal techniques exist to assess SpTA significance (Kasser and Cheney [35], Lemon et al. [37]), but their statistical properties have not been studied, so their reliabilities are unknown. MFA was suggested as a more rigorous PSE detection method, but its reliability is also unknown.

In this paper, we investigate the statistical properties of PSE detection via SpTA and MFA. We show that the rate of spurious detections from SpTA visual inspections is very sensitive to how one decides that a PSE exists. Sensible decision rules tend to be conservative, and thus have low probabilities of detecting PSEs. We show that MFA is neither conservative nor liberal, but has a rate of spurious detections that matches the chosen significance level. We also show that MFA often has higher probability than SpTA to detect PSEs, including in small samples. But MFA is limited to detecting PSEs in the $6-16ms$ post-spike window, which is mostly appropriate for monosynaptic connectivity. We develop a scan test that allows PSE detections at any latency; this test yields a p-value to assess PSE significance instead of relying on visual inspection.

On-line PSE detection is useful to inform the investigator of significant PSEs while data are collected. A visual SpTA inspection is difficult to implement; MFA is inconvenient because it requires partitioning the data in fragments. We propose an automatic test that is functionally equivalent to MFA, but better suited for real-time PSE detection: the single snippet analysis (SSA). We provide practical guidelines to apply SSA and SSA-scan tests for automatic off- and on-line PSE detection.

Finally, MFA and SSA tests and their scan versions rely on assumptions, such as large samples and linear SpTA baselines. We find that these tests are mostly robust to assumption misspecification. Nevertheless we propose bootstrap diagnostics to detect deviations from the assumptions, and to correct p-values when needed. In particular, we can diagnose when SpTA non-constant baselines affect the tests, and correct them, without explicitly estimating the baselines.

In summary, the primary utility of the automatic tests is objective and more efficient PSE detection. They detect functional connectivity without making assumptions about underlying anatomy. They can be applied automatically to many datasets, and can further be conducted on-line, while the data are collected. The scan test also provides a putative classification of PSEs based on the latencies at which they are detected. However, SpTA remains the essential tool for definitive classification of PSEs.

Electromyography (EMG), Corticomotoneurons (CMN), Post-spike effect (PSE), Inter-spike interval (ISI), Spike-Triggered Average (SpTA), Multiple-Fragments-Analysis (MFA), Single-Snippet Analysis (SSA), Scan-Test

5.2 INTRODUCTION

The motor cortex was originally defined as an area of cortex from which muscle contraction was elicited (Fritsch and Hitzig [20]). We now know that both direct (monosynaptic) and indirect (polysynaptic) projections originate from the motor cortex and terminate in the motoneuronal pools of the primate spinal cord. Projections from subcortical and spinal structures also converge in these pools, and together, determine the excitability of the motor units responsible for muscle contraction. A key research question centers on the relative contributions of these different sources and how they combine to generate movement.

A neuron's effect on motoneuron excitability is typically detected with the classic method of spike-triggered averaging (SpTA,Fetz et al. [16], Fetz and Cheney [12], McKiernan et al. [40]). After each cortical spike, a short EMG segment (snippet) from a target muscle is collected. If the cortical neuron generates a post-spike effect (PSE) in the EMG, a characteristic waveform will emerge in the average of these EMG snippets. Since many factors in addition to the recorded spikes contribute to muscle excitability, the effect of a single neuron on the EMG is weak and requires many snippets to be averaged for a clear result, even in the case of monosynaptic projections.

SpTA is a computationally simple test, but it has limitations. First, the large number of spikes required to clearly visualize the PSE (at least 2000, but up to 20000 spikes, Fetz and Cheney [12]) limits the number of unique behavioral conditions possible in an experiment. Second, SpTA relies on visual inspection and does not provide a statistical significance measure, such as a p-value, so detection is subjective; and it may be hard to distinguish real PSEs from fluctuations in the EMG average, especially in small samples. It is also tedious when many datasets must be inspected. More formal techniques have been suggested to assess PSE significance from an SpTA (Kasser and Cheney [35], Lemon et al. [37]), but their properties, statistical power and significance level, have not been studied, so their reliabilities are unknown. The power of a test is the probability that it will detect real PSEs, and the significance level, denoted by α, the maximum rate of spurious detections. The significance level α is especially important, because when a PSE is detected, it gives us the guarantee that the PSE is spurious with probability less than α. Therefore, a PSE detection test is trustworthy only if its observed significance level matches the nominal chosen level α, regardless of the number of spike-triggers in the dataset. It is particularly important that the

test be trustworthy in small samples, when visual inspections of SpTAs cannot easily distinguish possible PSEs from background EMG variations.

In this paper, we first review another formal PSE detection test, the multiple-fragment analysis (MFA, Poliakov and Schieber [53]), and we offer a simpler, more flexible, and approximately equivalent alternative: the single snippet analysis (SSA). We then compare the performances of SSA, MFA, and SpTA, and propose an additional test designed to find PSEs at any latency, the SSA-scan test. We study the statistical properties of these tests and propose diagnostics tools to validate their p-values. These tests can be used on-line, while data are collected, to inform the investigator of significant PSEs.

5.3 METHODS

We review the methods currently available to detect PSEs at fixed latencies (sec. 5.3.1), propose a method that is approximately equivalent but more direct to calculate (sec. 5.3.2), and introduce the scan test for the detection of PSEs at any latency (sec. 5.3.3). Bootstrap methods are used to check the validity of the assumptions the tests rely on, and to adjust p-values when they are biased as a result of questionable assumptions (sec. 5.3.4).

5.3.1 POST SPIKE EFFECTS ARE CURRENTLY DETECTED USING SPIKE TRIGGERED AVERAGING OR MULTIPLE-FRAGMENT ANALYSIS

A spike-triggered average (SpTA) shows the changes in a muscle's EMG activity following spikes from a cortical neuron. Pre-analysis, EMG is usually rectified to minimize the cancellations caused by averaging overlapping positive and negative components of motor unit action potentials. Given K cortical spikes and simultaneously recorded EMG activity, rectified spike-triggered EMG snippets are collected around every spike, and the SpTA is computed by averaging these snippets across time according to

$$SpTA(t) = \frac{1}{K}\sum_{k=1}^{K} EMG_k(t), \tag{5.1}$$

where typically, $t = -20:40ms$ relative to the spike trigger at $t = 0$. A wide interval allows the base-line mean (M) and standard deviation (SD) of EMG fluctuations in the pre- and post-trigger periods to be estimated. A PSE at time t^* is considered present if $SpTA(t)$ exceeds $M \pm 2SD$ in a period around $t = t^*$. PSEs are further divided into post-spike facilitation and suppression effects. The times when the SpTA exits and re-enters the bounds are called the PSE onset and offset; the extremum between onset and offset is called the peak of the effect. The peak width at half maximum (PWHM) is the excursion width at half the height between the PSE peak and the baseline mean. PSEs are also classified as pure or synchrony effects. If the PSE peak or trough begins at a latency suitable for the conduction time from the cortical neuron to the muscle, and is narrow enough to reflect monosynaptic or disynaptic connectivity, the PSE is considered as pure. However, many PSEs do not meet this criteria and are classified as synchrony PSEs, because the PSE onset is earlier than the shortest possible conduction time from cortex to muscle, or the PSE is too wide for a single synaptic input. Synchrony PSEs appear when the motoneuronal pool receives synaptic inputs synchronized with spikes from the recorded cortical neuron (see Schieber [61] for details).

An alternative detection test is the Multiple-Fragments Analysis (MFA) of Poliakov and Schieber [53]. The K EMG snippets previously used in Eq. 5.1 are now divided into $G = \sqrt{K}$ groups (G fragments), and their respective SpTAs calculated; let $SpTA_g(t)$ denote the SpTA in fragment $g = 1,\ldots,G$. Then for all g, one calculates the contrast between the peak and the baseline of $SpTA_g(t)$ as

$$X_g = \overline{SpTA_g}([6,16]ms) - \frac{1}{2}\left(\overline{SpTA_g}([-4,6]ms) + \overline{SpTA_g}([16,26]ms)\right),$$

where $\overline{SpTA_g}([a,b]ms)$ is the average of $SpTA_g(t)$ values over $t \in [a,b]$ (the spike-trigger is at $t = 0$).

Values of X_g that deviate significantly from zero provide evidence of a PSE, which Poliakov and Schieber formalize by calculating the test statistic

$$T_{MFA} = \frac{\bar{X}}{SE(\bar{X})}, \tag{5.2}$$

where $\bar{X}$ is the sample mean of the X_g's and $SE(\bar{X})$ is its sample standard error. Then the null hypothesis of no PSE is rejected at the 5% significance level if $|T_{MFA}| > 1.96$ (this is a two tailed

t-test); the p-value is $2(1-\Phi(T_{MFA}))$, where Φ is the standard normal cumulative distribution. This test relies on the assumption that T_{MFA} is standard normal when no PSE is present; we discuss assumptions in sec. 5.3.4.

MFA test variants There are two MFA test variants. Both use $G=\sqrt{K}$ fragments, as advocated by Poliakov and Schieber, to ensure that each fragment contains a reasonably large number of EMG snippets, but they use a different repartition of snippets per fragment: Poliakov and Schieber divide the experimental time into G periods of equal length and assign to fragment g the snippets in period g, while Davidson (Davidson et al. [9]) forms fragments of equal sizes by grouping every $\sqrt{K}$ consecutive snippets. We denote the corresponding test statistics by T_{MFA} and T_{MFAE} respectively, where the E in MFAE stands for "equal number of snippets".

One-sided tests If suppression or facilitation PSEs are of particular interest, we may prefer a one- rather than a two-sided test to gain power to detect the PSEs of interest. The tests are modified trivially by using only one tail of the null distribution of T to calculate p-values. Specifically, we reject the hypothesis of no facilitation (or no suppression) PSE at the 5% significance level if $T_{MFA}>1.645$, with p-value is $(1-\Phi(T_{MFA}))$ (or $T_{MFA}<-1.645$, with p-value is $\Phi(T_{MFA})$).

5.3.2 SINGLE SNIPPET ANALYSIS (SSA) IS CONCEPTUALLY SIMPLER THAN MULTIPLE FRAGMENT ANALYSIS

The SpTA and MFA tests rely on comparing the value of the SpTA at a fixed latency window to the baseline SpTA value adjacent to that window. The former uses a direct comparison, while the latter compares their difference to zero, since $\bar{X}$ in eq. 5.2 is effectively the average SpTA in the fixed window, minus the average SpTA adjacent to that window. The single snippet analysis (SSA) test measures the same contrast using individual rectified snippets, rather than fragment averages. SSA calculates the test statistic

$$T_{SSA}=\frac{\bar{Y}}{SE(\bar{Y})}, \tag{5.3}$$

where

$$Y_k=\overline{EMG_k}([6,16]ms)-\frac{1}{2}\left(\overline{EMG_k}([-4,6]ms)+\overline{EMG_k}([16,26]ms)\right),$$

is the mean of EMG snippet k in the fixed window minus its baseline in the adjacent windows, $\bar{Y}$ is their sample average, and $SE(\bar{Y})$ is the sample standard error of $\bar{Y}$. Then the null hypothesis

of no PSE is rejected at the 5% significance level if $|T_{SSA}| > 1.96$, with p-value $2(1-\Phi(T_{SSA}))$. One-sided tests can also be carried out, as in the previous section. And like the MFA test, the SSA test relies on the assumption that the null distribution of T_{SSA} is standard normal; we discuss assumptions in sec. 5.3.4.

The SSA test is effectively an MFA test with only one snippet per fragment, so we should not expect much difference between the MFA/MFAE and SSA tests in practice. We introduced T_{SSA} because its calculation is more direct than T_{MFA} (there is no need to fragment and average the data) and perhaps more intuitive. Due to its simplicity, SSA is also better suited for detecting PSEs on-line, while data are being collected (see Appendix F). It is also more flexible, because one can easily combine spike triggers from non-consecutive time epochs, since only one Y_k value per spike is required to calculate T_{SSA}.

5.3.3 A FIXED LATENCY TEST CAN BE SCANNED ACROSS THE SPTA TO DETECT PSES AT ANY LATENCY

Let T denote the fixed-latency detection statistic of choice, be it T_{MFA}, T_{MFAE}, or T_{SSA}. When we test for a PSE, the assumption is that the SpTA has maximal differential amplitude at a certain lag post-spike (e.g. approximately $l = 11ms$ for a classic monosynaptic PSE). Depending on axonal and motoneuronal conduction velocities, the largest differential SpTA amplitude might occur at a different lag, which we would like to determine. Our detection test consists of scanning T along the EMG snippets, collecting the largest value of T, and testing its statistical significance. More specifically, letting $T(l)$ denote the statistic calculated on the portion of the EMG snippets centered at time l, so that $T(l)$ with $l = 11$ ms is the test statistic for fixed-latency detection in eqs. 5.2 or 5.3, we propose to use the following scan test statistic:

$$S = \max_{l} T^2(l) \tag{5.4}$$

for the detection of PSEs at any latency. If there is no PSE, $T(l)$ should not be significantly different from 0 for any l, and S should be small. But if there is an effect at lag l^*, then $T^2(l^*)$ should be comparatively larger than $T^2(l)$ for $l \neq l^*$, and thus S should be larger. Hence a comparatively

large value of S is evidence of a facilitation or suppression PSE in the data. To quantify what *comparatively large* is, we need the null distribution of S, i.e. its distribution under the null hypothesis that there is no effect in the data.

Under the null hypothesis, $T(l)$ is approximately standard normal for all $l = 1,\ldots,L$, as argued in Secs 5.3.1 and 5.3.2, so $T^2(l)$ is approximately Chi-square distributed with one degree of freedom (χ^2_1). If we assume that the $T(l)$ are mutually independent, then a standard probability calculation yields the null distribution of S,

$$f_S(s) = L f_{\chi^2_1}(s)[F_{\chi^2_1}(s)]^{L-1}, s \geq 0, \tag{5.5}$$

where $f_{\chi^2_1}$ and $F_{\chi^2_1}$ are the χ^2_1 probability and cumulative probability density functions, and L is the number of time points scanned. Then if s_{obs} denotes the observed value of the scan test statistic, the p-value is

$$p = P(S \geq s_{obs}) = \int_{s_{obs}}^{+\infty} f_S(s)ds, \tag{5.6}$$

where we integrate from s_{obs} to $+\infty$ since large values of S provide evidence against the null hypothesis of no PSE. We reject the null hypothesis when $p \leq 5\%$, and conclude that there is a PSE at lag $\hat{l} = \arg\max_l T^2(l)$. Note that the integral in eq. 5.6 is intractable so it must be calculated numerically using a computer package or via a bootstrap simulation (sec. 5.3.4). See also Appendix G for an equivalent test, whose p-value is trivial to calculate.

Eq. 5.5 relies on $T(l), l = 1,\ldots,L$, being mutually independent, an assumption that is clearly violated since successive values of $T(l)$ use overlapping EMG portions. We reduce the dependence between successive values of $T(l)$ by scanning $T(l)$ only at every m lags; for example, with $m = 2$, we scan $T(l)$ at $l = 1,3,5,....$ Then Eq. 5.5 still provides the null distribution of S, with L denoting the number of scanned lags l. The bootstrap methods in sec. 5.3.4 are useful to determine a value of m that satifies the assumptions. We found that $m = 3ms$ was the smallest value that reduced the serial correlation enough to provide accurate p-values, without decreasing the power to detect PSEs. Details and examples are in Appendices B, E and F.

One-sided tests If facilitation PSEs are of primary interest, we prefer a one- rather than a two-sided test to gain power. In that case we use the test statistic

$$S = \max_l T(l), \tag{5.7}$$

whose null distribution is easily shown to be

$$f_S(s) = L\phi(s)[\Phi(s)]^{L-1}, s \geq 0 \tag{5.8}$$

where ϕ and Φ are the standard normal probability and cumulative probability density functions. The p-value is calculated as per eq. 5.6, and the null hypothesis of no facilitation PSE rejected if $p \leq 5\%$. If detecting suppression PSEs is of primary interest, we use the one-sided test statistic $S = \max_l(-T(l))$, with null distribution and p-value as in eqs. 5.8 and 5.6.

5.3.4 THE BOOTSTRAP CAN BE USED TO DIAGNOSE AND REMEDY VIOLATIONS OF PARAMETRIC TEST ASSUMPTIONS

All fixed-latency detection tests rely on the assumption that the null distribution of the test statistic T (eqs. 5.2 or 5.3) is normal with mean zero and variance one. This assumption might be violated for reasons that cannot always be anticipated. For example, the normality assumption is justified by the central limit theorem for large sample sizes; but how large a sample we need depends on how far from normal the distributions of X_g in eq. 5.2 and Y_k in eq. 5.3 are. The mean of T will not be zero if the SpTA is not linear in t, as pointed out by Davidson et al. [9]. The variance of T might deviate from one if $SE(\bar{X})$ and $SE(\bar{Y})$ are poor estimates of the true standard errors, which could happen if X_g and Y_k have excessively skewed distributions. The scan test based on S (eqs. 5.4,5.7) relies in addition on the $T(l)$ being mutually independent.

Questionable assumptions can bias p-values. Then the tests' rates of spurious detections might not match the nominal significance level α, in which case the tests are not trustworthy. Biased p-values that are larger than about 10% should not be of much concern, since an adjustment is unlikely to change the outcome of the test (that is, retain the hypothesis of no PSE). But assumptions should be checked when p-values are close to the significance level α. We do this using bootstrap diagnostics (Canty et al. [6]).

To check the assumptions of the fixed-latency test based on T, we obtain $R = 100$ bootstrap values of T, t_r^*, $r = 1,\ldots,R$, by repeatedly applying fixed-latency tests on snippets that do not contain PSEs, extracted from jittered spike trains (see the full algorithm in Appendix A). These are values we would expect T to have if the null hypothesis of no PSE was true. Hence the distribution

of T^* approximates the null distribution of T. To check if that distribution is the assumed standard normal, we generate a normal quantile plot of the t_r^*, and confirm that T is normally distributed if the points do not significantly deviate from a straight line. Further, if the sample mean m and sample variance s^2 of the t_r^*'s do not significantly deviate from 0 and 1, the fixed-latency detection parametric test is valid and the parametric p-value can be trusted. If the normal plot is straight but m or s^2 deviate from their nominal values of 0 and 1, the p-values should be calculated from a normal distribution with mean and variance m and s^2 rather than from a standard normal distribution. If the normal plot is not straight, a bootstrap p-value should be obtained using a large bootstrap simulation; see Appendix A. This sequential process is outlined in Figure 5.1.

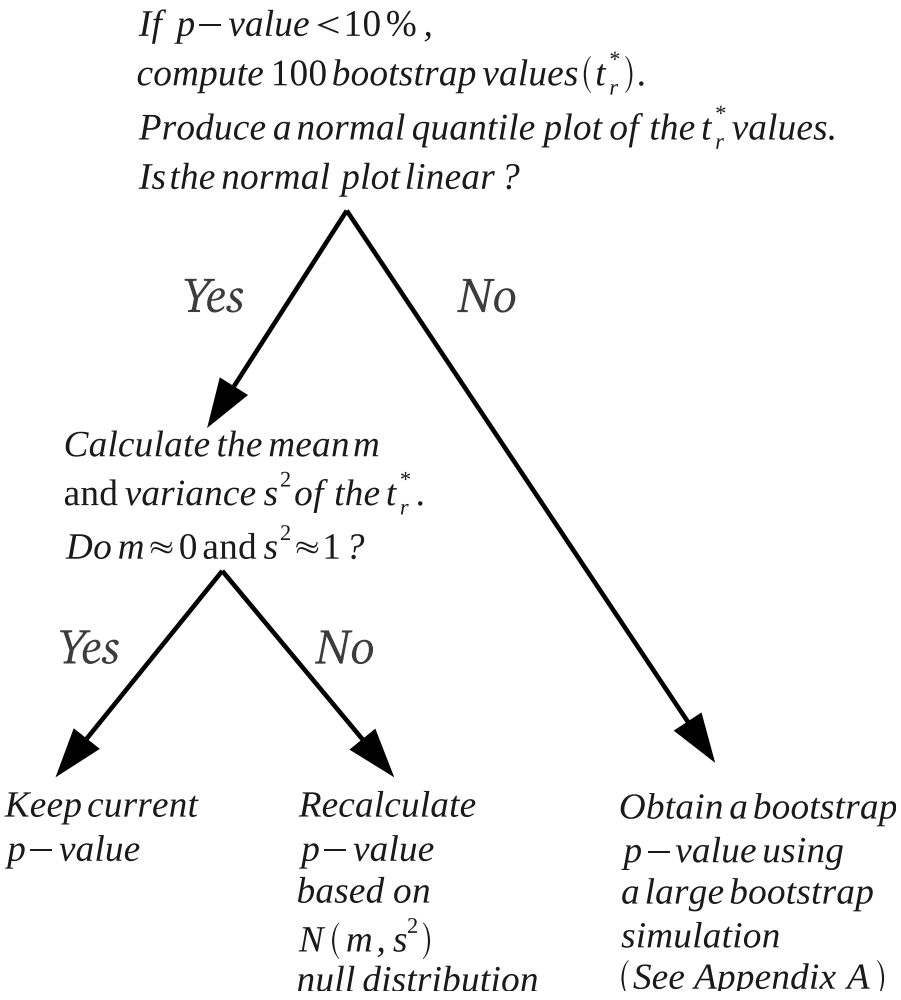

Figure 5.1: **Diagnosing and correcting violations of parametric test assumptions**

To vet the scan test based on S, we produce a quantile-quantile (QQ) plot of $R = 100$ bootstrap values of S, obtained by the algorithm in Appendix A, versus the theoretical quantiles of the nominal null distribution f_S in eq. 5.5 or 5.8. If the points lie near the line with mean 0 and slope 1, the parametric p-value can be trusted. Otherwise a bootstrap p-value should be calculated (see Appendix A). Appendix B contains examples of diagnostic plots.

5.4 RESULTS

Our goals are to examine the properties of the MFA, SSA, and SSA-scan tests, and to compare these automatic tests to PSE detection using the SpTA. We begin with short descriptions of the datasets we used. We continue with a review of the properties of statistical tests of hypotheses in Section 5.4.2, which serves as a guide for comparing the various PSE detection tests in Section 5.4.3. In Section 5.4.4, we focus on detecting PSEs of various strengths and widths; and in Section 5.4.5, on PSE detection at any post-spike latency, to illustrate the application and properties of the SSA-scan test. Finally, in Section 5.4.6, we consider PSE detection in the presence of non-stationary baselines.

5.4.1 EXPERIMENTAL DATASETS

The digit-flexion dataset was collected in Dr. Marc Schieber's lab. It consists of simultaneously recorded spike trains from 2 neurons and EMG activity from 9 muscles, while a monkey performed visually cued individuated flexion and extension movements of the right fingers and/or wrist (see Schieber [61] for details). One neuron showed visible post-spike effects (PSEs) in 5 muscles and the other in 8 muscles. EMG activity was recorded using stainless steel wire electrodes implanted percutaneously, bandpass filtered at $300 - 3000Hz$, and sampled at $5000Hz$.

The grasp dataset was collected in our lab, while a monkey performed reach-to-grasp movements to a variety of objects at different spatial locations and orientations. Every unique combination of object and location/orientation was presented 20 times, and generated a total of up to 2000 cortical spikes during the movement, a sample size often too small to detect PSEs reliably using

SpTA. This dataset contains spike trains from 171 neurons and EMG activity from 16 muscles, recorded over 34 days. EMG activity was recorded using custom made patch electrodes sutured to the epimysium (adapted from Miller et al. [42]), bandpass filtered at $100-2000Hz$, and sampled at $4882.8Hz$. This task involves higher levels of muscle contraction than unloaded wrist/digits flexion/extension, which results in higher mean EMG levels.

The precision-grip dataset was collected in Dr. Roger Lemon's lab. It consists of simultaneously recorded spike trains from 9 neurons and EMG activity from 7 muscles, while a monkey squeezed two spring-loaded levels between thumb and index finger (see Jackson et al. [33] for details). EMG activity was recorded using custom made patch electrodes sutured to the epimysium (adapted from Miller et al. [42]) and sampled at $5000Hz$.

5.4.2 PROPERTIES OF TESTS: POWER AND RATE OF SPURIOUS DETECTIONS

A statistical test of hypotheses yields either the correct decision, or one of two types of error. In the current context, a type 1 error occurs when the test detects a PSE that does not exist (this is a spurious detection), and a type 2 error when the test fails to detect an effect. The probabilities of these two error types vary in opposite directions, so errors cannot be eliminated. The accepted way to proceed is to design a test that has a pre-specified maximum probability of a type 1 error, $\alpha = 5\%$ say, usually referred to as the significance level. Then if a PSE is detected, it means either that the PSE exists in the data, i.e. the test yielded the correct decision, or that the test made a spurious detection. Since the truth is unknown, we can never be sure which conclusion is the correct one, but at least we know that the probability of a spurious detection is less than $\alpha\%$. For a detection test to be "trustworthy", it is therefore crucial that its rate of spurious detections be less than the nominal value α; in that case, we say that the test has "an assured significance level". A test should also have high power, where power is defined as the probability of detecting an effect, or equivalently as one minus the probability of making a type 2 error. When there is no effect in the data, the probability of detecting a spurious effect is α; hence the power equals α. Otherwise, the power increases with the strength of the effect and with the number of samples. However, for a given significance level α and fixed sample and effect strengths, different tests can have different

power levels. To maximize the chances of detecting PSEs, it is therefore important to identify the tests that have more power.

We illustrate these ideas based on the power curves for the SSA and MFA/MFAE tests plotted in Figure 5.2AB. Figure 5.2A shows power against sample size K, and Figure 5.2B against the strength p of the PSE, where $p = 0\%$ means that there is no effect in the data, and $p = 100\%$ means that the effect is strong. We explain below exactly how we generated these curves, but we first focus on their interpretation. First, we see that power indeed increases with sample size K and effect strength p, which means that it is easier to detect an effect if it is strong or if we have a lot of data (this is true intuitively and theoretically). Second, when there is no effect in the data (Figure 5.2B at $p = 0\%$), the powers of all three tests match the nominal level of spurious detections, $\alpha = 5\%$: these tests have assured significance levels and thus provide trustworthy conclusions. Third, the three tests have similar power curves, so none is better than the others. In the next sections, we show that these tests are often more powerful than PSE detection using the SpTA.

Estimating power. To estimate the power curves in Figure 5.2, and in all subsequent power figures, we first selected a "parent dataset" whose SpTA displayed a PSE, as shown in Figure 5.2C. To create a dataset of size K, we selected a spike trigger at random from the parent dataset, and retained that spike and its $(K-1)$ successors; we wrapped the spike train if fewer than $(K-1)$ spikes followed the selected spike. We then extracted the K corresponding EMG snippets, to which we applied the detection tests. We repeated this 1000 times, and estimated the power of the SSA and MFA tests by the proportions of times they each detected PSEs. We then repeated the simulation for many values of K, and plotted the detection proportions of each test against K in Figure 5.2A. We used half the number of spike triggers in the parent datasets as the maximum value of K, to avoid simulating the same repeat datasets. To create a test dataset with effect strength p, we first sampled a dataset of size K as described above, with K fixed at half the total number of spike triggers. In that dataset, we then jittered (normal jitter with SD $100ms$) the spikes times of a randomly selected sub-block of size $K \cdot (100 - p)$ to remove time-locked PSEs, and kept the remaining $K \cdot p$ spikes unchanged. We extracted the corresponding EMG snippets, to which we applied the detection tests. We estimated the power of the SSA and MFA tests by the proportions of times the tests detected PSEs in 1000 such samples. Note that when $p = 0\%$, all spike triggers are jittered, so the test datasets contain no time-locked PSEs. Conversely, no triggers are jittered

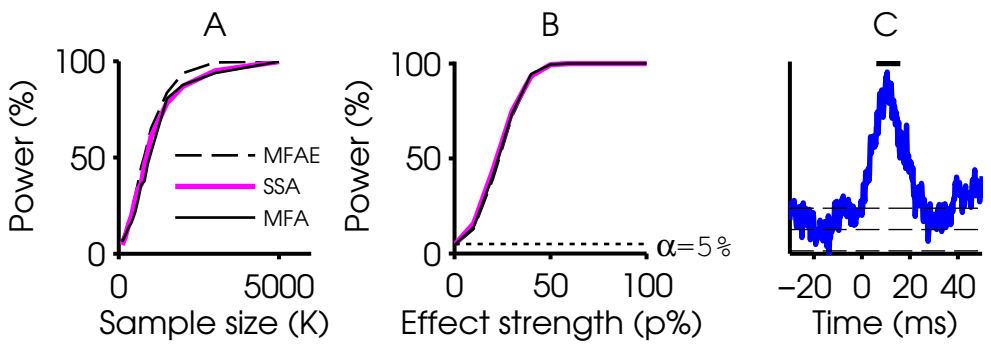

Figure 5.2: **Power comparison between MFA/MFAE and SSA tests.** **(A)** Power as function of sample size K (number of spikes used). For every K, power is estimated as the percentage of detections in 1000 test-datasets. **(B)** Power as function of effect strength p (percentage of non-jittered snippets), with sample size held constant at half the number of spikes in the parent dataset. For every p, power is estimated as the percentage of detections in 1000 test-datasets. At $p = 0\%$, there is no PSE in the data. At $p = 100\%$, the effect strength is the same as in the parent dataset. **MFA/MFAE and SSA tests have comparable power levels.** **(C)** SpTA for the digit-flexion parent dataset, calculated using all 19067 spikes. The vertical bar on top spans the $6-16ms$ window used by the automatic detection tests. The horizontal dashed lines are the SpTA baseline mean and mean$\pm$2SD in baseline window $[-20ms, -10ms]$.

when $p = 100\%$, so the test datasets contain PSEs of strengths similar to the parent dataset (Figure 5.2C).

The power curves in Figure 5.2 depend on the parent dataset used for the simulation. To verify that our conclusions do not depend on the parent dataset, we reproduced the same plots using 11 single-digit and 3 grasp parent datasets; some of these plots are in Appendix C. Our simulations confirmed that SSA and MFA/MFAE were trustworthy tests, with rates of spurious detections approximately equal to the nominal significance level $\alpha = 5\%$. SSA and MFAE had similar power curves, and these were higher than the power curves of MFA, except in two digit-flexion datasets, one of which is shown in Appendix C. These two datasets were collected from muscles with low EMG contraction levels, and thus contained a large proportion of low-valued EMG snippets;

no other datasets shared that characteristic. The chronological order of the low content snippets appeared to be key to MFA performing better, because all tests became equally powerful when we permuted the EMG snippets at random before forming the fragments.

5.4.3 SpTA AND SSA POWER COMPARISON

SpTA is the current gold standard for identifying, evaluating, and classifying PSEs. PSEs are detected by visual inspection of bumps or troughs in the SpTA. MFA/MFAE and SSA tests are designed to detect PSEs automatically, without human intervention. In this section we show that SpTA visual detection does not have an assured significance level, so it is not a trustworthy test. We also show that the SSA test has an assured significance level, and more power to detect PSEs than SpTA. However, we stress that SSA is not designed to classify the PSEs that are detected; SpTA is still required for that purpose, so we do not suggest that the automatic tests replace SpTA altogether. We do not show results for the MFA/MFAE tests, because they are approximately functionally equivalent to SSA, as noted in the previous section.

Automated SpTA detection test. To produce the results and graphs in this paper, we applied PSE detection tests to almost half a million datasets. Visual examinations of that many SpTAs would be exceedingly time consuming, so we formulated an automated SpTA detection rule that emulates visual examination. For every SpTA, (i) we calculated its mean M and standard deviation SD in a baseline window; we considered three baseline windows: $[-5,5]ms$ around the spike-trigger (Kasser and Cheney [35]), $[-20,-10]ms$ pre-spike trigger (McKiernan et al. [40]), and $[-30,-10]ms$ pre-spike trigger (Schieber [61]); the three corresponding automated SpTA tests are called SpTA1, 2, and 3. (ii) To mimic the scanning of a visual inspection, we identified all SpTA excursions outside the $M \pm 2SD$ lines, and retained those with onset times in the $[-5,20]ms$ range as potential PSEs. (iii) We calculated the areas of these excursions, and determined the peak width at half-maximum (PWHM) of the excursion with the largest area. If that PWHM exceeded a $3ms$ threshold, the excursion was deemed a PSE; we chose $3ms$ so the test would have power to detect the narrow PSEs that often occur when the number of spike triggers is small; we discuss that choice further below. Finally, in datasets where the SpTA exhibited a ramping baseline, we subtracted from the SpTA its fit from a linear regression, prior to applying the automated SpTA

test (Bennett and Lemon [2]). SSA was corrected automatically by applying the procedure in sec. 5.3.4 and Figure 5.1. This procedure consists of implicitly subtracting a non-parametric estimate of the SpTA baseline; see sec.5.4.6.

This automated procedure is quite faithful to a visual inspection, but it may be more liberal, i.e. detect PSEs more often than a visual inspection would. Indeed, investigators sometimes use additional features in the SpTA to decide on PSE significance: a small dip in the SpTA prior to the PSE onset is often present in PSEs thought to be monosynaptic, while the presence of multiple excursions outside of the mean $\pm$ 2SD bounds might be taken as evidence against PSE significance. Hence human visual PSE detection is somewhat more conservative than detection using the automated SpTA test, which we will keep in mind when comparing power curves.

We applied SSA and automated SpTA tests to datasets simulated from the single-digit parent dataset, whose SpTA in Figure 5.3C contains a pure PSE (PWHM=5ms). The simulation is the same as for Figure 2, and is described in the previous section. Figure 5.3AB shows the resulting power curves as functions of sample size K and effect strength p: SSA is clearly more powerful than the automated SpTA tests, for all sample sizes and effect strengths. For example, Figure 5.3A shows that in datasets of size $K = 7000$ spike triggers, the probability that SSA will detect the PSE is close to 100%, whereas the powers of the automated SpTA tests are about 60-70%; the power of SpTA visual inspection might yet be lower, as mentioned above. Figure 5.4 also shows the SpTAs of three randomly selected test datasets of size $K = 800$, 1000, and 7000. These datasets do contain PSEs, since they are sub-sampled from the data whose SpTA is in Figure 5.3C, but the PSEs are hard to detect by the naked eye in such small samples. When we applied the detection tests, SSA detected PSEs in all cases, with p-values $p = 0.009$, 0.007, and 0.001, respectively. All automated SpTA tests failed to detect PSEs in Figure 5.4AB, and only test SpTA1 (baseline window $[-5, +5]ms$) detected a PSE in Figure 5.4C.

We applied the same simulation to 10 other single-digit parent datasets and 19 precision-grip parent datasets, which spanned a continuum from pure PSEs to combinations of pure-synchrony PSEs and synchrony PSEs, with PWHM values ranging from 4ms to 15ms, onsets greater than 3ms, and offsets less than 18ms. (See the next section for narrow PSEs, wide synchrony PSEs and PSEs at later latencies.) These PSEs are classified as medium to strong, based on their mean percent increase (MPI) and peak percent increase (PPI) values. Our conclusions were consistent

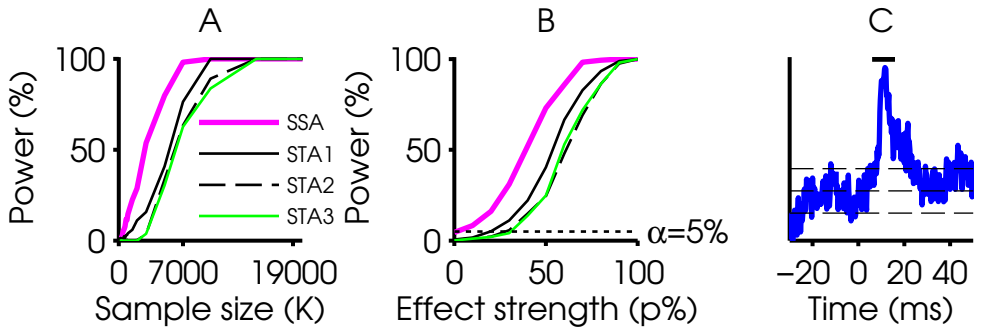

Figure 5.3: **Power comparison between SSA and SpTA tests.** Three variants of the automated SpTA were tested: SpTA1 uses the time window $[-5ms, 5ms]$ to calculate the SpTA baseline mean and SD; SpTA2 uses $[-20ms, -10ms]$; SpTA3 uses $[-30ms, -10ms]$. The PWHM threshold is $3ms$. Power as function of **(A)** sample size K, and **(B)** effect strength p. **SSA has better power than SpTA for all sample sizes and effect strengths.** Note: when $p = 0\%$ in **(B)**, there is no PSE in the data; SSA has the expected rate of spurious detections, $\alpha = 5\%$; the automated SpTA tests have spurious detection rates below α, which means that they are conservative. **(C)** SpTA for the digit-flexion parent dataset, calculated using all 32087 spikes. The vertical bar on top spans the $6-16ms$ time window. The horizontal dashed lines are the SpTA baseline mean and mean$\pm$2SD in baseline window $[-20ms, -10ms]$.

across datasets: SSA had consistently more power to detect PSEs than all automated SpTA tests. Nevertheless, we stress again that, while our analyses suggest that SSA is the better detection test, SpTA remains an essential tool to classify them.

We drew another important conclusion from our simulations: SSA maintains the desired rate α of spurious detections across datasets, as can be seen in Figures 5.2B, 5.3B, 5.6B, 5.7B, 5.8B, and 5.9B at $p = 0\%$, so it is a trustworthy test. We reproduced the simulation study on subsamples of various sizes, and verified that this conclusion extended to samples of all sizes. This is an important property: if SSA detects a PSE, we are guaranteed that the probability that it is spurious is less than α. SpTA detection does not control well the rate of spurious detections, and thus does not offer such a firm guarantee. To see this, consider Figure 5.3B at $p = 0\%$: the rates of spurious detections

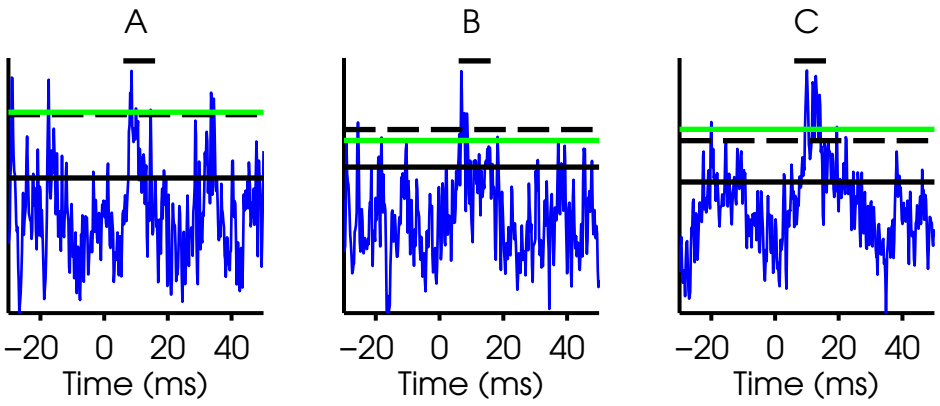

Figure 5.4: **Application of SSA and SpTA detection tests to three small datasets.** The SpTA in Figure 5.3C is calculated using all 32087 spikes in a digit-flexion dataset, and shows a clear PSE. The SpTAs in **(A,B,C)** use the same data but are calculated from three random subsets of $K = 800$, 1000, and 7000 consecutive spikes, respectively. The sub-sampled data do contain PSEs, but they are hard to detect by the naked eye in such small samples. The horizontal lines indicate the mean+2SD lines used by the three SpTA tests to determine the PSE onset and offset. All automated SpTA tests fail to detect the PSE in **(A,B)**. In **(C)**, only SpTA1 detects the PSE. In contrast, SSA detects the PSE in all cases, with p-values **(A)** $p = 0.009$, **(B)** $p = 0.007$, and **(C)** $p = 0.001$.

for all automated SpTA tests are about 1%, so these tests are trustworthy; but because the rates are below the nominal significance level $\alpha = 5\%$, the tests are also conservative, and thus have low power. The PWHM threshold in Figure 5.3B was $3ms$. Using a smaller PWHM threshold allows more PSEs to be detected, and thus increases power. This is indeed what we see in Figure 5.5, which shows power curves for PWHM thresholds 0.5, 1, 2, 3, and $4ms$, with simulations based on the parent dataset. Figure 5.5 also shows that the rates of spurious detections increase with smaller PWHM thresholds; 0.5 and $1ms$ give unacceptably high rates ($> 25\%$); $3ms$ is the largest threshold that maintains the rates below 5%. However, the $3ms$ PWHM threshold that yields SpTA rates of spurious detections of about 1% in Figure 5.3B, yields 5% in Figures 5.8B and 5.9B, and 1% in Figure 5.6B. Decreasing the PWHM threshold to $2ms$ increase these rates above the significance level α for the data in Figure 5.8C (shown in Figure 5.5); the same happens with the data in Figure

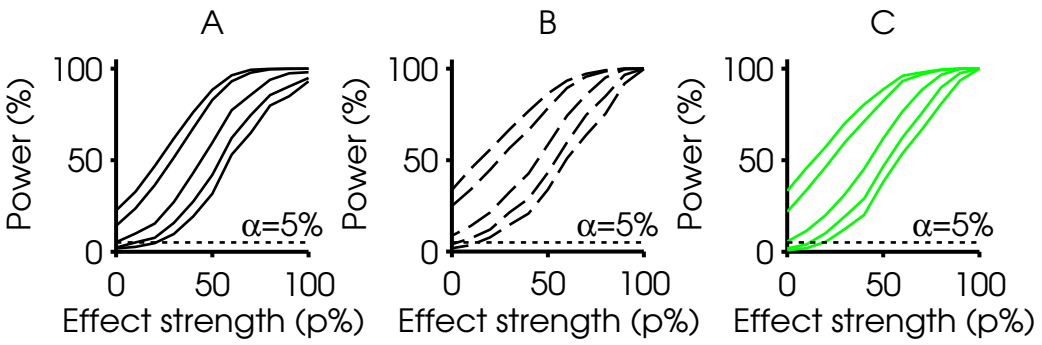

Figure 5.5: **Effect of the peak width at half maximum (PWHM) threshold on the detection power of the automated SpTA tests.** **(A)** Power curves for SpTA1 ($[-5ms, 5ms]$ baseline window), **(B)** SpTA2 ($[-20ms, -10ms]$ baseline window), and **(C)** SpTA3 ($[-30ms, -10ms]$ baseline window), as functions of effect strength p, the percentage of non-jittered snippets in the precision-grip parent dataset, whose SpTA is shown in Figure 5.8C. The 5 curves in each panel correspond to 5 PWHM thresholds: $0.5ms$ (top curves), 1, 2, 3, and $4ms$ (bottom curves). **The power of SpTA tests are very sensitive to the PWHM threshold.** In particular, there is no PSE in the data when $p = 0\%$, and the rates of spurious detections are well above the nominal level of $\alpha = 5\%$ for PWHM thresholds $2ms$ and smaller. The smallest PWHM threshold yielding a spurious detection rate around 5% is $3ms$, while larger PWHM thresholds render the tests conservative, as noted in Figure 5.3.

5.9C (not shown). Yet a $2ms$ threshold yields a 5% rate for the data in Figure 5.6C (shown in Appendix Figure 5.19), and only about 1% for the data in Figure 5.7C. Further decreasing the PWHM threshold to $1ms$ yields spurious detection rates larger than α for the data in Figure 5.6C (shown in Appendix Figure 5.20) and in Figure 5.7C (shown in Appendix Figure 5.21), and much larger than α for the data in Figure 5.8C (shown in Figure 5.5). Other datasets might yet give different results. This shows that the powers and rates of spurious detections of SpTA tests are very sensitive to the PWHM threshold and how sensitive they are depends on the datasets under investigation. Because it is not possible to determine a good PWHM threshold for a given dataset a priori, SpTA detection may not have an assured significance level, or may have low power.

5.4.4 DETECTION OF NARROW PSEs, WIDE SYNCHRONY PSEs, AND PSEs AT LATER LATENCIES

Our findings in the previous section suggest that SSA is the more trustworthy and powerful test to detect PSEs which overlap, at least partially, with its $6-16ms$ post-trigger detection window. But a fixed $10ms$ wide detection window cannot be optimal to detect all PSEs, e.g. PSEs that are much narrower or much wider than $10ms$, and PSEs that appear at later latencies, due to long axonal conduction times. In this section, we investigate if, and when, SSA retains good detection power in these situations.

Figure 5.6AB shows the power of SSA and automated SpTA tests for the precision-grip parent dataset whose SpTA is shown in Figure 5.6C; the sample size is large (64572 spike triggers) so the PSE appears clearly, but it is narrow, with PWHM $= 3ms$. Clearly, SSA has better power than SpTA for all sample sizes K and effect strengths p, even though the PSE onset and offset are $9ms$ and $12ms$ post-spike, which spans only about 30% of the SSA's $10ms$ detection window. A large part of why the SpTA tests have low power is that their rates of spurious detections are well below the nominal significance level α. Because we know that the PSE to be detected here is narrow, we lowered the PWHM threshold to $2ms$ to increase the power of the automated SpTA tests. Figure 5.19 in Appendix C shows the resulting power curves: SpTA tests now have better power, and have rates of spurious detections around α, yet SSA remains competitive despite its less than optimal $10ms$ wide detection window. Note however that we warn strongly against the practice of tweaking the PWHM threshold in real applications. Indeed we do not know a priori if the PSE to be detected is wide or narrow, and lowering the PWHM threshold could cause the SpTA rates of spurious detections to exceed the nominal significance level α, potentially by a large margin. This was discussed in the previous section.

The previous precision-grip dataset was large (64572 spike-triggers). Grasp datasets contain small numbers of spike triggers (see the experiment description in section 5.4.1), so detectable PSEs are few, and they are small and narrow. Figure 5.7C shows an example. Figure 5.7AB shows that all tests have limited power ($< 30\%$) to detect such a narrow PSE with so little data, but that SSA remains the more powerful test. Note that we used a PWHM threshold of $2ms$ in Figure 5.7AB, yet the spurious detection rates and power curves of all SpTA tests are very low.

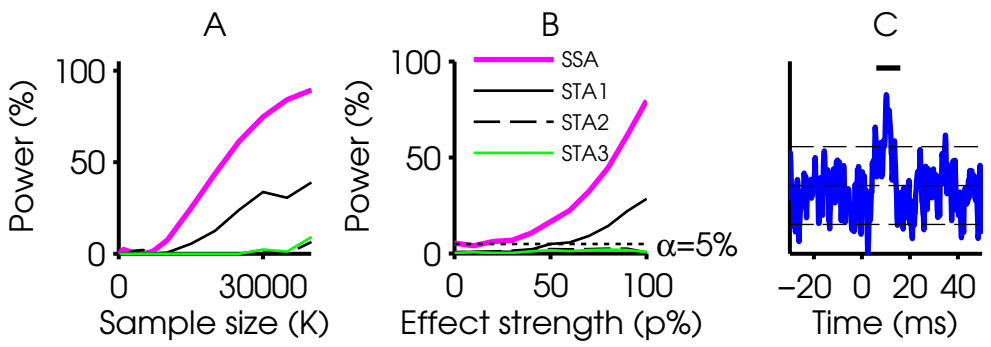

Figure 5.6: **Power comparison between SSA and SpTA tests applied to a narrow PSE.** The three variants of the automated SpTA were applied with PWHM threshold $3ms$. Power as function of **(A)** sample size K, and **(B)** effect strength p. **SSA has better power than SpTA for all sample sizes and effect strengths.** For example, SSA requires $K = 8000$ spikes to detect the PSE at least 5% of the time; SpTA1 requires $K = 15000$ spikes, respectively, to achieve the same detection power; while SpTA2 and SpTA3 never achieve detection power of 5%. **(C)** SpTA for the precision-grip parent dataset, calculated using all 64572 spikes. The vertical bar on top spans the $6-16ms$ time window. The horizontal dashed lines are the SpTA baseline mean and mean$\pm$2D in baseline window $[-20ms, -10ms]$.

Figure 5.8 concerns a wide synchrony PSE with PWHM $11ms$, onset $-0.6ms$ pre-spike, and offset $16.2ms$ post-spike. Despite using a less than optimal fixed detection widow, SSA remains more powerful than SpTA tests, for all sample sizes K and effect strengths p. Note that we used a PWHM threshold of $3ms$ to run the SpTA tests, because we knew that the data contained a wide PSE. By chance, this yielded rates of spurious detections approximately equal to the desired nominal level $\alpha = 5\%$. We wrote "by chance" because, as discussed in the previous section, a particular PWHM threshold does not guarantee a desired rate of spurious detections. In real applications, we would have no knowledge of the PSE width to help select a PWHM threshold, until a large enough sample was collected and the PSE detected by the naked eye.

Finally, Figure 5.9 concerns a late synchrony PSE with PWHM $10ms$, onset $8.6ms$ post-spike, offset $24.6ms$ post-spike, and with much of the EMG content contributing to the PSE outside

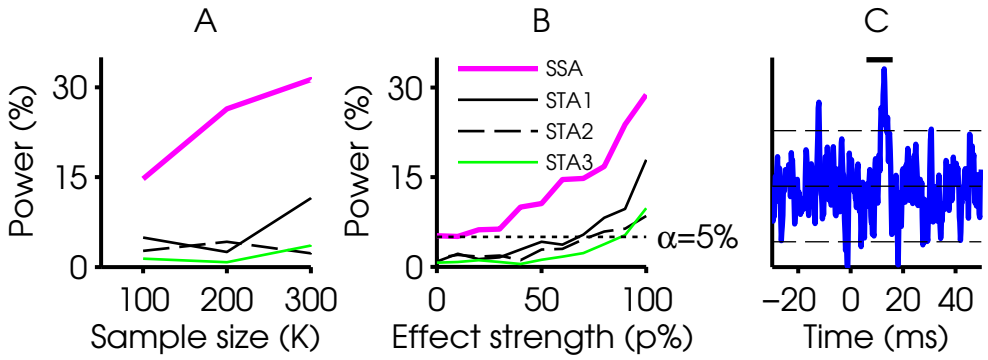

Figure 5.7: **Power comparison between SSA and SpTA tests applied to a small PSE.** The SpTA tests used a PWHM threshold of $2ms$. The grasp parent dataset contains only 673 spikes; its SpTA in **(C)** shows a clear, albeit small, PSE. Power as function of **(A)** sample size K, and **(B)** effect strength p. All tests have low detection power (below 30%), but **SSA has better power than SpTA for all sample sizes and effect strengths.**

of SSA's $10ms$ detection window. In that case, the SpTA tests have better power, which is not surprising since they scan the SpTA to detect PSEs at any latencies, whereas SSA uses a fixed detection window. But SSA can also be scanned, as described in the next section.

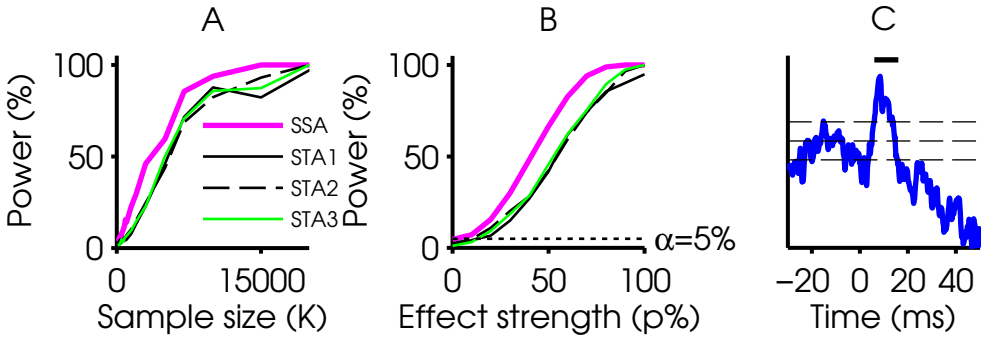

Figure 5.8: **Power comparison between SSA and automated SpTA tests applied to a wide PSE.** The SpTA tests used a PWHM threshold of $3ms$. Power as function of **(A)** sample size K, and **(B)** effect strength p. **SSA has better power than SpTA for all sample sizes and effect strengths. (C)** The precision-grip parent dataset has 38430 spikes, and contains a wide synchrony PSE: $PWHM = 11ms$, onset $-0.6ms$ pre-spike, offset $16.2ms$ post-spike. The vertical bar on top spans the $6-16ms$ time window. The overlayed baseline mean and mean$\pm$2SD were calculated in the $[-20ms, -10ms]$ time widow prior to baseline subtraction.

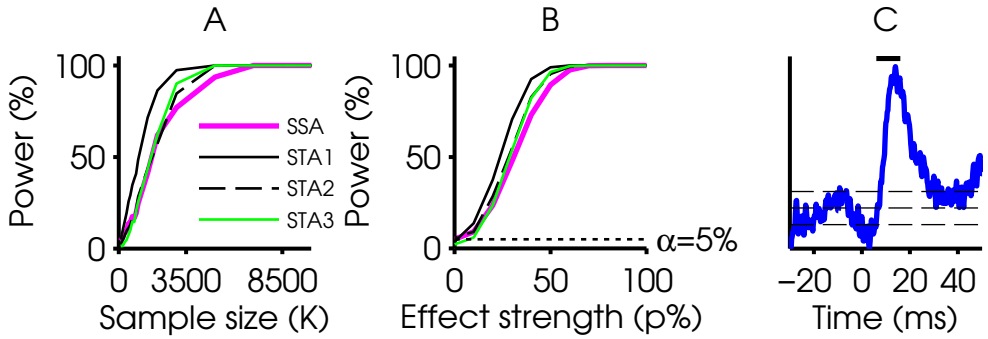

Figure 5.9: **Power comparison between SSA and automated SpTA tests for a wide late synchrony PSE.** The SpTA tests used a PWHM threshold of $3ms$. Power as function of **(A)** sample size K, and **(B)** effect strength p. **SSA has lower power than SpTA for all sample sizes and effect strengths.** The power of SSA is low because the EMG that contributes to the bump in the SpTA is mostly outside the $10ms$ wide detection window used by SSA. The SSA-scan test should be used instead, and performs better, as shown in Figure 5.11. **(C)** The digit-flexion parent dataset has 32087 spikes, and contains a wide late synchrony PSE: $PWHM = 10ms$, onset $8.6ms$ post-spike, offset $24.6ms$ post-spike. The vertical bar on top spans the $6-16ms$ time window. The overlayed baseline mean and mean$\pm$2SD were calculated in baseline window $[-20ms, -10ms]$.

5.4.5 SSA-SCAN TEST

The $6-16ms$ fixed detection window of SSA and MFA tests is designed to capture the effect of corticomotoneuronal action potentials. The SSA-scan test consists of repeatedly performing the SSA test using a sliding detection window, finding the largest putative PSE and testing its significance (section 5.3.3). One could also scan the MFA or MFAE test, but we focus on SSA since these tests are approximately equivalent. By removing the restriction of a fixed window, scan tests mimic the scanning of SpTA visual inspections, and thus allow PSEs in a range of latencies to be detected, including PSEs from both CMN and non-CMN sources.

Figure 5.10 shows the power of the SSA-scan test to detect the synchrony PSE in the single-digit dataset, whose SpTA was shown in Figure 5.2C (PWHM $15.4ms$, onset $1.6ms$, offset $22.2ms$). Power was estimated following the simulation described in section 5.4.2. In addition, we also stored the post-spike latencies at which SSA-scan detected PSEs, to study not only its detection power, but also its accuracy to locate PSEs. Figure 5.10A is a heat map of the detection power at post-spike latencies l in the $6-25ms$ range (Y-axis), as a function of the PSE strength p (X-axis): the SSA-scan test detects the PSE at latencies around $12-13ms$ post-spike, which is the correct range since the PSE (Figure 5.2C) has onset $1.6ms$ and offset $22.2ms$. The darkening of the colors from left to right indicates that the power increases with the effect strength p. The information in Figure 5.10A is summarized in Figure 5.10B, which shows three curves: the total power inside the PSE duration window, $1.6-22.2ms$ post-spike, the total power outside of that window, and the sum of the two, as functions of the PSE strength p. The latter curve shows that SSA-scan is trustworthy, since its rate of spurious detections (i.e. its detection power when there is no PSE at $p = 0\%$) equals the nominal $\alpha = 5\%$. The first two curves show that SSA-scan detects the PSE at the correct post-spike latency for all effect strengths p, and that no spurious detections are made outside the $1.6-22.2ms$ window when the PSE is strong.

Note that the fixed-latency SSA test has better power than SSA-scan to detect the PSE in Figure 5.2C. This can be seen by comparing the power curves in Figures 5.10B and 5.2B: the latter curve is above the former for all p; for example, at PSE strength $p = 40\%$, SSA and SSA-scan have detection powers 94% and 75% respectively. This is not a failure of the SSA-scan test, but is to be expected, since the scan test searches everywhere for a PSE that happens to be in the fixed detection

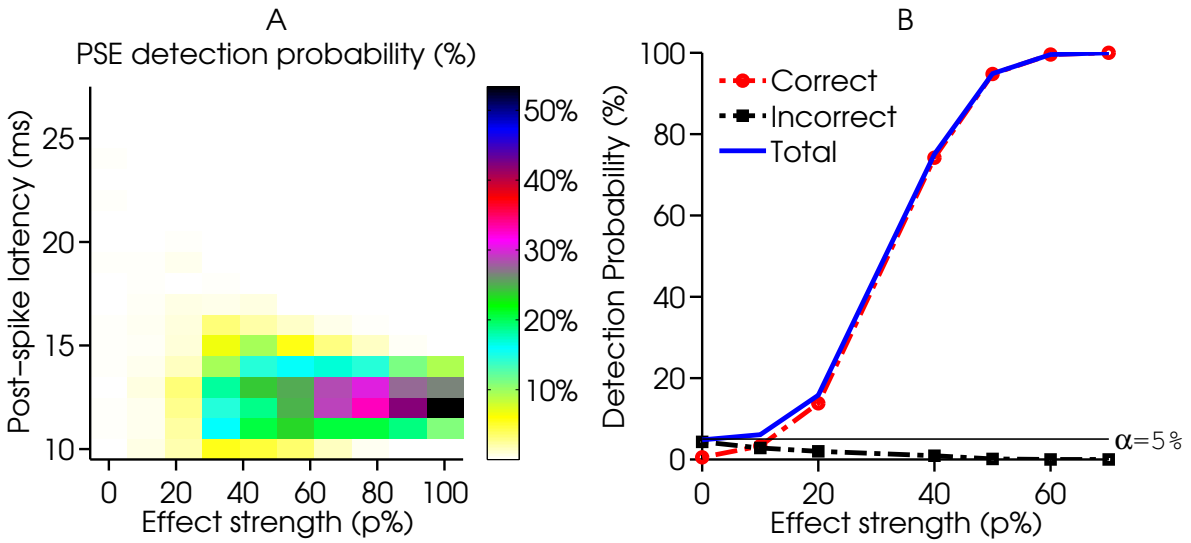

Figure 5.10: **Power of the scan test applied to PSEs of varying effect strengths.** The SpTA of the digit-flexion parent dataset is shown in Figure 5.2C. We created test datasets with varying effect strengths by jittering $(100-p)\%$ of the EMG snippets in the base dataset; when $p = 0\%$, test datasets do not contain PSEs; when $p = 100\%$, they contain PSEs with the same effect strength as the parent dataset. **(A)** Heat map of detection probabilities as function of post-spike latency (Y-axis) and effect strength (X-axis). PSEs are never detected at latencies beyond the onset and offset of the original PSE. **(B)** Detection probabilities from **(A)** as function of effect strength, summed across post-spike latencies (columns). The three curves correspond to detections at the correct latencies ($1.6-22.2ms$ post-spike), detections at incorrect latencies, and all detections. The latter curve shows that when $p = 0\%$, the scan test has the expected rate of spurious detections, $\alpha = 5\%$.

window of the SSA test. To make an analogy, imagine that our car keys are lost somewhere in the house. Then if the keys are in the bedroom, the probability of finding them if we search only the bedroom is higher than if we search the whole house, given a fixed amount of time. Searching only the bedroom is akin to searching only for PSEs at a fixed latency. But if the keys are somewhere else, which we do not know a priori, then there is no other option than conducting a full search. Our next example treats such a situation.

Consider again the late synchrony PSE in Figure 5.9, for which most of the EMG content that contributes to the PSE is outside the fixed $10ms$ detection window used by SSA. Figure 5.11A shows the power of SSA-scan to detect that PSE, and Figure 5.11B is the corresponding heat map for the SpTA1 test (baseline window $[-5,+5]ms$ post-spike); the heat maps for the other two SpTA tests were almost identical to SpTA1. Figure 5.11C summarizes the information in panels A and B, in the format of Figure 5.10B, and shows that SSA-scan performs as well as the best automated SpTA test. However, we reiterate that SSA-scan is a safer test since it has the expected rate of spurious detections, whereas SpTA tests do not control that rate well. Figures 5.11AB further shows that the automated SpTA tests do not locate the PSE as accurately as the SSA-scan test. Note that comparing Figures 5.11C and 5.9B also reveals that SSA-scan has more power than the fixed latency SSA test to detect the PSE in this dataset.

We obtained similar results across datasets. In particular, we simulated a very late PSE by shifting the spikes contributing to a monosynaptic PSE $55ms$ back in time, and jittering their times, which created a dispersed PSE around $60ms$ post-spike; SSA has no power to detect that PSE, but SSA-scan did detect it at the correct latency; see Appendix D.

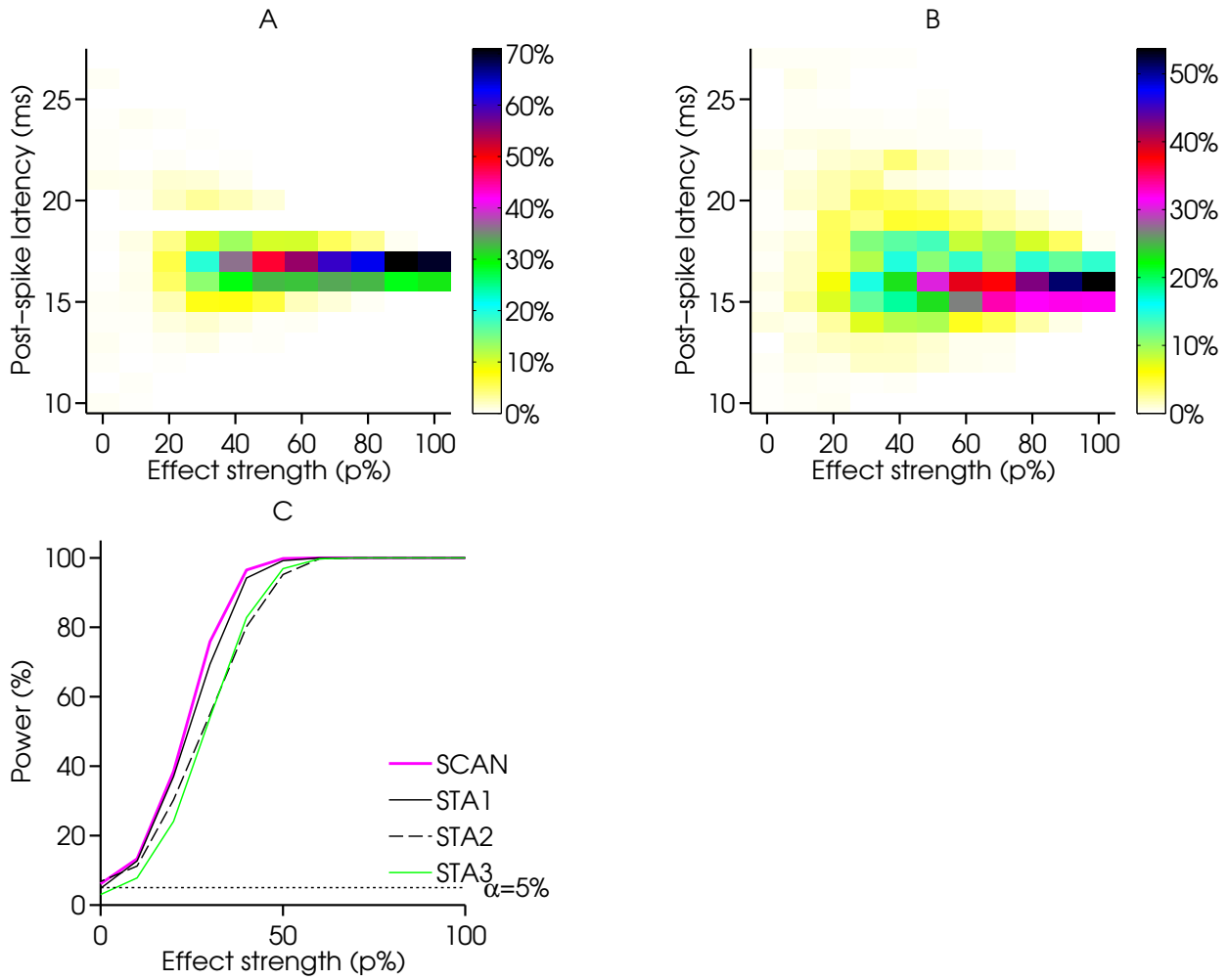

Figure 5.11: **Power of the scan and automated SpTA tests applied to late synchrony PSEs of varying effect strengths.** The SpTA of the digit-flexion parent dataset is shown in Figure 5.9C. This PSE had a PWHM of 10*ms* and onset-offset times of 8.6*ms* and 24.6*ms*. We created test datasets with varying effect strengths by jittering $(100-p)\%$ of the EMG snippets in the base dataset; when $p = 0\%$, test datasets do not contain PSEs; when $p = 100\%$, they contain PSEs with the same effect strength as the parent dataset. **(A)** Heat map of detection probabilities for SSA-Scan, as function of post-spike latency (Y-axis) and effect strength (X-axis). PSEs are never detected at latencies beyond the onset and offset of the original PSE **(B)** Heat map of detection probabilities for SpTA1 (baseline window from $-5ms$ to $+5ms$, PWHM threshold $3ms$), as function of post-spike latency (Y-axis) and effect strength (X-axis). We show SpTA1 since it was the most powerful of all SpTA tests in (C). PSEs are never detected at latencies beyond the onset and offset of the original PSE, but the latencies are more variable than in (A). **(C)** Detection probabilities from (A,B) as function of effect strength, summed across all post-spike latencies (columns). Compare to Figure 5.9B. Detection probabilities for SpTA1 and SpTA3 are also shown (heat maps not shown). **The SSA-Scan test outperformed all automated SpTA tests.**

5.4.6 SpTA BASELINES

The majority of PSEs we inspected occurred on top of non-constant baselines. To correct the SpTA, the accepted way to proceed is to estimate its baseline and subtract it from the SpTA, so that meaningful estimates of the PSE onset, offset, and PWHM can be calculated. An estimate of the SpTA baseline is also used to adjust the SSA and MFA tests as we now describe. First, recall that these tests consist of (i) calculating a test statistic T, which is effectively the standardized difference between the average SpTA in the $6-16ms$ post-spike and the average SpTA in the two windows immediately preceding and succeeding it, and (ii) comparing T to zero: a value of T close to zero means that there is no PSE, and a value that deviates from zero gives evidence of a PSE; the statistical significance of the deviation from zero, measured by a p-value, is calculated from a normal distribution centered at zero. However, if the SpTA baseline is not constant, T should be compared not to zero, but to the value of T calculated from the SpTA baseline, m, say. That is, the p-value that measures the significance of the deviations of T should be calculated from a normal distribution centered not at zero, but at m. This is described fully in sec. 5.3.4. Note that when the SpTA baseline is flat, the value of T calculated from the SpTA baseline is $m = 0$, obviously. But it is easy to see that m is also zero when the SpTA baseline is non-constant but linear; hence, the SSA and MFA tests correct automatically for linear baselines, and may be robust to baselines that are close to linear.

The adjustments to SpTA, SSA, and MFA tests require an estimate of the SpTA baseline. If it is linear, a common practice is to use the fit of a linear regression to the SpTA. The method of Davidson et al. [9] applies more generally to arbitrary SpTA baselines. It is computed as follows: (i) artificial spike triggers placed every $1ms$ in an $80ms$ window around an observed spike trigger are used to compute the EMG baseline for that trigger; spreading artificial triggers has the effect of spreading the EMG content that might contribute to a PSE, so it is no longer time locked to the observed trigger; averaging over 80 triggers yields a smooth baseline estimate; (ii) this is repeated for every observed spike trigger; (iii) the SpTA baseline is obtained as the average over observed triggers of their estimated EMG baselines. The bootstrap methods of sec. 5.3.4 provide a closely related estimate of the SpTA baseline: (i) given an observed trigger, a single artificial trigger is created by jittering the time of the observed trigger; we use a normal jitter with SD $30ms$; jittering

the trigger has the effect of jittering the EMG content that might contribute to a PSE, so it is no longer time locked to the observed trigger; (ii) this is repeated for all observed triggers; (iii) a "null" SpTA is obtained as the average of the EMG snippets of the artificial triggers; (iv) we repeat this 100 times, and estimate the SpTA baseline as the average of the 100 null SpTAs. It is clear that the bootstrap estimate of the SpTA baseline is very closely related to the estimate of Davidson et al. [9]. But we prefer our bootstrap procedure because it provides not only an SpTA baseline estimate with which to correct the SSA and MFA tests[1], but also diagnostics to check and correct the distributional validity of the parametric SSA and MFA tests; see sec. 5.3.4 and Appendices A and B.

Figure 5.12 shows the SpTAs of three datasets that have non-constant baselines, with overlaid bootstrap baseline estimates, and estimates using the method of Davidson et al. [9]. The two sets of estimates match closely. The SSA test detects PSEs in the three datasets, with p-values 6×10^{-8},1.14×10^{-8} and 0.0026 respectively. Because the p-values are well below the significance level $\alpha = 5\%$, and because the baselines are close to linear, the bootstrap diagnostic methods of sec. 5.3.4 determined that the p-values of the SSA tests did not require any adjustment to correct for the non-linear baseline. Other datasets, especially those with fewer spike-triggers, required p-values adjustments; see Appendix B.

[1]The bootstrap methods of sec. 5.3.4 do not require that the SpTA baseline be calculated explicitly to correct for non-constant baseline; the correction is done implicitly with the values of T in the 100 null SpTAs, whose average is the value m mentioned above. Similarly, the correction for the scan-test uses the bootstrap values of the test statistic S.

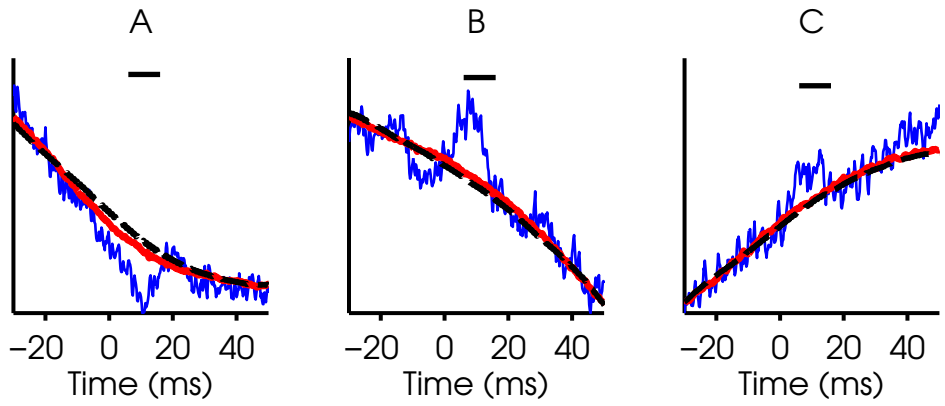

Figure 5.12: **Estimation of PSE baselines using the bootstrap. (A,B,C)** SpTA of three precision-grip datasets that show non-constant, non-linear, baselines, with bootstrap estimated baselines (section 5.3.4) overlaid in solid grey; and estimated baselines by the method of Davidson et al. [9] overlaid in dashed black. The two baseline estimates are almost identical. The vertical bar on top spans the $6-16ms$ time window. SSA detected this **(A)** PSS with p-value 6×10^{-8}, **(B)** PSF with p-value 1.14×10^{-8}, and **(C)** PSF with p-value 0.0026. Note that even though the SpTAs have non-constant baselines, our bootstrap diagnostic determined that the SSA test p-values were accurate. This is not surprising because (i) SSA is not affected by linear SpTA baselines, (ii) the baselines in (A,B,C) are close to linear, and (iii) the p-values are very small so a bootstrap adjustment would not change them much.

5.4.7 THRESHOLDING EMG SNIPPETS

It is common practice to apply sweep filtering prior to computing the SpTA, and discard EMG snippets that do not contribute to the PSE. Sweep filtering is typically done by thresholding EMG snippets. To determine if this has an effect on the automatic detection tests, we repeated the comparison of the detection powers of SSA and MFA (section 5.4.2), using only the EMG snippets above threshold. We used two methods to discard EMG snippets with low content: the first calculated a constant threshold from an EMG segment where the muscle was inactive, and discarded snippets below that threshold (McKiernan et al. [40]); the second calculated a threshold based on root-mean-square (RMS) EMG value in an EMG segment where the muscle was inactive (David-

son et al. [9]). The two thresholding methods gave similar results. We found that thresholding had no effects on SSA and MFA tests, except in the same two datasets that already gave atypical results in sec. 5.4.2. These datasets were recorded from muscles with low EMG contraction levels and contain a large proportion of low-valued EMG snippets. Thresholding did not affect the powers of SSA and MFAE tests, but the MFA test did lose power after thresholding. This provides further evidence that the chronological order of the low content snippets affects the MFA test.

Our results suggest that thresholding is not needed. But (McKiernan et al. [40]) reported that in some cases, including low-content EMG snippets in the SpTA diluted the PSE, so it was beneficial to apply sweep filtering. It is reasonable to assume that even SSA and MFA could suffer reductions in power if the PSE was diluted by too many snippets that did not contribute to it. A possible compromise would be to conservatively threshold snippets using a low threshold, to eliminate only the snippets that contain no active EMG content at all, since snippets containing low EMG activity levels may still contribute to the PSE.

5.5 DISCUSSION

Two analytical tools to detect post-spike effects (PSEs) have been described in the literature: spike-triggered averaging (SpTA) and Multiple Fragment Analysis (MFA). Conventional evaluation of SpTAs is visual, and involves a subjective assessment of PSE significance that often depends on prior experience. Some more formal techniques have been suggested to assess PSE significance in an SpTA (Kasser and Cheney [35], Lemon et al. [37]), but their properties, power and significance level, had not studied. The significance level, i.e. the maximum rate of spurious PSE detections, is especially important for investigators. MFA is a formal statistical test, so it provides a p-value to assess the statistical significance of PSEs. But a detailed review of its statistical properties was never published, so it was not clear when it could be trusted, or when its underlying assumptions were valid.

In this paper, we introduced the Single Snippet Analysis (SSA) as a simpler alternative to the Multiple Fragments Analysis (MFA). Both tests are formal, i.e. they provide p-values and do not require visual inspection. SSA and MFA have similar power levels, and have equivalent utility.

But SSA is simpler to calculate and perhaps more intuitive: MFA requires segmenting the data and calculating fragment SpTAs; SSA only requires one simple statistic to be computed for every spike-triggered sample. This makes SSA better suited than MFA for on-line PSE detection and for combining data across experimental epochs or repeat trials. For example, combining data from different time epochs in an experiment (e.g. only movement epochs) can be done by using only the spikes from the epochs of interest as the input to SSA, since no time segmentation is required.

SSA and MFA are designed to find PSEs at a predetermined post-spike latency, since they use a fixed $10ms$ detection window $6-16ms$ post-spike. But axonal velocities of both corticospinal neurons and spinal motoneurons affect PSE latency, which may cause monosynaptic PSEs to appear at later latencies. Disynaptic suppression and polysynaptic excitatory effects may also appear at long latencies. Because SSA cannot always detect pure or synchrony PSEs whose waveforms extend beyond the $10ms$ detection window, we proposed the SSA-scan test, which consists of performing the SSA in a sliding detection window. By relaxing the constraint of a fixed window, the SSA-scan test is generally useful for detecting a wide range of post-spike effects.

To study the statistical properties of SSA, SSA-scan, and SpTA, we formulated an automated SpTA detection test that replicates the conventional visual criteria applied to SpTA. It consists of selecting the excursion with the maximal area outside of the SpTA baseline mean $\pm$ 2SD, and calculating its peak width at half maximum (PWHM). We considered that excursions were significant if their PWHM exceeded $3ms$. This threshold was the smallest value that kept the rates of spurious detections below the nominal significance level α in our datasets. However, there is no guarantee that a $3ms$ threshold would control the rates of spurious detections in other datasets. We also showed that a $3ms$ PWHM threshold sometimes gave the SpTA test very low power to detect PSEs. Using a smaller PWHM threshold increases the power, but comes at the risk of not controlling the spurious detection rate. In contrast, the SSA and SSA-scan tests automatically maintain the rates of spurious detection close to the nominal significance level, without sacrificing power to detect PSEs.

For most of the datasets we inspected, SSA had better power than SpTA to detect PSEs, for all sample sizes (number of spike triggers) and for all PSE strengths (percentage of spikes contributing to the PSE). In large datasets with obvious PSEs, all tests could detect the PSEs equally effectively. But SSA did better in small samples, and in datasets with small PSEs. SSA has another major

advantage over SpTA: its rate of spurious detections is assured to be less than $\alpha = 5\%$, which means that if a PSE is detected, we know that the probability that the detection is spurious is less than α. The SpTA test offers no such guarantee, since its rate of spurious detections depends critically on the PWHM threshold, as discussed above, and to some extent on the baseline window used to assess the significance of the PSE. Optimal values for these quantities cannot be selected a priori.

SSA and MFA both rely on modeling assumptions, which, if not met, might bias their p-values. We listed these assumptions and identified situations when they might be violated, which includes small sample sizes, skewed distributions of the test-statistics, and non-linear baselines (SSA and MFA tests are not affected by non-constant baselines that are linear). We developed bootstrap procedures to diagnose when the assumptions hold, and correct p-values when they don't. For example, our bootstrap diagnostics detects non-linear SpTA baselines, and the bootstrap correction implicitly consists of estimating the baseline non-parametrically, and removing its effects from the data.

Finally, we demonstrated that rigorous PSE detection could be fully automated, using the practical guidelines in Appendices E and F. The SSA and SSA-scan tests require no segmentation of the data in fragments, so p-values can be recomputed in real time as more data is acquired. However we stress that, while the SSA and SSA-scan tests have proven reliable and powerful to detect PSEs, the SpTA remains an essential tool to classify them.

We conclude with a direction for improvement. SSA uses a $10ms$ detection window, yet can generally detect PSEs of varying widths. However, it was unable to detect a very narrow, possibly monosynaptic, PSE that appeared clearly in the SpTA of one grasp dataset. That SpTA used only 700 snippets, which partly explains the failure of the detection test; a larger sample would have provided the test with more power to detect the narrow effect. However, when we reduced the SSA test detection window to $5ms$, it detected a significant PSE, despite the small sample size. But then conversely, the SSA detection test based on a $5ms$ detection window had lower power than the same test based on a $10ms$ window, when applied to grasp and digit-flexion datasets with wider PSEs. This shows clearly that the power of the test depends on the width of the detection window, as one might expect. Note that only the power of the SSA test is affected by the width of the detection window; the rates of spurious detections match the nominal α, so the test remains

trustworthy, even when it has low power. This is in sharp contrast to the automated SpTA tests, whose powers and rates of spurious detections are affected by the choice of PWHM threshold. We plan to design an SSA test that is invariant to the spread of the effect, while retaining high power for all types of PSEs.

5.6 ACKNOWLEDGEMENTS

Our work was supported by grant *NS*050256.

The authors wish to thank Dr. Marc Schieber, Prof. Roger Lemon and Dr. Andrew Jackson for their contribution of datasets. Dr. Schieber's work was supported by grant *NS*27686.

This project also acknowledges the use of the Cornell Center for Advanced Computing's "MATLAB on the TeraGrid" experimental computing resource funded by NSF grant 0844032 in partnership with Purdue University, Dell, The MathWorks, and Microsoft.

5.7 APPENDIX A – BOOTSTRAP DIAGNOSTICS: PROCEDURE

Bootstrap values for the SSA/MFA test or the scan test, with test statistics T and S, are obtained as follows:

- For $r = 1 \ldots R$

1. Create the rth bootstrap sample by jittering the original cortical spike train to destroy any potential time-locked PSE. We determined that for our data, a normal jitter with SD $30ms$ was sufficient. See Appendix A.1.
2. a. Bootstrap values of T: calculate t_r^*, the value of the SSA/MFA test statistic T in bootstrap sample r.
   b. Bootstrap values of S: for all time lags l, calculate $t_r^*(l)$, the value of the SSA/MFA test statistic $T(l)$ in bootstrap sample r, and take s_r^* to be the maximum of the $t_r^*(l)$.

Bootstrap diagnostics for the SSA/MFA test consists of a normal quantile plot of the 100 bootstrap values t_r^*. Bootstrap diagnostics for the scan test consists of a quantile-quantile (QQ) plot of the 100 bootstrap values s_r^* versus the theoretical quantiles of the nominal null distribution f_S in eq. 5.5 or 5.8. If the points do not significantly deviate from a straight line, we conclude that the distribution of the t_r^* values is the assumed standard normal; or the distribution of the s_r^* values matches the theoretical quantiles of the nominal null distribution f_S. Further, if the sample mean m and sample variance s^2 of the t_r^*'s do not significantly deviate from 0 and 1, the fixed-latency detection parametric test is valid and the parametric p-value can be trusted. If the normal plot is straight but m or s^2 deviate from their nominal values of 0 and 1, the p-values should be calculated from a normal distribution with mean and variance m and s^2 rather than from a standard normal distribution.

If the normal plot is not straight, a bootstrap p-value should be obtained as follows:

• Bootstrap p-values for SSA/MFA tests: the histogram of the R bootstrap values of $t_r^*(11ms)$ approximates the null distribution of T. The bootstrap p-value for the two-sided detection test is $2q$ if $q<1/2$ or $2(1-q)$ if $q>1/2$, where q is the proportion of bootstrap samples for which $t_r^* \geq t_{obs}$, and t_{obs} denotes the observed value of T in the data.

P-values for one-sided tests are modified according to which tail of the null distribution is relevant.

• Bootstrap p-value for scan test: the histogram of the R values s_r^* approximates the null distribution of S. The bootstrap p-value for the two-sided scan test is the proportion of bootstrap samples for which $s_r^* \geq s_{obs}$, where s_{obs} is the observed value of S in the data.

P-values for one-sided tests are modified according to which tail of the null distribution is relevant.

A small simulation, $R = 100$ say, is adequate for diagnostics. But calculations of bootstrap p-values require a larger simulation to be accurate, $R = 1000$ at least. If the bootstrap p-value is within 3% of the significance level – for example between 2% and 8% when $\alpha = 5\%$ – then R should be increased to $10,000$. see Ventura [68] sec.18.4 for details.

5.7.1 APPENDIX A.1 – OBTAINING BOOTSTRAP SAMPLES

A bootstrap sample has the same size as the observed sample, and the distribution the data would have if the null hypothesis H_0 was true. That distribution is typically unknown, and the greatest challenge in conducting bootstrap tests is to design appropriate estimates for it. In our situation, H_0 only specifies that there is an absence of time-locked PSE in the EMG; there are many ways to create bootstrap data that satisfy H_0 and the p-value will depend which way we use (see Ventura [68], sec. 18 for details). One option is to keep the EMG trace untouched and randomize the ISIs of the cortical neuron spike train, thereby destroying any potential time-locked effect. However, the resulting EMG snippets are unlikely to resemble the snippets we would have seen if H_0 was true. For example in our data, the EMG trace tends to be larger when cortical neurons, either time-locked or not, spike a lot, so that many of the EMG snippets used to obtain an SpTA have large values. Randomizing the ISIs would thus yield data that contain fewer large valued EMG snippets than real data would. Figure 5.13 shows the observed SpTA for one digit-flexion dataset and the SpTA obtained after randomizing the cortical spike ISIs: the PSE disappeared, but the pre- and post-randomization SpTAs are dramatically different as well.

An alternative to randomization is to jitter the spikes, which preserves the approximate firing rate of the cortical neuron (see Harrison and Geman [25] for a justification), while spreading any potential time-locked effect. To gain maximum power to test for an effect, the jitter should be large enough to destroy the effect completely, but not so large that it will change the characteristics of the EMG snippets, like ISI randomization did. Fig 5.14A shows the same observed SpTA as in Fig 5.13, along with SpTAs obtained by jittering the cortical spikes using a normal jitter with SD σ: $\sigma \geq 30ms$ appears to destroy the time locked effect completely, while retaining approximately the overall shape of the SpTA outside of the monosynaptic window. We say *approximately* because the SpTA becomes flatter as the jitter increases, so that the amount of jitter might affect the p-values. Fortunately, our test statistics (T_{MFA}, T_{SSA}, T_{MFAE} in sec. 5.3.1 and 5.3.2) are based on SpTA contrasts, which are less sensitive to σ. This is illustrated in Figure 5.14B, which shows $T_{SSA}(l)$ as a function of l. We see that the values of $T_{SSA}(l)$ stabilize for $\sigma \geq 30ms$, which implies that the null distributions of $T_{SSA}(l)$ does not depend much on σ when $\sigma \geq 30ms$, and in turn implies that p-values are not sensitive to the exact amount of jitter applied to destroy potential PSEs (in

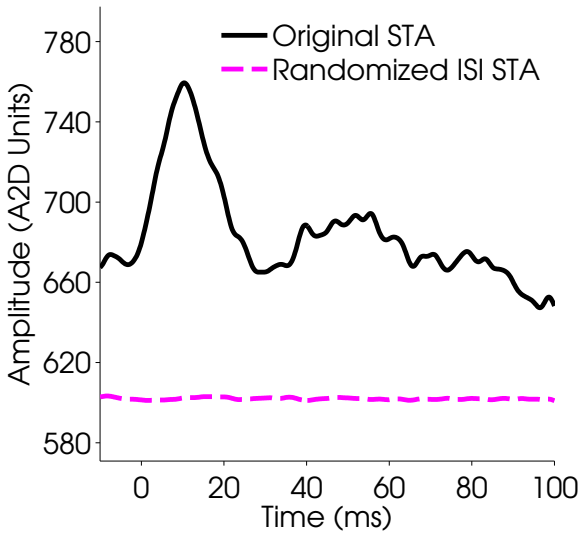

Figure 5.13: SpTA from a digit-flexion movement dataset overlayed with the SpTA obtained after randomizing the cortical spikes inter-spike intervals. Randomizing ISIs removes the PSE, but also changes the SpTA outside of the PSE duration window.

statistical jargon, our test statistics are pivotal; see Ventura [68], sec 18.4). In this paper, we used $\sigma = 30ms$ based on Figure 5.14.[2] We suggest reproducing this plot for any new datasets, since they might have different characteristics than ours.

[2]Recall that we used $\sigma = 100ms$ to remove locked effects from test datasets, because we were not concerned about the test data looking like the real data. Bootstrap samples must look like the real data, although they must contain no locked PSE.

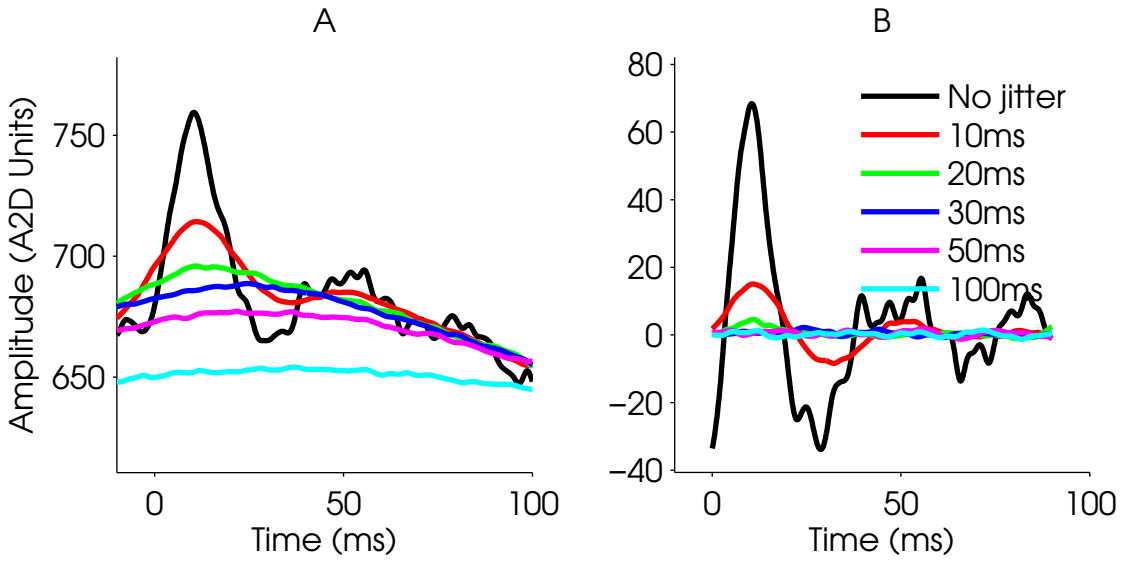

Figure 5.14: **(A)** SpTA from a digit-flexion dataset overlayed with SpTAs obtained after jittering the cortical spikes times with values drawn from a normal distribution with mean zero and SD σ; $\sigma \geq 30ms$ destroys the PSE for this dataset. **(B)** The test statistic $T_{SSA}(l)$ as a function of l (latency post-spike). $T_{SSA}(l)$ is not sensitive to the jitter SD when $\sigma \geq 30ms$.

5.8 APPENDIX B – BOOTSTRAP DIAGNOSTICS: EXAMPLES

5.8.1 APPENDIX B.1 – VERIFYING SSA AND MFA TEST ASSUMPTIONS

The MFA, MFAE, and SSA tests rely on the assumption that the null distribution of their test statistics T (eqs. 5.2 or 5.3) are standard normal. That is, when PSEs are not present in the data, we expect values of T to be normally distributed with mean zero and variance one. Violations of this assumption might bias p-values, and lead to discrepancies between rates of spurious detections and the nominal significance level, and in turn renders the tests untrustworthy.

Consider again Figures 5.2B, 5.3B, 5.6B, 5.7B, 5.8B and 5.9B in the main text , and Figures 5.18CD, 5.21B and 5.19B in Appendix C. When there is no PSE in the data (effect strength $p = 0\%$), the rates of spurious detections of MFA and SSA tests match the nominal significance level α: the tests are trustworthy. We simulated the same power curves for many other parent datasets,

and for many subsets of these parent datasets. In the vast majority of cases, SSA and MFA had the desired rates of spurious detections. But not always. For example, in several small datasets, the MFA and SSA tests had rates of spurious detections around 3% to 7%, instead of the nominal $\alpha = 5\%$; before the bootstrap diagnostics and corrections were applied. The small sample size might be the cause of the problem, but it is typically difficult to pinpoint why and when assumptions fail. This is why diagnostics are crucially important to detect these situations.

We illustrate the bootstrap diagnostics on two datasets: 600 spikes sampled from a digit-flexion dataset (Figure 5.15C), and 500 spikes sampled from a grasp dataset (Figure 5.15D). The SpTAs for these two samples are in Figure 5.15A,B. Detecting the PSE by visual inspection is difficult in such small sample. The SSA test applied to these two samples yields p-values 0.1% and 5.6%: we respectively reject and retain the null hypothesis of no PSE at the 5% significance level. Results for the MFA and MFAE were similar. The p-values are close to $\alpha = 5\%$, so we produce the bootstrap diagnostic plots in Figure 5.15CD. The 100 bootstrap values of T_{SSA} in Figure 5.15C follow approximately a standard normal distribution, so that the SSA test p-value for that dataset ($p = 0.1\%$) can be trusted: we reject the null hypothesis and conclude that a PSE is present, and we know that the detection is spurious with probability less than 5%. The normal quantiles plot in Figure 5.15D for the second sample is approximately straight, which confirms that the null distribution of T_{SSA} is Gaussian, but the sample mean and variance are $m = 0.06$ and $s^2 = 0.89^2$, instead of the assumed $m = 0$ and $s^2 = 1$. We recompute the p-value based on the $N(0.06, 0.89^2)$ distribution, which shifts it from 5.6% to 2.6%, and changes the outcome of the test: we now conclude that there is a PSE in Figure 5.15B, and the probability that the PSE is spurious is less than 5%.

The diagnostics in Figure 5.15C are representative of what we observed with most datasets, especially in large datasets (i.e. good diagnostics that validate the parametric p-value). This suggests that the assumed standard normal null distribution for the fixed-latency test statistics T_{MFA}, T_{SSA}, and T_{MFAE} is usually valid. Figure 5.15D is a rare example when the p-value needs to be adjusted.

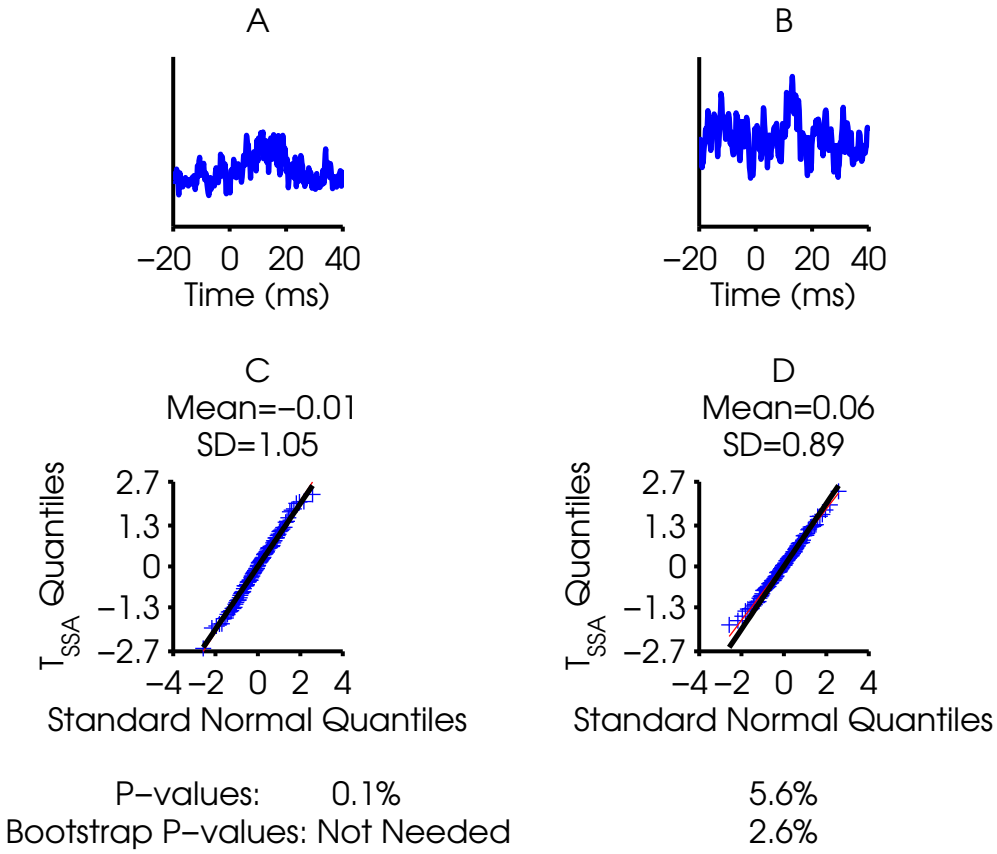

Figure 5.15: **(A,C)** Digit-flexion dataset of size $K = 600$ spikes **(B,D)** Grasp dataset of size $K = 500$ spikes. **Top row:** SpTAs. **Bottom row:** Bootstrap diagnostic plots for the SSA test applied to the two datasets. The normal quantile plots are approximately linear in (C,D), but the mean and variance deviate from 0 and 1 in (D). The outcome of the SSA test can be trusted in (C) but the p-value in (D) needs to be adjusted. Recomputing the p-value in (D) changes the test from non-significant to significant: **SSA p-values : (C)** 0.1% **(D)** 5.6%; **Bootstrap p-values: (C)** Not needed **(D)** 2.6%

5.8.2 APPENDIX B.2 – CHECKING THE SCAN TEST ASSUMPTIONS

All fixed-latency detection tests rely on the assumption that the null distribution of the test statistic T is normally distributed with mean zero and variance one. The scan test relies on the same assumption for $T(l)$ at all lags l, and in addition on the $T(l)$ being mutually independent. The

latter assumption is obviously violated when $T(l)$ is scanned at every single post latency lag, since successive scans use overlapping EMG portions. The dependencies should decrease if we scan $T(l)$ at every m steps, where m is to be determined, as we show below.

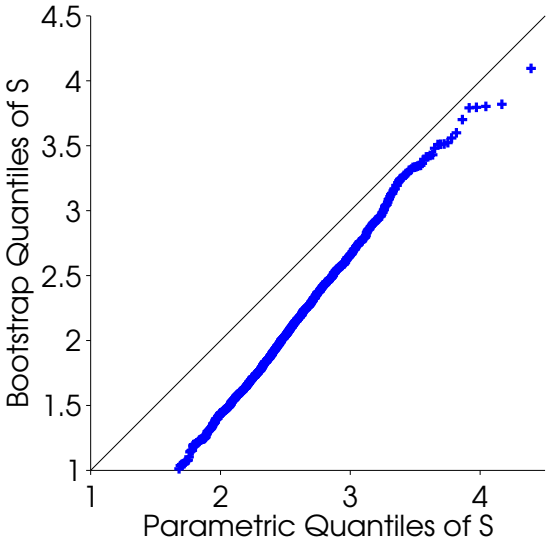

Figure 5.16: Diagnostics QQ-plot for the scan test applied to one of the datasets in Figure 5.10 at $p = 0\%$. A QQ-plot is a visual technique to test if a sample has a given distribution. It plots that distribution against the distribution of the sample. If the sample has that distribution, the plot should form a straight line, approximately. Deviations from a straight line gives evidence that the sample has a different distribution.

Figure 5.16 shows the bootstrap diagnostic plot for the SSA-scan test S (sec. 5.3.4, Appendix A) applied to one of the datasets used in Figure 5.10; other datasets gave similar results. Here, we scanned $T(l)$ at all latencies. This plot compares the quantiles of the *approximate* theoretical null distribution of S in Eq. 5.8, to the quantiles of the bootstrap null distribution of S, which is the *true* null distribution of S. The two distributions do not match since the points do not lie close to the straight line. The points lie below the line, so the distribution in eq.5.8 is shifted to the right of the null bootstrap distribution; hence p-values calculated from eq. 5.8 are biased upwards, i.e. they are larger than they should be, so the test is conservative. Indeed we observed that the rate of spurious detections of SSA-scan at $p = 0\%$ in Figure 5.10 was below the nominal $\alpha = 5\%$, before the bootstrap diagnostics were applied (not shown). Because eq. 5.8 is a poor approximation

to the distribution of S, we must compute bootstrap p-values (Appendix A). However, we know from the diagnostic plot that p-values are biased upwards, so we can afford to recompute only the p-values that are somewhat above $\alpha = 5\%$, say in the $[5,10]\%$ range. It would be a waste of time to recompute the other p-values, since a bootstrap adjustment is unlikely to shift them on the other side of $\alpha = 5\%$. Figure 5.10B shows the power curves of the SSA-scan test after the bootstrap diagnostics and corrections were applied. The rate of spurious detections matches the nominal significance level α, so the test is trustworthy. To summarize, the SSA-scan test is trustworthy if the following procedure is applied: (a) apply the scan test using the distribution in eq. 5.8 to calculate the p-value; (b) if the p-value is close to α, produce the diagnostic plot in Figure 5.16; (c) if the diagnostic plot deviates from the line, obtain a bootstrap p-value.

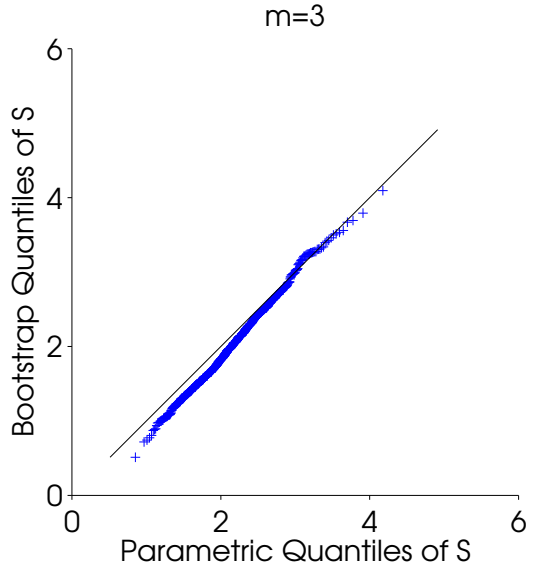

Figure 5.17: Bootstrap diagnostic plot for the $m = 3$ scan test applied to the dataset in Figure 5.10 with $p = 0\%$. Compare to Figure 5.16.

An alternative strategy is to decrease the influence on the scan test of the most contentious independence assumption, by scanning $T(l)$ at every m lags only, to decrease the serial correlation between successive values of $T(l)$. This is the m-scan test. We want to choose m large enough to reduce the serial correlation substantially, but not so large that we risk missing PSEs, and thus decrease the power of the test. The smallest m that yielded adequate diagnostic plots in our datasets was $m = 3ms$. Figure 5.17 shows the diagnostic plot when $m = 3ms$; (compare to Figure 5.16, when

the test is scanned at all lags): the points now lie close to the line, which validates the use of eq. 5.8 to calculate the p-value: bootstrap p-values are not needed. Moreover, in such cases, scanning at every $m = 3ms$ lag did not reduce the test's power to detect PSEs. Hence we recommend using the scan test with $m = 3ms$ rather than scanning the test at all possible lags, since the test retains good power, and avoids the calculation of bootstrap p-values. Note that $m = 3ms$ may not be optimal for all datasets, but this should not be of concern, since diagnostic plots such as Figures 5.16 and 5.17 help determine an adequate m; alternatively, bootstrap p-values can be calculated, as above.

5.9 APPENDIX C – EXTRA SSA, MFA, AND MFAE TESTS POWER EXAMPLES

Figure 5.18 shows the estimated power curves of SSA, MFA, and MFAE tests applied to two datasets, as function of the sample size (K, top row) and effect strength (p, bottom row). Our extensive simulations suggested that the SSA and MFAE tests had better power than the MFA test when applied to many but two datasets. The power curves for one of these two atypical datasets are shown in Fig 5.18B,D, where it is clear that the two MFA tests outperform the SSA test. This atypical digit flexion dataset was collected from a muscle with low EMG contraction levels, and thus contained a large proportion of low-valued EMG snippets; only one other digit flexion dataset shared that characteristic. The chronological order of the low content snippets appears to be key reason why the MFA tests are superior, since their advantage vanishes when we permute the EMG snippets before forming the fragments. Figure 5.18A,C shows the power curves of SSA and MFA/MFAE test applied to a grasp dataset. The MFA test has lower power than the other two tests; except when the sample size K is very small ($K < 150$ spikes), although that was not generally the case across datasets.

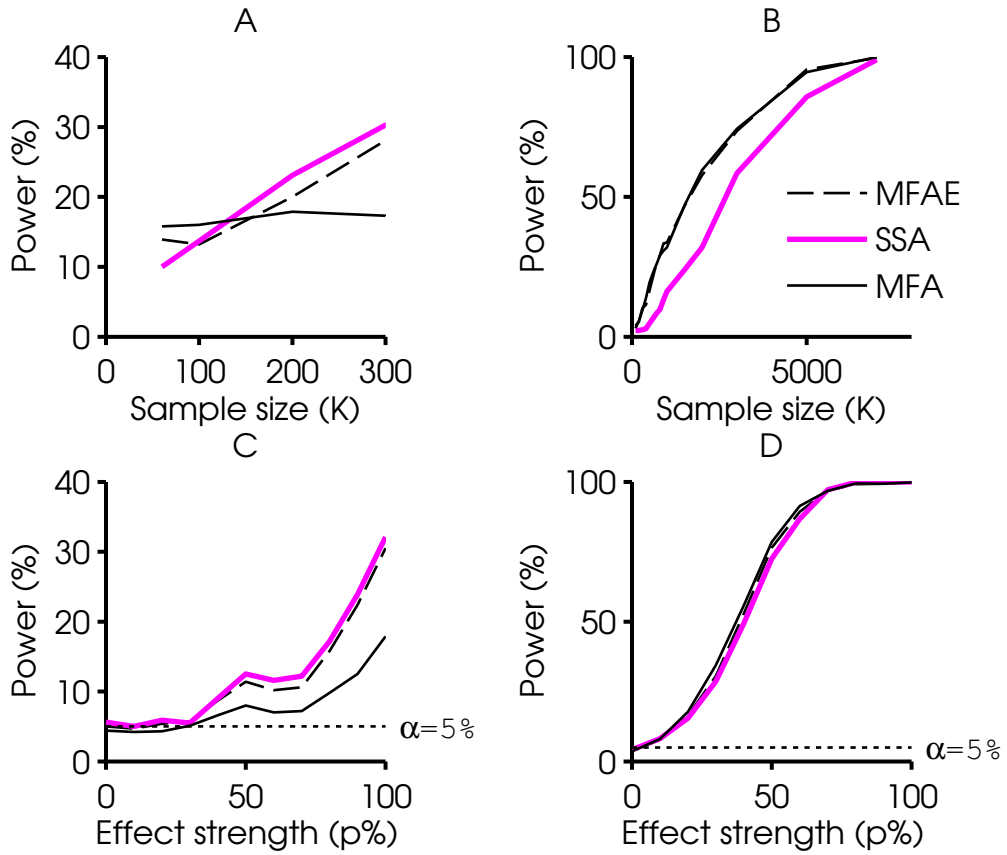

Figure 5.18: **Power curves.** **(A,B)** Power as function of sample size K (number of spikes used). For every K, power is estimated as the percentage of detections in 1000 test-datasets. **(C,D)** Power as function of effect strength p (percentage of non-jittered snippets), with sample size held constant at half the number of spikes in the parent dataset. For every p, power is estimated as the percentage of detections in 1000 test-datasets. At $p = 0\%$, there is no PSE in the data. At $p = 100\%$, the effect strength is the same as in the parent dataset. The power curves in **(A,C)** are for a typical grasp dataset, where SSA/MFAE show better power than MFA. The power curves in **(B,D)** are for an **atypical** digit-flexion dataset, where MFA/MFAE show better power than SSA. We suspect the cause is the high percentage of low-valued EMG snippets in this datasets.

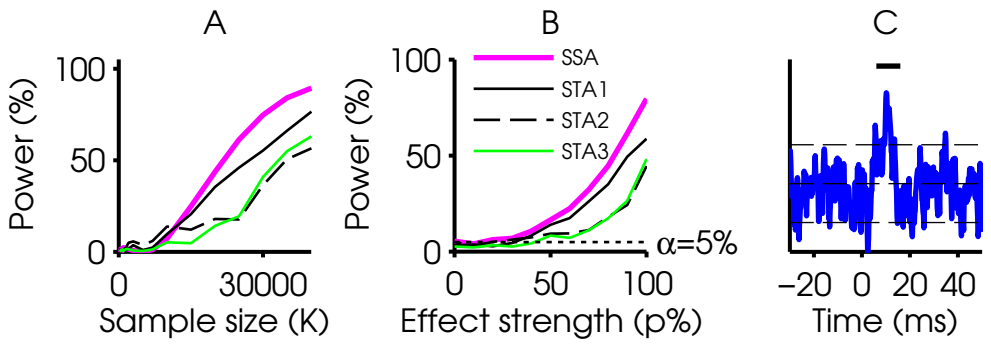

Figure 5.19: **Power comparison between SSA and SpTA tests applied to a narrow PSE.** The three variants of the automated SpTA were applied with a **PWHM threshold of** $2ms$, to increase their chances of detecting very narrow effects (compare to Figure 5.6 with PWHM threshold of $3ms$). We did not modify SSA. Power as function of **(A)** sample size K, and **(B)** effect strength p. **SSA has better power than SpTA for all sample sizes and effect strengths.** **(C)** SpTA for the precision-grip parent dataset, calculated using all 64572 spikes. The vertical bar on top spans the $6-16ms$ time window. The horizontal dashed lines are the SpTA baseline mean and mean$\pm$2D in baseline window $[-20ms, -10ms]$.

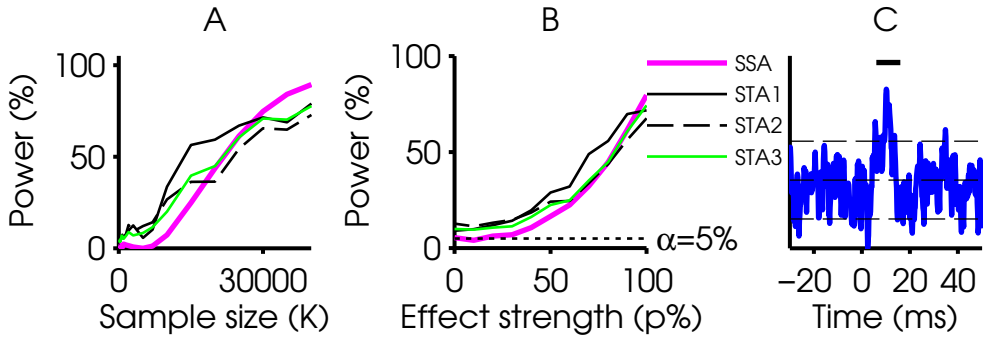

Figure 5.20: **Power comparison between SSA and SpTA tests applied to a narrow PSE.** The three variants of the automated SpTA were applied with **PWHM threshold** $1ms$ (compare to Figure 5.6 with PWHM threshold of $3ms$). Power as function of **(A)** sample size K, and **(B)** effect strength p. The vertical bar on top spans the $6-16ms$ time window. The horizontal dashed lines are the SpTA baseline mean and mean$\pm$2D in baseline window $[-20ms, -10ms]$.

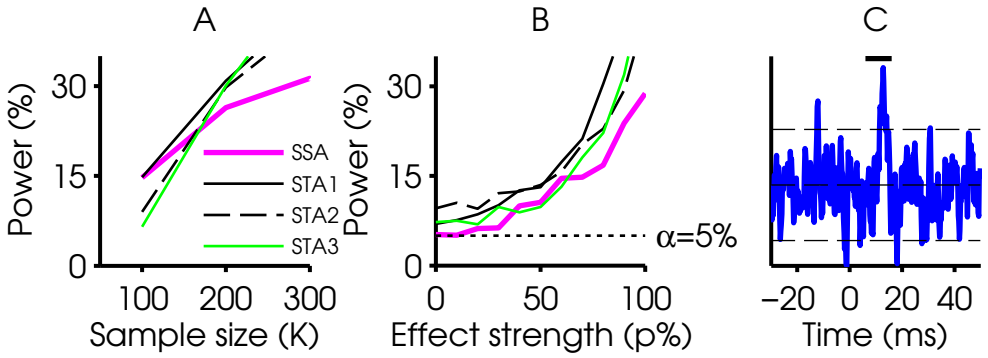

Figure 5.21: **Power comparison between SSA and SpTA tests applied to a small PSE.** The SpTA tests used a **PWHM threshold of** $1ms$ (compare to Figure 5.7 with PWHM threshold of $2ms$). The grasp parent dataset contains only 673 spikes; its SpTA in **(C)** shows a clear, albeit small, PSE. Power as function of **(A)** sample size K, and **(B)** effect strength p.

5.10 APPENDIX D – EXTRA SSA-SCAN TEST POWER EXAMPLE

Figure 5.22 shows the result of a power study applied to a modified parent dataset: before we generated the test datasets, we shifted all cortical spikes in the parent digit-flexion dataset 55*ms* back in time and jittered them with a SD of 8*ms*, to create a more disperse effect at a different latency. Our scan test was able to detect the PSE around the correct post-spike latency. The estimated latency is more variable than in Figure 5.10A and the power is lower, but this is to be expected since the PSE to be detected is more dispersed.

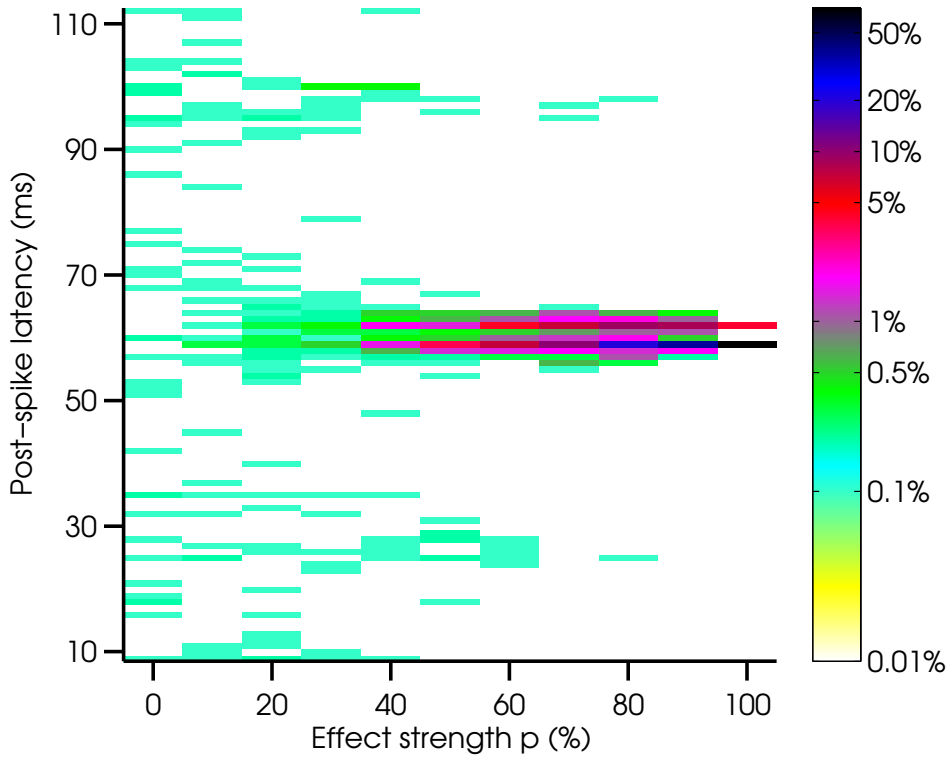

Figure 5.22: Heat map of detection probabilities for SSA-Scan, as function of post-spike latency (Y-axis) and effect strength (X-axis). The SpTA of the digit-flexion parent dataset is shown in Figure 5.3C. We first displaced all spikes by $50ms$ and jittered them with values drawn from $N(0,8ms)$, to create a displaced, broader PSE. We then created test datasets with varying effect strengths by jittering $(100-p)\%$ of the EMG snippets in the modified parent dataset; when $p = 0\%$, test datasets do not contain PSEs; when $p = 100\%$, they contain PSEs with the same effect strength as the modified parent dataset. The PSE is detected at the correct latency.

5.11 APPENDIX E – OFF-LINE PSE DETECTION

We give practical guidelines to use SSA and scan tests to detect PSEs off-line, i.e. when spikes and EMG data have already been collected. Appendix F details guidelines for on-line usage. Figure 5.1 summarizes the steps to verify test assumptions for SSA, all of which can be automated. For the majority of datasets we examined, even those with very few spike triggers, SSA test assump-

tions were met and p-values were unbiased. Few cases required that the p-values be calculated parametrically based on the $N(m, s^2)$ null distribution. No case actually required a full bootstrap simulation. Hence, automatic PSE detection is likely to be fast.

We use the following automatic procedure to calculate SSA p-values: given K spikes and simultaneously recorded EMG, extract K rectified spike-triggered snippets, for each snippet compute its Y_k value, i.e. the mean EMG in the effect window minus its baseline in adjacent windows. Use all Y_k values to compute T_{SSA} according to eq. 5.3. Approximate the mean and standard deviation of the null distribution of T_{SSA} by computing 100 bootstrap values of T_{SSA}. This is done by repeating the following steps 100 times: jitter the spike train, extract spike-triggered snippets and compute the value of T_{SSA} in that sample, denoted t_r^* (see sec. 5.3.4 and Appendix A for details). Compute the sample mean, m, and variance s^2 of the 100 t_r^* values, and use the normal $N(m, s^2)$ distribution to calculate the SSA p-value. This p-value is valid if the null distribution is Gaussian, which was the case in almost every dataset we inspected. To check if the null distribution is Gaussian, fit a linear regression to the normal probability plot of the 100 t_r^* values and verify the R^2 value is above 0.7. If not, compute the p-value using a full bootstrap simulation (Appendix A). A full bootstrap simulation in a dataset containing 5000 spike triggers takes about 5 minutes using custom Matlab code running on an average personal computer (2.3GHz processor, 4GB of RAM), which is reasonable given how seldom bootstrap p-values are required.

The SSA test looks for PSEs around $6-16ms$ post-spike latency. For neuron-muscle pairs with longer conduction delay, where PSEs might appear at later latencies, the SSA-scan test should be used. We found that scanning the SpTA every $m = 3ms$ satisfied the scan test independence assumption (sec. 5.4.5). We used the following procedure: given K spikes and simultaneously recorded EMG, extract the K rectified spike-triggered snippets. Decide on a reasonable latency range where the PSE peak might appear, for example $11-25ms$. For each peak latency value l, compute the Y_k value per snippet using the appropriate time windows, and use all the Y_k values to calculate $T_{SSA}(l)$. For example, SSA uses peak latency $l = 11ms$ and the appropriate time window is $6-16ms$. With $m = 3$, the next peak latency is $l = 14ms$, and the appropriate time window is from $9-19ms$. Once $T_{SSA}(l)$ is calculated for all l, calculate eq. 5.4 or 5.7 to find the the largest putative PSE, and compute its p-value using eq. 5.6. In most datasets, the scan test assumptions were met and p-values were valid. To check the scan test assumptions, fit a linear regression to

the normal probability plot of 100 bootstrap scan test values, and verify that R^2 is above 0.7. If not, calculate a bootstrap p-value (Appendix A), or increase m. A full bootstrap simulation for 5000 spikes can be computed in about 6 minutes using custom Matlab code running on an average personal computer (2.3GHz processor, 4GB of RAM).

We followed the procedures above to automate PSE detection in the datasets we examined. The tests can offer putative classification of PSEs as monosynaptic or polysynaptic based on latency, but the final decision is left to the investigator. When the PSE shape is of interest, an SpTA can be computed. The magnitude of the PSE is measured by the T_{SSA} test statistic value: it is a normalized measure, so PSE magnitudes can be compared across muscles and experimental conditions. This measure is conceptually similar to the mean-percent-increase (MPI) commonly used, although it is normalized by the SD of the differential EMG values (SD of the Y_k values), rather than by the baseline SpTA mean.

5.12 APPENDIX F – ON-LINE PSE DETECTION

The automatic PSE detection tests can also be used to detect PSEs on-line, while the data are collected. This will help inform the investigator about which neuron-muscle pairs to focus on. The SSA test is especially well suited for on-line detection due to its simplicity, since it requires only the calculation of Y_k for each new spike trigger; no data segmenting and no data storage is needed.

We proceed as follows. First, set the initial values:

- $K = 0$ number of recorded triggers
- $\bar{Y} = 0$ mean of the Y_k's
- $\overline{Y^2} = 0$ mean of the Y_k^2's.

Then, for every new trigger:

1. Extract the rectified EMG snippet and calculate its Y_k
2. Update $\bar{Y} \longrightarrow (K\bar{Y} + Y_k)/(K+1)$
3. Update $\overline{Y^2} \longrightarrow (K\overline{Y^2} + Y_k^2)/(K+1)$
4. Update $K \longrightarrow K+1$

5. Calculate $T_{SSA} = \frac{\bar{Y}}{SD(\bar{Y})}$ (eq.3), where $SD^2(\bar{Y}) = (\overline{Y^2} - K \cdot (\bar{Y})^2)/K/(K-1)$

6. Calculate the p-value $p = 1 - 2\Phi(T_{SSA})$.

   $p < \alpha$ provides evidence of a PSE around $6-16ms$ post-spike. Hence if $p >> \alpha$, the chance that a PSE exists is very small, and recording should be stopped.

Steps 5. and 6. can be performed at regular intervals rather than after each new spike trigger. In step 6., we use the standard normal null distribution of T_{SSA}, and we do not check assumptions because (i) we save time, and (ii) we found that in the vast majority of cases, the assumptions were either met, or the SSA test was robust to misspecification of the assumptions. The assumptions can be checked off-line once all the data are collected (Appendix E).

To detect PSEs at a range of latencies, we use the SSA-scan test, which consists of performing SSA using shifted effect windows. For a reasonable peak latency range of $11-25ms$, the first T_{SSA} value would be computed with the $6-16ms$ effect window centered at $l = 11ms$. The second T_{SSA} window would be centered $3ms$ later, at $l = 14$ms, and use the effect window $9-19ms$ post-spike. For a peak latency range of $11-25$ms with $m = 3$, this means calculating six $T_{SSA}(l)$ values. This is implemented on-line, by extending the previous algorithm to calculate the six $T_{SSA}(l)$ values, and replacing step 6. by:

6. Calculate $S = \max_l T_{SSA}(l)$ (eq. 5.4 or 5.7) and its p-value (eq.5.6).

Again, step 6 can be performed at regular intervals rather than after each new spike trigger (for example, every minute). Step 6 takes less than one second using custom Matlab code running on an average personal computer ($2.3G$Hz processor, 4GB of RAM), so the scan test is efficient for on-line PSE detection.

5.13 APPENDIX G – AN EQUIVALENT SCAN TEST

The p-value of the scan test (eq. 5.6) requires a numerical integration. The modified scan test described below is equivalent, but its p-value in eq. 5.12 is trivial to calculate.

Recall that $T(l)$ is the statistic calculated on the portion of the EMG snippets centered at time l. $T^2(l)$ is approximately χ^2_1 distributed. Large values of $T^2(l)$ provide evidence against the null

hypothesis of no PSE at lag l, with p-value calculated as

$$P(l) = P(T^2(l) \geq t^2_{obs}(l)) = 1 - F_{\chi^2_1}(t^2_{obs}(l) \tag{5.9}$$

where $F_{\chi^2_1}$ is the χ^2_1 cumulative probability density function, and $t_{obs}(l)$ is the observed value of $T(l)$ in the data. Under the null hypothesis, the distribution of $P(l)$ is uniform on $[0,1]$, and large values of $T^2(l)$ correspond to small values of $P(l)$.

We propose the alternative scan test statistic:

$$\tilde{S} = \min_l P(l) \tag{5.10}$$

for the detection of PSEs at any latency. If there is no PSE, $P(l)$ is relatively large for all l, so $\tilde{S}$ is large. If there is an effect at lag l^*, then $P(l^*)$ should be smaller than $P(l)$ for $l \neq l^*$, and thus $\tilde{S}$ should be smaller. Hence a comparatively small value of $\tilde{S}$ is evidence of a facilitation or suppression PSE in the data. To quantify what *comparatively small* is, we need the null distribution of $\tilde{S}$. If we assume that the $T(l)$ are mutually independent, then a standard probability calculation yields the null distribution of $\tilde{S}$, $f_{\tilde{S}}(s) = Lu(s)[1-U(s)]^{L-1}$, where u and U are the Uniform[0,1] probability and cumulative probability density functions, and L is the number of scanned lags. This simplifies to

$$f_{\tilde{S}}(s) = L(1-s)^{L-1}, s \in [0,1]. \tag{5.11}$$

Hence the p-value of this scan test is

$$p = P(\tilde{S} \leq \tilde{s}_{obs}) = \int_0^{\tilde{s}_{obs}} f_{\tilde{S}}(s)\, ds = 1 - (1-\tilde{s}_{obs})^L, \tag{5.12}$$

which is trivial to calculate. This scan test is equivalent to the original scan test, which means that their p-values in eqs. 5.12 and 5.6 are equal, by construction.

One-sided tests If facilitation PSEs are of primary interest, we replace $P(l)$ in eq. 5.9 by $P(l) = P(T(l) \geq t_{obs}(l)) = 1 - \Phi(t_{obs}(l)$. If detecting suppression PSEs is of primary interest, we use $P(l) = P(T(l) \leq t_{obs}(l)) = \Phi(t_{obs}(l)$. The rest of the procedure remains unchanged.

6.0 FUNCTIONAL CONNECTIVITY BETWEEN MOTOR CORTEX AND MUSCLES

In Chapter 3, we have shown that muscle activations and joint angles change in an object-specific manner across attitudes. In Section 4.1, we found that similarly, motor cortical neurons change their firing rates in an object-specific manner, suggesting that motor cortical tuning is task-dependent. In Sections 4.2, 4.3, 4.4 and 4.5, we have investigated the multivariate linear relationship between the firing rates of individual neurons and EMG, JA and JA velocities. We concluded that both EMG and kinematic features were encoded in the neural firing rates; although JA and JA velocities were better predictors of neural firing rates than EMG. Furthermore, neuron-specific combinations of EMG and kinematic features were better predictors than individual muscles or joints, functional groups (e.g. MCP joints, finger muscles), or synergies extracted using PCA/ICA. This fits well with a view of the motor cortex as a distributed system, where individual neurons represent fractions of task-relevant information. In Section 4.6, we demonstrated that by combining the mean activity of around 50 sequentially recorded neurons, we were able to predict both mean muscle activations and mean JA. We concluded that the neural activity contained synergistic information related to EMG, not independently present in individual neurons.

Based on these findings, we hypothesized that functional connections between neurons and muscles are flexible, and change with task requirements. We observed that kinematic features are better represented in the firing rates of individual neurons across all task conditions; which may indicate that driving inputs to motor cortical neurons, which we assume represent task requirements, are related to kinematic features. It is known that motor cortical activity from multiple neurons is combined, by cortical networks, sub cortical areas and spinal cord neurons, to facilitate muscle activation; and the nature of cortico spinal functional connectivity determines how this neural activity generates muscle activation. We suggest that this connectivity is dynamic in nature, since most neurons we examined did not encode muscle activity as well as kinematic features, but their combined

activity was a good predictor of muscle activity; hence it is possible that individual neurons were correlated with muscles activations for some portions of the task but not for others. Investigating functional connectivity, is therefore of great importance, and is our focus in this chapter.

We define functional connectivity as $P(\Delta EMG \text{ at time } t+\Delta t | \text{spike at time t}, X)$. When Δ is on the order of hundreds of milliseconds, we examine long-time scale functional connectivity. This is traditionally done using sample-correlation coefficients (see Section 1.3 for details). When Δ is on the order of tens of milliseconds, we examine short-time scale functional connectivity, traditionally done using spike-triggered averaging (SpTA). Since SpTA has low detection power and unknown significance level, especially with small sample sizes, we developed novel methods to estimate short-time scale functional connectivity, which were presented in Chapter 5.

Figure 6.1 contains a diagram of functional projections to alpha motoneuronal pools. The recorded motor cortical neuron, on the top right, projects either directly (CM cell) or indirectly (via spinal interneurons) to the motoneuronal pool; and in either case, its synaptic contribution is very small compared to the other inputs. Motoneuronal pools receive most of their inputs from spinal interneurons (indicated by bigger arrow heads), but also from sensory neurons and CM cells. The motoneuronal pool integrates the inputs and facilitates EMG in the muscle. All inputs to the motoneuronal pool, except for the recorded cortical neuron, are represented by X in the functional connectivity equation. When functional connectivity is static, the activity of the recorded cortical neuron always correlates well with the activity of all other inputs to the motorneuronal pool, and so always correlates well to EMG activity. When functional connectivity is dynamic, the activity of the recorded cortical neuron does not always correlate well with all other inputs, and so does not always correlate well to EMG activity.

We first examine static long-time scale functional connectivity between individual neurons and muscles in Section 6.1. We then propose an encoding model for long-time scale dynamic functional connectivity between one neuron and multiple muscles in Section 6.2. We examine an alternative decoding connectivity model in Section 6.3, which allows us to investigate short-time scale functional connectivity in Section 6.4.

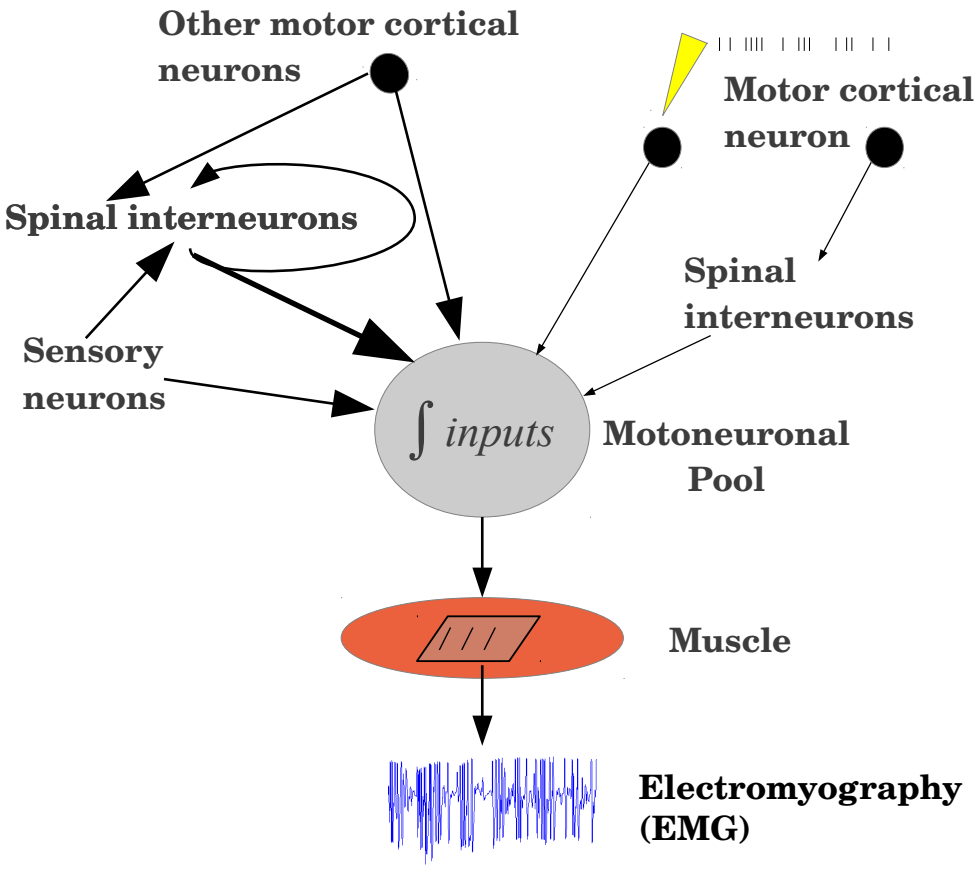

Figure 6.1: **Functional connectivity diagram:** The recorded motor cortical neuron, on the top right, projects either directly (CM cell) or indirectly (via spinal interneurons) to the motoneuronal pool. Motoneuronal pools receive most of their inputs from spinal interneurons (indicated by bigger arrow heads), but also from sensory neurons and CM cells. The motoneuronal pool integrates the inputs and facilitates EMG in the muscle. When functional connectivity is static, the activity of the recorded cortical neuron always correlates well with the activity of all other inputs to the motorneuronal pool, and so always correlates well to EMG activity. When functional connectivity is dynamic, the activity of the recorded cortical neuron does not always correlate well with all other inputs, and so does not always correlate well to EMG activity.

6.1 NEURAL CORRELATION TO EMG AND JA

In this section, we study long-time scale functional connectivity between neuron-muscle and neuron-joint pairs, using sample correlations. To assess the degree of correlation between the recorded neuronal activity and the 16 EMG, 23 JA and 23 JA velocities, we first calculated the fractional firing rate of every neuron, using 50*ms* bins, for every trial (see Section 2.2 for details about fractional firing rate). We also calculated the average EMG, JA and JA velocity in each of the 50*ms* bins, for every trial. EMGs were lagged by one bin width (50*ms* on average), and JAs were lagged by two bin widths (100*ms* on average), relative to the firing rate. We then calculated sample-correlation coefficients (according to Eq. 3.8), between the fractional firing rate of every neuron, and each of the covariates: the binned EMG, binned JA and binned JA velocities; for each of the attitudes. Correlation coefficients were calculated using all repeat trials from an attitude.

Monkey E's behavior consisted of 40 attitudes for the first few recording sessions, and 32 attitudes subsequently; therefore we only used the 32 attitudes common across all recording sessions. The analysis was performed using only recording sessions where JA data was valid, and neurons that have been well-isolated for the duration of an entire session (as indicated by our recording notes), with at least 10 repetitions to every attitude. Out of 200 task-modulated neurons, only 92 neurons met these criteria, and were used in this analysis.

Figure 6.2 shows the correlation values between 92 neurons recorded from monkey E and 16 muscles, for every attitude. Neurons are arranged in columns, and muscles in rows. 32 correlation values are plotted for every muscle, in rows, corresponding to 32 attitudes. The correlation vectors for all neurons were subjected to a clustering algorithm (K-means, using 8 clusters), and neurons with similar correlation vectors were plotted in groups. Some neurons recorded on the same day had similar correlation vectors, but the different groups contained neurons recorded across different days. The initial number of groups we chose was 10, but it exceeded the number of distinct groups we could visually identify. We incrementally decreased the number of groups to 8, the number of groups we could visually identify in the plot. We do not imply that neurons in the motor cortex divide into 8 functional groups, but rather point out that groups of neurons recorded over different days, at different areas of the motor cortex, show broadly similar muscle-correlation patterns for a range of movements.

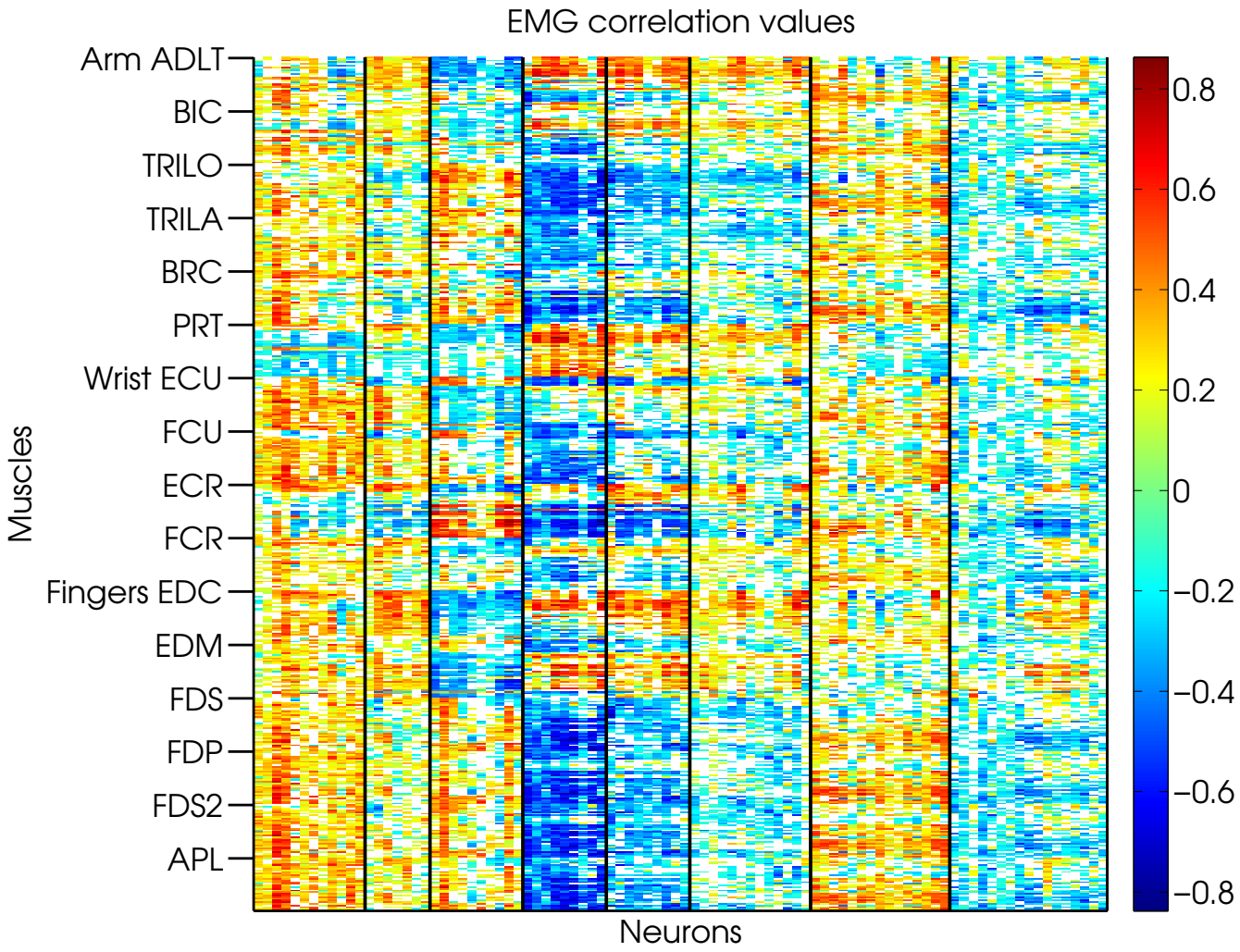

Figure 6.2: **Neuron-EMG correlation matrix: monkey E:** Heat map of correlation values between 92 neurons (columns) and 16 muscles (rows), for all task attitudes. Zero or missing correlation values were colored white. Spikes were converted to fractional firing-rates using 50*ms* bins; and EMG was averaged in the same 50*ms* bins, lagged by one bin relative to the firing rates. The sample correlation coefficient (Eq. 3.8) between every neuron and every muscle was computed from all trials belonging to every one of the 32 attitudes, resulting in 32 correlation coefficients per muscle, shown in rows. Neurons were clustered in 8 groups, according to similarity of correlation coefficients; group borders are shown as black vertical lines.

Examining the groups in Figure 6.2, from left to right, the first group is somewhat positively correlated to most muscles, but negatively correlated to pronator-teres and extensor carpi-radialis. Group 2 is similar to the first one, with differences mainly in the correlation magnitudes for some of the arm and finger muscles. Group 3 is positively correlated with the triceps, brachioradialis, extensor carpi-radialis, and the finger flexors. Group 4 is positively correlated to the deltoid, pronator-teres and the finger extensors. It is strongly anti-correlated to the finger flexors. Groups 5 and 6 are similar to group 4, with slight differences in correlation magnitudes. Group 7 is broadly correlated to most muscles, for a subset of the attitudes. Group 8 is not well correlated to any specific muscles. Based on these correlation patterns, and the muscles activation patters, we would hypothesize that neurons in groups 1,2 and 3 are active during the late reach phase and static grasp; and neurons in groups 4,5,6, correlated with muscles active at the beginning of the reach epoch, are mostly modulated during that epoch. Figure 6.5 shows a similar figure for monkey B, where we could visually identify 5 functional groups, three of which were similar to the groups found in Figure 6.2.

Figures 6.3 and 6.4 show the sample correlation coefficients to JA and JA velocities, accordingly, for monkey E. The neurons are arranged in columns, in the same order as Figure 6.2. The kinematics correlation coefficients support our hypothesis: neurons in groups 1 and 2 are positively correlated with MCP, PIP and DIP flexion velocity; which has the highest values during the preshape epoch. Neurons in group 3 are positively correlated with MCP, PIP and DIP flexion JA and so are likely to be active during the static grasp epoch. Neurons in groups 4,5,6 are negatively correlated with MCP, PIP and DIP flexion JA and JA velocity; or positively correlated to JA extension and JA extension velocity. Since fingers extend mostly during the first phase of the reach epoch, this finding supports our hypothesis as well. Neurons in group 7 show positive correlation to mostly to MCP, PIP and DIP flexion JA velocity, similarly to neurons in groups 1, and are therefore mostly active during the preshape epoch.

In Section 1.3.5, we described previous studies which examined the long time-scale correlation between muscle activity and the activity of motor-cortical neurons, some of which found consistent relationships between neuronal activity and muscle activations across behavioral tasks. In contrast, we observed that many neuron-muscle correlation coefficients in Figure 6.2 changed between attitudes. Such changes suggest that neural-muscle correlation is dynamic and attitude-dependent.

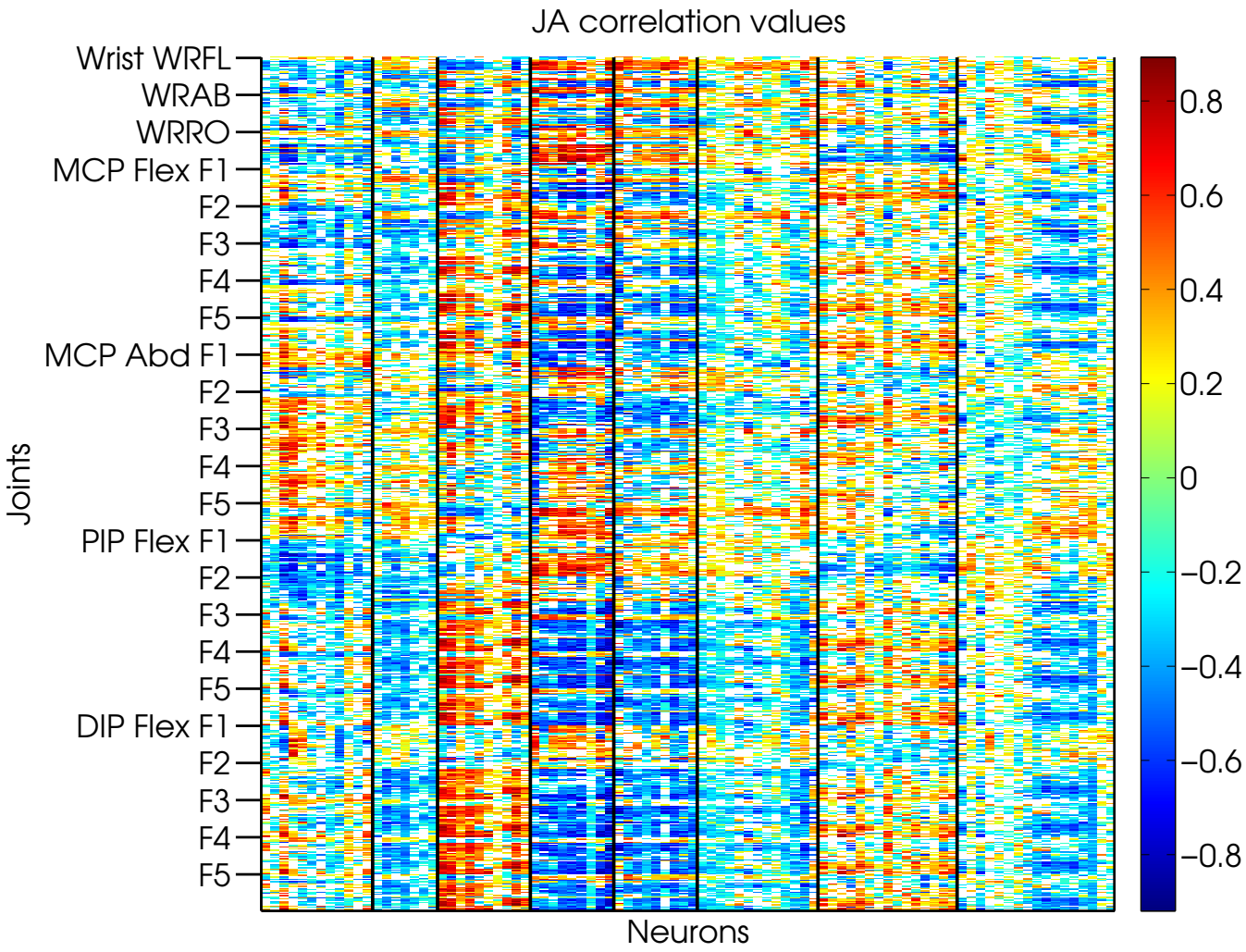

Figure 6.3: **Neuron-JA Position correlation matrix: monkey E:** Heat map of correlation values between 92 neurons (columns) and 23 JA (rows), for all task attitudes. Spikes were converted to fractional firing-rates using 50*ms* bins; and JA were averaged in the same 50*ms* bins, lagged by two bins relative to the firing rates. The sample correlation coefficient (Eq. 3.8) between every neuron and every JA was computed from all trials belonging to every one of the 32 attitudes, resulting in 32 correlation coefficients, shown in rows. The neurons are ordered according to Figure 6.2.

In the next two sections, we utilize two models to investigate whether changes in neuronal-muscle correlations are related to kinematic features.

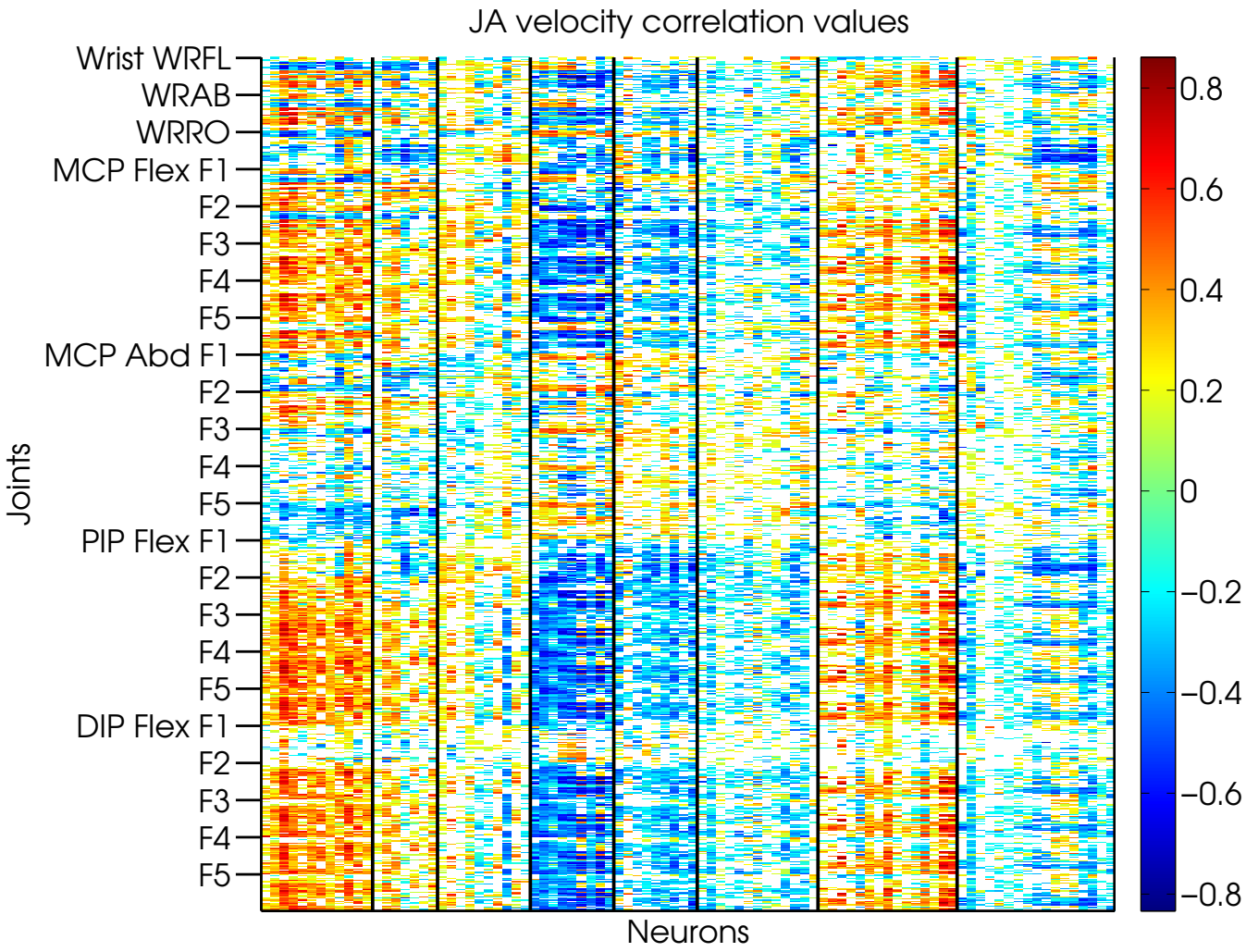

Figure 6.4: **Neuron-JA Velocity correlation matrix: monkey E:** Heat map of correlation values between 92 neurons (columns) and 23 JA velocities (rows), for all task attitudes. Spikes were converted to fractional firing-rates using 50*ms* bins; and JA velocities were averaged in the same 50*ms* bins, lagged by two bins relative to the firing rates. The sample correlation coefficient (Eq. 3.8) between every neuron and every JA velocity was computed from all trials belonging to every one of the 32 attitudes, resulting in 32 correlation coefficients, shown in rows. The neurons are ordered according to Figure 6.2.

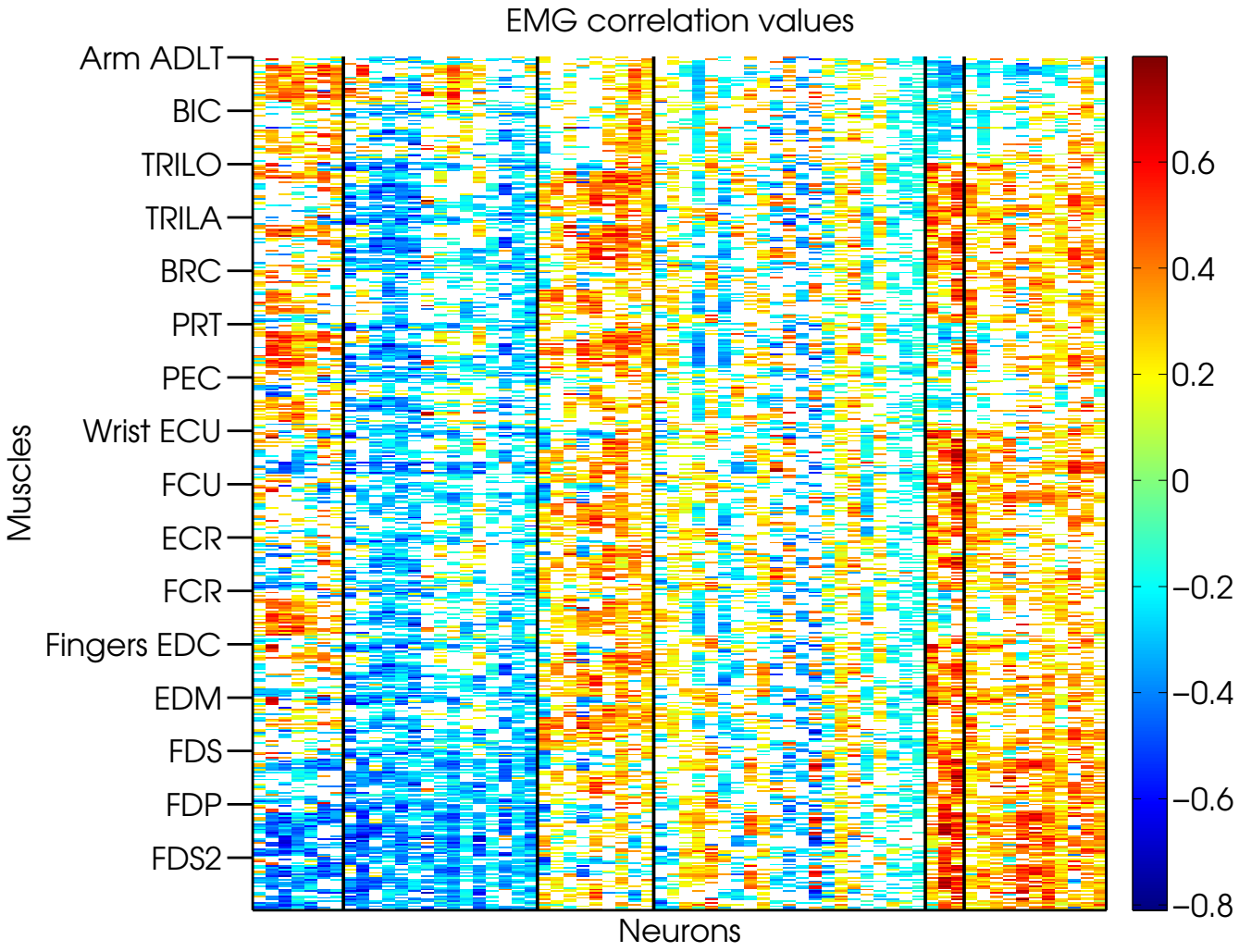

Figure 6.5: **Neuron-EMG correlation matrix: monkey B:** Heat map of correlation values between 66 neurons (columns) and 16 muscles (rows), for all task attitudes. Zero or missing correlation values were colored white. Spikes were converted to fractional firing-rates using 50*ms* bins; and EMG was averaged in the same 50*ms* bins, lagged by one bin relative to the firing rates. The sample correlation coefficient (Eq. 3.8) between every neuron and every muscle was computed from all trials belonging to every one of the 32 attitudes, resulting in 32 correlation coefficients per muscle, shown in rows. Neurons were clustered in 8 groups, according to similarity of correlation coefficients; group borders are shown as black vertical lines. The 32 attitudes shown here are slightly different than the ones for monkey E, in Figure 6.2 (see Table 1 for details).

6.2 LONG-TIME SCALE DYNAMIC FUNCTIONAL CONNECTIVITY I

In Section 6.1, we found that sample-correlation coefficients between neuronal firing rate and EMG often change between attitudes. To examine if changes in correlations were related to kinematic features, we modeled dynamic functional connectivity as linearly dependent on multiple joint angles. We used a generalized linear model (GLM) with both static and dynamic connectivity terms:

$$log(\lambda) = a_0 + \sum_{i=1}^{M} a_i(JA) \times EMG_i \tag{6.1}$$

where:

- λ is the neuron's firing rate, binned in $1ms$ bins, with binary values $(0, 1)$
- EMG_i is the rectified EMG for muscle i, binned in $1ms$ bins and spline-smoothed to extract the EMG envelope
- $a_i(JA)$ is a coefficient dependent on kinematic features, defined as: $a_i(JA) = b_{i,0} + \sum_{j=1}^{J} b_{i,j} \times JA_j$
- M is the number of muscles, J is the number of joint angles
- JA_j is the $j-th$ joint angle, filtered with a $10Hz$ low-pass filter and spline-interpolated to $1ms$ bins
- EMG was lagged by $50ms$, and JA was lagged by $100ms$ relative to the firing rates
- EMG and JA were z-scored prior to fitting the GLM

Substituting for $a_i(JA)$ in Equation 6.1 and expanding the terms yields:

$$log(\lambda) = a_0 + \sum_{i=1}^{M} [b_{i,0} + \sum_{j=1}^{J} b_{i,j}] \times EMG_i = a_0 + \sum_{i=1}^{M} b_{i,0} \times EMG_i + \sum_{i=1}^{M} \sum_{j=1}^{J} b_{i,j} \times JA_j \times EMG_i \tag{6.2}$$

which conceptually divides the model into *static* (the left sum) and *dynamic* (the right sum) components. The static connectivity model is similar to Equation 4.1; but the latter was fit using data averaged in $50ms$ bins, instead of $1ms$ bins. The dynamic connectivity model incorporates the interactions of all joint angles with the neuron-EMG correlation.

We fit the model to data from 129 neurons, using all samples from every trial, across all attitudes. Figure 6.6 shows a heat map of coefficients for all neurons, representing a "connectivity map" between every neuron and all recorded muscles, indicating which joint angles affect the

relationship between the neuron-muscle pairs. Neurons are arranged in columns, and GLM coefficients are arranged in rows. The data were normalized (z-scored) prior to fitting the GLM, to make coefficients comparable across neurons. The first 16 rows contain the static model coefficients, and the remaining 368 rows contain the dynamic model coefficients, ordered by muscle groups, and internally for every muscle, ordered by joint angles. The connectivity map is sparse, and neurons show dissimilar coefficients, suggesting that for every neural-muscle pair, correlations depend on different kinematic features. No individual muscle is assigned higher coefficients compared to the other muscles. When reordering the rows, so the coefficients are grouped by joint angles, and internally for every joint, ordered by muscles; no single joints show higher coefficients compared to the other joints (see Figure 6.7).

To investigate whether the dynamic connectivity terms contributed to firing rate prediction, we compared the predictive power of the full model in Equation 6.1, to a static model which included only the left sum in Equation 6.2. We compared the two models using two criteria: R^2 and AIC. First, we computed the R^2 between the conditional intensity $\hat{\lambda}$ (the GLM estimate) and $S(\lambda)$ (the spline-smoothed λ). We chose the smoothing parameters so the frequency content in $S(\lambda)$ and $\hat{\lambda}$ was similar. Figure 6.8 shows that the dynamic model outperformed the static model for all 129 neurons.

The Akaike Information Criterion (AIC) allows us to compare the goodness of fit between the two models. It is computed per model using $AIC = -2log(L) + 2P$, where $-2log(L)$ is the model deviance and P is the number of parameters in the model. L is the maximized likelihood, so that the deviance becomes smaller as the data becomes more likely under the given model. Because models with too many parameters may not generalize well to predict new data, the AIC accounts for the number of parameters in the model. A smaller AIC value indicates a more appropriate model. Figure 6.9 shows a comparison of the AIC values between the two models. For $90/129$ neurons, the dynamic model was a better fit; and for $39/129$ neurons, the static model was a better fit.

Figure 6.10 shows box-plots of the static (6.10**A**) and dynamic GLM coefficients computed across all neurons. Dynamic coefficients were grouped by JAs (6.10**B**) and by muscles (6.10**C**). The static coefficients distributions have slightly longer tails (indicated by longer whiskers), but

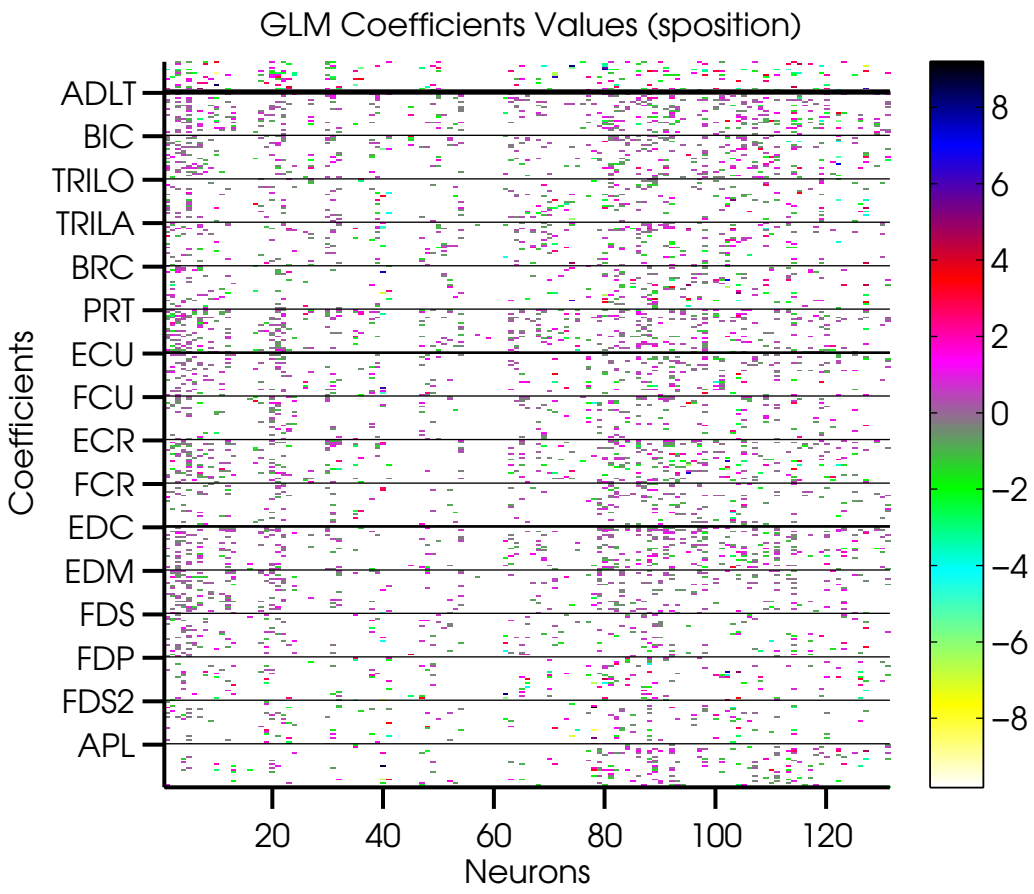

Figure 6.6: **Dynamic connectivity GLM coefficients: monkey E:** Heat map of GLM coefficients (defined in Equation 6.1) for 131 neurons, sorted by muscles. Data was normalized prior to fitting the GLM and the coefficients are comparable across neurons. Only significant coefficients are plotted. Neurons are arranged in columns, and GLM coefficients are arranged in rows. The first 16 rows contain the static coefficients, and the remaining 368 rows contain the dynamic coefficients. Dynamic coefficients are plotted per muscle, where muscles are grouped by arm, wrist and hand muscles. Dynamic coefficients per muscle are ordered by joint angle number (total of 23 JA per muscle). The heat map is sparse and there is no evident similarity between neurons, or any preference for specific muscles.

there is no preference for any single JA or muscle in any of the box-plots; indicating heterogeneous connectivity patterns between neurons and muscles.

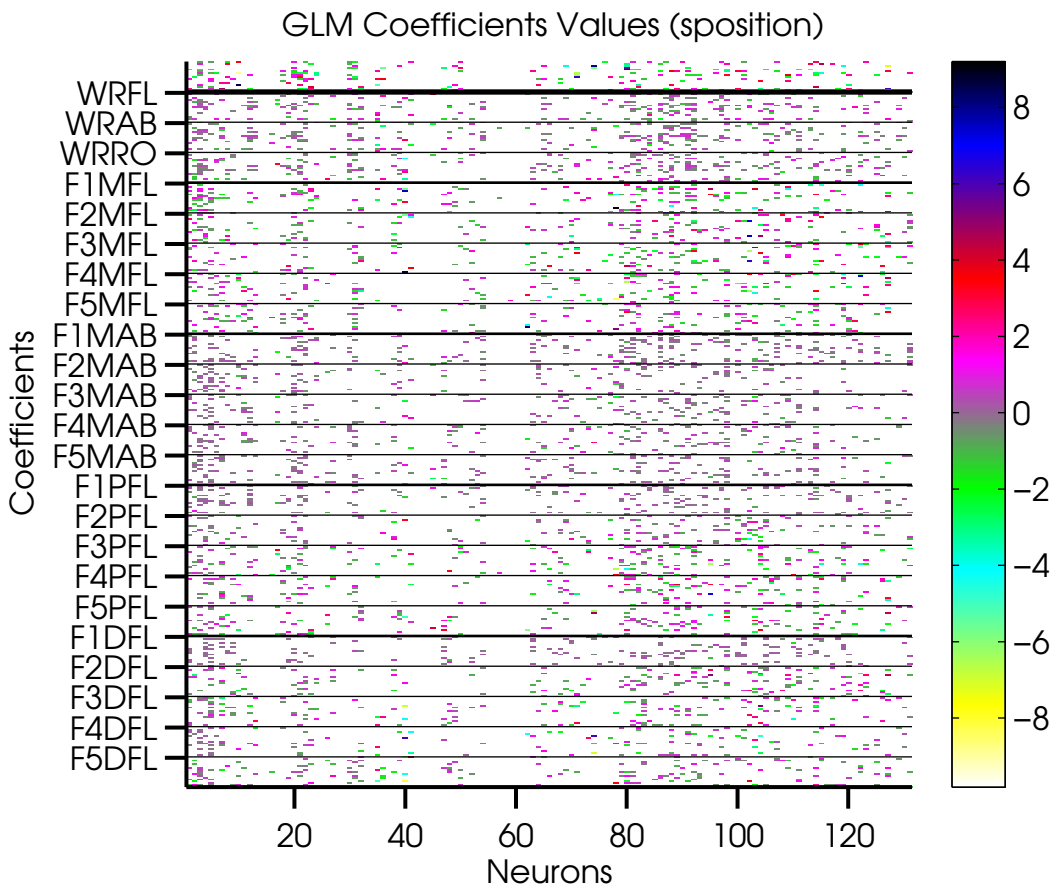

Figure 6.7: **Dynamic connectivity GLM coefficients: monkey E:** Heat map of GLM coefficients (defined in Equation 6.1) for 131 neurons, sorted by JAs.. Data was normalized prior to fitting the GLM and the coefficients are comparable across neurons. Only significant coefficients are plotted. Neurons are arranged in columns, and GLM coefficients are arranged in rows. The first 16 rows contain the static coefficients, and the remaining 368 rows contain the dynamic coefficients. Dynamic coefficients are plotted per joint, and joints are grouped by anatomical segments. Dynamic coefficients per joint are ordered by muscles (total of 16 muscles per JA). The heat map is sparse and there is no evident similarity between neurons, or any preference for specific joints. Compare to Figure 6.6, where rows are ordered by muscles.

We also fit a GLM in the form of Equation 6.1, where dynamic connectivity terms were dependent on both JA and JA velocity, so that:

$$a_i(JA) = b_{i,0} + \sum_{j=1}^{J} b_{i,j} \times JA_j + \sum_{j=1}^{J} c_{i,j} \times JAVel_j \tag{6.3}$$

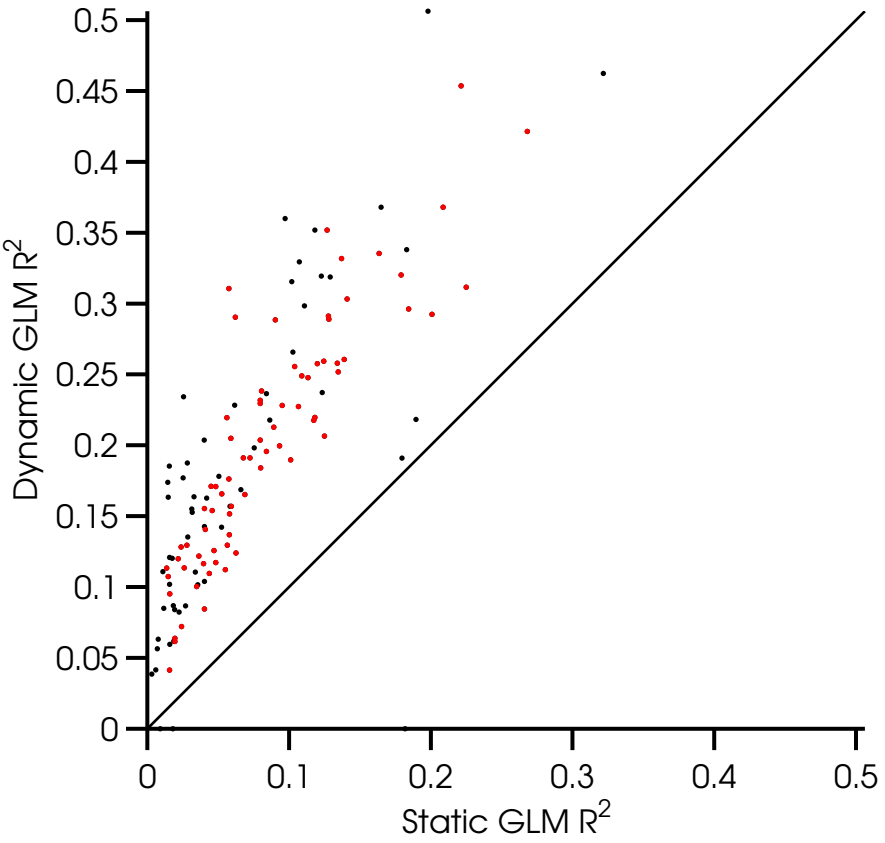

Figure 6.8: R^2 **comparison between dynamic and static connectivity models: monkey E:** The dynamic model was fit using Equation 6.1; the static model was fit using the left sum in Equation 6.2. R^2 values were computed between $S(\lambda)$, the spline smoothed λ, and $\hat{\lambda}$, the conditional intensity predicted by the two models. The dynamic model outperformed the static model for all neurons. The R^2 values for the 92 neurons used in Figure 6.2 are highlighted in red.

Figure 6.11 shows a comparison of R^2 between the JA only GLM and the JA-JA velocity GLM, where the JA only GLM is better only for 8 out of 125 neurons. Although the estimate R^2 is better for the JA-JA velocity GLM, it contains twice the number of parameters, compared to the JA only GLM. Figure 6.12 shows the AIC comparison between the two models, suggesting that the JA only GLM is more likely to generalize better for new data. Figures 6.13 and 6.14 show box-plots for the JA-JA velocity GLM coefficients, where most of the velocity related dynamic coefficients

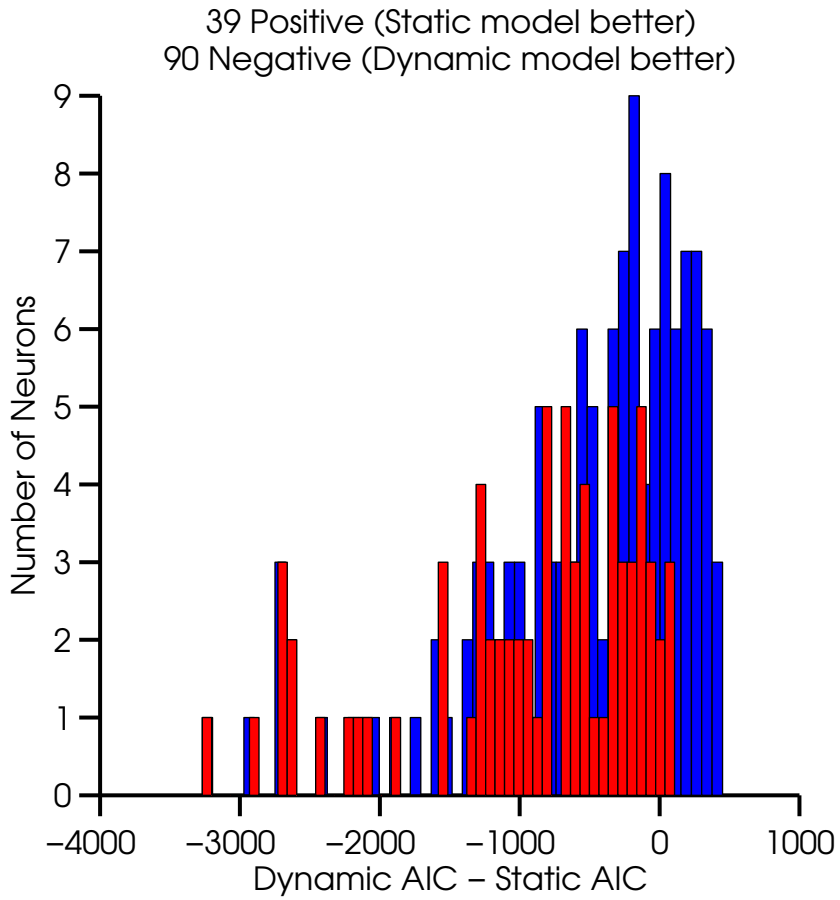

Figure 6.9: **AIC comparison between dynamic and static connectivity models: monkey E:** The dynamic model was fit using Equation 6.1; the static model was fit using the left sum in Equation 6.2. AIC values were computed using Matlab's GLM library. The histogram shows that the dynamic model predicts the firing rates better than the static model for most neurons. The blue histogram shows all neurons, the red histogram shows the 92 neurons from Figure 6.2.

are a lot smaller compared to the JA related dynamic coefficients; with the exception of the the MCP flexion velocities. Therefore, a hybrid model which includes the JA coefficients and the MCP-flexion velocity terms is likely to perform better than both models.

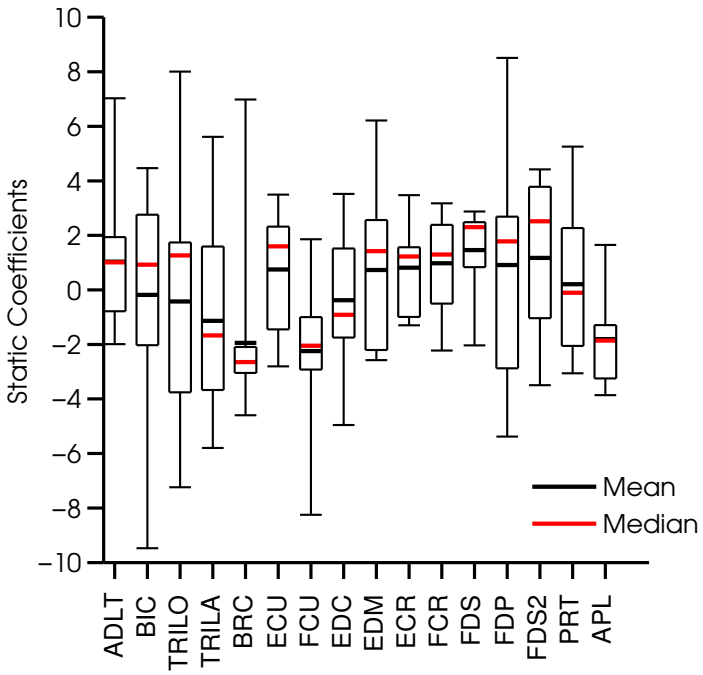

(**A**) GLM static coefficients

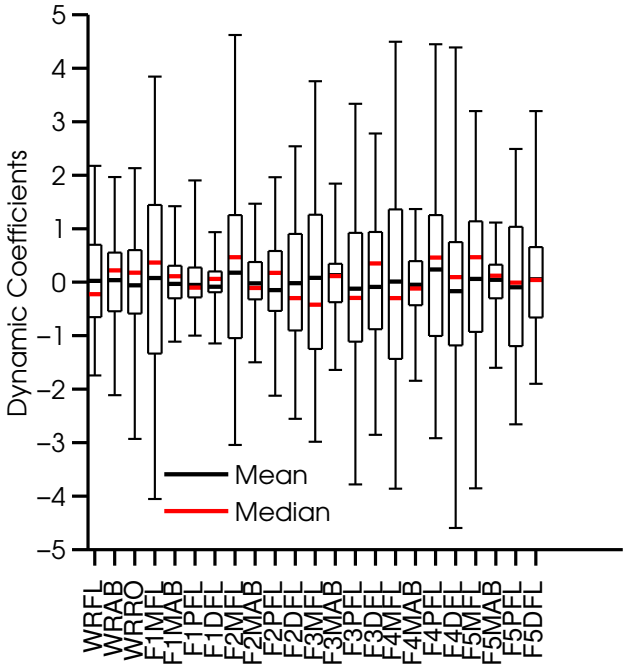

(**B**) GLM dynamic coefficients by JA

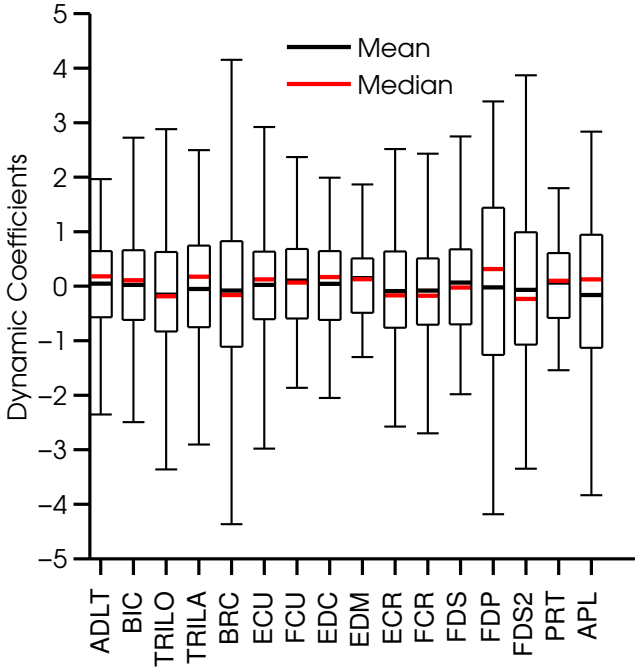

(**C**) GLM dynamic coefficients by muscle

Figure 6.10: **Connectivity GLM coefficients boxplot: monkey E:** Boxplot for the static and dynamic coefficients, computed across all neurons. The model was fit using Equation 6.1. The boundaries of the boxes are the 1^{st} and 3^{rd} quartiles. The mean and median are indicated by horizontal lines. The whiskers extend to the 5^{th} and 95^{th} percentiles, after removing outliers.

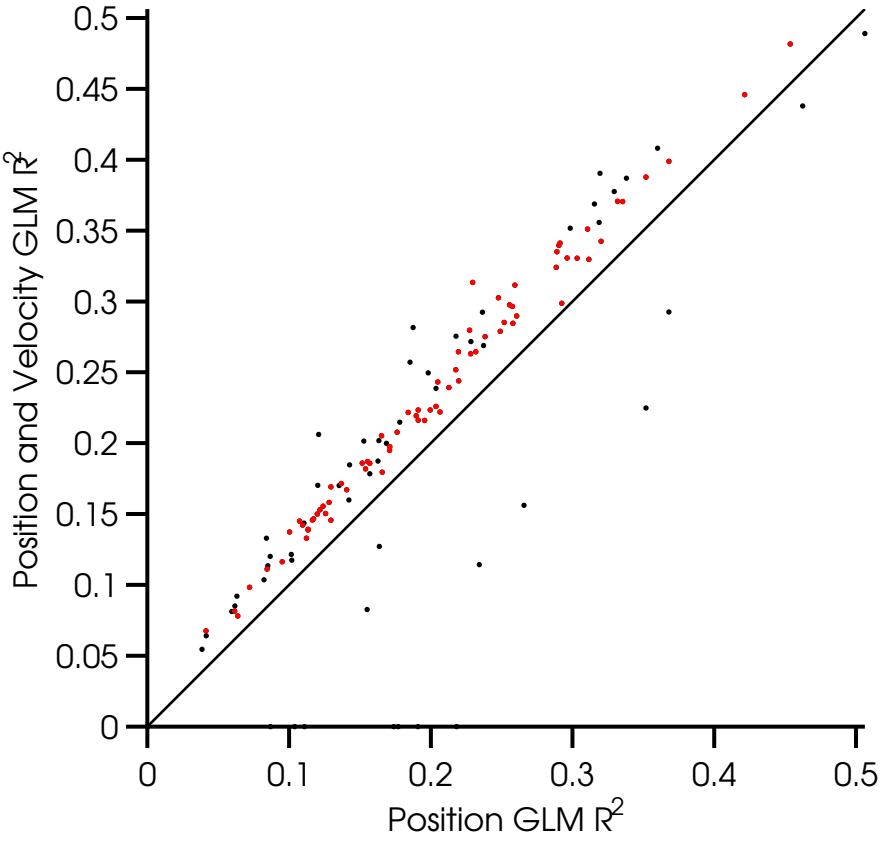

Figure 6.11: R^2 **comparison between JA only and JA-JA velocity connectivity models: monkey E:** The JA model was fit using Equation 6.1; the JA-JA velocity model was fit using Equation 6.1, with dynamic terms defined by Equation 6.3. R^2 values were computed between $S(\lambda)$, the spline smoothed λ, and $\hat{\lambda}$, the conditional intensity predicted by the two models. The JA-JA velocity model shows better R^2 values for 117 out of 125 neurons. The R^2 values for the 92 neurons used in Figure 6.2 are highlighted in red.

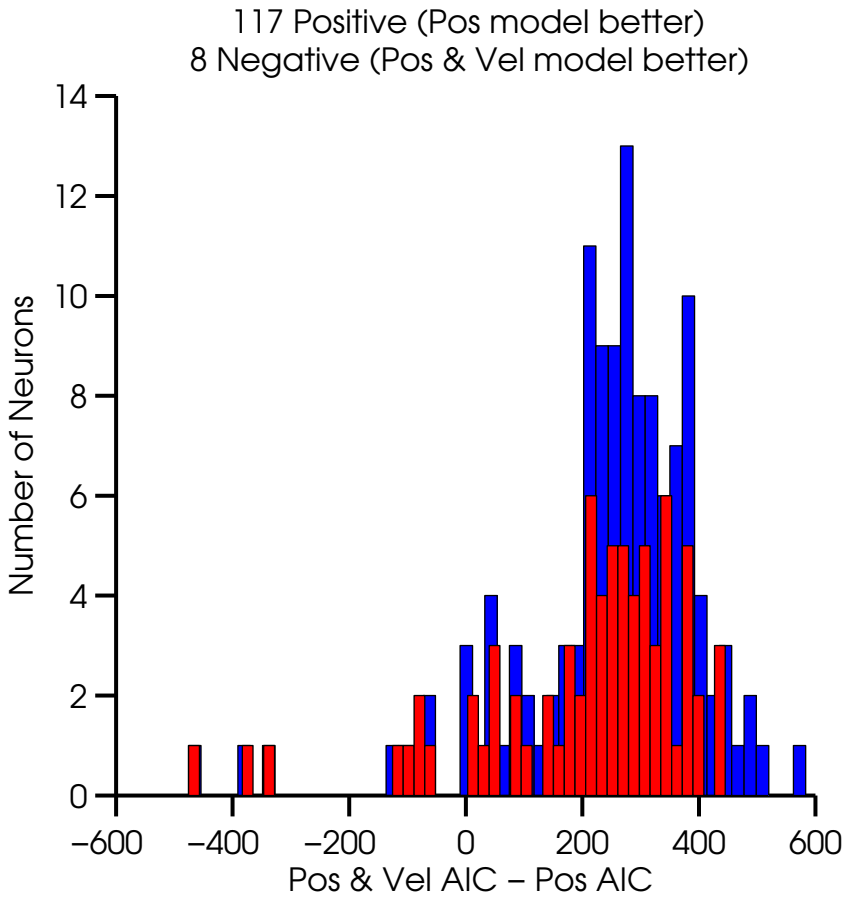

Figure 6.12: **AIC comparison between JA only and JA-JA velocity connectivity models: monkey E:** The JA only model was fit using Equation 6.1; the JA-JA velocity model was fit using Equation 6.1, with dynamic terms defined by Equation 6.3. AIC values were computed using Matlab's GLM library. The histogram shows that when taking into account the number of parameters in the models, the JA only model generalizes better compared to the JA-JA velocity model. The blue histogram shows all neurons, the red histogram shows the 92 neurons from Figure 6.2.

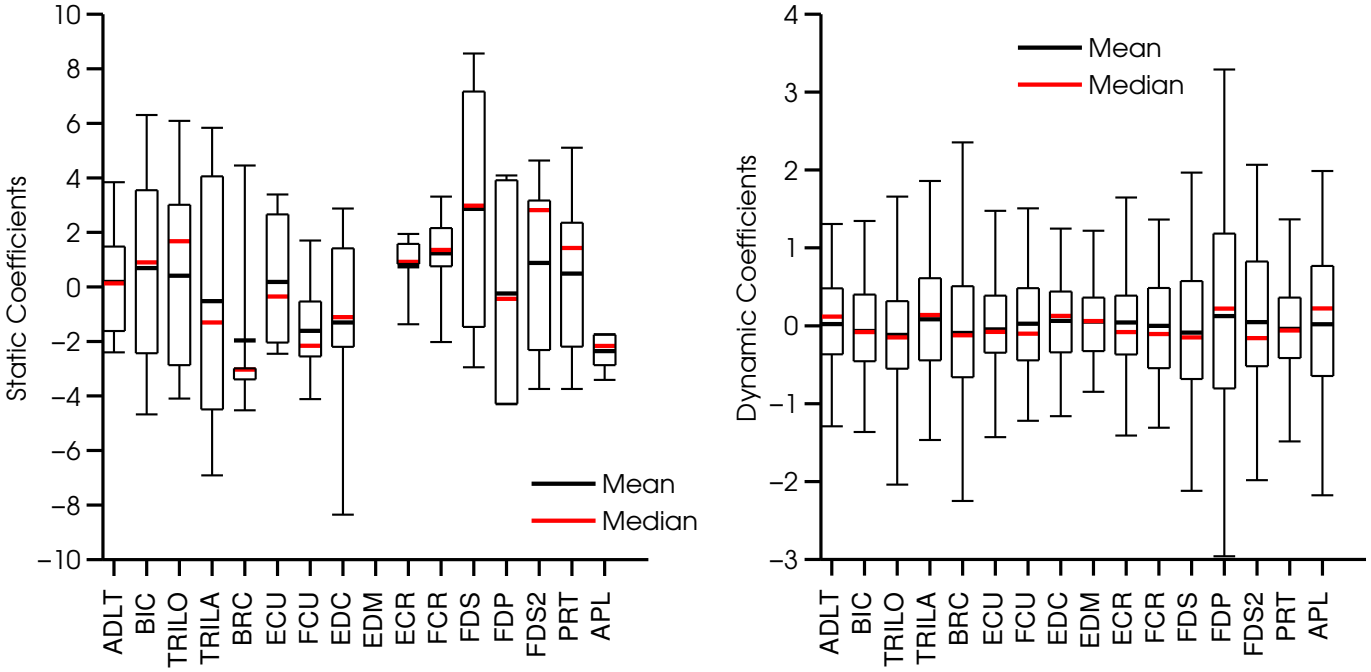

(**A**) GLM static coefficients

(**B**) GLM dynamic coefficients by muscle

Figure 6.13: **JA-JA velocity connectivity GLM coefficients boxplot: monkey E:** Boxplot for the static and dynamic coefficients, computed across all neurons. The model was fit using Equation 6.1, with the dynamic terms from Equation 6.3. The boundaries of the boxes are the 1^{st} and 3^{rd} quartiles. The mean and median are indicated by horizontal lines. The whiskers extend to the 5^{th} and 95^{th} percentiles, after removing outliers. See Figure 6.14 for the dynamic coefficients grouped by JA.

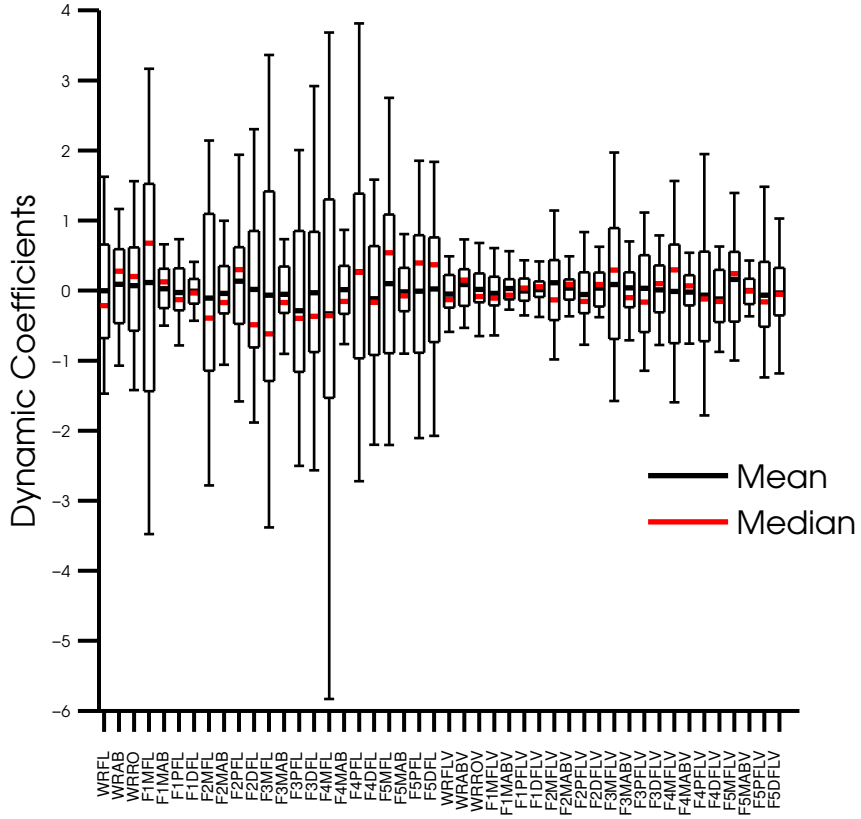

Figure 6.14: **JA-JA velocity dynamic connectivity GLM coefficients boxplot: monkey E:** Boxplot for the dynamic coefficients, computed across all neurons. The model was fit using Equation 6.1, with the dynamic terms from Equation 6.3. The coefficients are sorted (left to right) by JA coefficients for 23 joints, followed by JA velocity coefficients for 23 joints. With the exception of the MCP-flexion velocity coefficients, most velocity coefficients are smaller compared to the JA coefficients. The boundaries of the boxes are the 1^{st} and 3^{rd} quartiles. The mean and median are indicated by horizontal lines. The whiskers extend to the 5^{th} and 95^{th} percentiles, after removing outliers.

6.3 LONG-TIME SCALE DYNAMIC FUNCTIONAL CONNECTIVITY II

6.3.1 DYNAMIC CONNECTIVITY DECODING MODEL

The connectivity models we introduced in the previous section showed that dynamic connectivity improved firing rate prediction, compared to a static connectivity model. However, this improvement could be in part due to the large number of parameters in the models, providing it with a more flexible basis to fit the data, possibly accounting for non-linearities missed by the static model. In addition, these models are hard to interpret. Instead of fitting a connectivity model between every neuron and all muscles, we could fit an alternative model for every neuron-muscle pair, which is more interpretable.

We reversed the regression direction, and instead of predicting one neuron's firing rate from EMG activity of multiple muscles, we predicted the EMG activity of a single muscle from a combination of the firing rate of a single neuron, and the interaction between JAs and the firing rate, according to:

$$EMG_i = a_0 + a_1(JA) \times \lambda_{50} \tag{6.4}$$

where:

- λ_{50} is the neuron's fractional firing rate, binned in $50ms$ bins
- EMG_i is the rectified EMG for muscle i, binned and averaged in the same $50ms$ bins as λ_{50}
- $a_1(JA)$ is a coefficient dependent on kinematic features, defined as:
  $a_1(JA) = b_0 + \sum_{j=1}^{J} b_j \times JA_j$
- J is the number of joint angles
- JA_j is the $j-th$ joint angle, filtered with a $10Hz$ low-pass filter and binned in the same $50ms$ bins as λ_{50}
- EMG was lagged by $50ms$, and JA was lagged by $100ms$ relative to the firing rates
- Firing rates, EMG and JAs were z-scored before fitting the models

In order to show that dynamic functional connectivity plays a role in how motor-cortical neurons affect muscles, we should compare the model in Equation 6.4 to a model which includes only the firing rate of the neuron, such as:

$$EMG_i = a_0 + a_1 \times \lambda_{50} \tag{6.5}$$

However, we have to prove that model 6.4 is not simply better because model 6.5 is a bad model by itself. If the relationship between the EMG and firing rate is non-linear, model 6.4 could introduce a correction; which will not necessarily indicate that functional connectivity is dynamic. Instead, we could compare model 6.4 to a non-parametric model of the form:

$$EMG_i = a_0 + S(\lambda_{50}) \tag{6.6}$$

where $S(\dots)$ indicates the usage of regression splines. We chose to use Multivariate Adaptive Regression Splines (MARS) to ensure that any non-linearities between the firing rate and EMG are taken into account (we used the ARESLab package for Matlab, which follows the original formulation in Friedman [19]). Model 6.6 represents the best model we could fit between the firing rate and EMG. Therefore, if model 6.4 is better than model 6.6, then information present in the interaction terms of the firing rate and the JA data, which is not present in the firing rate alone, is contributed by the dynamic connectivity terms; and we can conclude that functional connectivity is both dynamic and dependent on kinematics.

We first fit models 6.4 and 6.6 to 152 neuron-muscle pairs, using all available data from all attitudes (we selected 9 well modulated neurons for this analysis). For every neuron, we selected the most correlated muscle as the one with the highest mean sample correlation across all attitudes, and subjected that pair to the analysis. 148 neurons showed that model 6.4 was better; with a mean R^2 difference of $11 \pm 8\%$ (mean$\pm$SD). All the coefficients in model 6.4 were significant, for all neurons. The largest coefficients were the ones involving JA flexion, and in general the MCP coefficients were larger than the PIP coefficients, which were larger than the DIP coefficients. Four muscles appeared at higher frequencies than others: deltoid, extensor carpi ulnaris, extensor digitorium communis and pronator teres.

Because most neurons, muscles and joints were simultaneously active during the reach to grasp movements, it is possible that model 6.4 was better due to broad task induced correlations between the selected muscles and the JAs used in the model. To vet this possibility, we randomized the firing rates within every trial for all neurons and repeated the analysis. 149 neurons showed that model 6.6 was now better than model 6.4; with a mean R^2 difference of $22 \pm 12\%$ (mean$\pm$SD). We concluded that three-way correlations between the neurons, muscles and JAs contributed to the goodness-of-fit of model 6.4; rather than two-way correlation between the muscles and JAs.

We then verified that our results generalized to all neuron-muscle pairs, by fitting models 6.4 and 6.6 using all possible 2432 neuron-muscle pairs. Again, model 6.4 was better than model 6.6 for 97% of the neurons (2375/2432), supporting the hypothesis that functional connectivity is dynamic and depends on kinematic features. Figures 6.15 and 6.16 show the R^2 comparison between the two models for all neuron-muscle pairs.

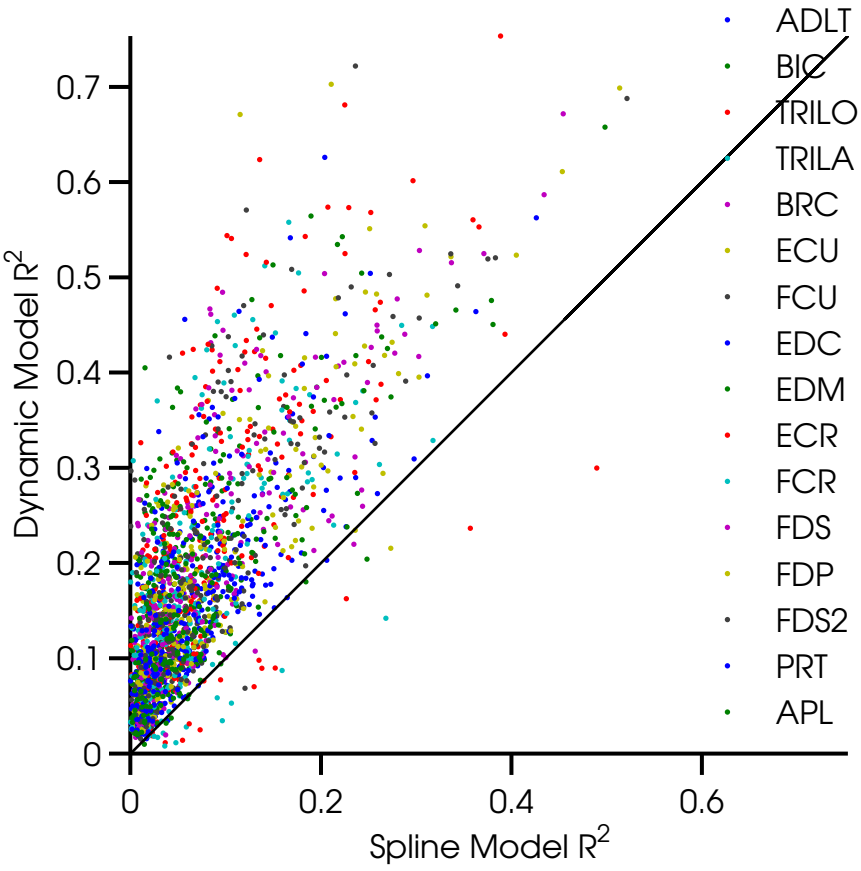

Figure 6.15: R^2 **comparison between dynamic and spline connectivity models: monkey E:** Comparison for 2432 neuron-muscle pairs between the dynamic model (Equation 6.4) and the spline model (Equation 6.6). Neuron-muscle pairs are colored by muscles. The dynamic connectivity model outperformed the spline connectivity model for 97% of the neuron-muscle pairs.

To check if three-way correlation contributed to model 6.4 for all neuron-muscle pairs, we randomized the firing rates of all neurons within trials, and re-fit model 6.4. Model 6.6 became superior for 96% of the neurons (2340/2432), with mean R^2 differences of $14 \pm 10\%$ (mean$\pm$SD); confirming that for most neuron-muscle pairs, function connectivity was indeed dynamic and de-

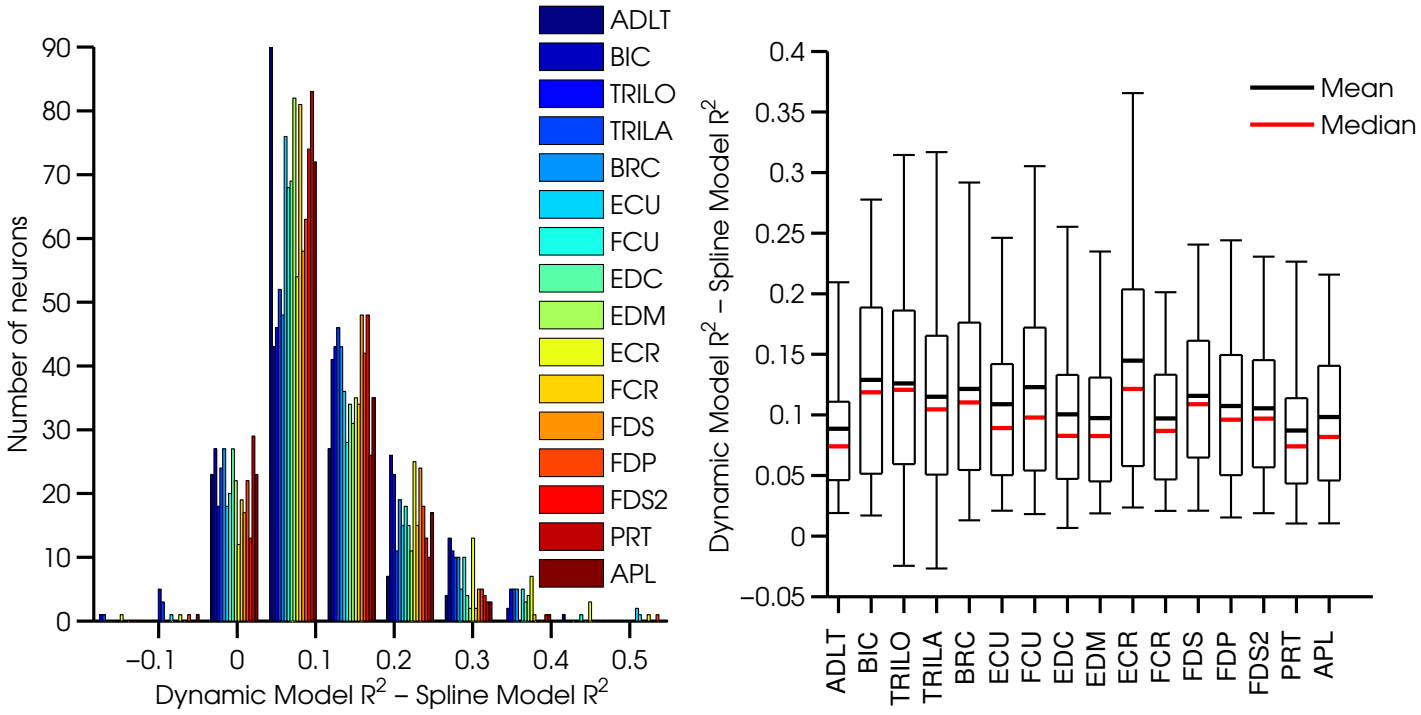

(**A**) R2 difference multi-histogram

(**B**) R2 difference box-plot

Figure 6.16: **Dynamic and spline connectivity models R^2 differences: monkey E:** The dynamic connectivity model was better for most neuron-muscle pairs. Pairs involving the deltoid show the least improvement in R^2 when fitting the dynamic model, while pairs involving extensor-carpi radialis show the most improvement when fitting the dynamic model.

pendent on joint angles. Figures 6.17 and 6.18 show the R^2 comparison between model 6.6 and model 6.4, after randomizing the firing rates, for all neuron-muscle pairs.

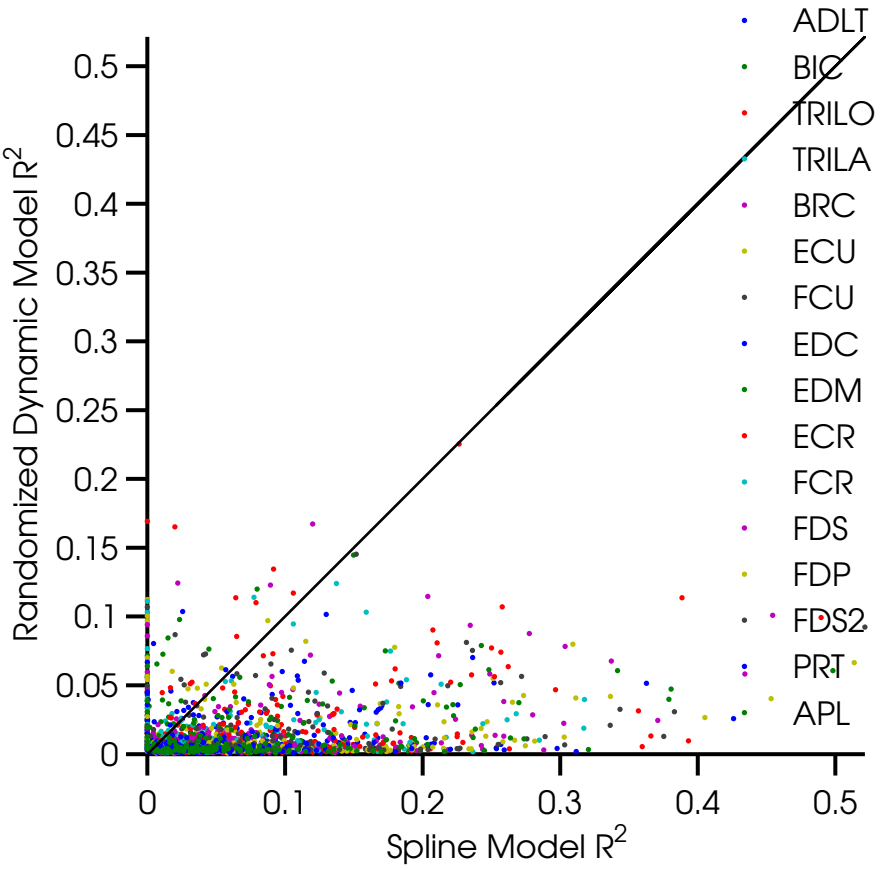

Figure 6.17: R^2 **comparison between randomized dynamic and spline connectivity models: monkey E:** Comparison for 2432 neuron-muscle pairs between the randomized dynamic model (Equation 6.4 with randomized firing rates) and the spline model (Equation 6.6). Neuron-muscle pairs are colored by muscles. After randomizing the firing rates, the spline model is better for 96% of the neuron-muscle pairs, in contrast to Figure 6.15. This indicates that three-way correlation between neurons, muscles and JAs contributed to the dynamic model, rather than two-way correlation between the muscles and JAs; supporting the hypothesis that functional connectivity is dynamic and dependent on kinematic features.

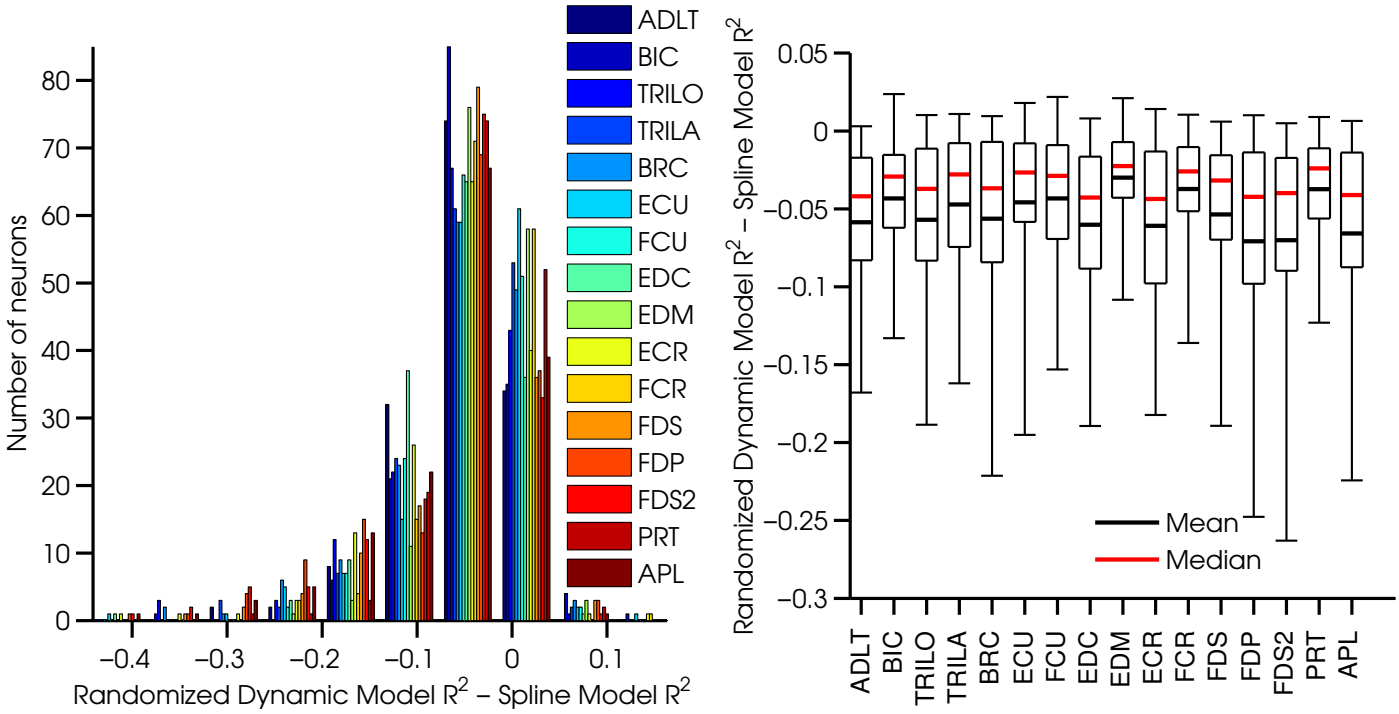

(**A**) R2 difference multi-histogram

(**B**) R2 difference box-plot

Figure 6.18: **Randomized dynamic and spline connectivity models R^2 differences: monkey E:** After randomizing the firing rates, the spline connectivity model becomes better for 96% of the neuron-muscle pairs. Pairs involving the finger and wrist muscles show the largest drops in R^2.

6.3.2 FEATURES OF DYNAMIC CONNECTIVITY

We concluded in Section 6.3.1 that functional connectivity between neurons and muscles is dynamic, in the sense that every neuron's correlation to muscle activations changes as a function of the wrist and hand joint angles. To determine patterns of kinematic-dependent functional connectivity, we plotted all the coefficients fitted using model 6.4 to all neurons-muscle pairs as a heat map, shown in Figure 6.19. The firing rates, EMG and JA were z-scored prior to fitting the models, hence the coefficients are comparable across neurons. Figure 6.19 shows that coefficient magnitudes are similar across neurons, and also across models. Thin horizontal banding is evident in all models, so to check if specific JAs were assigned higher coefficients than others, we re-plotted the heat map, with the coefficients grouped by joint angles. This heat map is shown in Figure 6.20, where clear horizontal banding can be seen, indicating that wrist flexion and finger MCP/PIP flexion JAs tended to receive higher coefficients, compared to other JAs. These JAs affected functional connectivity across all muscles, not just those acting the wrist and fingers.

Figure 6.21 shows a box plot of the 24 coefficient groups shown in Figure 6.20, produced by combining all JA interaction coefficients across models. Fingers MCP/PIP flexion JAs show the longest whiskers, indicating higher overall coefficient values.

To further validate our results from Section 6.3.1, where we showed that randomized firing rates did not predict EMG better when dynamic connectivity terms were added to the model; we also plotted heat maps of coefficients obtained from fitting model 6.4 to randomized firing rates. Figures 6.22 and 6.23 show that the dynamic coefficients magnitudes were up to three times smaller compared to Figures 6.19 and 6.20; and some light horizontal banding indicating higher coefficients for fingers MCP and PIP flexion JAs also showed, indicating the broad task-induced correlation between muscles and JAs; and not necessarily dynamic connectivity.

We concluded that hand shape, mainly affected by wrist and MCP flexion JAs, influenced long-time scale functional connectivity between all neurons and muscles, in a consistent way, across all attitudes. Functional connectivity to all muscles was affected, not only to those facilitating wrist and finger movements. Co-activation between neurons and muscles at these time scales was suggested to represent cortical contribution to motoneuronal excitation. Therefore, our findings

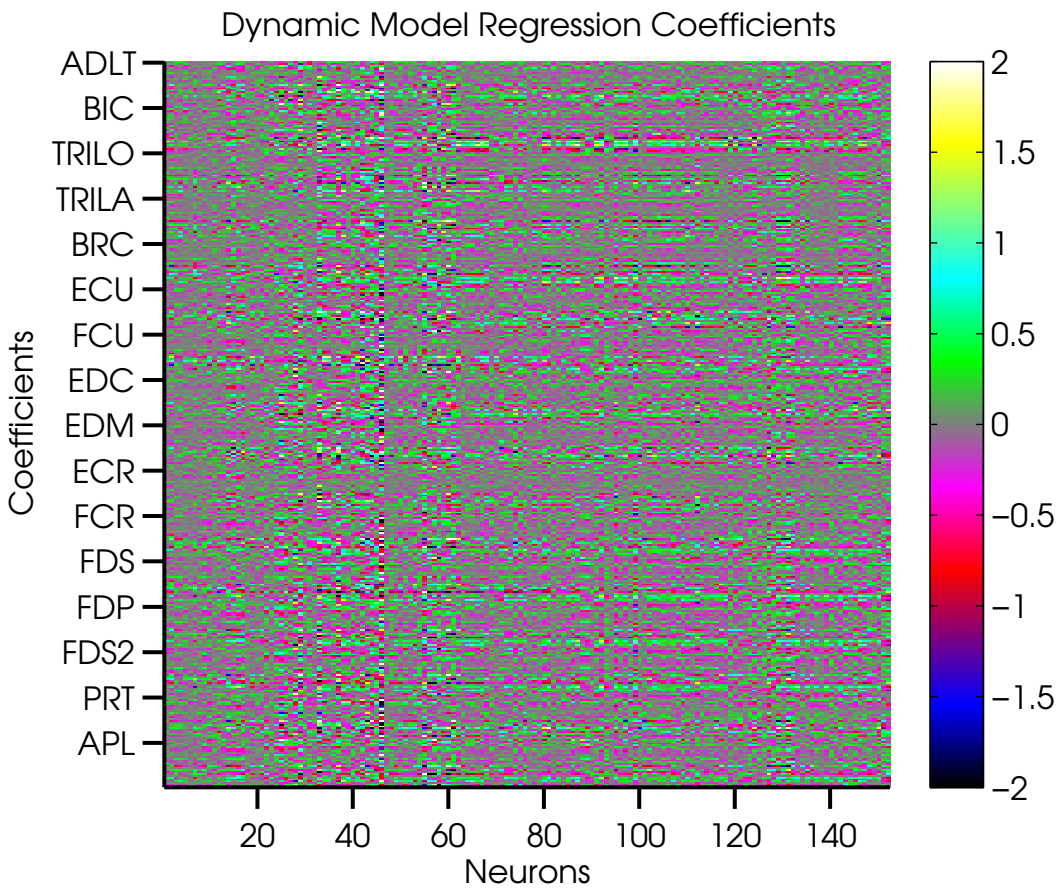

Figure 6.19: **Dynamic connectivity model coefficients heat map: monkey E:** Heat map of model 6.4 coefficients for 2432 neuron-muscle pairs. 152 Neurons are ordered in columns and 16 models (one for every muscle) are ordered in rows. Every model included 25 coefficients: one intercept, one coefficient for the neuron's firing rate and 23 coefficients describing the JA interaction with the firing rate. The intercept coefficients have been eliminated from the heat map, hence 24 coefficients are shown for every model, with the firing rate coefficient on the top row. Coefficients magnitudes are similar across models, and some horizontal banding can be seen for every model. See Figure 6.20 for a heat map where the coefficients are ordered by joints.

indicate that the contribution of individual neurons to motoneuronal excitation is affected by hand shape in a consistent way across a wide repertoire of grasping movements.

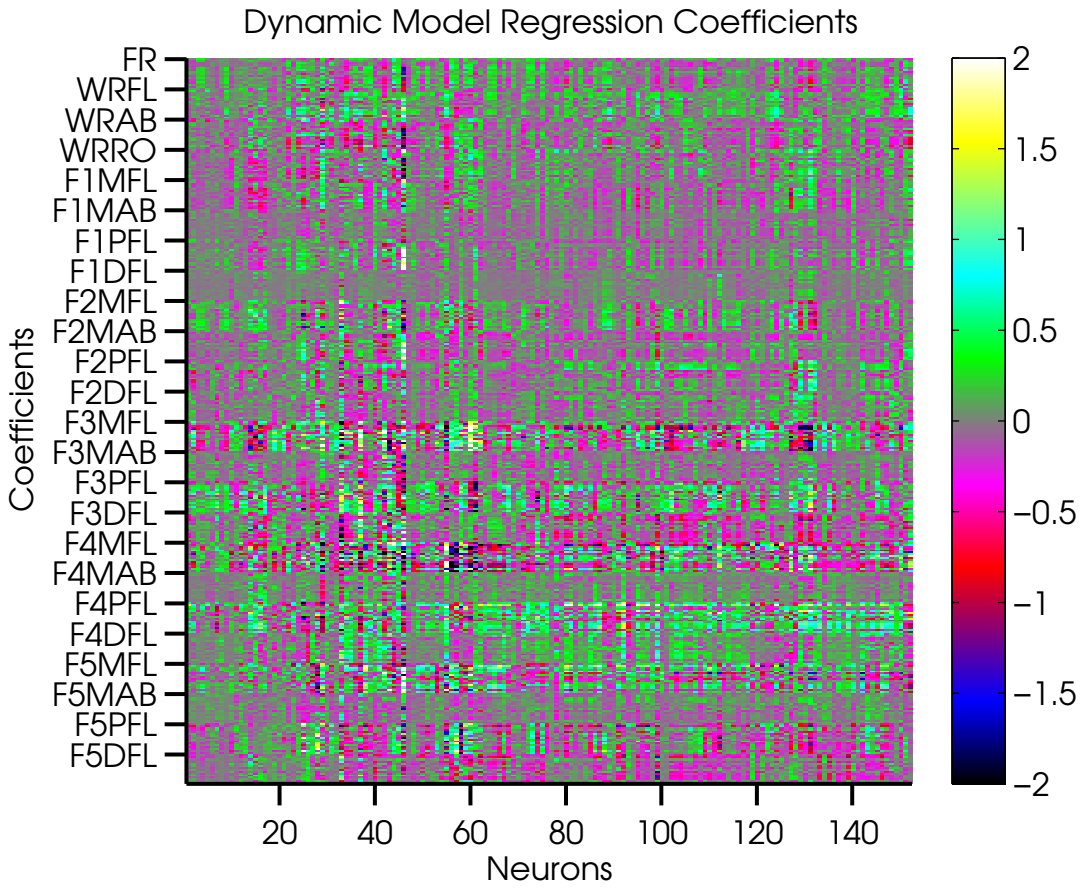

Figure 6.20: **Dynamic connectivity model coefficients heat map clustered by JA: monkey E:** Heat map of model 6.4 coefficients for 2432 neuron-muscle pairs. This is the same data as Figure 6.19, with coefficients clustered by JA across models. 152 Neurons are ordered in columns and 24 coefficient groups are ordered in rows. The first group (first 16 rows), shows the firing rate coefficients from all 16 models, for all neurons. The second to last groups show the JA interaction coefficients, clustered by specific JAs, for all neurons. Clear horizontal banding, indicating similarities across neuron-muscle pairs, can be seen for the wrist flexion, fingers MCP and PIP flexion JAs. Interaction coefficients for these JAs had relatively high coefficients compared to the other JAs.

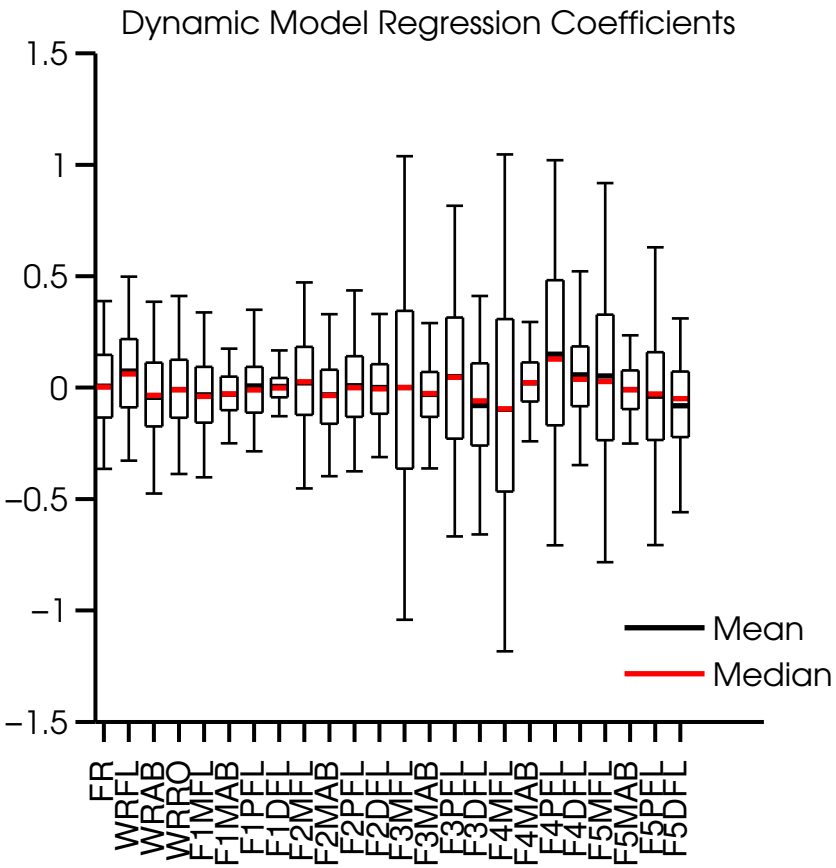

Figure 6.21: **Dynamic connectivity model coefficients clustered by JA box plot: monkey E:** Box plot of model 6.4 coefficients for 2432 neuron-muscle pairs. All fitted values from all models and all neurons were used to compute the box plot values for every JA interaction coefficient. Fingers MCP and PIP flexion JAs have longer distribution tails compared to the other JAs, indicating higher coefficient values for some of the neurons.

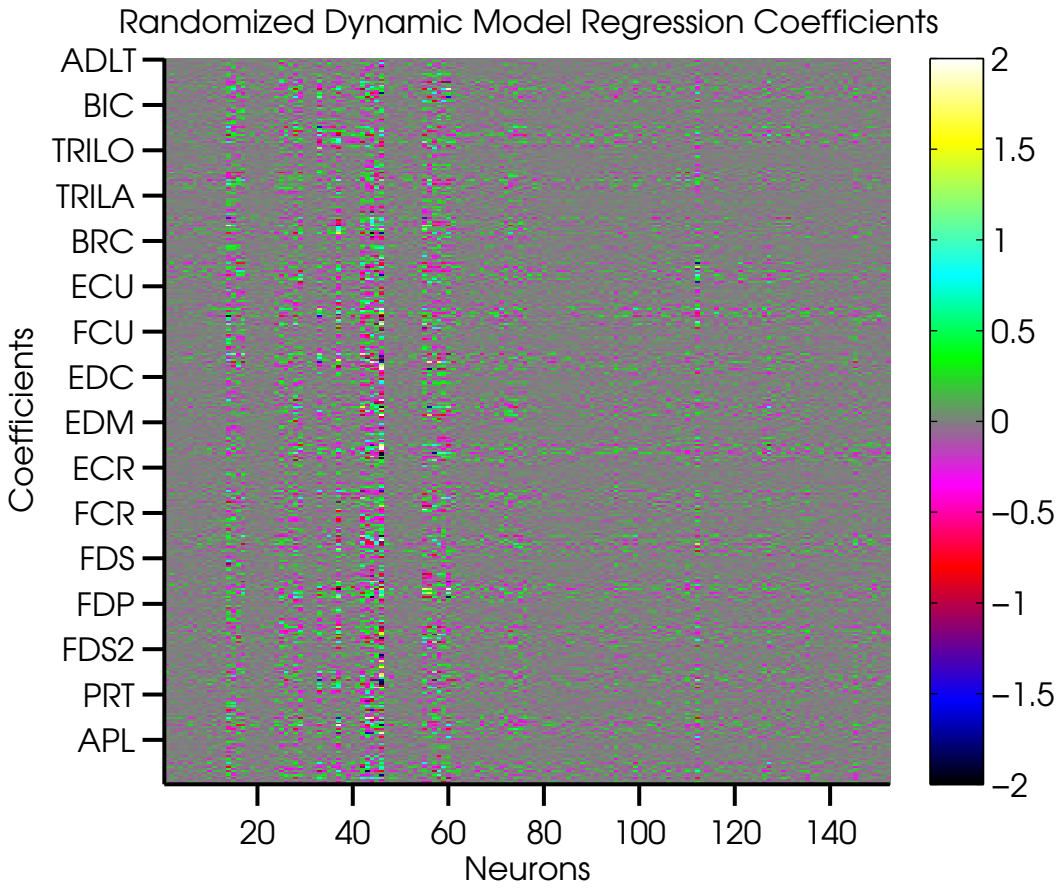

Figure 6.22: **Randomized dynamic connectivity model coefficients heat map: monkey E:** Heat map of model 6.4 coefficients for 2432 neuron-muscle pairs, fitted after randomizing the firing rates within each trial. Compare to Figure 6.19 for a coefficients heat map of the original firing rates, where the coefficients magnitudes are much bigger.

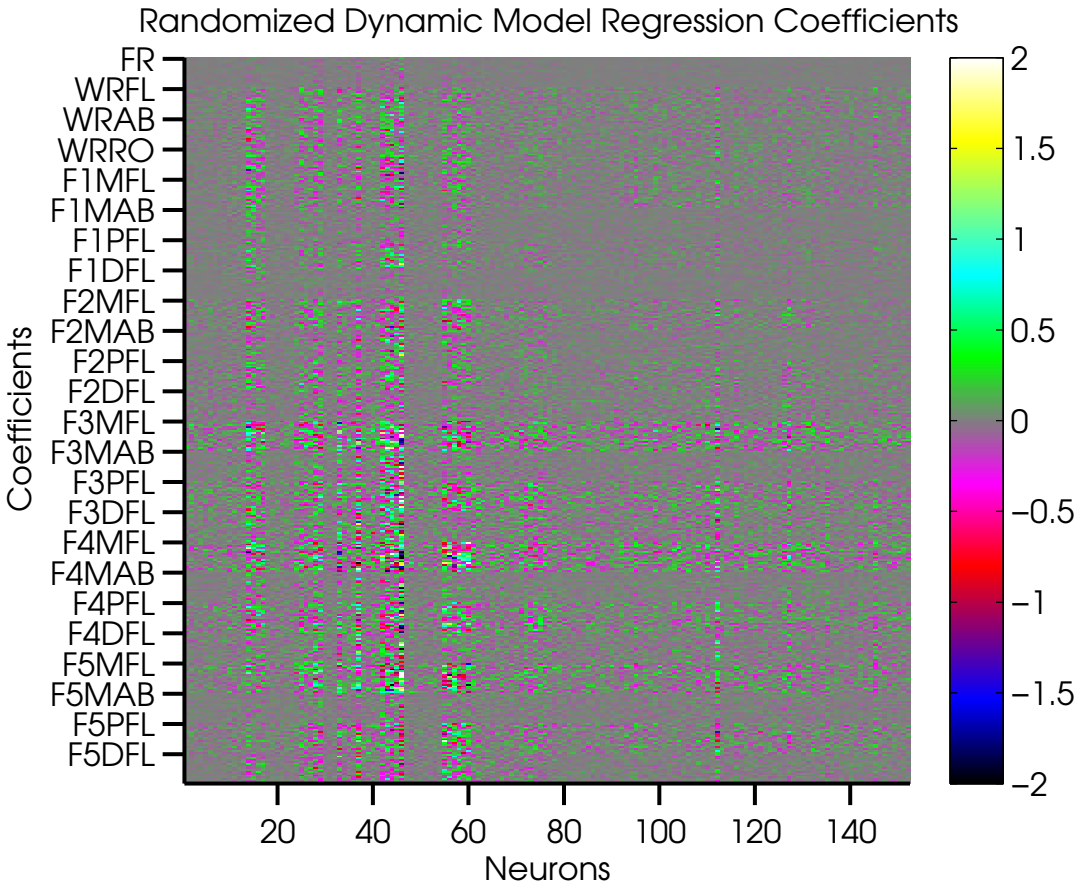

Figure 6.23: **Randomized dynamic connectivity model coefficients heat map ordered by JA: monkey E:** Heat map of model 6.4 coefficients for 2432 neuron-muscle pairs, fitted after randomizing the firing rates within each trial. This is the same data as Figure 6.22, with coefficients clustered by JA across models. Compare to Figure 6.20 for a coefficients heat map of the original firing rates. Some horizontal banding exists for the fingers MCP flexion JAs, but coefficients magnitudes are much smaller than Figure 6.20.

6.4 SHORT-TIME SCALE DYNAMIC FUNCTIONAL CONNECTIVITY

In Section 6.3, we have demonstrated that long-time scale functional connectivity (over a few hundred milliseconds) between neurons and muscles is dynamic, and dependent on kinematic features. That is, correlation between motor cortical neural activity and EMG changes as a function of the wrist and fingers joint angles. Since neural-muscle co-activation is thought to represent possible contribution to motoneuronal excitation via direct or indirect pathways, our findings imply that neurons change their effective connectivity to muscles based on task requirements. However, long-time scale co-activation does not necessarily indicate a causal relationship between neurons and muscles, in the form of direct synaptic influence. Some studies found correspondence between short- and long-time scale functional connectivity, so that neurons which demonstrated post-spike effects (PSEs) in muscles, tended to show long-time scale co-activation as well; while other studies found no such correspondence (see Section 1.3.2 for details). We therefore searched for PSEs, representing short-time scale functional connectivity, in our data.

We first collected spike-triggered EMG snippets using all spikes in every session, from all attitudes combined, and used SSA and the SSA-scan (introduced in Chapter 5) to find putative PSEs, in every neuron-muscle pair. Both tests are known to exhibit a 5% significance level, meaning that 5% of the times they find spurious PSEs. As a rough estimate, we should then expect 5% of the neuron-muscle pairs in a given session to be detected as containing PSEs, even if no PSEs exist in our data. SSA and SSA-scan found PSEs in around $5\% - 7\%$ of our neuron-muscle pairs. Visual examination of the SpTAs showed some convincing PSEs, given the large number of spike triggers (around $20000 - 30000$ spikes per neuron, per session); and some of them corresponded to our intra-cortical micro-stimulation (ICMS) results. Hence we concluded that some of these PSEs were probably not spurious. However, due to the small number of detected PSEs and the near chance detection rate, we could not draw convincing conclusions about their correspondence to long-time scale dynamic connectivity.

Using spikes from all attitudes combined could dilute attitude-specific PSEs, so the effect strengths would be too low for the automatic tests to detect them. We therefore tested if neuron-muscle pairs showed attitude-specific PSEs, by using spikes from every attitude separately. Every attitude contained, at most, 20 repeat trials, with an average of $500 - 1000$ spikes. The power

analyses we conducted in Chapter 5 showed that we should not expect SSA nor SSA-scan to detect all existing PSEs, due to the small sample sizes available. SSA and SSA-scan found PSEs in $5\% - 8\%$ the neuron-muscle-attitude triplets for every session. We visually inspected the PSEs, and cross-referenced them with our ICMS results. We found some of the PSEs to be convincing, and these occurred in neurons which also showed positive ICMS effects in the same muscle, at low thresholds.

In order to demonstrate dynamic short-time scale connectivity, we could examine changes in PSEs between attitudes. However, due to the small sample sizes available for each attitude, the SSA and SSA-scan detection power was low. As an alternative, we chose to test for correspondence between long- and short-time scale functional connectivity. Finding neuron-muscle pairs which showed *dynamic* long-time scale functional connectivity, and also showed PSEs when long-time scale connectivity was high; would provide physiological evidence to strengthen our dynamic connectivity hypothesis.

The coefficients in model 6.4 indicated which JAs influenced functional connectivity, but do not detail how connectivity changed as a function of JA. We used two models that conditioned functional connectivity on a single JA, to first find which JAs influenced functional connectivity, and then find changes in connectivity as a function of JA values throughout trials. The first model was similar to model 6.4, but found long-time scale dynamic functional connectivity in neuron-muscle-joint triplets:

$$EMG_i = a_0 + a_1 \times \lambda_{50} + a_2 \times \lambda_{50} \times JA_j \tag{6.7}$$

where:

- λ_{50} is the neuron's fractional firing rate, binned in $50ms$ bins
- EMG_i is the rectified EMG for muscle i, binned and averaged in the same $50ms$ bins as λ_{50}
- JA_j is the $j-th$ joint angle, filtered with a $10Hz$ low-pass filter and binned in the same $50ms$ bins as λ_{50}
- EMG was lagged by $50ms$, and JA was lagged by $100ms$ relative to the firing rates
- Firing rates, EMG and JAs were z-scored before fitting the model

The second model was a varying coefficients model (see Hastie et al. [26], section 6.4.2), which related EMG to firing rate and allowed the coefficients to vary as a function of the joint angle. For

a given range of JAs, the model was a linear model, but each of the coefficients varied as a function of JAs. This model allowed us to examine changes in functional connectivity as a function of JA.

$$EMG_i = a_0(JA_j) + a_1(JA_j) \times \lambda_{50} \tag{6.8}$$

where:

- λ_{50} is the neuron's fractional firing rate, binned in $50ms$ bins
- EMG_i is the rectified EMG for muscle i, binned and averaged in the same $50ms$ bins as λ_{50}
- JA_j is the $j-th$ joint angle, filtered with a $10Hz$ low-pass filter and binned in the same $50ms$ bins as λ_{50}
- EMG was lagged by $50ms$, and JA was lagged by $100ms$ relative to the firing rates

$a_0(JA_j)$ represented the change in EMG baseline as a function of JA_j, and $a_1(JA_j)$ represented the correlation, or long-time scale connectivity, between the neuron and muscle, as a function of JA_j. We implemented the model by sorting JA_j values and dividing their range to $K = 6$ equal bins (from the minimal JA value to the maximal JA value). For the $k-th$ bin, we used a local regression to regress the corresponding EMG_i and λ_{50} values, and fit $a_{k,0}$ and $a_{k,1}$.

The next example illustrates the application of these models for one neuron (monkey E, session 597, unit spk001a). We began by looking for PSEs in spikes collected for each attitude separately, using the automatic tests. SSA found PSEs in 6% of the attitude-muscle pairs (32/512), and SSA-scan found PSEs in 4% of the attitude-muscle pairs (21/512). Given that the tests have demonstrated significance levels around 5%, and sometimes more conservative significance levels, we concluded that some of the PSEs might be real. We reasoned that for every muscle, PSEs of the same type (post-spike facilitation- PSF, post-spike suppression- PSS) detected at similar post-spike latencies in different attitudes, were less likely to be spurious. We identified 7 PSEs which were detected for more than one attitude:

- *extensor carpi ulnaris* showed similar PSS for the button and the rectangle at the abduction target (Figure 6.24)
- *flexor carpi ulnaris* showed similar PSS for the handle at the extension target and the rectangle at the adduction target (Figure 6.25)

- *extensor digitorium communis* showed similar PSS for the button at the extension target and the precision object at the 45-left target (Figure 6.26)
- *extensor digiti minimi* showed similar PSS for the precision object at the 45-right and the cone at the flexion target (Figure 6.27)
- *flexor carpi radialis* showed similar PSF for the bar at the supination target and the disk at the flexion target (Figure 6.28)
- *extensor carpi radialis* showed similar PSS for the handle and the bar at the horizontal target (Figure 6.29)
- *pronator teres* showed similar PSS for the rectangle at the abduction target and the precision at the horizontal target (Figure 6.30)

We could not definitely conclude that all the above PSEs were not spurious, but the fact that most were detected by both SSA and SSA-scan, decreased that likelihood.

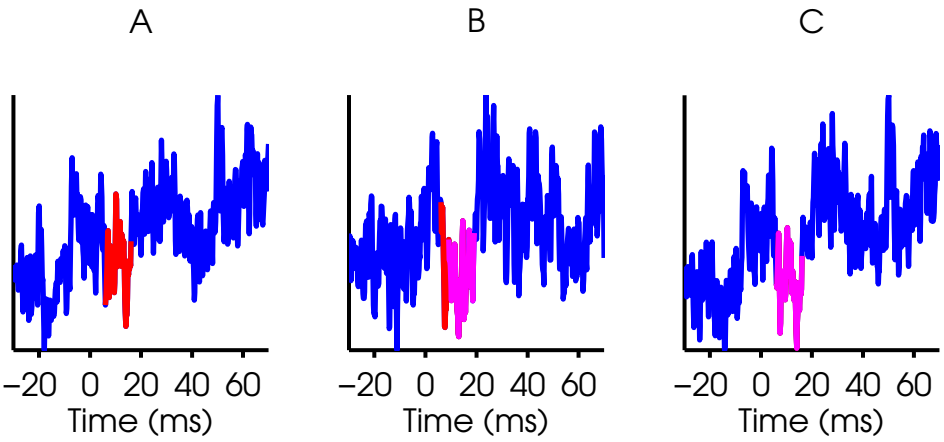

Figure 6.24: **SpTAs for session 597, cell spk001a, extensor carpi ulnaris:** An example of similar PSEs appearing in two attitudes. **(A)** SpTA compiled using 243 spikes for the button, abduction target attitude. SSA p-value was 0.008 **(B)** SpTA compiled using 334 spikes for the rectangle, abduction target attitude. SSA p-value was 0.009, SSA-scan p-values was 0.013 **(C)** SpTA compiled using 577 spikes, combining the spikes in (A,B). SSA p-value was 0.0002, SSA-scan p-values was 0.003

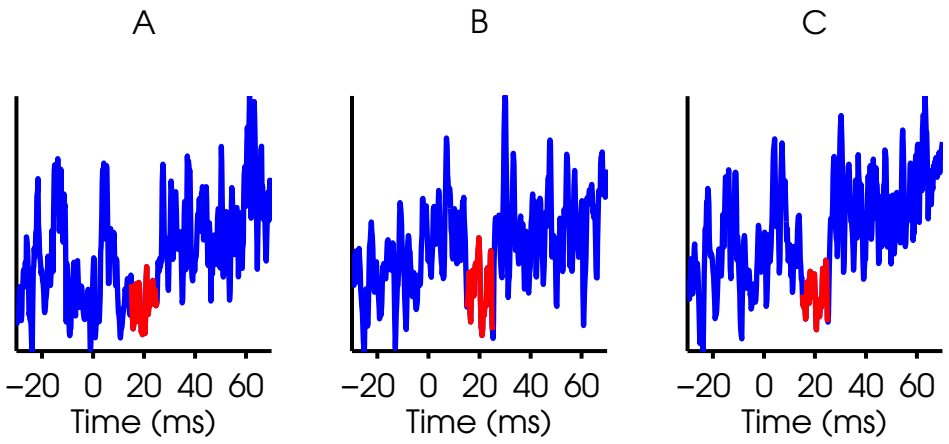

Figure 6.25: **SpTAs for session 597, cell spk001a, flexor carpi ulnaris:** An example of similar PSEs appearing in two attitudes. **(A)** SpTA compiled using 149 spikes for the handle, extension target attitude. SSA-scan found a synchrony PSE centered at 20*ms* post-spike with a p-value of 0.02 **(B)** SpTA compiled using 206 spikes for the rectangle, adduction target attitude. SSA-scan found a synchrony PSE centered at 20*ms* post-spike with a p-value of 0.02 **(C)** SpTA compiled using 355 spikes, combining the spikes in (A,B). SSA-scan found a synchrony PSE centered at 20*ms* post-spike with a p-value of 0.0001

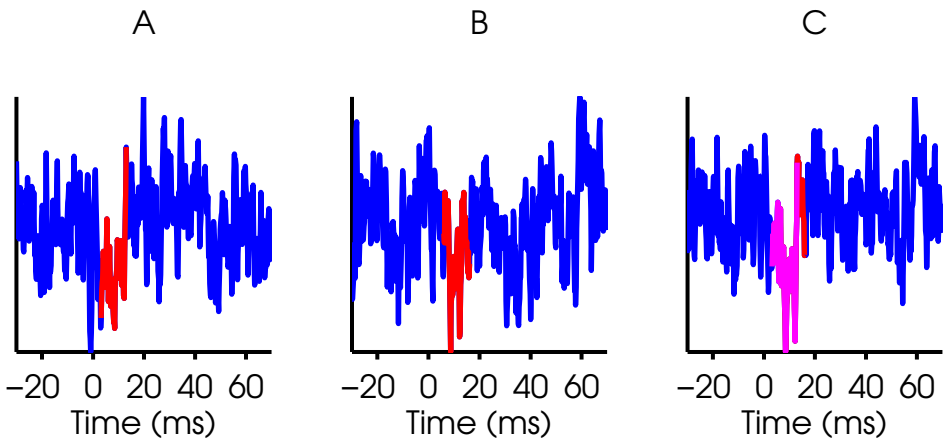

Figure 6.26: **SpTAs for session 597, cell spk001a, extensor carpi ulnaris:** An example of similar PSEs appearing in two attitudes. **(A)** SpTA compiled using 283 spikes for the button, extension target attitude. SSA-scan found a synchrony PSS around 8*ms* post-spike with a p-value of 0.03 **(B)** SpTA compiled using 293 spikes for the precision object, 45-left target attitude. SSA p-value was 0.02 **(C)** SpTA compiled using 576 spikes, combining the spikes in (A,B). SSA-scan found a synchrony PSS around 8*ms* post-spike with a p-value of 0.006, SSA p-value was 0.02

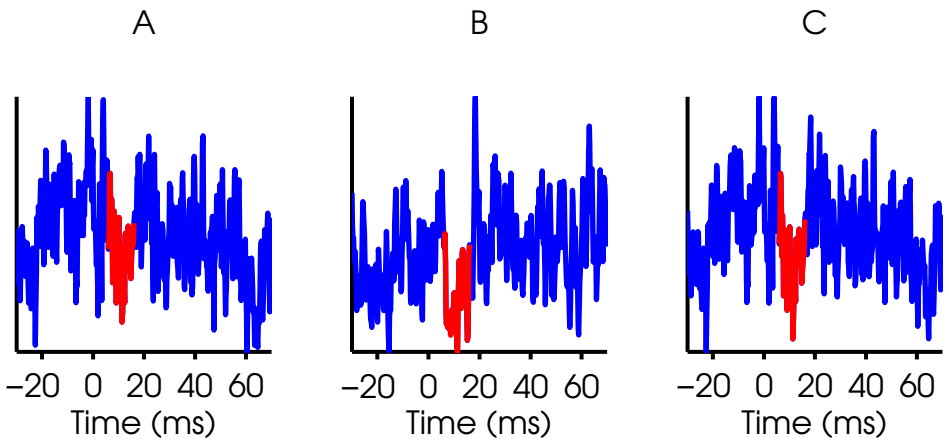

Figure 6.27: **SpTAs for session 597, cell spk001a, extensor digiti minimi:** An example of similar PSEs appearing in two attitudes. **(A)** SpTA compiled using 189 spikes for the precision object, 45-right target attitude. SSA p-value was 0.04 **(B)** SpTA compiled using 208 spikes for the cone, flexion target attitude. SSA p-value was 0.02 **(C)** SpTA compiled using 397 spikes, combining the spikes in (A,B). SSA p-value was 0.007

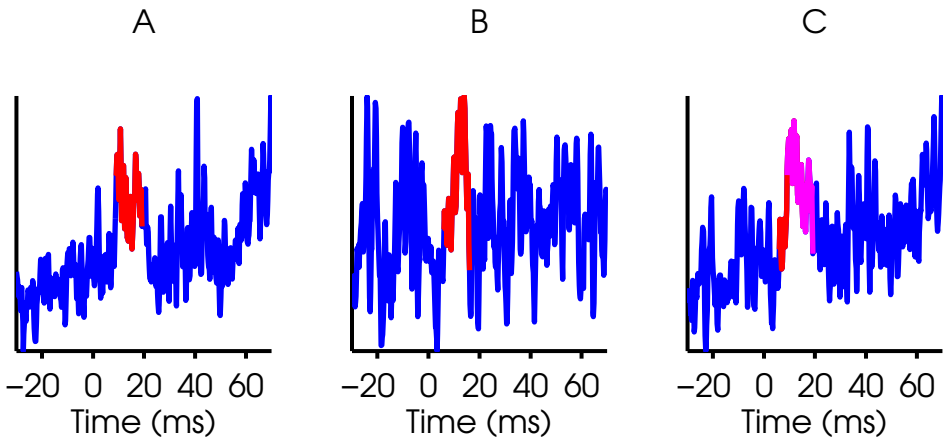

Figure 6.28: **SpTAs for session 597, cell spk001a, flexor carpi radialis:** An example of similar PSEs appearing in two attitudes. **(A)** SpTA compiled using 386 spikes for the bar, supination target attitude. SSA-scan found a synchrony PSE centered at 14*ms* post-spike with a p-value of 0.02 **(B)** SpTA compiled using 314 spikes for the disk, flexion target attitude. SSA found a synchrony PSE centered at 11*ms* post-spike with a p-value of 0.03 **(C)** SpTA compiled using 700 spikes, combining the spikes in (A,B). SSA-scan found a synchrony PSE centered at 14*ms* post-spike with a p-value of 0.006, SSA p-value was 0.01

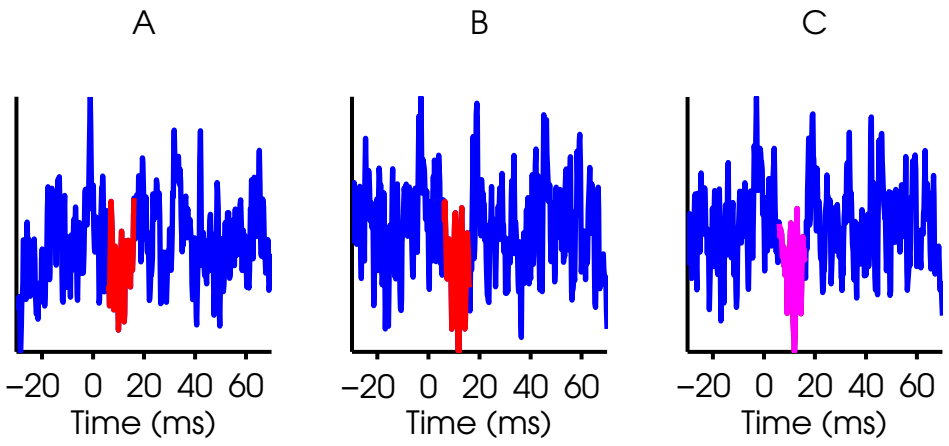

Figure 6.29: **SpTAs for session 597, cell spk001a, extensor carpi radialis:** An example of similar PSEs appearing in two attitudes. **(A)** SpTA compiled using 100 spikes for the handle, horizontal target attitude. SSA p-value was 0.01 **(B)** SpTA compiled using 437 spikes for the bar, horizontal target attitude. SSA p-value was 0.006 **(C)** SpTA compiled using 537 spikes, combining the spikes in (A,B). SSA p-value was 0.0005, SSA-scan p-value was 0.007

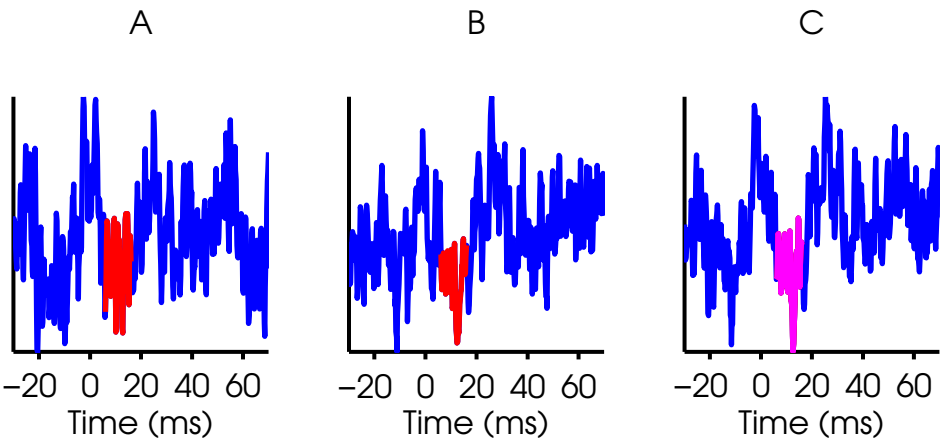

Figure 6.30: **SpTAs for session 597, cell spk001a, pronator teres:** An example of similar PSEs appearing in two attitudes. **(A)** SpTA compiled using 140 spikes for the rectangle, abduction target attitude. SSA p-value was 0.02 **(B)** SpTA compiled using 299 spikes for the precision object, horizontal target attitude. SSA p-value was 0.008 **(C)** SpTA compiled using 439 spikes, combining the spikes in (A,B). SSA p-value was 0.0004, SSA-scan p-value was 0.006

We next examined if corresponding PSEs could be found by using spikes occurring when the long-time scale neuron-muscle correlation was high. To find muscle-JA pairs demonstrating dynamic long-time scale correlation, we computed 368 models in the form of Eq. 6.7, one model for every muscle-JA pair; and compared their R^2 values to those from model 6.6, which included only the firing rate of the neuron. 79 muscle-JA pairs, spanning 13 muscles, showed higher R^2 values, indicating dynamic correlation conditioned on JA, and their coefficients are shown in Figure 6.31. Significant coefficients tended to appear in groups for specific muscles, rather than for specific JA, suggesting that dynamic correlation with each muscle was affected by multiple JAs. Figure 6.32 shows a comparison of EMG reconstruction correlations, between model 6.7 and model 6.6, for all 368 models. The 79 models from Figure 6.31, are the ones above the equality line in Figure 6.32.

We fit 79 varying-coefficients models (Eq. 6.8) to those muscle-JA pairs, and found, for each, the range of JA values during which the neuron-muscle connectivity was high. Figure 6.33 shows an example of coefficients fitted to model 6.8, for the brachioradialis-wrist flexion pair. The $a_0(JA_1)$ coefficient decreases with wrist extension (positive JA values), indicating that EMG baseline was low when wrist flexion JA values were in the 30-50 degrees range. The $a_1(JA_1)$ coefficient, represents the neuron-muscle correlation, and was high when wrist flexion JA values were in the 30-50 degrees range. We chose to use 30-50 degrees for this muscle-JA pair, since the confidence bounds around the coefficients were tighter for that range, and $a_1(JA_1)$ had positive values indicating positive co-activation of the neuron and muscle.

48 muscle-JA pairs showed clear relationships between JA values and neuron-muscle correlation, similarly to Figure 6.33. The other 31 muscle-JA pairs did not show such clear relationships, indicating that the correlation between the muscle activity and the firing rate of the neuron did not tend to consistently change as a function of JA values, but the interaction between the firing rate and JA values still contributed to EMG prediction.

We looked for PSEs in those 48 muscle-JA pairs, using only spikes occurring around when correlation was high (defined by a range of JA values). SSA found PSEs in 8% of the muscle-JA pairs (4/48), and SSA-scan found PSEs in 6% of the muscle-JA pairs (3/48). 4 PSEs had the same type and latency as PSEs detected using only spikes from single attitudes; strengthening their validity. These PSEs were also supported by ICMS results in related muscles. One such PSE was detected by both SSA and SSA-scan, and is shown in Figure 6.34A. This PSE was detected in the

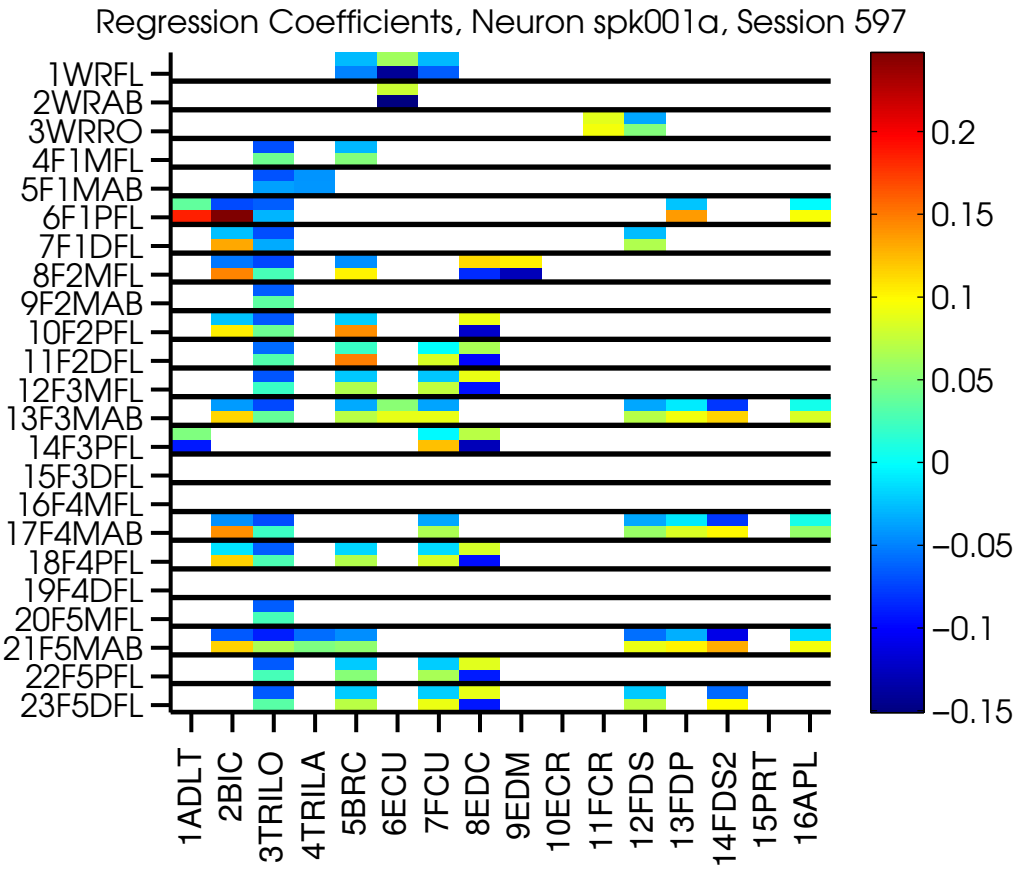

Figure 6.31: **Session 597, cell spk001a, model 6.7 coefficients:** Coefficients for 79 models are shown, with higher EMG reconstruction correlation than model 6.6. The EMG reconstruction correlations for the 79 models are shown in Figure 6.32, above the equality line. Two coefficients are shown for every model: the firing rate coefficient (top row), and the dynamic coefficient for a specific muscle and joint pair (bottom row).

brachioradialis, using 5193 spikes selected when the wrist was extended, with JA values of $30-50$ degrees (the neuron-muscle correlation as a function of wrist flexion is shown in Figure 6.33). The large number of spikes accompanied by low p-values and ICMS results suggested the PSE was real. Figure 6.35 shows a raster plot of spikes fired by this neuron, for all trials, with the spikes used to compile the SpTA highlighted in blue. These spikes are spread across attitudes, indicating that most spikes contributing to the PSE occurred when the wrist was extended to a certain degree,

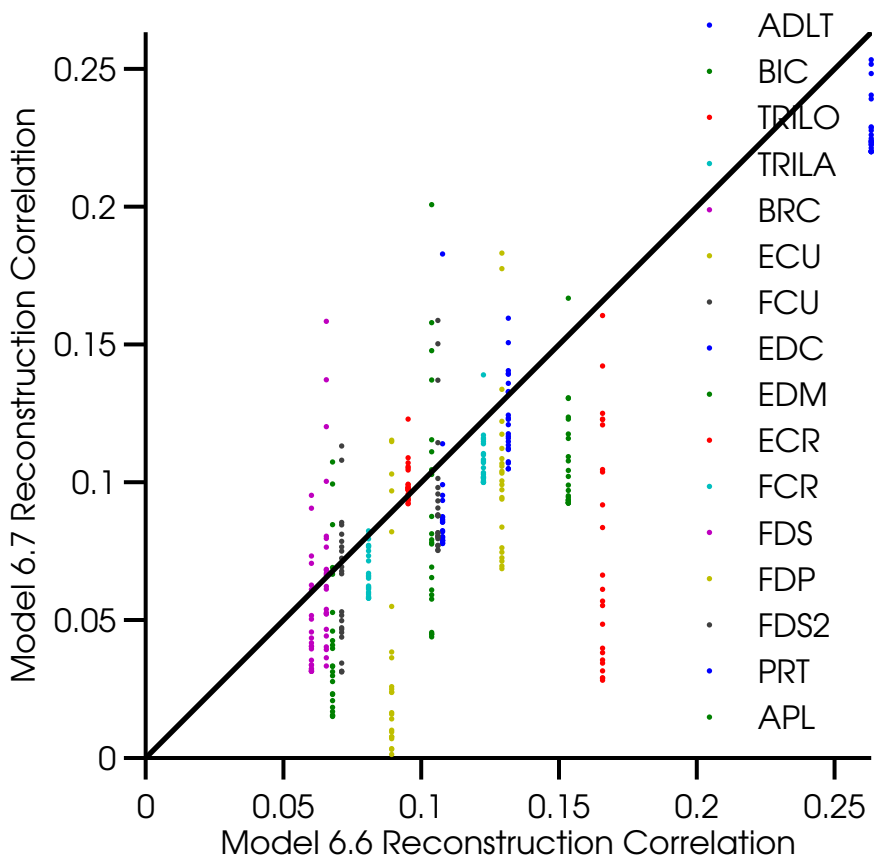

Figure 6.32: **Session 597, cell spk001a, comparison of reconstruction correlations between model 6.7 and 6.6:** Comparison of EMG reconstruction correlation for all muscle-JA pairs, for model 6.7 (dynamic connectivity model with one JA) and model 6.6 (static connectivity model). 79 models show better reconstruction correlation for the dynamic model, and their model 6.7 coefficients are shown in Figure 6.31.

rather than for specific attitudes. SSA also detected a similar PSF for this neuron-muscle pair, at the same latency, using only spikes from the cone at the extension target attitude (Figure 6.34B), further validating this PSE. In addition, ICMS performed via the recording electrode for this neuron showed effects in the brachioradialis muscle.

Conversely, we then tested another 168 muscle-JA pairs, comprising of the 31 muscle-JA pairs which showed dynamic connectivity conditioned on JA, but no clear relationships in model 6.8;

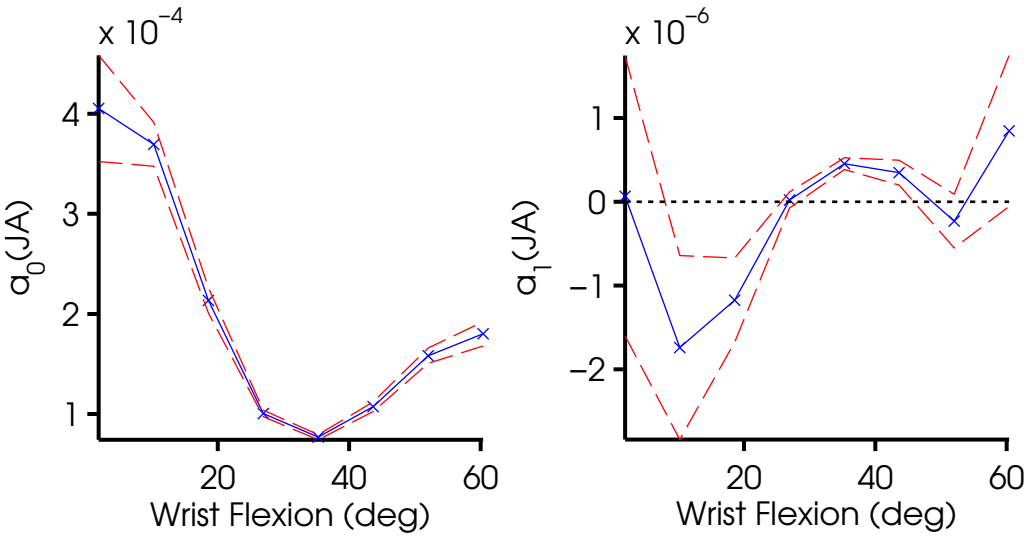

Figure 6.33: **Session 597, cell spk001a, model 6.8 coefficients:** Fitted varying model coefficients for one neuron-muscle-JA triplet. $a_0(JA)$ (Left) measures the change in EMG baseline as a function of JA. $a_1(JA)$ (Right) measures the change in firing rate-EMG correlation as a function of JA. Solid lines indicate the fits, dashed lines indicate coefficients 95% confidence bounds. For this pair, we selected $30-50^\circ$ as the JA range where correlation was the highest. In this case, EMG baseline was low for the selected JA range.

and 137 muscle-JA pairs which did not show dynamic connectivity. SSA and SSA-scan detected each significant PSE in 1% of the pairs (2/168); demonstrating that neurons-muscle-JA triplets with a clear relationships between JA values and neuron-muscle connectivity (determined using model 6.8), tended to show more PSEs.

We concluded that although we should not necessarily expect strong correspondence between long- and short-time scale connectivity, neuron-muscle pairs which demonstrated dynamic long-term connectivity, modulated by JA values; tended to show more PSEs than other neuron-muscle pairs. We repeated this analysis for a few additional neurons, with similar results. Some examples are shown in Figure 6.36.

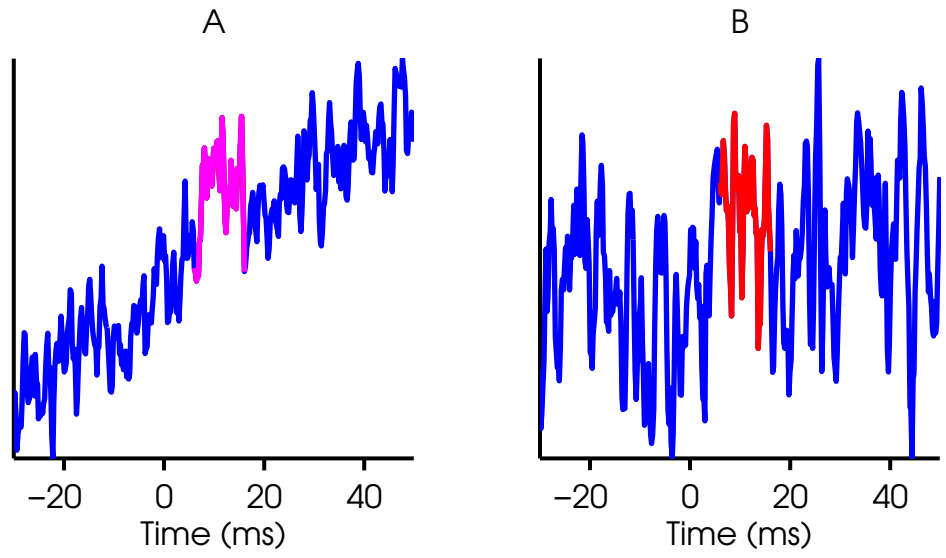

Figure 6.34: **SpTAs for session 597, cell spk001a, brachioradialis:** An example of similar PSEs detected using spikes from an attitude, and spikes selected when JA values were at a specific range. **(A)** SpTA compiled using 5193 spikes which overlapped times when the wrist flexion JA values were in the range of $30-50^{\circ}$ (wrist extension). SSA p-value was 0.001, SSA-scan p-value was 0.008 **(B)** SpTA compiled using 187 spikes for the cone at the **extension** target attitude. SSA p-value was 0.02. This PSF is at the same latency as the PSF in (A), and it occurred when the wrist was extended. This demonstrates that PSEs detected for certain attitudes can be better detected by selecting spikes occurring when long-time scale connectivity is high; and that some PSEs were conditional on kinematic features.

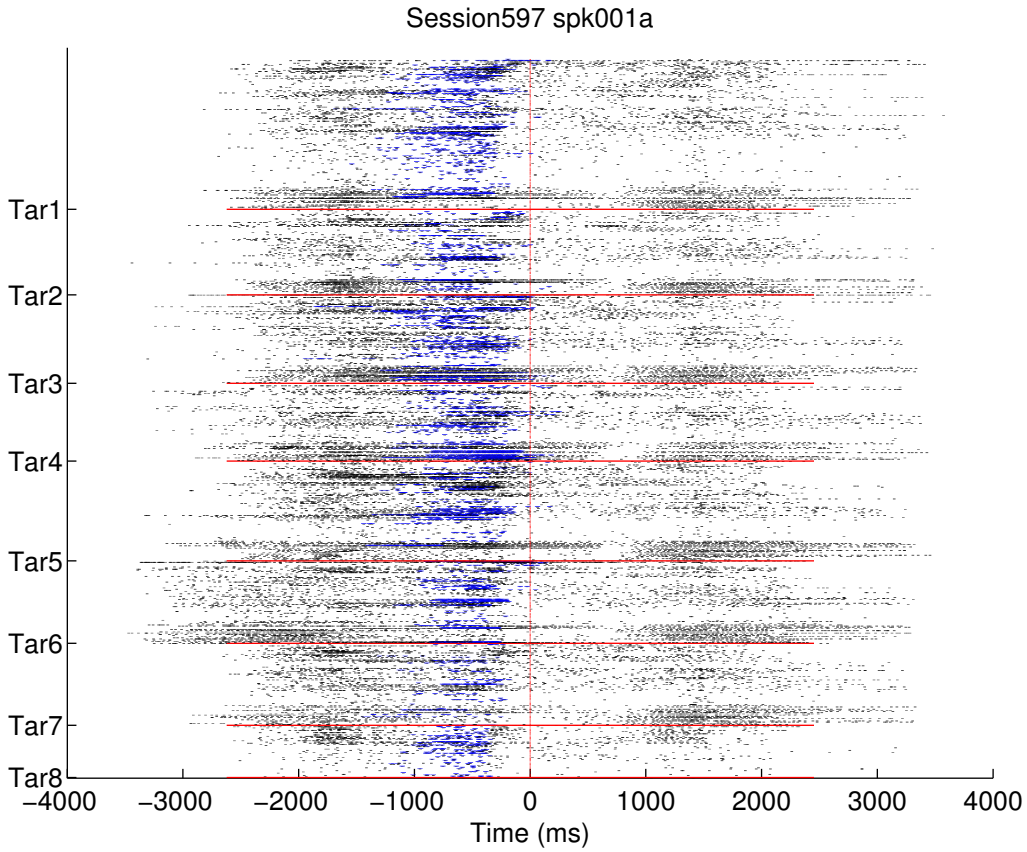

Figure 6.35: **Spike raster for session 597, cell spk001a:** The raster plot contains all available trials for this cell. Spikes which were used to compile the SpTA in Figure 6.34 are highlighted in blue; and are spread across all targets. All trials are aligned on the beginning of the static grasp epoch, at time zero.

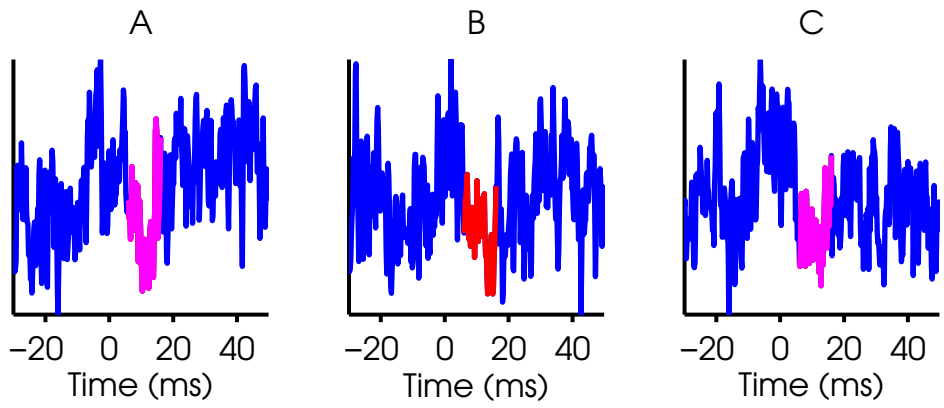

Figure 6.36: **SpTAs for session 597, cell spk003b, extensor digiti minimi:** An example of similar PSEs detected in two attitudes, and by using spikes occurring when JA values were at a specific range. **(A)** SpTA compiled using 513 spikes which overlapped times when the wrist flexion JA values were in the range of $40-70^{\circ}$ degrees (wrist extension). SSA p-value was 0.009, SSA-scan p-value was 0.04 **(B)** SpTA compiled using 99 spikes for the rectangle at the abduction target attitude. SSA p-value was 0.04. This PSS is at the same latency as the PSS in (A), and it occurred when the wrist was extended. **(C)** SpTA compiled using 95 spikes for the precision object at the horizontal target attitude. SSA p-value was 0.001. This PSS is at the same latency as the PSS in (A), and it occurred when the wrist was extended.

7.0 DISCUSSION

The motor cortex is the origin of the major direct path from cortex to muscles. Traditional analysis of this pathway is designed only to detect anatomical connectivity. Few studies have examined the effectiveness, or functional connectivity of this projection. These corticomotoneuronal (CM) cells, identified with physiological criteria signifying anatomical connectivity, make monosynaptic connections to motoneuronal pools in the spinal cord, but the analysis does not consider how this cortical output contributes to muscle contraction.

Conversely, we argue that even in the case of CM neurons, anatomical connectivity enables, but does not guarantee, functional connectivity. A single cortical neuron constitutes only a small fraction of all inputs to the motoneuronal pool, and the effects of its spikes depend on the simultaneous activity of all other motoneuronal inputs, as well as the state of the alpha motoneurons being facilitated. Hence, similar activity patterns of a CM cell result in different EMG patterns in its target muscles. In statistical terms, given a spike from a CM cell, the probability of observing a change in EMG activity of its target muscle is conditional on all other inputs to the motoneuronal pool. If functional connectivity is defined as the probability of observing a change in EMG activity of a muscle following the spikes of a cortical neuron, then, we suggest that functional connectivity is *conditional* on all inputs to the motoneuronal pool. The work presented in this thesis studies the principles of this dynamic functional connectivity between cortex and muscles.

Studying the relationship between motor cortical activity and movements following EMG activity is further complicated by the fact that the latter is not directly related to movements. First, the *combined* activity of multiple muscles acting on any joint determines the resulting joint movements. Second, the force generated by a muscle depends on the state of the joint (e.g. its orientation) and on other parameters, such as the muscle length, fatigue and velocity. Therefore, similar EMG activity patterns in a muscle might result in no movement, or different movements in the joints it

acts upon. The activity of a motor cortical neuron could then result in one of three possible outcomes: it could facilitate EMG, resulting in joint movement; it could facilitate EMG, resulting in no joint movement; or it could not facilitate EMG at all. Studying functional connectivity between motor cortical neurons and muscles is therefore an important step towards understanding the basic principles underlying motor control.

To study the way functional connectivity varies, we require a rich dataset with a wide repertoire of movements and muscle activations, using which we could generalize our conclusions. CM cells are thought to be involved in fine finger movements and direct control of wrist and finger muscles, and therefore we chose a task in which monkeys reached and grasped a variety of objects in different spatial orientations and locations.

During the task, we simultaneously recorded the activity of single neurons in the motor cortex, EMG activity from 16 muscles (see Table 3), and high-resolution kinematic data from the wrist and hands, enabling us to reconstruct hand movements with great detail. We focused our neural recordings on the caudal bank of the pre-central gyrus, an area that contains the majority of CM cells. We pursued three complementary directions of analysis: neural encoding of EMG and kinematic features; decoding of EMG and kinematic features; and the study of functional connectivity between neurons and muscles.

We began by testing neural correspondence to task parameters (Section 4.1). We found that 70% of the neurons were more active during *both* the reach and static grasp epochs than in the inter-trial epoch, indicating that most neurons did not divide into groups involved in either movements or generation of isometric force. Our sampled population of neurons divided into roughly three equal sized groups: one was more active during reach than during static grasp, the second was more active during static grasp than during the reach, and the third was similarly active in both. Interestingly, 90% of the neurons changed their firing rate according to the object being grasped, rather than its location or orientation, suggesting task dependent tuning.

We next studied how neurons encoded EMG and kinematic features (Sections 4.2, 4.3, 4.4) and concluded that neurons did not divide into distinct groups encoding either kinematics or EMG, but rather tended to encode both. However, neural firing rates were better predicted by joint angle values and velocities, than by EMG. Utilizing model selection techniques, we found that neuron-specific combinations of EMG and kinematic features were the best predictors of firing rates. How-

ever, neural firing rates were better predicted by joint angles and velocities, than by EMG. Overall, finger joint angle values and velocities accounted for most of the variance in the firing rates.

Muscle and kinematic synergies have been suggested as a possible way for the CNS to simplify the control of the high number of degrees-of-freedom in the hand. Studies using dimensionality reduction techniques have shown that EMG activity and kinematics collected during grasping movements can be represented in a lower dimensionality space, suggesting that these spaces are used by the motor cortex to control the hand. None of those studies investigated whether neural firing rates corresponded to the activation of those synergies. We used PCA and ICA to compute EMG and kinematic synergies, and investigated the correspondence of neural firing rates to the activation of both types of synergies (Section 4.5) and found that correlated joint movements and muscle activity, represented in the first few synergies extracted by PCA, were strongly encoded in the firing rates of many neurons. However, higher order synergies, representing individuated joint movements and muscle activity, were also encoded in the neural firing rates, but to a lesser extent. Since neurons encoded both lower and higher order synergies, our results do not support the idea that motor cortical neurons are controlling specific synergies.

In Section 4.6, we found that by combining the activity of sequentially recorded neurons, we were able to predict both EMG and joint angles, with average accuracies of 70% (measured by R^2). Since kinematic features were better represented in the firing rates of individual neurons, compared to EMG, we concluded that single neurons encoded EMG features weakly but consistently across the population.

Whether motor cortical neurons encode low-level parameters such as muscle force, or high-level parameters such as hand shape, their activity is combined by cortical networks, sub-cortical areas and spinal cord neurons, to facilitate muscle activation. Cortico-spinal functional connectivity indicates how motor cortical activity affects muscle activation, and was our focus in Chapter 6, where we investigated both long- and short-time scale functional connectivity from cortex to muscles. The weak linear relationship between neural firing rates and EMG, along with our finding that the population neural activity was a good predictor of EMG, led us to hypothesized that functional connectivity is dynamic in nature, and dependent on kinematic task requirements. That is, the effect that a single neuron's activity has on the facilitation of muscle activity changes as a function of the current and desired states of the hand. Any single motor cortical neuron potentially affects

multiple muscles, but its effect on any specific muscle depends on that muscle's contribution to moving the hand towards the desired task state.

We first examined how long-time scale functional connectivity between neurons and muscles changed across attitudes, assuming connectivity was static within attitudes (Section 6.1) and then estimated functional connectivity using sample correlations of the neural firing rates and the EMGs, using all repeat trials to every attitude. We concluded that neuron-muscle connectivity changed across attitudes, and were able to find 8 functional groups with similar correlation coefficients in our neural population; due to similarities in firing patterns for the different task epochs: i.e. neurons more active during the reach epoch, compared to the static grasp epoch, tended to show similar correlation coefficients to muscles.

We used two different models of long-time scale functional connectivity: an encoding model, predicting firing rate from a combination of all available EMGs and interaction terms between all available EMGs and kinematic features (Section 6.2); and a decoding model, predicting EMG of a single muscle, using the firing rate of a single neuron and interaction terms between all joint angles and the firing rate (Section 6.3). We compared the dynamic encoding model to a static model where the firing rate of the neuron was predicted by using EMG alone, and concluded that for all neurons, adding the dynamic terms improved firing rate prediction. We observed that wrist and MCP flexion JA values and velocities contributed most to the model, indicating they affected functional connectivity the most.

However, the improvement in firing rate predictions after adding the dynamic connectivity terms could also have been due to the extensive basis we provided the regression model with, by including all possible interactions between all EMGs and JAs. To eliminate this possibility, we used a decoding model, to examine functional connectivity in neuron-muscle pairs. We predicted single muscle EMG from a combination of the firing rate of a single neuron and interactions terms between all JAs and the firing rate. We modeled the interaction terms as linear dependencies of the firing rate contribution to EMG prediction on all JAs and compared these to a non-parametric model that predicted, predicting EMG from the firing rate of the neurons. The non-parametric model represented the best model we could fit, while ignoring dynamic functional connectivity. The decoding model outperformed the non-parametric model for 97% of the neurons we examined; suggesting that dynamic connectivity plays a role in how neurons facilitate muscles. To

eliminate JA-muscle correlations as the reason for the improved EMG prediction, we randomized the cortical firing rates and re-fit the decoding model. We found that for 96% of the neurons, the non-parametric model provided better EMG predictions than the randomized decoding model and concluded that 3-way correlation patterns between neurons, EMG and JA contributed to the decoding model, rather than 2-way correlations between EMG and JA. We observed that for the majority of neurons, wrist and finger flexion JA affected functional connectivity the most.

To provide additional support to our dynamic connectivity hypothesis, we studied short-term functional connectivity as well. Short-time scale functional connectivity is represented by post-spike effects (PSEs), brief changes in EMG (on the order of milliseconds), time-locked to spikes from a cortical neuron. PSEs represent activation of one or more alpha motoneuron, time-locked to the cortical spikes. The classical method of spike-triggered-averaging is often used to find PSEs, but it lacks a known significance level and its detection power is low for small sample sizes. We therefore developed two novel methods to detect PSEs, presented in Chapter 5: single-snippet analysis (SSA) and SSA-scan. This methods are formal, i.e. they provide p-values, and have an assured significance level, which is especially important in datasets with small sample sizes, like ours. Together, these methods are capable of finding PSEs at any post-spike latency.

We tested for PSEs in all available neuron-muscle pairs, using data from all attitudes combined, and found only a small number of statistically significant and convincing PSEs. The percentage of PSEs found was close to the 5% nominal significance level, opening the possibility that they were spurious. This was not surprising, since we expected functional connectivity to change between attitudes, and putative PSEs which would have appeared in certain attitudes, could be diluted when combining data across attitudes. We therefore tested for PSEs using spikes from every attitude separately, and found a higher percentage of PSEs; with some matching PSEs detected at similar post-spike latencies for different attitudes, which is consistent with dynamic connectivity. We used a simplified version of the long-term dynamic connectivity decoding model to find JA which affected the connectivity of every neuron-muscle pair; and then used a varying-coefficients model to detect the range of JA values at which long-time scale functional connectivity between the neuron and muscle was the highest. When the sample was limited to those specific optimal joint angle ranges, the PSE probability increased significantly indicating that PSEs were more likely to occur when long-term functional connectivity was high. In addition, the PSEs detected using

JA-triggered spikes often demonstrated similar latencies to PSEs found for the different attitudes for the same neuron-muscle pairs, providing additional, more specific, evidence to support our dynamic functional connectivity hypothesis.

We concluded that motor cortical neurons change their functional connectivity to muscles during reach-to-grasp movements, in a task-dependent manner. We suggest that the guiding principle governing changes in functional connectivity is that during movements, neurons are more likely to facilitate muscles which would move the wrist and hand towards a desired state. This desired state is determined by driving inputs to the cortical neurons, and is possibly somewhat represented in kinematic terms, as hinted by our findings that neurons are more linearly related to kinematic features than to EMG. Further studies are required to find how dynamic functional connectivity is affected by other parameters, such as force, muscle state and hand orientation.

BIBLIOGRAPHY

[1] S. N. Baker and R. N. Lemon. Computer simulation of post-spike facilitation in spike-triggered averages of rectified emg. *J Neurophysiol*, 80(3):1391–406, 1998. Baker, S N Lemon, R N Wellcome Trust/United Kingdom Research Support, Non-U.S. Gov't United states Journal of neurophysiology J Neurophysiol. 1998 Sep;80(3):1391-406.

[2] K. M. Bennett and R. N. Lemon. The influence of single monkey cortico-motoneuronal cells at different levels of activity in target muscles. *J Physiol*, 477 (Pt 2):291–307, 1994.

[3] N. A. Bernstein. *The Co-ordination and regulation of movements*. Pergamon Press Ltd., 1967.

[4] T. Brochier, R. L. Spinks, M. A. Umilta, and R. N. Lemon. Patterns of muscle activity underlying object-specific grasp by the macaque monkey. *Journal of Neurophysiology*, 92(3): 1770–1782, 2004.

[5] E. J. Buys, R. N. Lemon, G. W. Mantel, and R. B. Muir. Selective facilitation of different hand muscles by single corticospinal neurones in the conscious monkey. *J Physiol*, 381:529–49, 1986.

[6] A. J. Canty, A. C. Davison, D. V. Hinkley, and V. Ventura. Bootstrap diagnostics and remedies. *Canadian Journal of Statistics-Revue Canadienne De Statistique*, 34(1):5–27, 2006.

[7] A. d'Avella. Control of fast-reaching movements by muscle synergy combinations. *Journal of Neuroscience*, 26(30):7791–7810, 2006.

[8] Andrea d'Avella, Philippe Saltiel, and Emilio Bizzi. Combinations of muscle synergies in the construction of a natural motor behavior. *Nature Neuroscience*, 6(3):300–308, 2003.

[9] A. Davidson, R. Odell, V. Chan, and M. Schieber. Comparing effects in spike-triggered averages of rectified emg across different behaviors. *Journal of Neuroscience Methods*, 163 (2):283–294, 2007.

[10] A. G. Davidson, V. Chan, R. O'Dell, and M. H. Schieber. Rapid changes in throughput from single motor cortex neurons to muscle activity. *Science*, 318(5858):1934–1937, 2007.

[11] E. V. Evarts. Relation of pyramidal tract activity to force exerted during voluntary movement. *J Neurophysiol*, 31(1):14–27, 1968.

[12] E. E. Fetz and P. D. Cheney. Postspike facilitation of forelimb muscle activity by primate corticomotoneuronal cells. *J Neurophysiol*, 44(4):751–72, 1980.

[13] E. E. Fetz and D. V. Finocchio. Operant conditioning of specific patterns of neural and muscular activity. *Science*, 174(4007):431–5, 1971.

[14] E. E. Fetz and D. V. Finocchio. Operant conditioning of isolated activity in specific muscles and precentral cells. *Brain Res*, 40(1):19–23, 1972.

[15] E. E. Fetz and D. V. Finocchio. Correlations between activity of motor cortex cells and arm muscles during operantly conditioned response patterns. *Exp Brain Res*, 23(3):217–40, 1975.

[16] E. E. Fetz, P. D. Cheney, and D. C. German. Corticomotoneuronal connections of precentral cells detected by postspike averages of emg activity in behaving monkeys. *Brain Res*, 114(3): 505–10, 1976.

[17] E. E. Fetz, S. I. Perlmutter, Y. Prut, K. Seki, and S. Votaw. Roles of primate spinal interneurons in preparation and execution of voluntary hand movement. *Brain Res Brain Res Rev*, 40 (1-3):53–65, 2002.

[18] D. Flament and J. Hore. Relations of motor cortex neural discharge to kinematics of passive and active elbow movements in the monkey. *J Neurophysiol*, 60(4):1268–84, 1988.

[19] Jerome H. Friedman. Multivariate adaptive regression splines. *The Annals of Statistics*, 19 (1):1–67, 1991.

[20] Gustav Fritsch and Eduard Hitzig. On the electrical excitability of the cerebrum (in: Some papers on the cerebral cortex, translated and edited by von bomin g. springfield, il: Thomas, 1960, p. 73-96.). *Arch. f. Anat., Physiol. und wissenschaftl. Mediz., Leipzig*, (37):300–332, 1870.

[21] Q. G. Fu, D. Flament, J. D. Coltz, and T. J. Ebner. Temporal encoding of movement kinematics in the discharge of primate primary motor and premotor neurons. *J Neurophysiol*, 73(2): 836–54, 1995.

[22] A. P. Georgopoulos, J. F. Kalaska, R. Caminiti, and J. T. Massey. On the relations between the direction of two-dimensional arm movements and cell discharge in primate motor cortex. *J Neurosci*, 2(11):1527–37, 1982.

[23] A. P. Georgopoulos, A. B. Schwartz, and R. E. Kettner. Neuronal population coding of movement direction. *Science*, 233(4771):1416–9, 1986.

[24] S. B. Hamed, M. H. Schieber, and A. Pouget. Decoding m1 neurons during multiple finger movements. *Journal of Neurophysiology*, 98(1):327–333, 2007.

[25] M. T. Harrison and S. Geman. A rate and history-preserving resampling algorithm for neural spike trains. *Neural Comput*, 21(5):1244–58, 2009.

[26] Trevor Hastie, Robert Tibshirani, and J. H. Friedman. *The elements of statistical learning : data mining, inference, and prediction*. Springer series in statistics,. Springer, New York, NY, 2nd edition, 2009.

[27] C. M. Hendrix, C. R. Mason, and T. J. Ebner. Signaling of grasp dimension and grasp force in dorsal premotor cortex and primary motor cortex neurons during reach to grasp in the monkey. *J Neurophysiol*, 102(1):132–45, 2009.

[28] M. Hepp-Reymond, M. Kirkpatrick-Tanner, L. Gabernet, H. X. Qi, and B. Weber. Context-dependent force coding in motor and premotor cortical areas. *Exp Brain Res*, 128(1-2):123–33, 1999.

[29] R. N. Holdefer and L. E. Miller. Primary motor cortical neurons encode functional muscle synergies. *Experimental Brain Research*, 146(2):233–243, 2002.

[30] A. Hyngstrom, M. Johnson, J. Schuster, and C. J. Heckman. Movement-related receptive fields of spinal motoneurones with active dendrites. *The Journal of Physiology*, 586(6):1581–1593, 2008.

[31] T. Isa, Y. Ohki, B. Alstermark, L. G. Pettersson, and S. Sasaki. Direct and indirect cortico-motoneuronal pathways and control of hand/arm movements. *Physiology*, 22(2):145–152, 2007.

[32] Alan Julian Izenman. *Modern multivariate statistical techniques : regression, classification, and manifold learning*. Springer texts in statistics. Springer, New York ; London, 2008.

[33] A. Jackson, V. J. Gee, S. N. Baker, and R. N. Lemon. Synchrony between neurons with similar muscle fields in monkey motor cortex. *Neuron*, 38(1):115–25, 2003.

[34] A. Jackson, J. Mavoori, and E. E. Fetz. Correlations between the same motor cortex cells and arm muscles during a trained task, free behavior, and natural sleep in the macaque monkey. *Journal of Neurophysiology*, 97(1):360–374, 2007.

[35] R. J. Kasser and P. D. Cheney. Characteristics of corticomotoneuronal postspike facilitation and reciprocal suppression of emg activity in the monkey. *J Neurophysiol*, 53(4):959–78, 1985.

[36] H. G. Kuypers. Some aspects of the organization of the output of the motor cortex. *Ciba Found Symp*, 132:63–82, 1987.

[37] R. N. Lemon, G. W. Mantel, and R. B. Muir. Corticospinal facilitation of hand muscles during voluntary movement in the conscious monkey. *J Physiol*, 381:497–527, 1986.

[38] A. S. F. Leyton and C. S. Sherrington. Observations on the excitable cortex of the chimpanzee, orang-utan, and gorilla. *Experimental Physiology*, 11(2):135–222, 1917.

[39] C. R. Mason, J. E. Gomez, and T. J. Ebner. Hand synergies during reach-to-grasp. *J Neurophysiol*, 86(6):2896–910, 2001.

[40] B. J. McKiernan, J. K. Marcario, J. H. Karrer, and P. D. Cheney. Corticomotoneuronal postspike effects in shoulder, elbow, wrist, digit, and intrinsic hand muscles during a reach and prehension task. *J Neurophysiol*, 80(4):1961–80, 1998.

[41] B. J. McKiernan, J. K. Marcario, J. H. Karrer, and P. D. Cheney. Correlations between corticomotoneuronal (cm) cell postspike effects and cell-target muscle covariation. *J Neurophysiol*, 83(1):99–115, 2000.

[42] L. E. Miller, P. L. van Kan, T. Sinkjaer, T. Andersen, G. D. Harris, and J. C. Houk. Correlation of primate red nucleus discharge with muscle activity during free-form arm movements. *J Physiol*, 469:213–43, 1993.

[43] D. W. Moran and A. B. Schwartz. Motor cortical representation of speed and direction during reaching. *J Neurophysiol*, 82(5):2676–92, 1999.

[44] M. M. Morrow and L. E. Miller. Prediction of muscle activity by populations of sequentially recorded primary motor cortex neurons. *J Neurophysiol*, 89(4):2279–88, 2003.

[45] E. Olivier, S. N. Baker, K. Nakajima, T. Brochier, and R. N. Lemon. Investigation into non-monosynaptic corticospinal excitation of macaque upper limb single motor units. *J Neurophysiol*, 86(4):1573–86, 2001.

[46] S. A. Overduin, A. d'Avella, J. Roh, and E. Bizzi. Modulation of muscle synergy recruitment in primate grasping. *Journal of Neuroscience*, 28(4):880–892, 2008.

[47] L. Paninski. Superlinear population encoding of dynamic hand trajectory in primary motor cortex. *Journal of Neuroscience*, 24(39):8551–8561, 2004.

[48] L. Paninski, M. R. Fellows, N. G. Hatsopoulos, and J. P. Donoghue. Spatiotemporal tuning of motor cortical neurons for hand position and velocity. *J Neurophysiol*, 91(1):515–32, 2004.

[49] Wilder Penfield and Theodore Rasmussen. *The cerebral cortex of man; a clinical study of localization of function*. Macmillan, New York,, 1950.

[50] C. G. Phillips. Laying the ghost of 'muscles versus movements'. *Can J Neurol Sci*, 2(3): 209–18, 1975.

[51] E. Pierrot-Deseilligny. Transmission of the cortical command for human voluntary movement through cervical propriospinal premotoneurons. *Prog Neurobiol*, 48(4-5):489–517, 1996.

[52] Eric A. Pohlmeyer, Sara A. Solla, Eric J. Perreault, and Lee E. Miller. Prediction of upper limb muscle activity from motor cortical discharge during reaching. *Journal of Neural Engineering*, 4(4):369–379, 2007.

[53] A. V. Poliakov and M. H. Schieber. Multiple fragment statistical analysis of post-spike effects in spike-triggered averages of rectified emg. *J Neurosci Methods*, 79(2):143–50, 1998.

[54] A. V. Poliakov and M. H. Schieber. Limited functional grouping of neurons in the motor cortex hand area during individuated finger movements: A cluster analysis. *J Neurophysiol*, 82(6):3488–505, 1999.

[55] Robert Porter and Roger Lemon. *Corticospinal function and voluntary movement*. Monographs of the Physiological Society. Clarendon Press ; Oxford University Press, Oxford Oxford ; New York, 1993.

[56] J. A. Rathelot. Muscle representation in the macaque motor cortex: An anatomical perspective. *Proceedings of the National Academy of Sciences*, 103(21):8257–8262, 2006.

[57] J. A. Rathelot and P. L. Strick. Subdivisions of primary motor cortex based on cortico-motoneuronal cells. *Proceedings of the National Academy of Sciences*, 106(3):918–923, 2009.

[58] M. Saleh, K. Takahashi, Y. Amit, and N. G. Hatsopoulos. Encoding of coordinated grasp trajectories in primary motor cortex. *J Neurosci*, 30(50):17079–90, 2010.

[59] M. Saleh, K. Takahashi, and N. G. Hatsopoulos. Encoding of coordinated reach and grasp trajectories in primary motor cortex. *J Neurosci*, 32(4):1220–32, 2012.

[60] M. Santello, M. Flanders, and J. F. Soechting. Postural hand synergies for tool use. *J Neurosci*, 18(23):10105–15, 1998.

[61] M. H. Schieber. A spectrum from pure post-spike effects to synchrony effects in spike-triggered averages of electromyographic activity during skilled finger movements. *Journal of Neurophysiology*, 94(5):3325–3341, 2005.

[62] S. H. Scott, L. E. Sergio, and J. F. Kalaska. Reaching movements with similar hand paths but different arm orientations. ii. activity of individual cells in dorsal premotor cortex and parietal area 5. *J Neurophysiol*, 78(5):2413–26, 1997.

[63] Marshall Chance Spalding. *Characterizing the correlation between motor cortical neural firing and grasping kinematics*. PhD thesis, 2010.

[64] B. R. Townsend, L. Paninski, and R. N. Lemon. Linear encoding of muscle activity in primary motor cortex and cerebellum. *Journal of Neurophysiology*, 96(5):2578–2592, 2006.

[65] M. C. Tresch. Matrix factorization algorithms for the identification of muscle synergies: Evaluation on simulated and experimental data sets. *Journal of Neurophysiology*, 95(4):2199–2212, 2005.

[66] M. A. Umilta, T. Brochier, R. L. Spinks, and R. N. Lemon. Simultaneous recording of macaque premotor and primary motor cortex neuronal populations reveals different functional contributions to visuomotor grasp. *Journal of Neurophysiology*, 98(1):488–501, 2007.

[67] C. E. Vargas-Irwin, G. Shakhnarovich, P. Yadollahpour, J. M. K. Mislow, M. J. Black, and J. P. Donoghue. Decoding complete reach and grasp actions from local primary motor cortex populations. *Journal of Neuroscience*, 30(29):9659–9669, 2010.

[68] Valrie Ventura. *Bootstrap Tests of Hypotheses*, volume 7 of *Springer Series in Computational Neuroscience*, pages 383–398. Springer US, 2010.

[69] Larry Wasserman. *All of statistics : a concise course in statistical inference*. Springer texts in statistics. Springer, New York, 2004.

[70] E. J. Weiss. Muscular and postural synergies of the human hand. *Journal of Neurophysiology*, 92(1):523–535, 2004.